Phenomenological Aspects of Feebly Interacting Physics from Axions to Gravity

Beadle, Carl Robert

UNIVERSITÉ DE GENÈVE — FACULTÉ DES SCIENCES

Département de physique théorique — Professeur Francesco Riva

Département de physique théorique — Docteur Sebastian Ellis

Phenomenological Aspects of Feebly Interacting Physics from Axions to Gravity

THÈSE

Présentée à la Faculté des sciences de l'Université de Genève
Pour obtenir le grade de Docteur ès sciences, mention physique

Par

Carl Beadle

de

Winchester (Royaume-Uni)

Thèse N°5935

GENÈVE

.....

2025

UNIVERSITÉ DE GENÈVE

FACULTÉ DES SCIENCES

DOCTORAT ÈS SCIENCES, MENTION PHYSIQUE

Thèse de Monsieur Carl, Robert BEADLE

intitulée :

«Phenomenological Aspects of Feebly Interacting Physics from Axions to Gravity»

La Faculté des sciences, sur le préavis de

Monsieur F. RIVA, professeur assistant et directeur de thèse
Département de physique théorique

Monsieur S. ELLIS, docteur et codirecteur de thèse
Departement de Physique théorique

Madame C. BONVIN, professeure assistante
Département de physique théorique

Monsieur N. RODD, docteur
Theorical physics group, Lawrence Berkeley National Laboratory, Berkeley, USA

Monsieur M. MCCULLOUGH, docteur
Département de Physique théorique, CERN, Geneva, Switzerland

autorise l'impression de la présente thèse, sans exprimer d'opinion sur les propositions qui y sont énoncées.

Genève, le 2 août 2025

Thèse - 5935 -

La Doyenne

N.B. - La thèse doit porter la déclaration précédente et remplir les conditions énumérées dans les "Informations relatives aux thèses de doctorat à l'Université de Genève".

Abstract

The Standard Model constitutes an excellent effective description of nature for most strong, weak and electromagnetic processes. However a wealth of evidence exists telling us that there should be additional physics beyond it, coming from the combination of cosmological observation, experimental results and theoretical expectations. Additionally, recent concerted efforts have led to advances in modern small-scale precision experiments. They can be used to probe potential new weakly coupled light states, motivating studying them further. This thesis will make use of effective field theory techniques to explore a variety of topics relating to these light state extensions of the Standard Model. These techniques lead to applications which span from dark matter detection experiments to deriving theoretical positivity bounds, by using assumed fundamental principles such as unitarity and causality.

We begin by analysing the discovery potential of a specific class of dark matter experiments; spin-precession experiments. Concretely, we estimate their sensitivity to additional dark matter candidates that couple to electromagnetism directly; a kinetically mixed dark photon and axion with coupling $g_{a\gamma\gamma}$. If the dark matter couples weakly to electromagnetism, then it is possible to use such a spin-polarised sample to detect an induced magnetic field. This is because the magnetic shielding of such an experiment can be 'rung-up' by the dark matter. The sample is then affected by the genuine magnetic field that is induced. It is projected that if CASPEr-Gradient can measure the spin coupling at the level predicted for the QCD-axion then such a setup has sensitivity of $\epsilon \simeq 3 \cdot 10^{-16}$ and $g_{a\gamma\gamma} \simeq 2 \cdot 10^{-16}\,\mathrm{GeV}^{-1}$ for masses near $m \simeq 1\mu\mathrm{eV}$.

Following this we will see how geophysical phenomena can be exploited to search for these same dark matter candidates. We show that resonant conversion of dark matter into photons can occur in Earth's ionosphere, constituting a well-modelled and observed natural plasma environment. These qualities make it full of experimental potential for discovering dark matter. Through explicit computation of the signal and comparison with the dominant noise source of anthropogenic noise, we find that a simple antenna experiment has projective sensitivity of $\epsilon \simeq 10^{-14}$ and $g_{a\gamma\gamma} \simeq 10^{-11}\,\mathrm{GeV}^{-1}$ for masses in the range $10^{-9}\,\mathrm{eV} \lesssim m \lesssim 10^{-8}\,\mathrm{eV}$. Additionally these projections can be improved upon in a number of ways.

We then explore the phenomenological consequences of the quadratic coupling of QCD-axions to photons. Such an operator is shown to be more relevant in analysis than one might naïvely expect, taking inspiration from the analogous operator for pions. The unitarity of the theory demands that the coupling is reasonably sized. Motivating UV constructions are given for axion-like particles, to show that such large quadratic couplings are ubiquitous for all axions. We also explore how this imposes constraints on ultralight axions that make up dark matter.

Properties of effective QFTs such as unitarity, causality and locality can be used to constrain the coefficients of the effective action in this way quite generally. In the final sections we explore how such conditions are found in theories involving dynamical gravity, a case where standard techniques become ill-defined. Newly developed techniques are proposed. They are then used to place conservative theoretically consistent constraints on the space of theories involving light scalars and gravity. We see that these techniques remain robust under the inclusion of non-analytic loop effects, lending credence to their validity.

Résumé

Le modèle standard de la physique des particules (Standard Model) constitue une excellente description effective de la nature pour la plupart des processus d'interaction forte, faible et électromagnétique. Il existe une multitude de preuves indiquant qu'il devrait y avoir une physique supplémentaire au-delà, provenant de la combinaison d'observations cosmologiques, de résultats expérimentaux et d'attentes théoriques. En outre, des récents efforts concertés ont permis de progresser dans les expériences modernes de précision à petite échelle. Elles peuvent être utilisés pour sonder de potentiels nouveaux états légers faiblement couplés, ce qui motive l'étude de les approfondir. Cette thèse utilisera les techniques de la théorie effective des champs pour explorer une variété de sujets relatifs à ces extensions du Standard Model sous la forme d'états légers. Ces techniques conduisent à des applications qui vont des expériences de détection de la matière noire à la dérivation de limites théoriques de positivité, en utilisant les principes fondamentaux supposés tels que l'unitarité et la causalité.

Nous commençons par analyser le potentiel de découverte d'une classe spécifique d'expériences sur la matière noire, les expériences de précession de spin. Concrètement, nous estimons leur sensibilité à des candidats supplémentaires à la matière noire qui se couplent directement à l'électromagnétisme; un photon et un axion sombres cinétiquement mélangés avec un couplage $g_{a\gamma\gamma}$. Si la matière noire se couple faiblement à l'électromagnétisme, il est possible d'utiliser un tel échantillon polarisé en spin pour détecter un champ magnétique induit. En effet, le blindage magnétique d'une telle expérience peut être « remonté » par la matière noire. L'échantillon est alors affecté par le véritable champ magnétique induit. Les projections indiquent que si CASPEr-Gradient peut mesurer le couplage de spin au niveau prédit pour l'axion QCD, un tel dispositif a une sensibilité de $\epsilon \simeq 3 \cdot 10^{-16}$ et $g_{a\gamma\gamma} \simeq 2 \cdot 10^{-16}\,\mathrm{GeV}^{-1}$ pour des masses proches de $m \simeq 1\mu\mathrm{eV}$.

Nous verrons ensuite comment les phénomènes géophysiques peuvent être exploités pour rechercher ces mêmes candidats à la matière noire. Nous montrons que la conversion résonnante de la matière noire en photons peut se produire dans l'ionosphère terrestre, qui constitue un environnement naturel de plasma bien modélisé et observé. Ces qualités en font un site plein de potentiel expérimental pour la découverte de la matière noire. Grâce au calcul explicite du signal et à la comparaison avec la source de bruit dominante qu'est le bruit anthropique, nous constatons qu'une simple expérience d'antenne a une sensibilité projective de $\epsilon \simeq 10^{-14}$ et de $g_{a\gamma\gamma} \simeq 10^{-11}\,\mathrm{GeV}^{-1}$ pour des masses dans la gamme $10^{-9}\,\mathrm{eV} \lesssim m \lesssim 10^{-8}\,\mathrm{eV}$. En outre, ces projections peuvent être améliorées de différentes façons.

Nous explorons ensuite les conséquences phénoménologiques du couplage quadratique des axions QCD aux photons. Nous montrons qu'un tel opérateur est plus pertinent dans l'analyse que ce que l'on pourrait attendre naïvement, en nous inspirant de l'opérateur analogue pour les pions. L'unitarité de la théorie exige que le couplage soit grand. Nous motivons ces considérations par des constructions UV pour les particules de type axion, afin de montrer que de tels couplages quadratiques sont omniprésents pour tous les axions. Nous explorons également comment cela impose des contraintes sur les axions ultralégers qui constituent la matière noire.

Les propriétés des théories quantiques des champs (QFT) effectives telles que l'unitarité, la causalité et la localité peuvent être utilisées pour contraindre les coefficients de l'action effective de cette manière assez générale. Dans les dernières sections, nous explorons comment ces conditions sont trouvées dans les théories impliquant la gravité dynamique, un cas où les techniques standard deviennent mal définies. Des techniques nouvellement développées sont proposées. Elles sont ensuite utilisées pour placer des contraintes conservatrices théoriquement cohérentes sur l'espace des théories impliquant des scalaires légers et la gravité. Nous constatons que ces techniques restent robustes lors de l'inclusion d'effets de boucle non analytiques, ce qui donne du crédit à leur validité.

Acknowledgements

This thesis would not exist in this form without the extensive help from my supervisors Sebastian Ellis and Francesco Riva, to whom I am indebted for more than just revisions, physical insight and support. If I can take half of their intuition and zeal for the minutia of a physical problem forward with me in my career, I'll be doing well. I'm very grateful for the numerous discussions with both of them that shaped my understanding of BSM physics immensely. The variety of opportunities to go abroad for summer schools, workshops and conferences would equally not have been possible without them, so thank you both again. Finally, I have to also thank them for fostering such an amicable environment in the group; I don't think that I could have asked for a better environment in which to study for this PhD.

This naturally brings me to thanking past and present members of the group at UNIGE; Kara Farnsworth, Brian Henning, Denis Karateev, Dimitrios Kosmopoulos, Jonathan Kley, Marc Riembau, Philipp Schicho, Matt Walters, Fabio Bernardo, Francesco Bertucci, Olivier Delouche, Giulia Isabella, Davide Lombardo, Davide Perrone, Sara Ricossa and Francesco Serra. All of you have given me such different and useful perspectives on what it means to study high energy physics, and really opened my mind to the true span of the topic. It has been a joy to collaborate with you. Who would have thought that climbing, board games and drinks would be so important for research? Equally, the office would not have been as enjoyable a place without Francesco Iacovelli, Andrea Ianniccari, Niccolò Muttoni, Pietro Pelliconi and especially Martin Pijnenburg who was forced to listen to my drivel.

I am hugely appreciative of my amazing non-local collaborations too; Paolo Bilisco, Andrea Caputo, Luc Darmé, Jacob Leedom, Raffaele Tito D'Agnolo, Jérémie Quevillon, Mario Reig, Nick Rodd, Hoa Vuong and Tevong You. I learned a lot from you about physics, the nature of research and how to present your work to others. I hope to use this advice wisely.

Special thanks to Surjeet Rajendran, for inviting me over to Baltimore and Asher Berlin for hosting me at Fermilab. That trip refreshed me like nothing else could. I must also thank Prateek Agrawal, Andrei Parnachev and Dymtro Volin, all of whom have given me solid advice, or a break at key moments, which I'll always remember.

The doctoral journey allows you to meet some great people along the way; Caleb, Jury, Amara, Dalila, Eren, Koschi and Rémy, thanks for all the laughs. It has been great getting to know you.

I want to thank my family for appreciating me in spite of my physics; Mum, Dad, Anna, Kate and Emma. Thank you for your support throughout this process, and for putting up with my pointless rants even if they were too filled with jargon to be intelligible. Additionally, a very direct thank you to Dodo and Granda for their support during my time in Dublin that helped me to get here. A special thanks to my Grandmon, for educating the masses in the UK about current physics research, whether they like it or not!

Most deservingly, thank you Han, for many more reasons than I can write here. I cannot wait for our next chapter to unfold together in Canada.

Contents

Chapter 1

Introduction

1.1 Introduction overview

The central topic of this thesis is very low energy particle phenomenology and its description through the use of effective field theory (EFT) methods. EFT-like methods have always been employed throughout physics, long before QFT existed, in that the relevant scales for a given problem are always identified before a calculation is performed. For example in our Solar system of approximate size 10^{14} m, for astrophysical sized effects like the orbits of planets, the most relevant force to consider is gravity and the others are safely ignored. This is because gravity is mediated by a massless boson. Zooming in to 10^{11} m, we appreciate that electromagnetism becomes relevant, as the Solar wind influences the plasma surrounding the planets. Strictly speaking electromagnetism is also mediated by a massless boson, and so should propagate infinitely far like gravity meaning that it is difficult to pin the exact scale where electromagnetic effects become relevant. One major reason that we do not consider electromagnetism in astrophysics is that we are lucky to live in a Universe which is charge neutral; electromagnetic waves are screened on long length scales and also will not interact strongly with large uncharged objects such as the Earth. These two forces, and in particular electromagnetism, reign supreme from anthropic scales, right past atomic lengths down to the sizes of nuclei, roughly larger than 10^{-15} m, within the Sun. Here, the nucleons within nuclei are bound together by the exchange of pions, which give the first hints of the existence of nuclear forces. The pion mediators have a characteristic mass preventing them from being relevant at larger distances. The effective theory used to describe the interactions of pions and nucleons is called chiral perturbation theory (χPT). We observe that the nuclei within the Sun fuse together to make larger nuclei emitting photons and neutrinos. In order to understand this more properly, we have to zoom in further. Below 10^{-15} m the strong force is seen to be mediated by gluons, with the baryons and mesons composed of quarks and gluons. On these scales and smaller quantum chromodynamics (QCD) becomes the relevant description for the strong nuclear force. If we are to look at scales on the order 10^{-18} m, then we see that the weak nuclear force is mediated by additional massive bosons. The relevant description to use for processes with comparable energies would be the Standard Model. This can be used to explain the addition of the neutrinos in the earlier nuclear fusion. Beyond these length scales we know that we should expect something to happen before 10^{-35} m, as this is where quantum mechanical effects from gravity are expected to become relevant.

In this thesis we will discuss a variety of applications of EFTs. We will first use EFTs pragmatically to study the relevant phenomenology for dark matter experiments. After this we will explore the theoretical self-consistency of EFTs, in particular for theories involving gravity. Throughout this introduction we will develop the EFT perspective necessary to understand these goals. The tenets for the EFT user will be introduced through an exploration of the standard model EFT. Before this we will introduce a motivating example that predates QFT, to show that the EFT philosophy is a natural refinement of older techniques.

Hydrogen Model Once the relevant scale has been identified, there is still work to do. We have to identify the most appropriate mathematical framework to use, the symmetries of the problem and whatever remaining

ratios of scales can be taken. We can step back and identify one archetypical example coming from the early days of quantum mechanics when physicists wanted a good model of the hydrogen atom, that could hopefully be extended to more complicated atoms. Their problem was threefold: they had to identify the relevant framework for their calculations, the symmetries of the problem and whatever dimensional parameters seemed most relevant to the atom. Heisenberg and Schrödinger saw two separate sides of the quantum mechanical coin while trying to find the new framework. Their viewpoints initially seemed unrelated until Dirac revealed that their formulations of quantum mechanics were actually the same, and that the problems were nicely formulated in terms of Hamiltonian mechanics. This defined the framework. For an atom, it would seem very unnatural that the dynamics of the electron around the nucleus should depend very strongly on the microphysics within the nucleus itself, with approximate size 10^{-15} m. This can be substantiated upon by looking at the multipole expansion of the electron's Coulomb interaction with the nucleon's internal degrees of freedom and we see that the dipole is suppressed by $R_{\text{nucleus}}/R_{\text{atom}} \sim 10^{-5}$. Therefore the system was taken to be well described by the Hamiltonian

$$H = \frac{\mathbf{p}_e^2}{2m_e} + \frac{\mathbf{p}_p^2}{2m_p} - \frac{\alpha}{|\mathbf{r}_e - \mathbf{r}_p|}\,, \tag{1.1}$$

where $\mathbf{p}_{e/p}$, $\mathbf{r}_{e/p}$ and $m_{e/p}$ are the momenta, displacement and masses of the electron and proton respectively, which should be the appropriate degrees of freedom, and α is the fine structure constant. We work to leading order in α, as it is measured to be a small number. Since the electron is much lighter than the proton, m_e is approximately equal to the reduced mass of the system, allowing the motion of the proton to be effectively decoupled from the electron in the centre of mass coordinates in the infinitely heavy limit for the proton. In this language we now see that the above Hamiltonian has a good $SO(3)$ rotational symmetry about the proton. More formally, this means that the Hamiltonian commutes with $L^i = \epsilon_{ijk} r_e^j p_e^k$. It should be stressed here that the symmetries of a physical problem simplify analysis hugely, so it is very beneficial to identify them early.[1] Because the energy of the system is the eigenvalue of the Hamiltonian, we see that the energies cannot depend on the angular momentum quantum numbers, otherwise rotations would change them. This implies that the answer can only depend on the principal quantum number n whose size is related to the radius, and on physical grounds we know that as n increases an electron's energy should increase, because the electron will be less tightly bound to the proton. We can also use dimensional analysis to see that the only length and energy scales in the problem that can be constructed are $(m_e\alpha)^{-1}$ and $m_e\alpha^2$ respectively. It can be shown using the semi-classical methods of Bohr's model [1] that the radius scales proportionally with n^2. Combining these facts gives the formula for the energy levels for hydrogen

$$E_n = -\frac{m_e\alpha^2}{2n^2}\,. \tag{1.2}$$

We did not need to solve the Schrödinger equation to find this answer, merely identify the relevant framework, symmetries and scales of the problem was sufficient. We also made use of the large ratios of the measured dimensionful quantities to enhance the rotational symmetry.

Standard Model EFT This notion has been honed over time to a high level of sophistication in particle physics [2–5]. Here the ultimate goal is to describe the entire particle content of our Universe. As non-relativistic Hamiltonian mechanics was the most appropriate framework for the atom, QFT is the most appropriate for this task. Symmetry plays an even more important role than it did for the Hydrogen atom, as the particles themselves are classified by their symmetry properties. The appropriate scales are those of the relevant operators in the effective action, and also the cutoff scale of the EFT, this is the energy scale near which new particle content or new dynamics is expected. The standard model (SM) of particle physics consists of the renormalizable part of a larger EFT [6–9]. Its particles are representations of the Poincaré group; 12 fermions and 13 bosons. Each of the particles is charged under the gauge group $SU(3)_C \times SU(2)_L \times U(1)_Y$ according to the experimentally determined values and such that there are no gauge anomalies, summarised in the following table

[1] Further, the Universe's particle content seems to be organised by its symmetry structure.

Q_i	u_i^c	d_i^c	L_i	e_i	φ
$(\mathbf{3},\mathbf{2})_{1/6}$	$(\bar{\mathbf{3}},\mathbf{1})_{-2/3}$	$(\bar{\mathbf{3}},\mathbf{1})_{1/3}$	$(\mathbf{1},\mathbf{2})_{-1/2}$	$(\mathbf{1},\mathbf{1})_{1}$	$(\mathbf{1},\mathbf{2})_{1/2}$

Table 1.1: Standard model particle charge assignment.

The Lagrangian for this EFT can be written as the sum of all singlet operators made from these fields,

$$\mathcal{L} = \mathcal{L}_{\leq 4} + \sum_n \frac{1}{\Lambda_{\text{n.p.}}^n} \mathcal{O}_n \,, \tag{1.3}$$

where $\mathcal{L}_{\leq 4}$ contains the relevant and marginal operators and the remaining 'irrelevant' operators are suppressed by the scale of new physics $\Lambda_{\text{n.p.}}$. Relevant operators are those with negative mass dimension, marginal operators are dimensionless and irrelevant have negative mass dimension. The operators of $\mathcal{L}_{\leq 4}$ form the following SM Lagrangian

$$\begin{aligned}\mathcal{L}_{\leq 4} = &-\frac{1}{4} G^A_{\mu\nu} G^{A\mu\nu} - \frac{1}{4} W^I_{\mu\nu} W^{I\mu\nu} - \frac{1}{4} B_{\mu\nu} B^{\mu\nu} + \left(D_\mu \varphi\right)^\dagger \left(D^\mu \varphi\right) + \mu^2 \varphi^\dagger \varphi - \lambda \left(\varphi^\dagger \varphi\right)^2 \\ &+ i \left(\bar{L}^i \not{D} L^i + \bar{e} \not{D} e + \bar{Q}^i \not{D} Q^i + \bar{u}^i \not{D} u^i + \bar{d}^i \not{D} d^i\right) - \left(Y^e_{ij} \bar{L}^i \, \varphi e^j + Y^u_{ij} \bar{Q}^i \tilde{\varphi} u^j + Y^d_{ij} \bar{Q}^i \varphi d^j \; + \text{h.c.}\right) \,,\end{aligned} \tag{1.4}$$

where G, W and B denote the gauge bosons, φ is the Higgs boson, $\tilde{\varphi^I} = \epsilon_{IJ} (\varphi^J)^\star$, the fermion doublets are denoted by capital letters, the Yukawa matrices are denoted by Y and the flavour indices are left explicit. The above Lagrangian accounts for the electroweak symmetry breaking we see in nature when the Higgs field gains its expectation value and the well-known story that follows [10–13]. The most relevant effects are captured by this part of the Lagrangian and the higher order operators are omitted in the spirit of EFTs.

It is noteworthy that the accidental global symmetries of Baryon number conservation $U(1)_B$ and the Lepton number conservation laws $U(1)_L$ are an output of this construction. The symmetries do not require any specific values for the Yukawas, or other measured parameters, only that the irrelevant operators be ignored, due to a large separation of scales before new physics appears. These symmetries are explicitly broken upon the inclusion of the irrelevant operators in the EFT, for example the Lepton number violation occurs upon the inclusion of the dimension 5 Weinberg operator[2]

$$\mathcal{L}_5 = \frac{c_{ij}}{M} \left(\bar{\tilde{L}}^i \, \varphi\right) \left(\tilde{\varphi}^\dagger \, L^j\right) \, + \text{h.c} \,. \tag{1.5}$$

So, baryonic and leptonic conservation is expected until at least some high scale '$M \gg 100\,\text{GeV}$', near where the SM is assumed to be UV completed. It is an experimental fact that both of these symmetries are respected quite well in nature [14], which could imply that the physics corresponding to (1.5) is high-scale. This is a perfectly valid explanation for the quality of the symmetries which moves the explanation to higher scales.

Furthermore, there are additional approximate symmetries of the SM that emerge once some values of the SM input parameters have been measured. These can be used advantageously in modelling the lower energy phenomena we observe. For example, there are approximate chiral symmetries for the low mass quarks broken both by confinement and their non-zero masses. There are also approximate flavour symmetries like the $SU(3)_V$ symmetry leading to the famous *eightfold way* and also incidentally the isospin symmetries of the lower energy hadrons. These are themselves broken by the mass differences of the light quarks. We see that the symmetry breaking pattern [15–18] is extremely important in constructing a low energy theory. We can use all the symmetries to build another lower energy EFT called chiral perturbation theory (χPT) to describe the dynamics of the low energy hadrons [19–21]. The way this works practically is that one begins with the chiral symmetries and then specifies the symmetry breaking pattern by saying that the quark condensate spontaneously breaks the chiral symmetries to the diagonal

$$SU(2)_L \times SU(2)_R \to SU(2)_V \,, \tag{1.6}$$

[2] A non-unique list of dimension 6 and lower operators in non-redundant bases can be found in [7, 8].

for example, in the case of the up and down quarks. Then one builds an EFT by using the coset construction, matching the global currents in the high energy theory to those in the low energy theory. For the up and down quark example, we can define the 2×2 matrix U containing the pions that transform non-linearly under the $SU(2)_V$

$$U = \exp\left(i\frac{\sqrt{2}}{f_\pi}\Pi\right) \quad \text{with} \quad \Pi = \begin{pmatrix} \pi^0/\sqrt{2} & \pi^+ \\ \pi^- & -\pi^0/\sqrt{2} \end{pmatrix} . \tag{1.7}$$

Further breaking can be accounted for by using spurions. As an example, one can account for the quark masses, which explicitly break the symmetries, by introducing a spurious mass 'field' χ that transforms covariantly under the symmetries and then setting it to a background value in the low energy theory. Such a construction is used to describe pion dynamics at energies far below the chiral symmetry breaking scale set by $\Lambda_{\rm QCD}$, resulting in the Lagrangian

$$\mathcal{L} = \frac{f_\pi^2}{4}\mathrm{Tr}\left(\partial_\mu U \partial^\mu U^\dagger + \chi U^\dagger + \chi^\dagger U\right) . \tag{1.8}$$

The pions can also be coupled to gauge fields by introducing a covariant derivative such as

$$D_\mu U = \partial_\mu U + ie\, A_\mu \left[Q, U\right] , \quad \text{with} \quad Q = \begin{pmatrix} 2/3 & 0 \\ 0 & -1/3 \end{pmatrix} . \tag{1.9}$$

This construction will be very useful in chapter 4, where it is minimally modified by the presence of an additional light pseudoscalar field.

Today the study of low energy phenomena is well-motivated, both experimentally and theoretically, for those interested in extending the SM. While its successes cannot be downplayed, beyond the Standard Model (BSM) physics is necessary to explain various issues associated with observations and theoretical issues. The SM's problems are not singular in their nature in that there are several seemingly unrelated issues, coming from cosmology, high-energy experiment and internal theoretical questions. In this introduction we will point out a number of the SM's issues, which motivate the study of low energy phenomenology that follows in the remaining chapters of this thesis. We will do this by starting with operators of highest dimension in the EFT and moving down in dimension to the most relevant. Not all of the SM's problems are discussed here, for example there will be no mention of neutrino oscillations [22], nor problems associated with flavour [23].

1.2 Is dark matter irrelevant?

Given the successes of the SM, all of the operators higher than dimension 4 are suppressed by the scale of new physics which is assumed to be much larger than the electroweak scale. This is precisely why the nomenclature of irrelevant operators is appropriate. All operators are constructed to be singlets under the SM symmetries, where the expectation is that the SM symmetry group is contained within the group of the UV complete theory. UV completions of the SM can be matched to the coefficients of the SMEFT in order to impose constraints [24–27].

Dark Matter A noteworthy problem highlighted by these (and all other operators in the SMEFT) is that there is insufficient particle content to correctly account for the observed Dark Matter (DM) making up $\sim$ 25% of the energy budget of the Universe. DM is required to explain a variety of astrophysical observations, for example to explain structure formation [28], the rotation velocities of galaxies [29] and the centre of mass positions in galactic collisions [30, 31]. Furthermore, there is evidence for its existence from CMB measurements [32]. There are also few compelling alternatives to the DM paradigm, without a considerable modification of our understanding of gravity [33, 34]. Additionally, alternative explanations can often describe one phenomenon well, but also require the presence of additional DM to explain the remaining observations[35], motivating the study of DM phenomenology further.

SM particles lack the required properties to explain the observed phenomenon attributed to DM. DM is not relativistic [36], ruling out the worst potential SM DM candidate of the photon immediately. Additionally,

DM should couple weakly (if at all) to light, or it would have been observed by non-gravitational means, meaning that none of the charged leptons or hadrons are viable. It should also be relatively stable [37], which discounts the unstable weak bosons and any mesons, or potential glueballs formed in the strong sector [38]. Unbound neutral hadrons like the neutron are also unstable, meaning that the only possibilities for hadronic matter to make up DM comes from composite dark objects called massive compact halo objects (MACHOs), or more exotic states such as strangelets [39]. MACHOs do allow for a percentage of DM to be made from SM matter, but crucially not all of DM can be accounted for this way [40–42]. This leaves the neutrinos as the only remaining SM option; they are electrically neutral, interact very weakly and appear massive. However, they move too fast upon production. Even if they could be produced in a way that were sufficiently '*cold*', the Pauli exclusion principle prevents them from having a large enough number density required to match the inferred energy density required [43]. One possibility is that right-handed neutrinos make up the DM, these are not present in the SM as written above [44]. They would couple to the SM Lagrangian through a renormalizable neutrino portal ($Y^\nu \bar{L}\varphi N + \text{h.c.}$), unless a symmetry were to forbid the operator. This alone motivates the extension of the SM by additional particle content.

WIMPs Particle DM remains a compelling hypothesis to explain the missing energy density. Existing evidence does not pinpoint any particular mass, nor coupling strength to visible matter. The irrelevant operators in the SMEFT may offer potential explanations by encoding information of BSM dark sectors. New particles are expected to appear at the scale of the UV completion. This new particle content, if sufficiently stable, can make up the DM. We can postulate the existence of an additional heavy particle χ that interacts with SM particles very weakly, through a coupling $g \ll 1$. By dimensional analysis it will have a scattering cross-section annihilating into SM particles scaling as $\sigma \sim g^4/m_\chi^2$. This allows the DM abundance to be populated thermally in the early Universe, in a *freeze-out* mechanism. An approximate solution of the Boltzmann equation for the χ number density shows that the energy density is inversely proportional to the thermally averaged cross-section and velocity of χ

$$\frac{\Omega_\chi}{(0.27)} = \frac{10^{-26}\,\text{cm}^3\,\text{s}}{\langle \sigma_\chi\, v_\chi \rangle}\,. \tag{1.10}$$

Fixing the annihilation cross-section to have that near the weak scale allows the DM density to be consistent with observation. Variations on this argument and supersymmetric extensions of the SM, where SM superpartners like Higgsinos or Winos are expected, motivated the weakly interacting massive particle (WIMP) to become the archetypical DM candidate. The above argument is known as the WIMP miracle as it seemed to predict that the WIMP should exist near the electroweak scale. Unfortunately, the WIMP has not been discovered in any DM matter experiment and constraints on it are becoming increasingly tight. WIMP parameter space is now highly constrained from null results at large-scale scattering direct detection experiments [45–49], LHC searches [50, 51] and astrophysical searches [52–55]. Looking again at the cross-section $\sigma \sim g^4/m_\chi^2$ we see that the mass can naïvely be much larger than the weak scale if the coupling is brought down to compensate, which could either be achieved by some tuning or as the result of loop factors.

There is a theoretical upper limit for the mass of these WIMPs. Because their abundance is populated thermally, it has been shown using unitarity ($g \ll 4\pi$) that they can have masses of at most $\lesssim 100\,\text{TeV}$ [56]. This constraint on masses can be circumvented if there is no requirement that the relic abundance is populated thermally. Opening this door allows the number of DM particle candidates to grow enormously, leading to a modern hypothetical particle zoo, spanning many orders of magnitude in mass and incorporating particles of many different kinds. The theoretical upper bound for a DM particle now comes from equating the size of a particle to its Schwarzschild radius; the largest mass it can have before just being a black hole $m_{\text{DM}} \lesssim 10^{19}\,\text{GeV}$. The lowest mass is constrained by the fact that the DM must be at least as small as the smallest Galaxies that we have observed $m_{\text{DM}} \gtrsim 10^{-21}\,\text{eV}$ [57]. This results in a mass window spanning ~ 50 orders of magnitude [58]!

Light Bosonic DM One possible mechanism to form the DM abundance called the misalignment mechanism applies to bosons, it can lead to DM candidates which have extremely different phenomenology to a WIMP, and that are not accounted for in the SM Lagrangian as written. It can be shown that light bosons 'ϕ' may

redshift as DM with the correct abundance by considering their equation of motion in a background FLRW metric, after inflation. The equation of motion is

$$\ddot{\phi} + 3H\dot{\phi} + V'(\phi) = 0\,, \tag{1.11}$$

such that near the potential minimum the last term is well approximated by $m_\phi^2\phi$. This equation can be solved generically for any equation of state $\omega \neq -1$.

$$H = \frac{2}{3\,t}\left(\frac{1}{\omega+1}\right) \quad \Longrightarrow \quad \phi(t) = (mt)^{1/2-1/(1+\omega)}\left[\phi_1\,\mathcal{J}_{\left[\frac{1}{2}-\frac{1}{1+\omega}\right]}(mt) + \phi_2\,\mathcal{Y}_{\left[\frac{1}{2}-\frac{1}{1+\omega}\right]}(mt)\right]\,, \tag{1.12}$$

where $\phi_{1,2}$ are undetermined coefficients, $\mathcal{J}$ and $\mathcal{Y}$ are Bessel functions. For example, in radiation domination, where $\omega = 1/3$, this solution becomes

$$\phi(t) = (mt)^{-1/4}\left[\phi_1\,\mathcal{J}_{\frac{1}{4}}(mt) + \phi_2\,\mathcal{Y}_{\frac{1}{4}}(mt)\right]\,. \tag{1.13}$$

If $\dot{\phi}|_{t=0} = 0$, then the field remains frozen near its initial values for some time of size $\sim m^{-1}$, due to Hubble friction. One such light bosonic candidate is a pseudoscalar called an axion-like particle (ALP). It is assumed to arise from the breaking of a symmetry at some scale f_a, as the Goldstone boson of the spontaneously broken group. Assuming that there is standard cosmology, it can be shown [59] that the relic abundance associated to such a field formed by this mechanism is

$$\Omega_a \simeq 0.26\left(\frac{f_a\,\theta_0}{1.9\times10^{13}\,\mathrm{GeV}}\right)^2\left(\frac{m_a}{1\,\mu\,\mathrm{eV}}\right)^{\frac{1}{2}}\left(\frac{90}{g_\star\,(T_{\mathrm{osc}})}\right)^{\frac{1}{4}}\,, \tag{1.14}$$

where f_a is the symmetry breaking scale, θ_0 is the initial misalignment angle of the ALP in its potential, the combination $f_a\theta_0$ is the initial field value, m_a is the mass of the ALP, and $g_\star(T_{\mathrm{osc}})$ is the number of relativistic degrees of freedom at the onset of oscillations[3]. This is interesting as it implies these bosonic particles can be made incredibly light, and still account for the observed DM in the Universe.

Although little is known about the specific particle properties to give preference to one candidate over another, some DM parameters can still be estimated using simple methods. Our local relative velocity through the DM halo can be found by appealing to the virial theorem. The virial theorem states that our speed at our radius in the galactic disk is given by

$$\langle v^2\rangle \simeq \frac{GM(R)}{R}\,, \tag{1.15}$$

where $R_\oplus \simeq 8.3$ kpc is our radius from the galactic centre and $M(R_\oplus) \simeq 10^{11}M_\odot$ is the total mass enclosed within this radius, resulting in the value $\langle v^2\rangle \simeq (220\mathrm{km\,s^{-1}})^2 \sim (10^{-3})^2$. It is also possible to infer the local energy density of the DM by a variety of means, one of which is to consider nearby stellar tracers and infer the local gravitational potential by modelling the vertical harmonic oscillations about the plane of the disk [64]. The value obtained by doing this is $\rho_{\mathrm{DM}} \sim 0.3\,\mathrm{GeV\,cm^{-3}}$. Typically constraints on the DM couplings to SM particles will be dependent on the background number density of the DM and can be rescaled as $\sqrt{\rho_{\mathrm{DM}}}$ assuming a different DM local energy density. It is very important to understand the various possibilities of formation mechanisms for DM when making any statements about discovery potential. This is because a typical DM direct detection experiment is sensitive to a combination of the coupling being probed and the local energy density of the DM. Other properties of wave-like DM can be probed through simulation, for example how they affect galactic formation.

Very light bosons do not suffer the same problem as neutrinos; their statistics do not prevent them from having the required number density to make up all the observed DM. In fact, if DM were to be composed

[3]This is the simplest known formation mechanism for DM candidates of this kind, though there exist a plethora of others [60–63].The above story can further be complicated by changing the initial conditions for the scalar, or by including more terms in the scalar's potential.

of these ultralight bosons, they could be treated as classical waves due to their high phase space occupation numbers, below around $\sim 10\,\mathrm{eV}$. In order to make up the total energy density of DM, then the number density must increase to compensate a decrease in mass. The phase space occupation number is

$$N = n_{\mathrm{DM}}\,\lambda_{\mathrm{DM}}^3 = \frac{\rho_{\mathrm{DM}}}{m_{\mathrm{DM}}}\,\frac{1}{(m_{\mathrm{DM}}\,v)^3}\,, \tag{1.16}$$

where we identify the wavelength of the particle as its de Broglie wavelength. We see that for masses lower than $m_{\mathrm{DM}} \lesssim 10\,\mathrm{eV}$ [65], the occupation number is larger than one, implying a classical, wave-like nature. The alternative, for DM particles with higher masses, would be to have "particle-like" properties. Of course, we live in a quantum mechanical world, where it is never completely fair to make this distinction. The reason it is a relevant picture to keep in mind is for the mechanism used to detect a potential experimental signature. For DM that comes in heavy lumps, one can watch a sample of nuclei very closely, for example, and wait to see if a lump collides with one to observe a recoil. This picture is less useful for the lighter DM. A much more useful one is that a signal from this DM is statistical in nature. The large number of particles become virialised leading to a phase space distribution given for example by the standard halo model distribution

$$f\left(\mathbf{v}\right) = \frac{1}{\mathcal{N}}\exp\left[-\frac{\left(\mathbf{v}+\mathbf{v}_{\mathrm{obs.}}\right)^2}{\langle v^2\rangle}\right]\,, \tag{1.17}$$

where $\mathbf{v}_{\mathrm{obs.}}$ is the velocity of the observer in the halo's rest frame and $\mathcal{N}$ is a normalisation for this distribution. All of the individual collisions are averaged over, resulting in a background of DM, where the expectation value and variance for the fields have known values [65]. This is true of the photons that we observe all the time in everyday life; it is very rare that we have to think about a single photon colliding with an antenna, almost always we only care about the smeared-out classical field.

Many of the experiments searching for this DM will try to exploit the coherence of the signal, and as the DM is non-relativistic the DM should be coherent. We expect that the DM is well described by a massive wave, meaning that there should be an approximate dispersion relation of the form

$$\omega\left(\mathbf{k}\right) \simeq m_{\mathrm{DM}}\left(1+\frac{1}{2}\frac{\mathbf{k}^2}{m^2}\right)\,. \tag{1.18}$$

Such a dispersion relation results in a non-relativistic group velocity. The signal should be centred around the mass of the DM, with a spread dictated by the virial velocity, or more accurately the speed of the Earth through the DM background. In turn this implies that there is a coherence time determined by the bandwidth of the DM wave itself,

$$\tau_{\mathrm{DM}} = \frac{1}{\Delta f} \simeq \frac{1}{m_{\mathrm{DM}}\,\langle v^2\rangle}\,. \tag{1.19}$$

Thus, the DM can be said to have an associated quality factor of size $Q \sim \langle v^2\rangle^{-1} \sim 10^6$. For timescales shorter than the coherence time of the signal, it is reasonably accurate to treat the bosons as a perfectly monochromatic signal with a frequency set by the mass

$$\phi_{\mathrm{DM}} \simeq \phi_i\,\cos\left(m_{\mathrm{DM}}\,t+\vartheta_i\right)\,, \tag{1.20}$$

where ϕ_i is an amplitude drawn randomly from a Gaussian distribution such that $\langle\phi^2\rangle = 2\rho_{\mathrm{DM}}/m_{\mathrm{DM}}$ and ϑ_i is a random phase. After one coherence time has elapsed then these parameters should be redrawn. This means that if the experiment occurs over multiple coherence times one must account for it in their analysis, with the signals adding incoherently. This will affect the scaling of a DM signal in time. We will elaborate on this further in a later section (2.7) for a specific experimental set up. Furthermore, there is another sting in the tail for ultra-coherent signals corresponding to the very low mass bosons. We move through the DM at approximately the virial speed, this means that over one coherence time we see a patch of DM with a coherence length

$$\lambda \simeq \frac{1}{m_{\mathrm{DM}}\,v}\,, \tag{1.21}$$

which is the de Broglie wavelength of the DM. There is no reason to expect that the patch we move through right this second has an amplitude that is comparable in size to $\sqrt{2\rho_{\rm DM}}/m_{\rm DM}$, as might be expected. We only demand that the variance of all the amplitudes drawn over many coherence times be of size $2\rho_{\rm DM}/m_{\rm DM}^2$. It is a possibility that we have been very unlucky on the draw in our patch, with an amplitude far below what one might naïvely expect. This would make it far more difficult to detect the DM in an Earth based laboratory experiment. For an idea of the timescales involved a mass of $m_{\rm DM} \simeq 10^{-18}\,\text{eV}$ has a coherence time of ten years. Thus, the lowest three decades $10^{-21}\,\text{eV} \lesssim m_{\rm DM} \lesssim 10^{-18}\,\text{eV}$ of allowed DM masses suffer from this potential issue.

Axions and Dark Photons Two natural kinds of particle to include in the category of light bosonic DM would be pseudoscalars and spin-1 vectors. We note that the effective theory in (1.4) including higher order operators is not appropriate as these extra light states are in the spectrum. This is because we have implicitly assumed that the scale of the new physics is above the electroweak scale. The addition of a light ALP leads to the low energy Lagrangian relevant for table-top experiment by the addition of the terms

$$\mathcal{L}_{\rm ALP} \supset -\frac{c_{a\gamma\gamma}}{f_a}\, a F^{\mu\nu}\tilde{F}_{\mu\nu} - \frac{c_{aNN}}{f_a}\partial_\mu a\, \bar{N}\gamma^\mu\gamma_5 N - \frac{c_{aee}}{f_a}\partial_\mu a\, \bar{e}\,\gamma^\mu\gamma_5 e\,, \tag{1.22}$$

where c_i is a number denoting the coupling strength of the ALP to the low-energy SM particle, e is the electron field, N is the nucleon field and F is for photons. Given an explicit UV model for the ALP the coefficients c_i are in principle computable. Each of these operators is dimension 5 and therefore suppressed by the scale of symmetry breaking[4].

A variety of experiments and proposals have been put forward to search for these couplings. See the following for a non-exhaustive subset [67–69]. In particular the coupling to SM photons has received much theoretical and experimental interest [70–80].

Many of the experiments used to detect this ALP photon coupling can be repurposed in some way to search for the other bosonic DM candidate mentioned, a kinetically mixed dark photon (DP). A massive DP could arise from an additional $U(1)$ gauge group broken by a compact scalar field, a possibility strongly motivated by UV completions of the SM [81–91]. Typically it is assumed that there is no matter charged under the additional $U(1)$ because otherwise it would be this matter that forms the bulk of the DM, as opposed to the DP. The most relevant operator coupling an additional massive $U(1)$ boson to the SM at the energy scales of interest is through a kinetic mixing to the photon, where we can write the standard Lagrangian for the photon and the Proca Lagrangian coupled through the kinetic terms [92],

$$\mathcal{L}_{\rm DP} \supset -\frac{1}{4}F_{\mu\nu}F^{\mu\nu} - \frac{1}{4}F'_{\mu\nu}F'^{\,\mu\nu} + \frac{1}{2}\epsilon\, F'_{\mu\nu}F^{\mu\nu} + \frac{1}{2}m_{A'}^2 A'_\mu A'^{\,\mu} - e\, A_\mu \mathcal{J}^\mu\,. \tag{1.23}$$

The DP field is denoted by primed quantities, ϵ is the kinetic mixing parameter and $\mathcal{J}$ is the electromagnetic current density[5]. It is assumed that we only work at energy scales well below the weak scale, so any effect of size G_F although present, is irrelevant. We see that the presence of the mixing term breaks the charge conjugation symmetry of both of the vectors, $A^{(\prime)} \to -A^{(\prime)}$. This allows for ϵ to be a naturally small number, as sending it to zero restores the symmetry. We also note that redefining the fields as $A' \to -A'$ shows that no physical observable can depend on the sign of ϵ, only the magnitude.

The fields in the Lagrangian as written are in the kinetic mixing basis, but one can perform a rotation to other in-vacuum bases. It is clear that if there are no currents for the additional $U(1)$ and no mass term then the effect of the kinetic mixing parameter can be rotated away. This implies that any physical effect should come proportional to the mass of the DP. Canonical kinetic terms can be obtained, while keeping the

[4] One could have included contact terms between the ALPs and the SM pseudoscalars built from the fermions. At tree-level there is a redundancy in this parametrisation. We choose to write the interactions such that the shift symmetry of the ALP is manifest [66].

[5] This is one of three possible renormalisable interactions that can be added to the SM Lagrangian, the others are scalar singlets coupled to the Higgs and right-handed neutrinos from earlier.

SM photon massless by the field transformation

$$A_\mu \to A_\mu + \frac{\epsilon}{\sqrt{1-\epsilon^2}} A'_\mu \,, \quad A'_\mu \to \frac{1}{\sqrt{1-\epsilon^2}} A'_\mu \,. \tag{1.24}$$

This results in the *mass-eigenstate* basis,

$$\mathcal{L}_{\rm DP} \supset -\frac{1}{4} F_{\mu\nu} F^{\mu\nu} - \frac{1}{4} F'_{\mu\nu} F'^{\mu\nu} + \frac{1}{2} m^2_{A'} A'_\mu A'^{\mu} - e\, A_\mu \mathcal{J}^\mu - e\, \frac{\epsilon}{\sqrt{1-\epsilon^2}} A'_\mu \mathcal{J}^\mu \,, \tag{1.25}$$

where the mass has been appropriately redefined. The fields remain canonically kinetically normalised under an arbitrary additional $SO(2)$ field rotation meaning that any other basis can be parametrised from this mass-eigenstate basis by a single angle 'φ'. Choosing the angle such that $\tan\varphi = -\epsilon/(1-\epsilon^2)^{-1/2}$, we obtain another important field basis called the *interaction basis*,

$$\mathcal{L}_{\rm DP} \supset -\frac{1}{4} F_{\mu\nu} F^{\mu\nu} - \frac{1}{4} F'_{\mu\nu} F'^{\mu\nu} + \frac{1}{2} m^2_{A'} A'_\mu A'^{\mu} + \frac{1}{2} m^2_{A'} \frac{\epsilon^2}{1-\epsilon^2} A_\mu A^\mu + m^2_{A'} \frac{\epsilon}{\sqrt{1-\epsilon^2}} A'_\mu A^\mu - e\, A_\mu \mathcal{J}^\mu \,, \tag{1.26}$$

where again the mass and charge have been appropriately redefined. It is named as such because only one field interacts with the SM currents. Performing calculations in any basis will result in the same physics although sometimes it is easier to see a physical effect in one as opposed to the others.

The stress-tensor of the system with no currents is determined by

$$T^{\mu\nu} = -F^{\mu\alpha} F^{\nu}_{\ \alpha} + \frac{1}{4} g^{\mu\nu} F^2 - F'^{\mu\alpha} F'^{\nu}_{\ \alpha} + \frac{1}{4} g^{\mu\nu} F'^2 + m^2 \left(A'^{\mu} A'^{\nu} - \frac{1}{2} g^{\mu\nu} A'^2 \right) \,, \tag{1.27}$$

from this we see that the system now differs massively from the photon alone because the trace of the stress tensor is

$$T^{\mu}_{\ \mu} = -m^2 A'^2 \,, \tag{1.28}$$

such that it is non-zero. This is because the mass introduces a scale, so now the theory cannot be conformally invariant like that of the photon. The new Lorentz force law can also be written in this language as

$$\partial_\mu T^{\mu\nu} = e \left[F^{\mu\nu} + \epsilon\, F'^{\mu\nu} \right] \mathcal{J}_\mu \,, \tag{1.29}$$

where we can interpret the right hand side to be a force density.

Stückelberg's Trick The above Proca Lagrangian containing a massive vector is gauge invariant. There is a nice trick due to Stückelberg to see that the Proca Lagrangian shows a special case of the Higgs mechanism. Writing the case of a $U(1)$ Higgs

$$\mathcal{L} = -\frac{1}{4} F'^{\mu\nu} F'_{\mu\nu} + |D_\mu \Phi|^2 + \mu^2 |\Phi|^2 - \frac{\lambda}{2} |\Phi|^4 \,, \tag{1.30}$$

which is manifestly gauge invariant and the Higgs has a charge g. The field Φ has a non-zero vev at $\nu = \sqrt{\mu^2/\lambda}$. In the radial parametrisation, the Lagrangian is then

$$\begin{aligned} \mathcal{L} = & -\frac{1}{4} F'^{\mu\nu} F'_{\mu\nu} + \frac{1}{2} (\partial_\mu \rho)^2 + \frac{1}{2} (\partial_\mu \alpha)^2 + \frac{\rho}{\sqrt{2}\nu} (\partial_\mu \alpha)^2 + \frac{\rho^2}{4\nu^2} (\partial_\mu \alpha)^2 \\ & - \sqrt{2}\nu g A'^{\mu} \partial_\mu \alpha \left(1 + \frac{\rho}{\sqrt{2}\nu} + \frac{\rho^2}{2\nu^2} \right) + g^2 \nu^2 A'^2 \left(1 + \frac{\sqrt{2}\rho}{\nu} + \frac{\rho^2}{2\nu^2} \right) + V(\rho) \,. \end{aligned} \tag{1.31}$$

The radial mode can be decoupled by taking the vev to infinity and Higgs' charge to zero, holding the combination fixed. What results is the Proca Lagrangian, if we work in the Lorenz gauge and with the identification of $2g^2\nu^2 = m^2_{A'}$. Therefore the Stückelberg mechanism can be thought of as the Higgs mechanism with an infinitely large vev. The DP's mass can also come from the usual Higgs mechanism, but decoupling the radial mode allows one to consider a massive DP whose phenomenology is independent of an additional scalar. Among others these wave-like DM candidates are both well-motivated [93–102], with modern precision experiments improving the chances of their detection.

1.3 Marginally puzzling strong sector

We now leave the world of cosmology and return to the SM Lagrangian. The marginal part of the of the SM contains all of the operators in Eq. (1.4) other than the Higgs mass term. First we note that it is possible to write an additional three terms which are naïvely consistent with the SM gauge group,

$$\mathcal{L} \supset \theta_Y \frac{g_Y^2}{32\pi^2} B^{\mu\nu}\tilde{B}_{\mu\nu} + \theta_W \frac{g_W^2}{32\pi^2} W^{I\,\mu\nu}\tilde{W}^I_{\mu\nu} + \theta \frac{g_s^2}{32\pi^2} G^{A\,\mu\nu}\tilde{G}^A_{\mu\nu}\,. \tag{1.32}$$

Terms with tildes correspond to the Hodge duals of the Faraday tensors ($\tilde{F}_{\mu\nu} = 1/2\varepsilon_{\mu\nu\alpha\beta}F^{\alpha\beta}$). Notably, each of these violate both parity and time reversal symmetries. One can see this most easily by considering the explicit example of $F\cdot\tilde{F}$ in electromagnetism, which is proportional to $\mathbf{E}\cdot\mathbf{B}$. Under parity the $\mathbf{B}$ field is even whereas the $\mathbf{E}$ is odd, so their combination must also be odd. The same argument applies to each of the terms listed. Likewise the photon is charge conjugate odd, meaning that $F\cdot\tilde{F}$ is charge conjugate even, because A_μ appears twice. Together this implies that $F\cdot\tilde{F}$ is CP odd, as well as each of the other operators.

Each of these terms is a total derivative. Because of this it can be shown that these angles are related to the topological nature of the vacuum structure of the gauge groups. This immediately allows us to set θ_Y to zero because the homotopy group, or equivalently the vacuum structure, of $U(1)$ is trivial. There are no non-trivial configurations of these fields to contribute in the path integral. The vacuum structure of $SU(2)$, which is homeomorphic to a sphere (S^3), is non-trivial. However, because the $SU(2)_L$ fields couple only to the left-handed fermions, one can perform a simultaneous rotation to the left-handed and right-handed fields such that this angle can be removed, within the SM. If one were to include higher dimension operators this is no longer true, if there is explicit violation of $B+L$, one sees that it is not possible to rotate the angle away [103]. Modulo this fact, the only remaining operator that we cannot simply rotate away is the one made of gluons. Chiral rotations will not leave the Yukawas invariant, so it is expected that θ has some physical effect. One important caveat to this is that if a single eigenvalue of the Yukawas were to be zero, then such a rotation would be possible, like for θ_W. Effects on physical observables can be computed by including the effects of instantons, or by including its effect in χPT.

SM CP Violation CP violation from the electroweak sector is a standard story in the SM, but we will give a quick recap for completeness. We set the Higgs to its expectation value, breaking $SU(2)_L$ spontaneously. It is desirable to diagonalise to the mass basis for the fermions while keeping the kinetic terms diagonal. This will introduce mixing in the couplings to the gauge bosons. This is possible through the use of a set of unitary matrices in flavour space, one for each doublet or singlet independently. Because the electromagnetic and strong gauge interactions are vector-like, there is no effect of this diagonalization for the right-handed fermions, who only see these forces. This is not true for the left-handed doublets, which have non-zero charge under the $SU(2)$. We see that the quark kinetic term contains

$$i\bar{Q}^i \not{D} Q^i \supset \left(\bar{u}^i_L\ \bar{d}^i_L\right)\left[\frac{1}{2}g_W \not{W}^I\sigma^I + \frac{1}{6}g_Y \not{B}\right]\begin{pmatrix} u^i_L \\ d^i_L\end{pmatrix}\,, \tag{1.33}$$

for example. After this unitary rotation there is an off-diagonal mixing sensitive to the rotations performed.

$$i\bar{Q}^i \not{D} Q^i \supset \frac{1}{\sqrt{2}} g_W \left\{(V^*_{uL})^{ji}\, V^{ik}_{dL}\ \bar{u}^j_L \not{W}^+ d^k_L + (V^*_{dL})^{ji}\, V^{ik}_{uL}\ \bar{d}^j_L \not{W}^- u^k_L\right\}\,. \tag{1.34}$$

The unitary CKM matrix $V_{\rm CKM} = V^\dagger_{uL}V_{dL}$ is a remnant of this diagonalization procedure. Although a generic unitary 3×3 matrix is expected to require 9 real numbers be specified, this is not true for the CKM matrix which only needs 4 because each quark can be rotated by a phase independently, without changing any physics. A global rotation can be discounted resulting in the removal of 5 degrees of freedom. The CKM matrix is then expressible in terms of three real angles and one phase. This is at odds with CP invariance, because the transformation properties of the currents and bosons require $V^\dagger_{\rm CKM} = V_{\rm CKM}$ for CP to be a good symmetry. CP violation is observed experimentally.

The CKM matrix entries are

$$V_{\rm CKM} = \begin{pmatrix} 1 & 0 & 0 \\ 0 & c_{23} & s_{23} \\ 0 & -s_{23} & c_{23} \end{pmatrix} \begin{pmatrix} c_{13} & 0 & s_{13}e^{-i\delta} \\ 0 & 1 & 0 \\ -s_{13}e^{i\delta} & 0 & c_{13} \end{pmatrix} \begin{pmatrix} c_{12} & s_{12} & 0 \\ -s_{12} & c_{12} & 0 \\ 0 & 0 & 1 \end{pmatrix} , \tag{1.35}$$

where the same parametrisation as [14] is chosen. The angle δ appears in physical observables through the Jarlskog invariant,

$$\mathcal{J} = s_{12}^2 c_{13}^2 s_{13} s_{23} c_{12} c_{23} \sin\delta \, , \tag{1.36}$$

because a trivial mixing (c_{ij} or $s_{ij} \to 0$) means that a pair of quarks becomes degenerate and will allow δ to be rotated away. The measured value of $\delta \simeq 1.20$, which is an $\mathcal{O}(1)$ number, indicating that CP is not a good symmetry of the SM. The Jarlskog can be written in terms of the Yukawa matrices as

$$J = \text{Im} \left(\text{Tr} \left[Y_u Y_u^\dagger, Y_d Y_d^\dagger \right]^3 \right) , \tag{1.37}$$

Strong CP Puzzle We are now at a point where the puzzle corresponding to θ can be seen. The strong-CP phase $\bar{\theta}$, is a flavour invariant combination of QCD's topological angle θ and the phase of the Yukawas

$$\bar{\theta} = \theta - \arg\left(\det\left[Y_u Y_d\right]\right) , \tag{1.38}$$

which is invariant under the anomalous $U_A(1)$ rotation of the quarks. By means of a rotation it can be placed entirely in front of $\tilde{G}G$, meaning that it will never show up in perturbation theory, only through non-perturbative effects. This angle can be related to the neutron electric dipole moment (eDM) in a classical way to illustrate the map between the eDM measurement and strong CP problem. A more complicated analysis can be done, using instantons or χPT, to verify this more intuitive picture. To get the correct quantum numbers of a neutron (electric charge, isospin etc), one posits that it is a combination of two down quarks and an up quark. The classical electric dipole moment for the neutron is the charge weighted vector sum of the quarks' relative positions

$$\mathbf{d}_n = \frac{e}{3} \left[(\mathbf{r}_u - \mathbf{r}_{d_1}) + (\mathbf{r}_u - \mathbf{r}_{d_2}) \right] , \tag{1.39}$$

where the subscripts denote the quarks in the neutron. The typical size of the neutron is $\sim 0.8\,\text{fm}$ set by the pion mass, implying that the maximum length of these vectors will be $1/m_\pi$. This would imply that $|d_n| \simeq e\phi/m_\pi$, if the angle 'ϕ' between the quark displacements were small. The estimate leaves something to be desired because it is not immediately clear physically why the angle ϕ should correspond to $\bar{\theta}$. One can improve on it by imagining that the quarks are not static, but undergoing motion from the internal forces. There should be a CP violating force acting on the quarks. We know from the above symmetry arguments that such a force must be proportional to a quark mass, because a zero quark mass allows for the CP violating effects to be rotated away. We can choose this order parameter as m_u, as the smaller of the quark masses. Those strong forces that violate CP should also come proportional to $\bar{\theta}$, presumably with a scale set by $\Lambda_{\rm QCD}$. These will naïvely be the more relevant forces, because the weak sector CP violation will be suppressed further by $m_W \simeq 100\,\Lambda_{\rm QCD}$. Likewise we know that restoring forces should be set by the binding energy in a nucleon which are also of scale $\Lambda_{\rm QCD} \sim m_n$. Combining these facts gives the estimate for the typical separation of the quarks in a neutron and therefore the eDM as

$$|d_n| \simeq c_n \, e \, \frac{m_u}{m_n^2} \bar{\theta} \, , \tag{1.40}$$

where c_n is some unaccounted for $\mathcal{O}(1)$ number. This is similar parametrically to that obtained using χPT [104].

The kernel of this 'strong-CP puzzle' is to explain why the neutron's eDM is so small, when there is no reason a priori that QCD should restrict it to small values. The experimentally determined value is

$|d_n| < 1.8 \times 10^{-26} e\,\text{cm}$ (90% CL) [105]. This is made yet more mysterious because we know that CP is not a good symmetry of the SM, which might have otherwise been used to explain the smallness of $|d_n|$. We also know that further sources of CP violation are expected to explain the observed matter anti-matter asymmetry in the Universe. The value obtained using the experimental value for the eDM is $\bar{\theta} \lesssim 10^{-10}$. To resolve the strong CP problem is to explain why the angle $\bar{\theta}$ is so small, without resorting to fine-tuning. Furthermore, as opposed to other theoretical problems of the SM, this one has no known anthropic resolution, without putting further priors onto the solution [106].

There are finite corrections to the parameter at four loops [107], with the estimate for the SM contribution being that $\bar{\theta} \simeq 10^{-19}$. Taking $\bar{\theta}$ to zero restores CP invariance in the strong sector, but not in the whole SM because of δ. One can see based on flavour symmetries that $\bar{\theta}$ runs very slowly in the SM [108]. The parameter receives no corrections to its running until at least 7-loop order. This is because the only source of CP violation in the SM is the CKM phase, and so a divergent diagram must appear proportionally to the Jarlskog [109]. This property is also not robust under SM extensions, which as argued before must exist. For example, in supersymmetric extensions to the SM there is running at one loop from the Gluino mass phase.

1.3.1 Symmetry solution and Axions

One popular solution to the puzzle postulates that there is a global $U(1)$ symmetry protecting the angle. This symmetry allows the $\bar{\theta}$ angle to be effectively rotated away. One way to realise it is to set one of the light quark masses to be zero, which we can see from the classical estimate (1.40) would make the neutron eDM zero. At the level of the Lagrangian this is because the left and right handed chiralities of this quark become decoupled, which introduces an additional anomalous $U(1)$ axial rotation. It is often said that for such a solution the puzzle is solved dynamically by the η' meson. Unfortunately, nature seems to disfavour this solution. Lattice results show that the lightest quark has a mass incompatible with zero by $26\,\sigma$ [110].

QCD-Axions Instead, there could be an additional global $U(1)_{\text{PQ}}$ called Peccei-Quinn symmetry after its initial proponents. This symmetry is spontaneously broken, resulting in an additional particle, called the axion, which is the pNGB associated to the broken group [111–113]. QCD generates a potential for the axion which is periodic in the newly dynamical QCD CP-violating angle. This potential is minimised when this angle is zero, meaning that the axion is a dynamical way to make the observed $\bar{\theta}$ compatible with zero. Because the PQ symmetry is explicitly broken by chiral symmetry breaking, the axion has a mass given by $m_a \simeq m_\pi f_\pi / f_a$. This linear relation between the mass of the axion and the scale of symmetry breaking is known as the QCD-axion line. Additionally, such an axion will inherit a coupling to photons determined both by the choice of $U(1)_{\text{PQ}}$ fermion and gauge boson charges in the UV and pion mixing in the IR.

1.3.2 Quality problem

The axion solution is an elegant EFT solution to the strong CP puzzle, that can be probed experimentally through detection of an axion at the QCD-axion line. However, it is very important to address why the global Peccei-Quinn symmetry is of such high quality, when it need not be. This is again a concern inherited from UV thinking. There are expected non-perturbative sources of symmetry breaking coming from QCD itself, which set the axion's potential at low energies. The expectation that we have is that exact global symmetries are not realised in nature. Naïvely this is because there is at least explicit violation of global symmetries coming from gravity [114]. In symbols, if ϕ is the complex scalar, whose axial mode is the axion, then there is an expectation that

$$\mathcal{L} \supset \sum_n c_n \frac{1}{M^{n-4}} \left(\phi^n + \text{h.c.}\right) , \tag{1.41}$$

terms such as these should be present in the Lagrangian, where $M \leq M_{Pl}$. These terms also contribute to the axion's potential. This means that the axion obtains a new mass term not necessarily centred around the theta angle. This is what is required for the strong CP puzzle to be solved. It appears as though we

should demand that

$$\left(\frac{f_a}{M}\right)^{n-4} f_a^4 \lesssim 10^{-10}\,\Lambda_{\rm QCD}^4\,, \tag{1.42}$$

to suppress the non-QCD contributions to the axion mass. Enforcing this implies that operators with $n \lesssim \lceil 86/(19-r)\rceil$ should be tuned to small values in order for the axion solution to not be spoiled, if M is chosen at the Planck scale and $f_a = 10^r$ GeV. For example, if $f_a = 10^{12}$ GeV then, $n \lesssim 13$.

The tuning can be realised by demanding a number of additional discrete symmetries, for example a $\mathbb{Z}_{14}$ symmetry can allow the tuning required [115]. There are also other ways to invoke the required high quality $U(1)_{\rm PQ}$. For example the axion can be a component of a gauge field on some higher dimensional manifold [116]. The shift symmetry inherited from gauge symmetry is protected.

It could also be that treating the symmetry breaking from gravity in this way is flawed. Outside of some simple regimes, we are largely ignorant of how to include the effects of gravity in EFT analyses. For example, in explicit constructions in string theory [117] it appears as though these contributions to the axion potential are not relevant, rendering the problem a non-issue. Furthermore, axions are generically predicted in string theory, as a consequence of compactifying extra-dimensional manifolds [118–121]. Thus, finding many axions would provide evidence in favour of string theory. For these reasons, the QCD-axion is a well-motivated example of one of the light pseudoscalar DM candidates mentioned in the previous subsection.

1.4 Relevant problems from Gravity

We now move to the most relevant operators in Eq. (1.4). Note that there are no dimension 3 operators in the SM. As written the only operator included is $\mu^2\phi^\dagger\phi$, where μ has mass dimension 1. Currently this appears to be the sole dimensionful quantity of the SM. Already it presents us with a question: "why does the weak scale have the size that it does?". This question is referred to as the electroweak hierarchy problem; a potential problem for naturalness. It has motivated many extensions of the SM, with clear links to the study of supersymmetry [122–124], composite models for the Higgs [125, 126], mirror world models for the Higgs [127] and many more. We must also however add another dimensionful operator to the Lagrangian, the identity operator Λ, which contains no fields. Λ is the most relevant operator that we may possibly write, with the coupling having mass dimension four. It respects all of the SM model symmetries and so should be included, from an EFT perspective[6].

The expectation that physics is blind to Λ cannot be correct; upon including gravity such a term acts as the cosmological constant. Implicitly in the construction of the SMEFT is that any mass scale of non-SM particles is larger than the electroweak scale. We have seen that new light pseudoscalar or vector particles can be added to the spectrum and this assumption is not true. The new states have not been observed because of a sufficiently weak coupling. Even without appealing to unknown new particle content, we know that this same reasoning applies to gravity. An EFT description of gravity requires the existence of an additional massless spin-2 boson, called the graviton, which can be thought of as resulting from gauging Poincaré symmetry. One can then introduce a connexion to minimally couple the gravitons to the SM particles, in the same way as for the other SM gauge bosons, and the Einstein-Hilbert action as the most relevant diffeomorphism invariant term that can be written down. This recovers the equivalence principle of GR upon inclusion of the most relevant operators. Scattering computations are also possible within this EFT involving gravity and match expectations from GR. As one might expect, there are hints that gravity behaves contrary to the way the usual EFT construction works. Gravity *does* care about the size of Λ. It appears as the cosmological constant in Einstein's equations. One can think of the term physically as the energy density associated to the vacuum itself. Λ also poses a naturalness problem, although a much more severe one, known infamously as the cosmological constant problem.

[6] In flat space, there is no Feynman rule associated with it, and it receives corrections only from bubble diagrams, thus it will not contribute to any scattering amplitude of the SM particles. This is no longer true upon the explicit inclusion of gravity.

Problems with Λ Dark energy accounts for approximately $\sim 70\%$ of the Universe's energy budget and causes its accelerated expansion [36, 128–131]. The question of dark energy is intimately linked to the cosmological constant problem. Estimating the energy density associated with the vacuum by computing bubble diagrams, one finds that the result is highly sensitive to the energy scales at which the computation is done, and which states are included. For example, computing the vacuum diagrams expected to correct Λ, we see that the naïve estimate is that Λ should have a size determined by the fourth power of the cutoff scale M^4. For example, in a very low energy theory involving particles only lighter than electrons, one has the expectation that $\Lambda \sim m_e^4$, where we know that the electron gives a threshold correction when we match to a theory where electrons are again dynamical. In the SM the heaviest particle is the top, meaning that one expects that the low energy should have a value $\Lambda \gtrsim m_t^4$ without significant tuning, where we expect that there is a theory containing new particles of masses above the top's. We already see the running of Λ is extremely sensitive to the states in the spectrum, which is due to how relevant it is as a parameter. The measured value $\Lambda_{\rm meas} \sim (10^{-3}\,{\rm eV})^4$ is an unnaturally small value within the EFT of the SM and gravity. It is important to recognise that this statement is not about comparing the measured value $\Lambda_{\rm meas}$ and an unphysical regulator dependent quantity, as is sometimes claimed. Within any given EFT there is no problem, or internal inconsistency whatsoever. One computes correlation functions using the usual methods, defines the physical observables that one would like to use as inputs, and then all other physical observables are computable, within the EFT's regime of validity. Instead, it is a UV problem. If Λ should be a quantity that is calculable, from UV parameters alone, then it is *very* difficult to build a model valid to high energies 'M' such that $\Lambda \sim M^4$ is not true. Given that we have fairly strong control of electroweak and strong physics up to $\sim 10\,{\rm TeV}$ scales, there appears to be a discrepancy of at least 64 orders of magnitude. However, we do not have good control at scales between these and M_{pl} scales, so one could argue that the tuning is as bad as ~ 120 orders of magnitude. Researchers look to resolve this in a variety of ways (see [132–134] and references therein), although there is currently no known solution to this problem. One can also appeal to anthropic reasoning to resolve this tension between the estimate and the measured value [135]. These arguments explain the discrepancy roughly by stating that we as observers would not exist to question the value of the cosmological constant, had it been any value other than one which allows us to exist in the first place. While this position does resolve the problem somewhat, it does not provide a mechanism by which it can be disregarded as an explanation.

The reason that we should care about this disconcerting difference between the measured result and the expected one stems from how we expect EFT models to work. Naturalness is a criterion used to quantify the features of a physical model. Loosely speaking (technical) naturalness [136] can be thought of as follows: one expects all dimensionful parameters of a model to be related to the cutoff scale of the model by order one numbers involving couplings. Any parameter of the model which differs significantly from this expectation should be explainable using a symmetry argument i.e. seemingly unnaturally small numbers should be protected by a symmetry and setting these numbers to exactly zero should restore the (non-anomalous) symmetry. It is implicit in this story that one should also address why the parameter remains small as one runs the parameters by integrating out the high-energy modes. In other words, the notion of naturalness corresponds to the lack of requirement of fine-tunings in the model[7]. Any model that does not posses these features is said to have a naturalness problem. It is precisely this notion of naturalness that allows us to make parametric estimates without always resorting to solving complicated differential equations. The relevant scales of a problem are typically all that is needed to roughly get the answer; for example the period of a simple pendulum is $\sim \sqrt{l/g}$, the Bohr radius is $\sim (\alpha m_e)^{-1}$ and the hydrogen energy levels are $\sim -m_e\alpha^2/n^2$ which are only wrong by $\mathcal{O}(1)$ numbers and found by dimensional reasoning alone. Less trivial examples come from the naïve estimates performed in calculations of amplitudes using Feynman diagrams.

Now that these criteria have been loosely established, we can comment on whether the SM is a natural model, or not. The most commonly stated theoretical problems of the SM are those of the cosmological constant problem, the electroweak hierarchy problem and the strong-CP puzzle. The small parameters

[7] A theory is known as Dirac natural [137] if all of its dimensionless parameters are of order one, but this is a much stricter requirement than that of technical naturalness.

associated with these problems have been labelled: Λ, μ and θ respectively. Furthermore, it is widely acknowledged that the severity of the problems is worst for Λ which has been discussed already, then μ, θ is the least severe. The level of severity is linked to how relevant the associated operator is in the EFT. This might initially look confusing, as taking $\Lambda, \mu \to 0$ naïvely appears to restore scale invariance of the SM, implying that these parameters *are* naturally small. The resolution to this apparent contradiction, is that classical scale invariance is typically a bad symmetry at the quantum level, broken by loop effects [138, 139]. The two parameters are indeed unprotected by any genuine symmetry. Furthermore as they correspond to relevant operators in the SM, they receive plenty of IR contributions in their running. There has been a lot of model building work done to try to address both of these problems as well as anthropic considerations for both [135, 140].

While it is still conceivable that there is nearby physics that can explain the size of μ, it is clear that something is going very wrong if we wish to avoid fine tuning Λ at least. Note that it was the inclusion of gravity that upgraded the constant term in the Lagrangian from an innocuous and ignorable term to the most poorly estimated physical parameter ever. It stands to reason that the resolution to the problem lies in treating the SM and dynamical gravity like any other EFT. This has been explored in the literature, with holographic arguments implying that we should expect gravity to not distinguish between UV and IR like our typical Wilsonian EFTs should [141]. There could also be problems related to the other postulates typically assumed to be true in constructing any normal EFT. We are then motivated to explore what problems emerge from gravity when it is treated as an EFT.

1.4.1 EFT self-consistency arguments

Gaining information about gravity through its embedding into an EFT may initially appear opaque. We can learn about the properties of the UV by seeing the implications that UV assumptions have on an IR EFT. So far, we have been using EFTs as tools to describe physics at the boundary between measurable phenomena and the unknown. Universality can be seen through the guise of EFTs as the principle that different high-energy theories converge to the same effective description at low energies. This fact naïvely allows EFTs to be applied agnostically to a wide range of systems, including gravity, BSM physics and pion physics, as described above. However, this universality also limits any given EFT's intrinsic predictive power.

Strictly speaking, the only robust predictions within an EFT are the low-energy analytic structures, governed by the interplay of calculable loop effects and unknown Wilson coefficients. The question of which low-energy phenomena can be described consistently within an EFT plays an important role in BSM physics. Even minimal assumptions about the UV theory, such as unitarity or causality, constrain EFTs with testable features. This philosophy aligns with the bootstrap community. Exploiting unitarity and the analytic properties of scattering amplitudes, implied by the Lorentz-invariant causal structure of QFT [142, 143], it is possible to characterise the space of UV-completable EFTs, via positivity bounds and dispersion relations on their Wilson coefficients [144–152]. Applications of these techniques have been found in QCD [153–164], quantum gravity [165–195] and physics beyond the Standard Model [196–208] as a non-exhaustive list of examples. These tools have been used to prove the a-theorem in 4-dimensions [209, 210] and to show that EFTs dominated by soft interactions [147, 166, 211], such as EFTs with weakly broken Galilean symmetry [149, 150], or higher-spin particles parametrically lighter than the EFT cutoff [205, 212, 213], are inconsistent.

1.4.2 Requirements for self-consistent EFT

The non-perturbative bootstrap program champions the use of the requirements of causality, analyticity, unitarity, locality and crossing symmetry, where these requirements have some overlap.

Causality implies analyticity throughout physics, it is not only important for the S-matrix bootstrap program. This fact will be used both in chapters 2, 5 and 6 so we can keep the discussion more general. Consider a function 'f' whose value at time t depends on the value of some other function 'g' at all preceding

times as

$$f(t) = \int_{-\infty}^{\infty} \mathrm{d}\tau\, \chi(t-\tau)\, g(\tau)\ , \quad \text{where} \quad \chi(t-\tau) \propto \theta(t-\tau)\ , \tag{1.43}$$

here χ is known as the susceptibility function. It can be interpreted as the propagation of the non-relativistic signal f coming from the source g. This immediately implies that in Fourier space the functions are related by

$$f(\omega) = \chi(\omega)\, g(\omega)\ . \tag{1.44}$$

If the quantities f and g are real observables, then it implies that χ is also real. The statement of causal propagation is encoded in the proportionality to the Heaviside function. From this and the definition of Fourier transform we see that $\chi^\star(\omega) = \chi(-\omega)$, implying that the real part of $\chi(\omega)$ is even and the imaginary part is odd. Further $\chi(\omega)$ can be analytically continued in the upper-half plane through the relation

$$\chi(\omega) \equiv \int_{-\infty}^{\infty} \mathrm{d}\tau\, \chi(\tau)\, e^{i\omega\tau} = \int_{0}^{\infty} \mathrm{d}\tau\, \chi(\tau)\, e^{i\omega\tau}\,. \tag{1.45}$$

The function $\chi(\omega)$ is analytic in the upper-half plane, as a consequence of the Heaviside in the time domain. Cauchy's residue theorem says that an arbitrary contour integral in this plane of the following quantity will vanish

$$\oint \mathrm{d}\omega' \frac{\chi(\omega')}{\omega' - \omega} = 0\,. \tag{1.46}$$

Deforming this contour, we find the Kramers-Kronig relations, that constrain the form of $\chi(\omega)$ strongly, such that specifying the imaginary part fully determines the real part or vice-versa

$$\chi(\omega) = \frac{1}{i\pi} \int_{-\infty}^{\infty} \mathrm{d}\omega' \frac{\chi(\omega')}{\omega' - \omega}\,. \tag{1.47}$$

While this is a very simplistic toy-model it captures how implementing causality determines the analytic structure of a transfer function. In chapter 2 the above susceptibility represents the magnetic susceptibility, where f takes the place of spin and g is a magnetic field, and the argument must be modified slightly to account for additional indices. In chapters 5 and 6 this susceptibility takes the place of the S-matrix itself, upon modifying the above toy model sufficiently. Similar relations exist between micro-causality and analyticity of the S-matrix in QFT.

Unitarity the statement that information is conserved in a system (as long as all modes of the system are properly accounted for). In classical mechanics this is heavily linked to Liouville's theorem, where the phase space volume is conserved under time-evolution. For a quantum mechanical system we can quantify the information content by the von Neumann entropy,

$$S_{\text{vN.}}(\rho) = -\mathrm{Tr}\,(\rho \log \rho)\ , \tag{1.48}$$

where ρ is the density matrix of the system. The information contained in ρ is the total information content of the system. Under unitary time-evolution '$U(t)$', this information is conserved

$$S_{\text{vN.}}\left(U\rho U^\dagger\right) = -\mathrm{Tr}\left[U\rho U^\dagger\, U \log(\rho)\, U^\dagger\right] = S_{\text{vN.}}(\rho)\ . \tag{1.49}$$

Using the previous toy model, unitarity is implemented by demanding the integral relation

$$\int \mathrm{d}\tau\, |f(\tau)|^2 \leq \int \mathrm{d}\tau\, |g(\tau)|^2\ , \tag{1.50}$$

where we now implicitly absorb any dimensional differences into χ, such that f and g have the same dimension, to make this a sensible comparison. Using Parseval's theorem then the following holds in frequency space

$$\int \mathrm{d}\omega\, |\chi(\omega)|^2\, |g(\omega)|^2 \leq \int \mathrm{d}\omega\, |g(\omega)|^2\ , \tag{1.51}$$

which must hold regardless of the spectrum of g. Taking it to be a single damped plane wave it is straightforward to show that for any ω in the upper-half plane $|\chi(\omega)| \leq 1$. In the case of magnetic susceptibility, this fact can be used to help see how signals scale in time under different regimes 2.7.

The S-matrix is schematically defined as the operator corresponding to the projection of asymptotically free states at plus and minus infinity,

$$S_{\alpha\beta} =_{\text{out}} \langle\beta|\alpha\rangle_{\text{in}} = \langle\beta| \Omega^{\dagger} (t \to +\infty) \Omega (t \to -\infty) |\alpha\rangle = \langle\beta| S |\alpha\rangle \ , \tag{1.52}$$

where Ω is known as the Møller operator and we have defined the S-matrix as this product. The above non-relativistic description is not immediately applicable to S-matrix unitarity, which can instead be stated as the following operator equation

$$SS^{\dagger} = S^{\dagger}S = \mathbb{I} \, . \tag{1.53}$$

Strictly speaking such a definition is only sensible when smearing against a wave packet of states, such that there is non-trivial mixing between Hamiltonian eigenstates. The optical theorem may be derived from this equality and the decomposition of S into the trivial and interacting parts $S = \mathbb{I} + iT$.

$$-i \left(T - T^{\dagger}\right) = TT^{\dagger} \, . \tag{1.54}$$

Consider the scattering of two particles to two other particles, denoting the incoming momenta by p_i and outgoing by k_i. The above operator statement takes the form

$$-i \langle k_1 k_2| \left(T - T^{\dagger}\right) |p_1 p_2\rangle = \sum_{\psi} \langle k_1 k_2| T |\psi\rangle \langle\psi| T^{\dagger} |p_1 p_2\rangle \ , \tag{1.55}$$

where the sum is taken over all intermediate states. In the forward-limit (the limit of no transverse momentum exchange between the particles, or $t \to 0$) the resulting expression, quantifying the link, follows

$$2 \, \text{Im} \left[\langle p_1 p_2| T |p_1 p_2\rangle\right] = \sum_{\psi} |\langle p_1 p_2| T |\psi\rangle|^2 \ . \tag{1.56}$$

This powerful theorem then links the imaginary part of the amplitude to the cross-section in the forward limit. Frequently the momentum conserving Dirac delta functions are factored out, and the new object $\mathcal{M}$ referred to as the amplitude.

$$(2\pi)^d \, \delta^d (p_1 + p_2 - k_1 - k_2) \, \mathcal{M} (s, t) \equiv \langle k_1 k_2| T |p_1 p_2\rangle \ . \tag{1.57}$$

For theories involving massless particles, such as gravity, the forward limit may be divergent. In these cases, one can exploit unitarity away from the forward limit by appealing to the partial wave expansion of the amplitude

$$\mathcal{M} (s, t) = \sum_{l=0}^{\infty} \mathcal{M}_l (s) \, \mathcal{P}_l \left(1 + \frac{2t}{s}\right) \ , \tag{1.58}$$

where $\mathcal{P}_l(\cos\theta)$ are Gegenbauer polynomials in d-dimensions and reduce to the standard Legendre polynomials in $d = 4$. This basis diagonalises the statement of S-matrix unitarity, where $\text{Im}[\mathcal{M}_l(s)] > 0$.

Dispersion relations allow us to relate low-energy properties of the amplitude, namely Wilson coefficients, to the high energy representations. Dispersion relations exploit the analytic properties and the crossing-symmetry of amplitudes in complex energy to relate integrals of the amplitude in the IR to integrals in the UV, using Cauchy's theorem. This is largely possible because of the boundedness of the amplitude at large energies. There exists an N such that

$$\lim_{|s| \to \infty} \frac{\mathcal{M} (s, t)}{s^N} \to 0 \, . \tag{1.59}$$

It has been proved for theories with a mass gap that the amplitude grows as $\mathcal{M} \lesssim s \log^2(s)$ in four dimensions and so $N \geq 2$ will result in the desired boundedness [214, 215]. For theories involving the exchange of massless

gravitons the choice $N \geq 2$ gives the correct boundedness [216] for $d > 4$. The earlier property of unitarity then implies positivity properties for the UV integrals, which translate into consistency conditions for the low-energy EFT coefficients. An important example of one of these dispersion relations is that of the arc variable, defined as a twice subtracted dispersion relation of form

$$a_n(t) = \int_{\frown} \frac{\mathrm{d}s}{2\pi i s} \frac{\mathcal{M}(s,t)}{[s(s+t)]^{n+1}}, \tag{1.60}$$

which is named for its arc-shaped contour in s of radius M^2. The contour is deformed such that it probes the discontinuities of the UV theory, along the real s-axis, which are positive in the forward limit by the optical theorem. This shows that the arcs are themselves are positive in the forward limit. From here one can use this positivity to impose constraints on the allowed Wilson coefficients in the IR theory.

In the analysis of scattering amplitudes, the notion of maximal analyticity is also sometimes assumed, where one assumes that the amplitude is analytic in both s and t up to the physical cuts [217–219]. This allows one to make more identifications between the UV and IR than might otherwise be possible. It is an additional unproven assumption about the form of the amplitude, although there are no known counterexamples which do not violate locality, unitarity.

1.4.3 Positivity for problematic theories

One particular question to address is how can Wilson coefficients be constrained in a theory involving dynamical gravity? Gravity is problematic because of the massless graviton exchanges resulting in IR divergent kinematics. This is relatively easy to see without reference to a Lagrangian, consider the scattering of scalars through gravitons. In four dimensions the three-point interactions are uniquely fixed by dimensional analysis and helicity structure to be[8]

$$\mathcal{M}(1^0, 2^0, 3^{++}) = \kappa \left(\frac{[31][32]}{[12]}\right)^2 \quad \text{and} \quad \mathcal{M}(1^0, 2^0, 3^{--}) = \kappa \left(\frac{\langle 31\rangle\langle 32\rangle}{\langle 12\rangle}\right)^2, \tag{1.61}$$

where we have implicitly omitted the irrelevant phase of the amplitude and also $\kappa = 1/M_{Pl}$. Gluing these three-points together yields one of the channels

$$\kappa^2 \frac{1}{p^2} \left(\frac{[p1][p2]}{[12]}\right)^2 \left(\frac{\langle -p3\rangle\langle -p4\rangle}{\langle 34\rangle}\right)^2 = \kappa^2 \frac{t^2}{s}, \tag{1.62}$$

up to terms which are zero on-shell. We can use the crossing symmetries of the diagram to see that the term should actually be proportional to $\kappa^2 tu/s$, meaning that the full amplitude at tree-level is

$$\mathcal{M}^{\text{grav}}_{\text{tree}} = \kappa^2 \left(\frac{tu}{s} + \frac{ts}{u} + \frac{su}{t}\right). \tag{1.63}$$

A pole has already developed at $t \to 0$. This pole corresponds to the Coulomb pole of graviton exchange, leading to the $1/r^2$ force of attraction between all massive particles.

One has to be careful in discussing IR effects involving photons or gravitons. The above Coulomb pole is a genuine physical effect of having a massless graviton mediator in the theory. Such theories are also plagued by unphysical IR divergences that appear order by order in perturbation theory. These are a basic consequence of the fact that asymptotic states cannot be described well by free particle states in theories with long range interactions. One can remove these fictitious divergent pieces by considering inclusive observables, by redefining the asymptotic states or by excising them directly from the amplitude.

[8] Here we use the $d = 4$ spinor-helicity notation of [220, 221] such that $[ij]$ denotes $1/2$ positive helicity for legs i and j and $\langle ij\rangle$ denotes $1/2$ negative helicity.

How positivity bounds are found consistently in theories involving gravity is an important question to address, as everything we know interacts gravitationally and, in principle, bounds for these theories give information about the space of possible UV completions containing gravity! It is especially pertinent at very low energies, where all massive particles have been integrated out of the theory, leaving only an EFT for the remaining light states. Here, the forward limit is divergent and we must appeal to less simple methods to find self-consistency conditions for the theory. This issue was partially overcome in [179, 185] by treating dispersion relations not as functions of t, but as distributions to be smeared against appropriate functional measures. The method proposed was designed to avoid only the Coulomb singularity. However, this is only part of the issue, as the inclusion of loop effects involving gravitons lead to contributions to the amplitude at small t at least as poorly behaved as [222],

$$\delta\mathcal{M}(s,t) \propto s^2 \log(-s)\,(-t)^{\frac{d-4}{2}} \quad (\times \log(-t) \quad \text{in even dimensions}). \tag{1.64}$$

The method of [185] relies on crossing-symmetry and exploits a mixture of $t \neq 0$ information (the twice-subtracted dispersion relation), combined with dispersion relations obtained with additional subtractions and their derivatives evaluated strictly at the *forward limit* $t = 0$. Due to this feature, the validity of the procedure is limited only to a tree-level idealisation in which $M_{\rm P} \to \infty$ and all Wilson coefficients vanish $g_n \to 0$, and effectively all loops are neglected. It is clear that this and its first derivatives are also divergent in the forward limit for dimensions less than 7. This further singular behaviour is not accounted for in this smearing method. We would like to have a method robust against the inclusion of these quantum mechanical effects in order to ensure that the constraints we make are conservative. Achieving this can act as a link between the positivity program and the numerical bootstrap program and may act as a step towards addressing the cosmological constant problem.

1.5 Dissertation outline

This thesis is divided into two parts; the first part will cover light dark matter candidates and their experimental signatures and the second will look at conditions for EFTs involving gravity. The logical flow of the thesis follows the topics as they were introduced in this introductory chapter. We will begin in chapter 2, by looking at how a proposed experiment; CASPEr-Gradient, can be repurposed beyond its intended use, to search for the axion coupling to photons and the DP kinetic mixing parameter. In chapter 3, with this repurposing philosophy in mind, we see if we can repurpose basic terrestrial information that we already have access to, to set constraints or propose new searches for ultralight DM. Next in chapter 4 we look at the axions, and ask about their quadratic coupling to photons. Naïvely, this is a highly suppressed operator and so one might think that it is never phenomenologically relevant. Here we address whether this is true or not, by looking at the self-consistency of the low energy QCD-axion EFT. Then in the final chapters 5 and 6, we seek to address what methods can be used to find positivity constraints even in very poorly behaved theories with bad IR behaviour.
Here is some more information on each chapter individually.

Ch2: Casting New Light on DM NMR

This chapter is based on a pre-print written in collaboration with Sebastian Ellis, Nicholas Rodd and Jacob Leedom [223]. In it, it is demonstrated that nuclear magnetic resonance based searches for DM have intrinsic and powerful sensitivity to dark photons and the axion-photon coupling. An instrument such as CASPEr-Gradient begins with a large sample of nuclear spins polarized in a background magnetic field. In the presence of axion DM coupled to nucleons, the spin ensemble feels an *effective magnetic field* $\mathbf{B} \propto \nabla a$. However, the spin ensemble feels the presence of *any* perturbing magnetic field in its precession as an additional torque, that acts to tilt the spins and generates a potentially observable precession. A real field can be generated by a kinetically mixed dark photon within the shielded region the sample is placed, or by an axion coupled to photons through its interaction with the background magnetic field. If CASPEr-Gradient were to reach the QCD axion prediction of the axion-nucleon coupling, it would simultaneously be sensitive to kinetic mixing

of $\epsilon \simeq 3 \times 10^{-16}$ and axion-photon couplings of $g_{a\gamma\gamma} \simeq 2 \times 10^{-16}\,\mathrm{GeV}^{-1}$ for $m \simeq 1\,\mu\mathrm{eV}$. It is a worthwhile endeavour to see if multiple DM signals can be probed by the same means because of our ignorance as to the nature of DM and also economic necessity.

Ch3: Dark Matter Constraints from Earth

This chapter is largely based on a letter written in collaboration with Sebastian Ellis and Andrea Caputo [224]. It covers ideas which aim to constrain DM parameter space using resources of the Earth directly. Firstly, it will be shown that considering something as simple as the lack of observation of the anomalous heating of the Earth's core can provide a fair constraint. We see from this exercise that there are non-trivial effects to consider in medium, such as using the correct propagating degrees of freedom and also how to account for boundary effects with kinetic mixings present.

Following this, the possibility of resonant conversion of wave-like DM into low-frequency radio waves in the Earth's ionosphere will be demonstrated, and a search for this signal is proposed. Resonant conversion occurs when the DM mass and the plasma frequency coincide, defining a range $m_{\mathrm{DM}} \sim 10^{-9} - 10^{-8}\,\mathrm{eV}$ where this approach is best suited. Owing to the non-relativistic nature of DM and the typical variational scale of the Earth's ionosphere, the usual linearised approach to computing DM conversion cannot be used. Therefore a second-order boundary-value problem is solved instead, effectively framing the ionosphere as a driven cavity filled with a positionally-varying plasma. Then a radio based experiment using an electrically-small dipole antenna is proposed to target the radio waves generated during the conversion. Such an antenna is applicable as it has a large bandwidth and can be built from widely available components. Additionally, the primary noise source is external to the experimental set-up, coming from human-made sources. This proposal can be orders of magnitude more sensitive to DP and axion-like particle DM in the relevant mass range than pre-existing constraints.

Ch4: Quadratic couplings of axions to photons

This chapter is based on a paper written in collaboration with Sebastian Ellis, Jérémie Quevillon and Pham Ngoc Hoa Vuong [225]. It is shown that the QCD axion couples to the electromagnetic kinetic term at one loop with a coupling larger than one might naïvely anticipate. One might expect that the shift symmetry of the axion should result in such an operator being extremely subdominant. The heuristic reason that this expectation fails is that the axion acquires an IR contribution to its mass at the same scale as its quadratic coupling to photons. The same is true of neutral pions, which also have a larger than expected quadratic coupling to photons. The result is that if axions make up DM, they induce temporal variation of the fine structure constant α, which is severely constrained by a variety of means. These constraints are recast for the QCD axion parameter space. How to generalise the finding to axion-like particles is also discussed and the resulting constraints are shown.

Ch5: Consistent Positivity at Finite-t

This chapter is based on a pre-print written in collaboration with Giulia Isabella, Davide Perrone, Sara Ricossa, Francesco Riva and Francesco Serra [226]. In it we study bounds arising from the analyticity and unitarity of scattering amplitudes in the context of effective field theories with massless particles, in particular with massless scalars and gravitons. We provide an approach that only uses dispersion relations away from the forward limit to set constraints on EFT Wilson coefficients. This is suitable to derive constraints in the presence of gravity, in a way that is robust with respect to radiative corrections. The method not only allows us to avoid the Coulomb pole, but also the singularities associated with calculable loop effects, which would otherwise diverge. Further, we describe under what circumstances smeared distributions are sensitive to the individual coefficients of a Taylor expansion, such as the amplitude stemming from an EFT.

Ch6: EFTs involving gravity at finite Mandelstam-t

This chapter too is based on another pre-print written in collaboration with Giulia Isabella, Davide Perrone, Sara Ricossa, Francesco Riva and Francesco Serra [222]. We explore the impact of loop effects on positivity in EFTs containing dynamical gravity. Focusing on massless particles coupled to gravity, we address the treatment of forward-limit divergences from loop discontinuities and establish necessary conditions for maintaining computational control in perturbation theory. The loop corrections to the scattering amplitude of scalars is computed using modern on-shell methods. While loop effects remain small, ensuring consistency in our approach leads to a significant impact on previously derived bounds, even at tree level. The robust constraints found will be compatible with UV completions involving gravity. This study represents a foundational step toward bridging the gap between the tree-level results of the positivity program and the fully non-perturbative S-matrix bootstrap, which relies on ansatz-driven methods [227].

Chapter 2

Casting New Light on DM NMR

2.1 Chapter overview

This chapter points out that previously proposed DM NMR experiments, like CASPEr-Gradient have non-trivial sensitivity to additional couplings such as the axion's coupling to photons $g_{a\gamma\gamma}$ and the DP kinetic mixing parameter. The basic reason why this is true is that the spin sample of the experiment exists encased within metallic shielding. The shielding forms a conductive cavity that can be *rung up* by the aforementioned DM candidates . The sample can then experience a torque from the magnetic field modes. We will discuss this idea more quantitatively in the remainder of the chapter, as well as how a typical NMR experiment such as CASPEr-Gradient operates. First the basic idea will be discussed. The results will be presented and compared against pre-existing constraints. Additional information about ringing up the cavity modes is presented in 2.6. Then we will show in 2.7, the rate at which the DM induced magnetization grows in CASPEr in all regimes [228]. Given the confusion that has appeared in the literature around these scalings, we believe it is useful to outline our additional derivation. Lastly, in Sec. 2.8 we provide a detailed description of the transition from a microscopic transition of individual spins to a macroscopic magnetized sample as relevant for DM NMR.

2.2 DM NMR Experiments Have Additional Sensitivity

Planned experiments aim to cover enormous swathes of unexplored ultralight DM parameter space. Unexpected signals could emerge. For example, these devices can detect relativistic signals such as a cosmic axion background [229, 230] or gravitational waves [231–235]. In this chapter we instead demonstrate that *even sensitivity to DM signals have been overlooked*: devices designed to search for one type of wave DM can be strongly sensitive to another. More to the point, ongoing efforts to detect axion DM coupled to nucleons with nuclear magnetic resonance (NMR), for example by CASPEr-Gradient [236, 237], would be highly sensitive to the axion-photon coupling and dark photon DM. Given our near-complete ignorance as to the nature of DM, it stands that these situations should be highlighted whenever possible.

To justify our claim we recall the basics of axion NMR. Consider a sample of nuclear spins aligned in a background magnetic field $\mathbf{B}_0$. In conventional NMR, one fires an electromagnetic wave through the sample that generates an interaction according to $\mathcal{H}_B = -\gamma \mathbf{B}\cdot\mathbf{S}$, with γ and $\mathbf{S}$ the nucleon gyromagnetic ratio and spin operator. Consequently, the spins are tipped into the plane transverse to $\mathbf{B}_0$ and begin to precess at the Larmor frequency, $\omega_0 = \gamma B_0$, yielding an oscillatory signal in the transverse plane. CASPEr-Gradient exploits the same physical principle. If the spins are immersed in an axion DM wave, then the axion-nucleon coupling, $\mathcal{L}_{aN} = g_N(\partial_\mu a)\bar{N}\gamma^\mu\gamma_5 N$, generates an interaction $\mathcal{H}_{aN} = -2g_N\nabla a\cdot\mathbf{S}$. By analogy to $\mathcal{H}_B$ the axion induces an *effective* magnetic field of the form $\mathbf{B}_{aN} = g_N(2/\gamma)\nabla a$. The axion field has an identical effect: DM tips the spins, which then precess leading to a detectable signal. There is a resonant enhancement when $\omega_0 \simeq m$ and therefore one performs a resonant search by scanning through values of B_0.

We can now explain our core insight: if DM generates a real rather than effective magnetic field, CASPEr-Gradient can also detect it. Consider first dark photon DM, $\mathbf{A}'$, that mixes with the visible photon via a kinetic mixing parameter ϵ [92]. To mitigate the impact of stray magnetic fields, the spin sample must be placed within a shielded region of geometric size L. The dark photon will penetrate that shield and generate a magnetic field $\mathbf{B}_{A'} \sim \epsilon m^2 L \mathbf{A}'$ [238]. Setting $B_{aN} \sim B_{A'}$, the qualitative dark-photon sensitivity in terms of the axion-nucleon coupling is $\epsilon \sim g_N v/\gamma m L$, with $v \sim 10^{-3}$ the local DM speed. We can rephrase the sensitivity as follows. Writing $g_N = c_N m/m_\pi f_\pi$, which depends on the pion mass and decay constant, we have

$$\epsilon \sim 10^{-16}\, c_N\, (\gamma_{\rm He}/\gamma)\, (10\,{\rm cm}/L), \tag{2.1}$$

assuming a helium-3 sample. Although an ambitious target, the ultimate goal of all axion experiments is QCD sensitivity, where $c_N \sim 1$. Note the above scaling is distinct from ideas to repurpose axion-photon searches for the dark photon, as in e.g. Ref. [80]. In those cases the dark photon sensitivity does not gain from the large magnetic field volume that is maximized for the axion sensitivity. Here, however, the scaling of both the axion and dark photon signal is controlled by the density of spins, or effectively the background magnetization.

A similar argument applies to the axion-photon coupling, $\mathcal{L}_{a\gamma\gamma} = -\frac{1}{4} g_{a\gamma\gamma} a F \widetilde{F}$, where axion DM couples to $\mathbf{B}_0$ and induces $B_{a\gamma} \sim g_{a\gamma\gamma} B_0 L (\partial_t a)$, where now L is the scale over which B_0 is generated. The expected sensitivity from $B_{aN} \sim B_{a\gamma}$ is $g_{a\gamma\gamma} \sim g_N v/\gamma B_0 L$, or taking $g_{a\gamma\gamma} \sim c_\gamma \alpha_{\rm EM} m/2\pi m_\pi f_\pi$,

$$c_\gamma \sim c_N\, (10\,{\rm T}/B_0)\, (\gamma_{\rm He}/\gamma)\, (10\,{\rm cm}/L). \tag{2.2}$$

This result demonstrates that at the highest frequencies – recall B_0 is tuned to adjust the resonant frequency – an instrument sensitive to the QCD axion value of c_N would also be sensitive to the QCD axion prediction of $c_\gamma \sim 1$.

In what follows we refine the qualitative results of Eqs. (2.1) and (2.2) culminating in the projections shown in Fig. 2.1. These results show the reach for several sensitivity estimates for CASPEr-Gradient that exist in the literature, specifically Refs. [228, 239], each shown for two different target nuclei, xenon-129 and helium-3. The results are compared to existing constraints from Refs. [240–260] and the theoretical predictions of Refs. [71, 73, 261, 262], see Ref. [263].

2.3 Principles of DM NMR

In the presence of a magnetic field, a spin with magnetic moment $\boldsymbol{\mu} = \gamma \mathbf{S}$ experiences a torque, and therefore precesses according to $\dot{\boldsymbol{\mu}} = \boldsymbol{\mu} \times \gamma \mathbf{B}$. Taking $\mathbf{B} = B_0 \hat{\mathbf{z}}$, the transverse coordinates $\mu_\pm = (\mu_x \pm i\mu_y)/\sqrt{2}$ evolve under the precession as $\mu_\pm(t) \propto e^{\mp i\omega_0 t}$. NMR extends this picture to a macroscopic sample of spins: $\boldsymbol{\mu}$ is promoted to $\mathbf{M}$, the magnetization within the material, and $\mathbf{B}$ to $\mathbf{H}$. We assume $\mathbf{H} = H_0 \hat{\mathbf{z}}$ up to small corrections, however, the dynamics in the sample is also controlled by spin-spin and spin-lattice interactions. These interactions exponentially damp coherent oscillations in the transverse and longitudinal directions, respectively, and are quantified by corresponding timescales T_2 and T_1. The system evolves according to the Bloch equations,

$$\dot{\mathbf{M}} = \mathbf{M} \times \gamma \mathbf{H} - \frac{M_x \hat{\mathbf{x}} + M_y \hat{\mathbf{y}}}{T_2} - \frac{(M_z - M_0)\hat{\mathbf{z}}}{T_1}, \tag{2.3}$$

with M_0 the steady state magnetization generated by H_0.

We now introduce DM into the system as a small correction to the magnetic field, $\mathbf{H} = H_0 \hat{\mathbf{z}} + \mathbf{H}_{\rm DM}$. While the aim of CASPEr-Gradient is to detect the effective magnetic field $\mathbf{H}^{\rm eff}_{\rm DM} = g_N (2/\gamma) \nabla a$, the goal of this paper is to highlight a broader range of possibilities. Taking $H_{\rm DM}/H_0 \ll 1$, we solve the problem perturbatively. At zeroth order, the steady state solution is $\mathbf{M} = M_0 \hat{\mathbf{z}}$. In general, both transverse components of $\mathbf{M}$ and $\mathbf{H}_{\rm DM}$ are coupled and must be accounted for carefully. If, however, we define $M_\pm = (M_x \pm i M_y)/\sqrt{2}$ and similarly $H^\pm_{\rm DM}$ the first order Bloch equations decouple, leaving

$$\dot{M}_+ = -T_2^{-1} M_+ - i(\omega_0 M_+ - \gamma M_0 H^+_{\rm DM}). \tag{2.4}$$

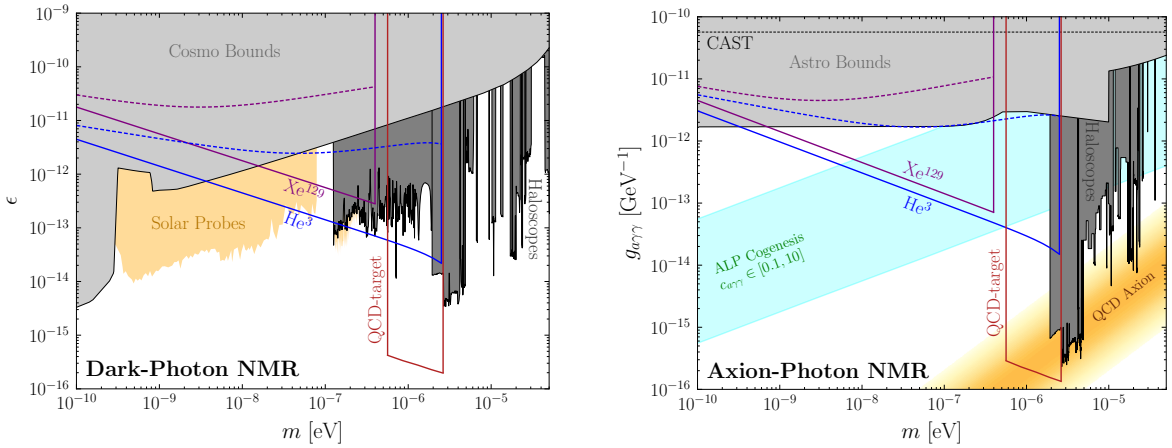

Figure 2.1: Projected reach of DM NMR to dark photons (left) and axions (right). Both searches can be performed *simultaneously* along with a search for the axion nucleon coupling. The purple and blue lines correspond to a sample constituted of xenon-129 ($\gamma = 12\,\mathrm{MHz/T}$, $n = 1.3 \times 10^{22}\,\mathrm{cm}^{-3}$) and helium-3 ($\gamma = 32\,\mathrm{MHz/T}$, $n = 2.8 \times 10^{22}\,\mathrm{cm}^{-3}$). Solid curves assume $T_2 = 100\,\mathrm{s}$, whereas dashed curves assume a line width limited by a part-per-million. A search capable of reaching the QCD axion prediction for g_N would have the sensitivity shown in red [228]. The reach assumes a single TM mode with the sample placed at the optimal radius of $r \simeq 0.77R$. See the text for further details.

Taking $M_+(0) = 0$ the solution to this equation is

$$M_+(t) = i\gamma M_0 \int_0^t dt'\, e^{-(t-t')/T_2} e^{-i\omega_0(t-t')} H^+_{\rm DM}(t'). \tag{2.5}$$

Accordingly, for a perfectly resonant DM field, $H^+_{\rm DM} = H_{\rm DM} e^{-i\omega_0 t}$, the magnetization grows as

$$M_+(t) = i e^{-i\omega_0 t}\, \gamma M_0 H_{\rm DM} T_2\, (1 - e^{-t/T_2}). \tag{2.6}$$

For $t \ll T_2$ DM drives a linear growth in the transverse component of the magnetization which continues until the amplitude begins to saturate once $t \sim T_2$. The dynamics are comparable for a more realistic model of a DM field with finite coherence. An exception occurs if the DM coherence time, $\tau_{\rm DM}$, is shorter than T_2, in which case for $\tau_{\rm DM} < t < T_2$ the growth of M_+ slows from linear to $\sqrt{t}$ [228]. Regardless, for $t \gg T_2, \tau_{\rm DM}$ the amplitude of the transverse magnetization saturates at $\gamma M_0 H_{\rm DM} T_2$.

In summary, DM drives the growth of a transverse oscillatory component to the magnetization. To provide a sensitivity estimate we must determine the appropriate backgrounds. Firstly, the spins within the sample generate an intrinsic noise source according to the fluctuation dissipation theorem. Specifically, Eq. (2.5) defines a susceptibility of $\chi_{++}(t) = i\gamma M_0 e^{-t/T_2} e^{-i\omega_0 t}\Theta(t)$ or $\chi_{++}(\omega) = i\gamma M_0/[i(\omega_0 - \omega) + T_2^{-1}]$. The imaginary part of this expression dictates the power spectral density (PSD) of the noise,

$$S^{\rm SP}_{M_+}(\omega) \simeq \frac{2\gamma M_0 T_s}{\omega V} \frac{T_2}{1 + (\omega - \omega_0)^2 T_2^2}. \tag{2.7}$$

This background is none other than the spin projection noise; the result as stated adopts the good resonator ($\omega_0 T_2 \gg 1$) and rotating wave approximations. The noise depends on the bulk magnetization $M_0 = n\gamma\omega_0/4T_s$, with n the spin density in the sample and T_s the spin temperature—from this we confirm the usual result that the form is independent of temperature.

The combined effect of DM and spin-projection noise is a transverse magnetization that leads to a corresponding magnetic field outside the sample. If the magnetization is measured inductively through a SQUID, there is an additional background contribution from the magnetometer itself. Further, thermal noise sources throughout the device contribute additional backgrounds. Nevertheless, for the parameters CASPEr intends to employ the dominant effect is spin projection noise.

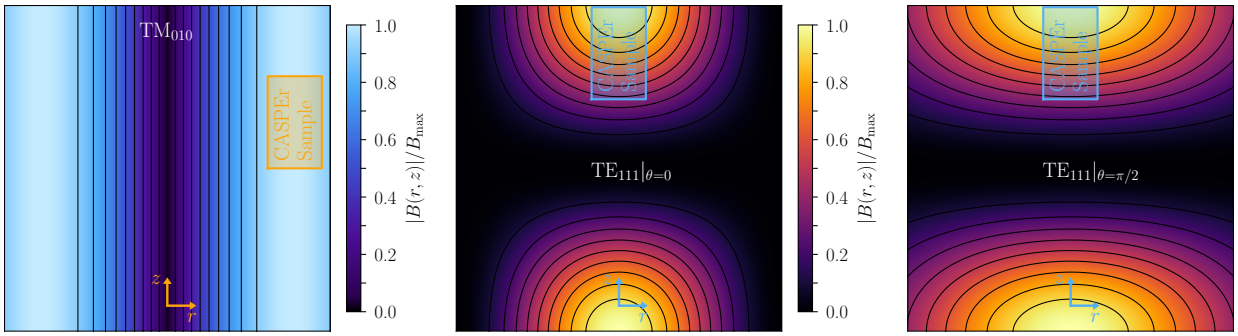

Figure 2.2: The profile of the physical magnetic fields DM could excite as compared the size of CASPEr's sample of nuclear spins. The contours denote 10% changes in the magnetic field value. The dominant mode the axion-photon coupling can excite is TM_{010}, whereas a dark photon can also excite the TE_{111} mode depending upon its polarization. The figure highlights that as the sample is moved within the magnetic field the response varies, opening a path to distinguishing different DM signals and even mapping out the dark photon polarization.

Accordingly, we can estimate the sensitivity by searching for a DM signal over the spin projection background. Working at high masses where $T_2 > \tau_{\rm DM}$, we imagine interrogating the system for a time $T = T_2$ so that the observed power is distributed over a frequency bin of width $2\pi/T_2$. For the bin centred around ω_0, the average spin projection noise power is $\bar{P}_{\rm SP} = \gamma^2 n T_2/16\pi V$. For the signal, after accounting for the finite coherence, the equivalent expression is $\bar{P}_{\rm DM} = (\gamma M_0 H_{\rm DM} T_2)^2 \tau_a/2\pi$. Assuming the signal and background magnetizations undergo Gaussian fluctuations, the power is distributed exponentially and we therefore expect the sensitivity limit to occur for $\bar{P}_{\rm DM} = \bar{P}_{\rm SP}$, or neglecting $\mathcal{O}(1)$ factors

$$H_{\rm DM} \sim \frac{v}{\gamma}\sqrt{\frac{m}{nT_2V}}, \tag{2.8}$$

where we took $M_0 = n(\gamma/2)$, assuming a hyperpolarized sample, and $\tau_a \sim 1/mv^2$. A longer measurement with $T > T_2$ would improve on this sensitivity by $(T/T_2)^{1/4}$; further, when $T_2 > \tau_a$ a gain can be made by accounting for the multiple frequency bins the signal appears in [228]. For the axion-nucleon coupling, where $H_{\rm DM} = g_N(2/\gamma)\nabla a \sim g_N(v/\gamma)\sqrt{\rho_{\rm DM}}$, Eq. (2.8) gives an estimated sensitivity of $g_N \sim \sqrt{m/\rho_{\rm DM} n T_2 V}$.

This ends our compact review of DM NMR. A more detailed discussion appears in the later sections and we now turn to the different forms of $\mathbf{H}_{\rm DM}$.

2.4 Dark Photon NMR

Consider the scenario where DM is a boson of a dark gauged U(1): a dark photon A'^μ. (We leave our discussion UV agnostic and refer instead to Refs. [264, 265].) This state can couple to the visible sector through the marginal operator $\frac{1}{2}\epsilon F^{\mu\nu}F'_{\mu\nu}$ parametrized by a kinetic mixing ϵ taken to be small throughout. Rotating the two gauge fields to remove the kinetic mixing transforms to the interaction basis, where the dark photon remains decoupled from standard model currents yet provides a source for the visible U(1), quantified by $J^\mu_{\rm eff} \simeq -\epsilon m^2 A'^\mu$.

This effective dark-photon current penetrates shielded regions, such as surrounds CASPEr-Gradient. Taking the shielded region to have parametric size L, DM NMR operates in the regime where $mL \ll 1$ and therefore the induced magnetic field dominates [238]. In that limit we can neglect the displacement current implying the relevant equation is $\nabla \times \mathbf{H} \simeq -\epsilon m^2 \mathbf{A}'$, confirming the parametric size of the induced magnetic field as $\epsilon m^2 L \mathbf{A}'$. From Eq. (2.8), the parametric sensitivity scales as

$$\epsilon \sim \frac{v}{\gamma L}\sqrt{\frac{1}{m\rho_{\rm DM} n T_2 V}}. \tag{2.9}$$

When compared to the scaling for g_N this result is consistent with Eq. (2.1).

To fully quantify the sensitivity we must consider how the modes of the shielded region can be driven by the dark-photon current and the geometry of the associated magnetic fields. We treat the shielded region as a cylindrical cavity (deviations away from this will not strongly impact our projections) and as $mL \ll 1$ the DM driving frequency is always much smaller than the electronic resonant frequencies ($\omega_0 \sim 1/L$), implying we can ignore dissipative effects. Further, the precise composition of the shielding material is not important, as the DM signal is at sufficiently high frequencies that the shield can be treated as a perfect conductor. We can then decompose the cavity field into the conventional transverse electric (TE) and transverse magnetic (TM) modes, each labelled by indices $\ell = (m, n, p)$ (for the azimuthal, radial, and longitudinal indices), from which the amount each mode is excited by the dark photon can be computed directly. The computation is standard and therefore not presented here, although the full details are provided in 2.6.

One aspect of the calculation that must be mentioned, however, is the spatial profile of the dark-photon induced magnetic field. This dictates the direction of the magnetic field experienced by the spin sample and opens the possibility of distinguishing various DM induced NMR signals; see Fig. 2.2. To understand the field profile, we first emphasize that it is the lowest accessible cavity modes that are dominantly excited. If $\mathbf{E}_\ell$ represents the field of a given mode, then the induced magnetic field depends on the following integral over the shielded volume,

$$\int dV\, \mathbf{E}_\ell^* \cdot \mathbf{J}_{\rm eff} \simeq -\epsilon m^2 \mathbf{A}' \cdot \int dV\, \mathbf{E}_\ell^*, \tag{2.10}$$

where the accuracy of the approximation exploits the spatial uniformity of DM over spatial scales $\mathcal{O}(L)$ [65]. The value of the final integral is suppressed for higher modes; indeed, it is an excellent approximation to only retain the lowest non-vanishing modes, TM_{010} driven by A'_z and TE_{111} driven by $A'_{x,y}$. Accordingly, the modes driven are sensitive to the polarization of the dark photon, a fact that could be exploited to not only measure the polarization distribution in the event of a detection but also to distinguish the signal from axion DM.

The spatial profile of the modes determines the ideal placement of the spin sample as shown in Fig. 2.2. For CASPEr-Gradient the sample is sufficiently smaller than the shielded region such that the sample can in principle be moved around and in the case of the TM_{010} mode can inhabit a region of uniform induced field. For other modes and a larger sample the effect of a non-uniform field across the sample must be accounted for. In detail, we take the shielding to have a radius of $R \simeq 9\,\mathrm{cm}$ and height of 18 cm, whereas the cylindrical sample has a height of 3 cm and radius of 2.5 cm. In Fig. 2.2 the axis of the sample is taken to be perpendicular to that of the shielding. Generally, the optimal placement is determined by looking for where the modes take their maximum value; for the TM_{010} mode the sample should be placed at a radius of roughly $0.77R$, whereas for the TE_{111} mode the sample should be placed on-axis radially and near the end caps longitudinally.

Comparing Eq. (2.9) to Fig. 2.1 we find that the parametric estimate for fixed T_2 accurately reflects the scaling of the full result, but overstates the sensitivity by roughly a decade. The difference is a combination of $\mathcal{O}(1)$ factors and roughly a factor of $\sim$1.8 suppression from the geometry of the cavity. The sensitivity breaks down for $m \gtrsim 1\,\mu\mathrm{eV}$ as the cavity modes begin to be driven resonantly. This breakdown is largely irrelevant to our projections because the largest mass value that can be observed is dictated by the externally applied magnetic field and is below the point where the Q-factor of the cavity must be specified. The weaker projections arise by assuming that the scan is limited by a part per million line-width at every frequency due to magnetic field inhomogeneities [266]. The effective T_2 is then frequency dependent, $T_2 \propto 1/m$, so that Eq. (2.9) predicts a flat sensitivity scaling with mass as approximately observed.

2.5 Axion-Photon NMR

The considerations for axion DM that couples through $\mathcal{L}_{a\gamma\gamma}$ are almost identical to those for the dark-photon. For axion DM, the leading effect is an induced current $\mathbf{J}_{\rm eff} \simeq g_{a\gamma\gamma}(\partial_t a)\mathbf{B}$. As the background magnetic field points along the axis of the cylindrical shielded region, from Eq. (2.10) it is apparent that the axion does

not couple to the TE modes, leaving the dominant contribution from the TM_{010} mode, again as shown in Fig. 2.2. For Fig. 2.1 we assume the sample is placed optimally. The quantitative sensitivity there can be determined as for the dark photon: $H_{\rm DM} \simeq g_{a\gamma\gamma} B_0 L(\partial_t a)$. A critical point, however, is that B_0 is not a fixed parameter, but is rather adjusted to scan through various DM masses. If we denote $\bar{B}_0$ as the magnetic field used to scan the largest mass in the search, $\bar{m}$, then $B_0 = \bar{B}_0(m/\bar{m})$. Finally, we can use Eq. (2.8) to obtain a parametric sensitivity of

$$g_{a\gamma\gamma} \sim \frac{v\bar{m}}{\gamma \bar{B}_0 L}\sqrt{\frac{1}{m\rho_{\rm DM} n T_2 V}}. \tag{2.11}$$

As for the dark photon, this result correctly reproduces the scaling in Fig. 2.1.

2.6 Driven cavity modes

Here we elaborate on the cavity modes that were briefly discussed before. A quick review of cavity modes is provided before a discussion of the selection rules for a DM signal that are dictated by the cavity's geometry.

2.6.1 Cavity Basics

We specialise the analysis to cylindrical cavities as the shielding of the CASPEr-Gradient experiment is well approximated by a cylinder, and because of its relative simplicity. All of our qualitative findings will extend to more general geometries. The cavity modes are determined by solving source-less Maxwell equations. We align the bore of the cylinder with the z-direction and decompose the electric and magnetic field as follows,

$$\begin{Bmatrix} \mathbf{E}(\mathbf{x},t) \\ \mathbf{H}(\mathbf{x},t) \end{Bmatrix} = \int \frac{d\omega dk}{(2\pi)^2} \begin{Bmatrix} \mathbf{E}(x,y,k,\omega) \\ \mathbf{H}(x,y,k,\omega) \end{Bmatrix} e^{i(kz-\omega t)}. \tag{2.12}$$

The fields satisfy the wave equation

$$\left[\nabla_T^2 + \mu\varepsilon\,\omega^2 - k^2\right] \begin{Bmatrix} \mathbf{E}(x,y,k,\omega) \\ \mathbf{H}(x,y,k,\omega) \end{Bmatrix} = \mathbf{0}, \tag{2.13}$$

where T indicates a sum over the transverse directions, whilst μ and ϵ are the permeability and permittivity.

The cavity walls are formed by the magnetic shielding which is used is to mitigate the effects of low-frequency external magnetic fields. This is normally achieved by using a metal alloy with very high magnetic permeability. These alloys usually have electrical conductivity values somewhere in the range $10^6 - 10^8\,\mathrm{S/m}$, typical of metallic materials. For frequencies away from a cavity resonance, it is then sufficient to approximate the walls of the cavity as perfectly conductive, recovering the following simple boundary conditions:

$$\mathbf{n} \times \mathbf{E} = \mathbf{0}, \qquad \mathbf{n} \cdot \mathbf{H} = 0, \tag{2.14}$$

where $\mathbf{n}$ denotes the normal direction from the surface of the conductor. For finite conductivity, the analysis is modified by introducing the generalised Ohm's law contribution to the cavity quality factor. Typically the quality of a cavity is limited by the heating of its walls. In general, the presence of the CASPEr spin sample within the cavity will provide a small modification to the modes. For simplicity, we neglect the impact of the sample on the calculation as it will only lead to minor impact on our projections.

In order to impose the boundary conditions, we label the two end-caps of the cylinder by $\mathcal{C}$ and the circular wall by $\mathcal{S}$. The cylinder is taken to have a radius R and height l_z. Imposing the boundary conditions of Eq. (2.14) on $\mathcal{C}$ determines the allowed values of k, and imposing them on $\mathcal{S}$ allows us to split the possible field configurations into two groups, the transverse magnetic (TM) and transverse electric (TE) modes. The TM modes satisfy $E_z\big|_{\mathcal{S}} = 0$ with $H_z = 0$ throughout the cavity. The TE modes instead satisfy $\partial_n H_z\big|_{\mathcal{S}} = 0$ and $E_z = 0$. The two sets of modes are further labelled by integers $\ell = (m, n, p)$ that determine the mode number in the azimuthal, radial, and longitudinal direction.

With the above requirements, the TM modes are given by

$$\begin{aligned} E_z(\mathbf{x},t) &= \phi(x,y)\,\cos(p\pi z/l_z), \\ \mathbf{E}_T(\mathbf{x},t) &= \nabla_T\phi(x,y)\,\frac{(p\pi/l_z)}{(p\pi/l_z)^2-\varepsilon\mu\,\omega^2}\,\sin(p\pi z/l_z), \\ \mathbf{H}_T(\mathbf{x},t) &= -\hat{\mathbf{z}}\times\nabla_T\phi(x,y)\,\frac{i\,\varepsilon\,\omega}{(p\pi/l_z)^2-\varepsilon\mu\,\omega^2}\,\cos(p\pi z/l_z), \end{aligned} \tag{2.15}$$

where ϕ is a function satisfying the two dimensional wave equation and $\phi\big|_{\mathcal{S}}=0$. The TE modes are similarly described

$$\begin{aligned} H_z(\mathbf{x},t) &= \psi(x,y)\,\sin(p\pi z/l_z), \\ \mathbf{H}_T(\mathbf{x},t) &= \nabla_T\psi(x,y)\,\frac{(p\pi/l_z)}{(p\pi/l_z)^2-\varepsilon\mu\,\omega^2}\,\cos(p\pi z/l_z), \\ \mathbf{E}_T(\mathbf{x},t) &= \hat{\mathbf{z}}\times\nabla_T\psi(x,y)\,\frac{i\,\mu\,\omega}{(p\pi/l_z)^2-\varepsilon\mu\,\omega^2}\,\sin(p\pi z/l_z). \end{aligned} \tag{2.16}$$

Here ψ plays the role of ϕ, and satisfies the modified boundary condition $\partial_n\psi\big|_{\mathcal{S}}=0$. Note for the TM modes p begins at 0, whereas for the TE modes the smallest value is 1. The transverse fields are described by Bessel functions,

$$\phi(x,y)\propto J_m(j_{mn}r/R)\,e^{im\theta},\qquad \psi(x,y)\propto J_m(j'_{mn}r/R)\,e^{im\theta}. \tag{2.17}$$

Here r and θ are the cylindrical coordinates, j_{mn} denotes the nth zero of the mth Bessel function and j'_{mn} denotes the nth zero of the mth Bessel function's derivative. The full set of modes form an eigenbasis of functions and so are orthogonal to each other when integrating over the volume of the cavity. The constants of proportionality in Eq. (2.17) can be chosen to ensure the modes are orthonormal, for instance we assume $\int dV\,\mathbf{E}_\ell\cdot\mathbf{E}^*_{\ell'}=\delta_{\ell\ell'}$, where the integral is taken over the shielded volume, V. The eigenfrequencies are

$$\omega_\ell^2=\frac{1}{\varepsilon\mu}\left[(j^{(\prime)}_{mn}/R)^2+(\pi\,p/l_z)^2\right]. \tag{2.18}$$

The geometry of the magnetic field for the lowest lying cavity modes is shown in Fig. 2.3 (cf. Fig. 2.2).

2.6.2 Driven Cavity Modes

The above discussion provides us with a complete set of modes within the cavity, allowing for a decomposition of arbitrary electric and magnetic fields. These can then be used to determine the form of the fields generated by an effective charge or current configuration as,

$$\left(\nabla^2-\varepsilon\mu\,\partial_t^2\right)\begin{Bmatrix}\mathbf{E}(\mathbf{x},t)\\ \mathbf{H}(\mathbf{x},t)\end{Bmatrix}=\begin{Bmatrix}\frac{1}{\varepsilon}\left(\nabla\rho_{\text{eff}}+\varepsilon\mu\,\partial_t\mathbf{J}_{\text{eff}}\right)\\ -\nabla\times\mathbf{J}_{\text{eff}}\end{Bmatrix}. \tag{2.19}$$

The electric field can be decomposed as,

$$\mathbf{E}(\mathbf{x},t)=\int\frac{d\omega}{2\pi}\,e^{-i\omega t}\sum_\ell c_\ell(\omega)\,\mathbf{E}_\ell(\mathbf{x}). \tag{2.20}$$

This result can be applied for the TE and TM modes separately. The coefficients are determined from Eq. (2.19) as,

$$c_\ell(\omega)=\frac{i\omega}{\varepsilon(\omega_\ell^2-\omega^2)}\int dV\,\mathbf{J}_{\text{eff}}\cdot\mathbf{E}^*_\ell. \tag{2.21}$$

The integral in this expression dictates a set of selection rules relating the form of the DM current to the modes generated, as explored in Eq. (2.10). Note that the gradient of the charge density has no effect on the

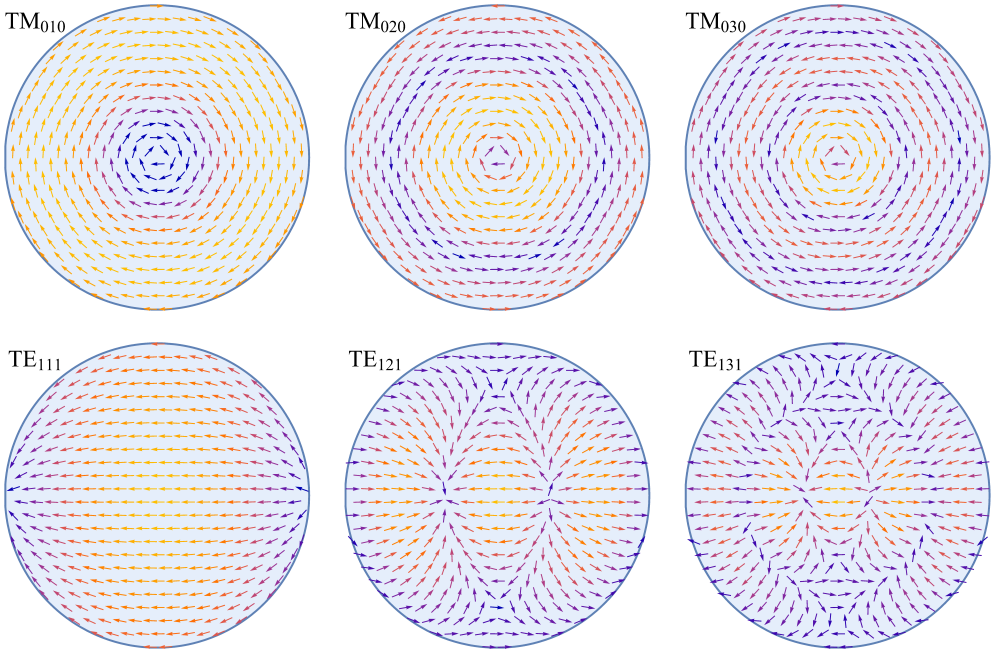

Figure 2.3: The transverse magnetic field geometry of the lowest lying modes of a cylindrical cavity. We set $\mu = \varepsilon = 1$ and show a section at $z = 0$ (i.e. at a cap). The heat map is such that yellow corresponds to larger field values and blue smaller.

divergence free field modes we consider [267–270]. The magnetic fields are fixed from the above discussion through Faraday's law. In detail,

$$\mathbf{H}(\mathbf{x}, t) = \int \frac{d\omega}{2\pi} e^{-i\omega t} \sum_{\ell} \frac{\omega_\ell}{\omega} c_\ell(\omega) \mathbf{H}_\ell(\mathbf{x}). \tag{2.22}$$

The focus of CASPEr-Gradient is on the DM parameter space where $\omega \ll \omega_\ell$. Therefore the induced magnetic field is parametrically larger than the induced electric field.

Given DM is non-relativistic and has a characteristic speed of $v \sim 10^{-3}$, the spatial scale the DM varies over is set by the de Broglie wavelength, $\lambda_{\rm dB} \sim 1/mv \sim 1\,{\rm km}\,(1\,\mu{\rm eV}/m)$ (or more accurately the coherence length [65]), which is far larger than any relevant experimental scale. This implies that it is an excellent approximation to take the DM effective current in Eq. (2.21) as spatially uniform, so that $c_\ell \propto \mathbf{J}_{\rm eff} \cdot \int dV\, \mathbf{E}_\ell^*$, as in Eq. (2.10). The symmetry of the modes is such that for the TE modes we require $m = 1$, p odd, and n arbitrary; $\int dV\, \mathbf{E}_\ell^*$ is then purely transverse, implying it is accessible to the dark-photon current, but not the axion-photon coupling. For the TM modes, $m = p = 0$, and the integral can be evaluated as

$$\text{TM modes:} \quad \int dV\, \mathbf{E}_{0n0}^* = (-1)^{n+1} \frac{2}{j_{0n}} \sqrt{V}\, \hat{\mathbf{z}}. \tag{2.23}$$

Being purely in the z-direction, all DM currents can excite these modes.

As long as the DM frequency is well below ω_ℓ, the lowest modes will be dominantly excited: higher modes are always more oscillatory and therefore suppressed by the volume integral, additionally as the excited modes have an even larger frequency, the DM is further still off resonance. The key modes are therefore TM_{010} and TE_{111}. If the ratio $R/l_z > 0.492$, then $\omega_{111}^{\rm TE} > \omega_{010}^{\rm TM}$ and vice versa. Therefore, if the diameter of the cylinder is roughly the same size as its length these frequencies are comparable.

An important point to emphasize is that the modes are not spatially uniform throughout the cavity. This determines the magnetic field as seen by the sample. The relative sizes of the sample and shielding matter;

a small sample will effectively see a uniform field across it whereas a large sample will resolve the mode. If the spin sample were comparable in size to the shielding, then the average magnetic field across it will be zero. In reality, one could improve upon this because the exact spatial profiles of all of the modes are known, meaning that even though the net field is zero, the magnetic field in a given domain of the sample is known. This allows one to either take local readings of the magnetic flux with a magnetometer across a portion of the sample, or to form particular geometries in the pickup loops such that the flux coming from different parts of the sample is additive. For example, the TE_{111} mode has a cross-section of the form shown in Fig. 2.3 near the upper cap. The magnetic field for this mode varies as $\cos(\pi z/l_z)$, such that at the bottom cap the magnetic field lines point the opposite direction. A gradiometer configuration of the pickup loop could exploit this variation, such that the two contributions are additive and the field can be seen.

Nevertheless, given the relatively small size of the CASPEr-Gradient sample compared to the shielded region, the field will be close to uniform across it. The magnetic field of the TM modes varies only radially, proportional to $J_1(j_{01}r/R)$. The field is largest at $r = j'_{11}/j_{01}R \simeq 0.77R$, and for a small deviation δr away from value we have,

$$\frac{\delta H}{H_{\max}} = -\frac{1}{2}\left(\frac{j_{01}}{j'_{11}}\right)^2 \left[(j'_{11})^2 - 1\right] \left(\frac{\delta r}{R}\right)^2. \tag{2.24}$$

For the sample, that implies the field varies by $\simeq 6\%$ across the sample (cf. Fig. 2.2). The analogous result for the TE modes is that the field takes its maximum values at the centre of the shielding at $r = 0$, but near the caps $z = 0$ or l_z. The fractional size of the magnetic field away from the optimal placement is set by

$$\frac{\delta H}{H_{\max}} \simeq -\frac{1}{2}(j'_{11})^2 \left(\frac{\delta r}{R}\right)^2 - \frac{\pi^2}{2}\left(\frac{\delta z}{l_z}\right)^2. \tag{2.25}$$

Note we have ignored the angular dependence, as it is only a small correction.

2.7 Time-scaling of CASPEr Magnetic Field Signals

Here a frequency-domain analysis of the time-scaling of the signal for a generic dark matter-induced magnetic field in an NMR experiment is provided. The results match those of Ref. [228], where a similar analysis was performed in the time domain for the axion-gradient signal.

We begin by detailing our conventions. The time-average of the square of a quantity $f(t)$ can be written in terms of the power spectral density (PSD) as

$$\langle f^2 \rangle = \lim_{T\to\infty} \frac{1}{2T}\int_{-T}^{T} dt\, \langle f(t) f^*(t)\rangle = \int \frac{d\omega}{2\pi}\, S_f(\omega), \tag{2.26}$$

where $2\pi\delta(\omega-\omega')S_f(\omega) \equiv \langle f(\omega) f^*(\omega')\rangle$ is the PSD of the quantity f, and T is the integration time. It will be useful to have approximate relations for the PSDs in the cases where $f(\omega)$ is real, narrow, and peaked at a given frequency ω_f, or broad and flat over a bandwidth $\delta\omega_f$:

$$S_f(\omega)|_{\mathrm{narrow}} \simeq \pi\langle f^2\rangle\left[\delta(\omega-\omega_f) + \delta(\omega+\omega_f)\right], \tag{2.27}$$

$$S_f(\omega)|_{\mathrm{broad}} \simeq \frac{\pi\langle f^2\rangle}{\delta\omega_f}\left[\Theta\left(\frac{\delta\omega_f}{2} + (\omega+\omega_f)\right)\Theta\left(\frac{\delta\omega_f}{2} - (\omega+\omega_f)\right) + \Theta\left(\frac{\delta\omega_f}{2} + (\omega-\omega_f)\right)\Theta\left(\frac{\delta\omega_f}{2} - (\omega-\omega_f)\right)\right].$$

The expressions above define the mean value of the PSD, as the power itself will be a stochastic variable if $f(t)$ is a random field.

Now these definitions have been given we can show how the magnetisation vector scales in time. The starting point is the Bloch equations in the $M_\pm \equiv (M_x \pm iM_y)/\sqrt{2}$ basis, given by (cf. Eq. (2.4))

$$\dot{M}_\pm = -T_2^{-1} M_\pm \mp i(\omega_0 M_\pm - \gamma M_0 H^\pm_{\mathrm{DM}}), \tag{2.28}$$

where we have omitted the time-dependence of the relevant quantities for notational simplicity. Note that the magnetic field induced by the DM generically has both x and y components. This can be solved straightforwardly as (cf. Eq. (2.5))

$$M_\pm(t) = \pm i\gamma M_0 \int_0^t dt'\, e^{-(t-t')/T_2} e^{\mp i\omega_0(t-t')} H^\pm_{\rm DM}(t') = \pm i\gamma M_0 \int_{-\infty}^{\infty} dt'\, W_\pm(t,t') H^\pm_{\rm DM}(t'). \tag{2.29}$$

To simplify the subsequent analysis, we have introduced a windowed susceptibility function $W_\pm(t,t') = \Theta(t')\Theta(t-t')e^{-(t-t')/T_2}e^{\mp i\omega_0(t-t')}$, with $\Theta(x)$ the Heaviside step-function. The form of Eq. (2.29) allows us to define the time-averaged quantity

$$\langle |M_\pm(t)|^2\rangle = (\gamma M_0)^2 \int_{-\infty}^{+\infty} \frac{d\omega}{2\pi}\, \tilde{W}_\pm(t,\omega)\tilde{W}^*_\pm(t,\omega) S^\pm_{\rm DM}(\omega), \tag{2.30}$$

where we introduce the DM PSD as $\langle H^\pm_{\rm DM}(\omega) H^{\pm,*}_{\rm DM}(\omega')\rangle = 2\pi\delta(\omega-\omega')S^\pm_{\rm DM}(\omega)$. The quantity $\tilde{W}_\pm(t,\omega)$ is the Fourier transform of the time-domain function defined above, in particular

$$\tilde{W}_\pm(t,\omega)\tilde{W}^*_\pm(t,\omega) = \frac{T_2^2}{1+(\omega\pm\omega_0)^2T_2^2}\left(1 + e^{-2t/T_2} - 2e^{-t/T_2}\cos[(\omega\pm\omega_0)t]\right). \tag{2.31}$$

We may now use Eq. (2.30) to evaluate the left hand side under various assumptions regarding the hierarchies in timescales; in particular, as between transverse relaxation time T_2, the DM coherence time $\tau_{\rm DM}$, and the integration time T, effectively the time at which we evaluate the magnetization. Throughout, we will assume that $\omega_0 = m$ in the final results we give, but not in the intermediate steps of the calculation. We divide the discussion between whether $T_2 \gg T$ or vice versa.

Relaxation time T_2 exceeds the integration time T. Consider first $T_2 \gg T$. We study the scaling of the magnetization for different assumptions regarding the hierarchy with $\tau_{\rm DM}$. In all cases, we can take the $T_2 \to \infty$ limit of Eq. (2.31), simplifying it to

$$\lim_{T_2\to\infty} \tilde{W}_\pm(t,\omega)\tilde{W}^*_\pm(t,\omega) = \frac{2(1-\cos[(\omega\pm\omega_0)t])}{(\omega\pm\omega_0)^2}. \tag{2.32}$$

The only difference will be whether we can resolve the signal, determined by the hierarchy between T and $\tau_{\rm DM}$. Consider first $T \ll \tau_{\rm DM}$. We can then invoke the narrow signal PSD approximation of Eq. (2.27), writing $S^\pm_{\rm DM}(\omega) \simeq \pi|H^\pm_{\rm DM}|^2\,[\delta(\omega-m)+\delta(\omega+m)]$. We therefore obtain,

$$\langle |M_\pm(t)|^2\rangle_{T\ll\tau_{\rm DM}\ll T_2} \simeq \langle |M_\pm(t)|^2\rangle_{T\ll T_2\ll\tau_{\rm DM}} \simeq \frac{1}{2}(\gamma M_0|H^\pm_{\rm DM}|)^2\, T^2. \tag{2.33}$$

Causality dictates that all results will also have a $\Theta(T)$ present, although we suppress that for simplicity. The physical origin of the $1/2$, which appears in all expressions, is that only half of the DM power is matched with the $\pm\omega_0$ resonant frequency—this is effectively the rotating wave approximation. If instead we have an integration time $T \gg \tau_{\rm DM}$, we cannot approximate the magnetic field PSD as a δ-function, and should instead use the broad approximation in Eq. (2.27), taking the width as $\delta\omega = 2\pi/\tau_{\rm DM}$. Then we find

$$\langle |M_\pm(t)|^2\rangle_{\tau_{\rm DM}\ll T\ll T_2} \simeq \frac{1}{2}(\gamma M_0|H^\pm_{\rm DM}|)^2\, T\tau_{\rm DM}. \tag{2.34}$$

Integration time T exceeds the relaxation time T_2. If the relaxation time is shorter than the integration time T, we must use the full form of the windowed susceptibility given in Eq. (2.31). However, we can still straightforwardly evaluate the scaling of the signal in the relevant regimes. If the signal coherence time exceeds T, we can once again approximate $S^\pm_{\rm DM}(\omega)$ as infinitely narrow, resulting in

$$\langle |M_\pm(t)|^2\rangle_{T_2\ll T\ll\tau_{\rm DM}} \simeq \frac{1}{2}(\gamma M_0|H^\pm_{\rm DM}|)^2\, T_2^2. \tag{2.35}$$

The other cases require $T \gg \tau_{\rm DM}$, so that the DM signal is well resolved and can be approximated as broad. Performing the integrals and carefully treating the hierarchy between T_2 and $\tau_{\rm DM}$, we find,

$$\langle |M_\pm(t)|^2 \rangle_{T_2 \ll \tau_{\rm DM} \ll T} \simeq \frac{1}{2} (\gamma M_0 |H^\pm_{\rm DM}|)^2 \, T_2^2, \tag{2.36}$$

$$\langle |M_\pm(t)|^2 \rangle_{\tau_{\rm DM} \ll T_2 \ll T} \simeq \frac{1}{2} (\gamma M_0 |H^\pm_{\rm DM}|)^2 \, T_2 \tau_{\rm DM}. \tag{2.37}$$

2.8 Microscopic to macroscopic description

The Bloch equations can be derived from a microscopic perspective [271–274]. The derivation clarifies the microphysical origin of the macroscopic equations. In this section, we discuss some of the salient aspects of this microphysical description and how they affect the analysis we present earlier in the chapter. Throughout this section we reserve the symbol H for the Hamiltonian and will use B for magnetic fields.

2.8.1 Master relaxation equation

A quantum spin system can be described by a density operator $\rho = p_j \, |\psi_j\rangle \, \langle \psi_j|$, where p_j is a weight for the state labelled by ψ_j, and summation is implied. This density matrix evolves according to the Liouville-von Neumann equation:

$$\frac{\mathrm{d}}{\mathrm{d}t} \rho = i \, [\rho, H] \, . \tag{2.38}$$

Observables can be calculated by taking the weighted trace $\langle Q \rangle = \mathrm{tr} \, (\rho \, Q)$. We may decompose the Hamiltonian into time independent and time dependent parts '$H = H_0 + H_I \, (t)$'. This choice allows us to account for interactions between the spin system and the reservoir, which is treated as being classical, in a simple manner. In the interaction picture, a quantity X is transformed as $\bar{X} \equiv \exp \, (i H_0 t) \; X \; \exp \, (-i H_0 t)$, and the evolution of the spin density per Eq. (2.38) is therefore

$$\frac{\mathrm{d}}{\mathrm{d}t} \bar{\rho} = i \left[\bar{\rho} \, (t) \, , \bar{H}_I \, (t) \right] \, . \tag{2.39}$$

We assume that environmental processes are characterised by a short correlation time τ_c such that $\tau_c \, \langle \bar{H}_I^2 \rangle^{1/2} \ll 1$. This corresponds to assuming that the environment is a thermal system, and $\tau_c \ll t \ll \langle \bar{H}_I^2 \rangle^{-1/2}$. $\langle \bar{H}_I^2 \rangle^{1/2}$ is the root-mean-square energy driving the system from the environment which dictates a natural largest timescale after which the system will have fully relaxed. Correlations between the density matrix and the interaction Hamiltonian representing the environment can therefore be neglected. We further assume that the evolution is only dependent on the current state of the system, meaning that we take the Born-Markov approximation. This allows us to rewrite the evolution equation in the form of the master equation [275, 276],

$$\frac{\mathrm{d} \bar{\rho} \, (t)}{\mathrm{d}t} = - \int_0^\infty \left[\langle \bar{H}_I \, (t) \, , \left[\bar{H}_I \, (t + \tau) \, , \bar{\rho} \, (t) \right] \rangle \right] \mathrm{d}\tau \, . \tag{2.40}$$

The upper limit of the integral has been extended to infinity as the short correlation times ensure that the integrand does not have support at large times. Formally, the calculation accounts for semi-classical fluctuations about a background density operator ρ_0 in thermal equilibrium, so the density matrix should be modified to $\rho \to \rho - \rho_0$. The classical background magnetisation M_0 can be thought of as being represented through the thermal background ρ_0, as we will see upon derivation of the Bloch equations.

2.8.2 The interaction Hamiltonian

The non-relativistic limit of the Dirac Lagrangian leads to the appropriate description for the interaction between the fermion spins and EM fields. The leading interaction between a magnetic field and spin in the $v/c \ll 1$ expansion is given by

$$\hat{H}_n \supset - \gamma \, \mathbf{B} \cdot \hat{\mathbf{s}}_n \, , \tag{2.41}$$

with the index n indicating that the full Hamiltonian is the sum over all spins. The coefficient γ is the species-dependent gyromagnetic ratio that accounts for substructure of the nuclei. The Hamiltonian of Eq. (2.41) is valid at the location of the spin in question '$\hat{\mathbf{s}}_n$'. To remove any ambiguities that may arise when taking volume averages of quantities to obtain macroscopic quantities, we can define the spin-density operator

$$\hat{\mathbf{S}}\left(\mathbf{x}\right) = \sum_n \hat{\mathbf{s}}_n \, \delta^{(3)}\left(\mathbf{x} - \mathbf{x}_n\right) , \tag{2.42}$$

such that $\int dV \, \hat{\mathbf{S}} = \sum_n \hat{\mathbf{s}}_n$. The validity of this definition is ensured as long as there is a sufficiently large scale separation between the typical inter-spin distance and the typical scale of variation of the applied magnetic field. This is always the case for the situations we consider. We can then decompose the applied magnetic field into a background field $\mathbf{B}_0$ entering the free Hamiltonian H_0, and interacting fields $\mathbf{B}_I$ in the interaction Hamiltonian H_I, with $\mathbf{B} \to \mathbf{B}_0 + \mathbf{B}_I$ in Eq. (2.41).

2.8.3 Thermal magnetisation vector: M_0

To derive the Bloch equations, we first define the macroscopic magnetisation vector in terms of the spin-density operator and a spatial window function $f(\mathbf{x})$ [277]

$$M^a\left(\mathbf{x}, t\right) \equiv \gamma \int \mathrm{d}^3 x' \, f\left(\mathbf{x}'\right) \left\langle \, \hat{S}^a\left(\mathbf{x} - \mathbf{x}'\right) \right\rangle , \tag{2.43}$$

where $\langle \cdot \rangle$ indicates that the weighted trace of the spin-density operator is taken, and a is a spatial index.

For the purposes of the experiment, the M_0 in the Bloch equations corresponds to a volume averaging across the entire spin sample, such that any local inhomogeneities are integrated out. Assuming an external magnetic field applied along the z-direction, the resulting $\mathbf{M_0} = M_0 \hat{\mathbf{z}}$. Starting from the thermal density matrix ρ_0, weighted by thermal Boltzmann factors, one can obtain Curie's law for the magnetisation vector from Eq. (2.43)

$$M_0 = \frac{n \gamma J}{2} \mathcal{B}_J \left(\frac{\gamma \, B_0}{k_B \, T_s} \right) , \tag{2.44}$$

where n is the number density of spins, J is the largest spin value, k_B is Boltzmann's constant and T_s is the spin temperature as in [278]. The function $\mathcal{B}_J$ is called the Brillouin function, taking the form

$$\mathcal{B}_J\left(x\right) = \frac{1}{J} \left[\left(J + \frac{1}{2} \right) \coth \left(\left(J + \frac{1}{2} \right) x \right) - \frac{1}{2} \coth \left(\frac{x}{2} \right) \right] . \tag{2.45}$$

When $J = 1/2$, the result reduces to

$$M_0 = \frac{n\gamma}{2} \tanh \left(\frac{\gamma B_0}{2 k_B T_s} \right) . \tag{2.46}$$

2.8.4 Non-thermal magnetisation vector: M^i

The full interaction Hamiltonian contains the interactions of spins with the magnetic field, the lattice and other spins. However, the analysis can be simplified by treating all interactions as spin-magnetic field, with the latter being generated by different sources. Therefore we decompose the B_I into contributions from excitations of the effective cavity containing the spin sample, fields generated by the spins, inhomogeneities in the applied magnetic field B_0, and the back-reaction field arising from radiation damping. The volume average of inhomogeneous fields is assumed to be zero. In the case of spin-induced fields, this is a good approximation. We can then use Eq. (2.40), expanded as

$$\dot{\rho} = i \, \left[\rho, H_0 + H_I\left(t\right)\right] - e^{-iH_0 t} \int_0^\infty \left[\langle \bar{H}_I\left(t\right), \left[\bar{H}_I\left(t + \tau\right), \bar{\rho}\left(t\right) \right] \rangle \right] \mathrm{d}\tau \, e^{iH_0 t} , \tag{2.47}$$

to obtain the equation of motion for the magnetisation. Retaining only the first term above, we recover the dissipationless part of the Bloch equations,

$$\dot{M}^a(\mathbf{x},t) = \gamma^2 \epsilon^{abc} \sum_n f(\mathbf{x}-\mathbf{x}_n) \langle \hat{\mathbf{s}}_n^b \rangle B^c(\mathbf{x}_n,t) \tag{2.48}$$

$$\simeq \gamma \epsilon^{abc} M^b(\mathbf{x},t)\ B^c(\mathbf{x},t)\ . \tag{2.49}$$

The Latin indices indicate spatial components of the vectors. To obtain the second line above, we make the approximation that the magnetic field does not vary significantly over the scale of the window function $f(\mathbf{x})$. Since the characteristic scale of this function is the typical inter-molecular spacing of $\mathcal{O}(\text{nm})$, this is a reasonable assumption. The magnetic field $B^c(\mathbf{x},t)$ above includes the applied background field B_0, as well as the signal and radiation damping fields. It is assumed that shimming leads to inhomogeneities whose volume average is negligibly small [279].

Dissipation in the system can be recovered by retaining the higher-order term in Eq. (2.47). This gives rise to terms that are typically of the form

$$\dot{M}^a \sim \gamma^3 \int \mathrm{d}^3x' \int_0^\infty \mathrm{d}\tau\, f(\mathbf{x}')\ R^{abcd} \langle \hat{S}^b(\mathbf{x}-\mathbf{x}') \rangle B^c(t)\ B^d(t+\tau)\ , \tag{2.50}$$

where R^{abcd} is a tensor contracting the indices of spin and magnetic fields with terms that can also have a trigonometric time dependence. The result is that dissipation depends on the auto-correlation function of the magnetic fields acting on the spin system. For temporally and spatially inhomogeneous fields these will typically be non-zero, and will therefore give non-vanishing contributions to such terms. Summing over all non-zero contributions of the form given in Eq. (2.50) leads to spin relaxation. Therefore, they dictate the magnitude of $T_{1,2}$ in the Bloch equations:

$$\dot{\mathbf{M}} = \mathbf{M} \times \gamma \mathbf{B} - \frac{M_x \hat{\mathbf{x}} + M_y \hat{\mathbf{y}}}{T_2} - \frac{(M_z - M_0)\hat{\mathbf{z}}}{T_1}\ . \tag{2.51}$$

We will now explain the significant processes that set the relevant timescales.

2.8.5 Timescales: T_1, T_2 and T_2^*

An intuitive model of both T_1 and T_2 relaxation timescales can be found in early works on NMR [280, 281]. From the form of the Bloch equations in Eq. (2.51), we can see that the organising principle behind relaxation is to determine whether a process contributes to longitudinal relaxation along $\mathbf{M_0}$, or to transverse relaxation along the two perpendicular directions. An observation that can be made is that the magnitude of the magnetisation vector in any direction at any time must remain $|M^a| \leq M_0$, if prepared such that it is initially so. This requirement can be used to show that $T_2 < 2\,T_1$ [282]. Different microscopic processes contribute to the two timescales; a subset of interactions that need to be accounted for are spin-lattice, spin-spin and back-action.

Consider the rate of transition $\Gamma_{\uparrow\downarrow}$ from state $|\uparrow\rangle$ to state $|\downarrow\rangle$, which will correspond to the timescale T_1. It is proportional to the square of the matrix element: '$\langle\downarrow| \hat{H}_I |\uparrow\rangle$', by Fermi's golden rule. Using the interaction Hamiltonian (2.41), we see that only magnetic fields in the transverse directions have non-vanishing matrix elements, because the states are orthonormal eigenstates of the spin-z operator. Therefore, we can estimate the mean transition rate as

$$\Gamma \sim \gamma^2 \langle B_T^2 \rangle \mathcal{S}(\omega_0)\ , \tag{2.52}$$

where $(\gamma B)^2$ comes from the state transition matrix element, and $\mathcal{S}(\omega_0)$ carries the spectral information of the magnetic fields evaluated at the Larmor frequency ω_0. Some of these magnetic fields are the result of spin-lattice interactions, where a spin exchanges energy with the lattice, contributing to relaxation in all directions. The energy exchange with the thermal bath of the lattice allows a spin flip that would otherwise be forbidden in a fixed background magnetic field. That only transverse magnetic field fluctuations 'B_T' can cause T_1 relaxation can also be seen from the explicit form of Eq. (2.50). These transitions are conceptually

the same as those in the two transverse directions i.e. from $|s_x;+\rangle$ to $|s_x;-\rangle$ or from $|s_y;+\rangle$ to $|s_y;-\rangle$. These transitions describe the same kind of dissipative spin flips in the transverse directions and will also have rates of the form (2.52). Alternatively, consider the transition from $|s_x;+\rangle$ to $|s_y;\pm\rangle$, related to the rotation of a spin. One can see that the corresponding matrix elements for the process do not vanish on insertion of any spin operator, meaning that this transition can occur from magnetic fields in any direction. These transitions are related to the dephasing of the spins, and can occur for arbitrary mixed states, not only eigenstates of the spin operators. We see from this that generally processes will contribute to T_2 and a subclass of these will contribute to T_1. Sufficiently long T_1 has been achieved experimentally so that in practice, T_2 is the limiting quantity for dark matter searches.

Spin-spin interactions contribute largely to T_2. These interactions are the result of local magnetic fields generated by each of the dipoles

$$\mathbf{B}\left(\mathbf{x}\right) = \frac{1}{4\pi}\left[\frac{3\hat{\mathbf{x}}\left(\hat{\mathbf{x}}\cdot\mathbf{m}\right)-\mathbf{m}}{\left|\mathbf{x}\right|^3}\right]. \tag{2.53}$$

A naïve estimate of the timescale associated to these local magnetic fields can be derived by taking $\mathbf{m}\sim\gamma$ and $x\sim n^{-1/3}$, so that nearby spins experience an additional field of magnitude γn, and therefore precess and decohere on a timescale $T_2\sim 1/n\gamma^2$. This estimate is confirmed through the more general analysis above. Inserting the magnitude of the local magnetic fields into Eq. (2.50), we find the same result. Intuitively the volume integral over the spin-density will become the magnetisation vector M as per the definition, the magnetic fields have values of size γn and their integral will be coherent only over the timescale $1/(n\gamma^2)$. Combining these we see $\dot{M}\sim\gamma^2\,M\,(n\gamma)^2\,\{1/(n\gamma^2)\}=M(n\gamma^2)$, recovering the estimate for T_2.

It is common practice in the literature to account for effects such as detector back-reaction and magnetic field inhomogeneities by introducing the timescale T_2^*. Where T_2 may be thought of as the parameter coming from the microphysics of the sample itself, T_2^* is determined by both the microphysics of the sample *and* interactions between the spins and detection apparatus. T_2 can be derived if a complete microscopic description of the spins is known. In practice we do not do this, although the size of the parameter can be determined to the order of magnitude level as above. From that estimate, the expectation is that $T_2\sim$ ms for ^{129}Xe and $T_2\sim 10\,\mu$s for ^{3}He.

The definition of T_2^*, arising as a sum of dissipation from within and outside the sample, implies it can be decomposed as

$$\frac{1}{T_2^*}\equiv\frac{1}{T_2}+\frac{1}{T_b}, \tag{2.54}$$

where T_b is a timescale associated with spin-bath interactions. (Here the bath captures the broader environmental effects that are not included in the previous spin-spin analysis.) Thus, it must always satisfy $T_2^*\leq T_2$. A dominant contribution to T_2^* comes from the small inhomogeneities in the externally applied magnetic field. This induces a spread in the Larmor frequencies of the spins across the sample, causing them to dephase. The stated level of inhomogeneities in the field is 2 ppm, which can be translated directly to the spread in frequencies [266]. For the mass scales of interest we see that this implies that T_2^* can be estimated to be 0.1 milliseconds.

Radiation damping occurs from back-reaction of the sample against the pickup coils, by Faraday's law of induction. Not all of the magnetic fields from the coils can be accounted for in T_2^*; some must be included directly in Bloch's equations. This is because a component will be spatially coherent across the entire spin sample and so must enter the Bloch equations as $\mathbf{B}$ to be self-consistent. The effect of radiation damping can be estimated by using considerations of the torque on the magnetisation vector as was done in a very early analysis of Ref. [283]. There, it was shown that one must solve a coupled system of equations, whereby the dynamics of the magnetic field are accounted for in the circuit equations and the spins by the usual Bloch equations.

2.9 Fluctuation-dissipation theorem for Spin Projection Noise

The fluctuation-dissipation theorem [284, 285] allows us to determine the thermodynamic fluctuations of the spins from the susceptibility of the system. Here we follow the approach to dissipation taken in Ref. [286], but applied to the system of spins. Semi-classically, we can compute the total energy dissipated by the system up to a time T as,

$$\begin{aligned} Q &= \int_{-\infty}^{T} dt\, \overline{\frac{dE}{dt}} = \int_{-\infty}^{T} dt \left\langle \frac{\partial H_I}{\partial B_n^a} \right\rangle \partial_t B_n^a \\ &= -\gamma \int_{-\infty}^{T} dt \sum_n \langle s_n^a \rangle\, \partial_t B_n^a. \end{aligned} \tag{2.55}$$

In the first line, we have used that the only time-dependence on the average energy $\overline{E}$ arises through B_n^a, and used the Hellmann-Feynman theorem to relate $\overline{\partial_B E} = \left\langle \partial_B H_I \right\rangle$. When writing $\langle \partial_B H_I \rangle$, we are implicitly assuming that the averaging includes the quantum averaging over states and the statistical averaging. To get the second line above, we have used the form of the interaction Hamiltonian in Eq. (2.41).

Next, we take the system to be a discrete number of spins, interacting with a magnetic field. Their time-evolution is dictated by the interaction Hamiltonian of Eq. (2.41). Additionally, we define the susceptibility of a single spin through the following integral, to encode causal dynamics of the spins

$$\gamma \langle s_n^a(t) \rangle = \int d\tau\, \alpha_{ab}(\tau)\, B_n^b(t-\tau), \tag{2.56}$$

where here we sum over repeated indices a, b that indicate spatial components, while the index n identifies the spin, and the position at which the magnetic field is evaluated. Note that α must be proportional to a Heaviside function to have the correct causal properties. In the frequency domain, the above expression can then be written as

$$\gamma \langle s_n^a(\omega) \rangle = \alpha_{ab}(\omega)\, B_n^b(\omega). \tag{2.57}$$

We can use this definition to evaluate Q, which after symmetrisation leads to

$$Q = \frac{i}{2} \sum_n \int \frac{d\omega}{2\pi}\, \omega B_n^a(\omega)\, B_n^b(-\omega)\, [\alpha_{ab}^*(\omega) - \alpha_{ba}(\omega)], \tag{2.58}$$

where the ordering of the indices a, b is physical, as $\alpha_{ab}(\omega)$ is not necessarily a symmetric matrix. To obtain this result we took $T \to \infty$ implying that this is a steady state calculation of the noise.

From here, the aim is to use Eq. (2.58) to obtain the PSD of the spins. We can achieve this by mapping the result onto a dissipation rate that is directly dependent on the spin PSD. On general grounds, we would expect that the time-averaged rate of change of energy for the system should scale as

$$Q \sim \Delta\omega\, \overline{S_{s_n^a s_m^b}}(\omega)\, \mathcal{R}(\omega; a, b; n, m)\ . \tag{2.59}$$

This is simply the statement that the thermally-averaged spin state PSD, $\overline{S_{s_n^a s_m^b}}(\omega)$, should set the average rate at which spins dissipate energy. The function $\mathcal{R}(\omega; a, b; n, m)$ will in general depend not only on the frequency, but also the orientation of the spins a, b and on their locations n, m. However, in the absence of long-range interactions causing correlations between spins at spatially-separate locations, or for short times, $\langle s_n^a(\omega) s_m^b(\omega) \rangle \propto \langle s_n^a(\omega)\, s_n^b(\omega) \rangle \delta_{nm}$. Therefore, we impose $\overline{S_{s_n^a s_m^b}}(\omega) = \overline{S_{s_n^a s_n^b}}(\omega)\, \delta_{nm}$. As a result, we can map Eq. (2.58) onto an equivalent expression given in terms of the thermally-averaged spin PSD $\overline{S_{s_n^a s_n^b}}(\omega)$, without needing to explicitly compute the PSD. We demonstrate this approach below.

We proceed by defining the non-thermally-averaged PSD for the spin operators as

$$2\pi\delta(\omega - \omega')\, S_{s_n^a s_m^b}(\omega) \equiv \frac{1}{2} \langle \psi |\, s_n^a(\omega) s_m^b(-\omega') + s_m^b(-\omega') s_n^a(\omega)\, | \psi \rangle\,, \tag{2.60}$$

where ψ denotes the state of the system. This definition has the properties required to be mapped onto a classical PSD. Setting the state of the system $|\psi\rangle$ to be a thermal state we read off the PSD as

$$\overline{S_{s_n^a s_m^b}}(\omega) = \pi\left(1 + e^{-\beta\omega}\right) \sum_{k,l} \frac{e^{-\beta E_l}}{Z} \langle l| s_n^a |k\rangle \langle k| s_m^b |l\rangle \ \delta(\omega - \omega_{kl}), \tag{2.61}$$

where ω_{kl} is the energy difference between states $|k\rangle$ and $|l\rangle$ and Z is the partition function. We can compute Q directly using Fermi's golden rule and see its dependence on the thermal PSD. For the thermally averaged energy loss we find that Q_{QM}, which is given semi-classically by Eq. (2.58), is also given quantum-mechanically by

$$Q_{\mathrm{QM}} = \pi\gamma^2 \sum_{m,n} \sum_{k,l} \int \frac{d\omega}{2\pi}\, \omega\, B_n^a(\omega) B_m^b(-\omega) \left(1 - e^{-\beta\omega}\right) \frac{e^{-\beta E_l}}{Z} \langle l| s_n^a |k\rangle \langle k| s_m^b |l\rangle \ \delta(\omega - \omega_{kl}). \tag{2.62}$$

This is precisely of the form given in Eq. (2.59), with $\mathcal{R}(\omega; a, b; n, m)$ given by

$$\mathcal{R}(\omega; a, b; n, m) = \gamma^2 \sum_{n,m} \omega\, B_n^a(\omega)\, B_m^b(-\omega) \tanh\left[\frac{\beta\omega}{2}\right] . \tag{2.63}$$

If the semi-classical and quantum mechanical rates of energy loss are identified – specifically, we equate Eqs. (2.58) and (2.62) – then using Eq. (2.61) we can extract the spin PSD as

$$\gamma^2\, \overline{S_{s^a s^b}} = \frac{i}{2} \left[\alpha_{ab}^* - \alpha_{ba}\right] \coth\left[\frac{\beta\omega}{2}\right]. \tag{2.64}$$

However, the quantity that we are really interested in is the PSD of the magnetisation vector. As in Eq. (2.43), we can take a volume average over the entire sample using the appropriate smearing function, obtaining the following form for the magnetisation vector in terms of the average spin state

$$M^a(t) = \frac{\gamma}{V} \sum_n \langle s_n^a(t) \rangle . \tag{2.65}$$

This object is of primary interest in an experiment when length scales smaller than the dimensions of the sample are unresolvable. We see that this definition and the definitions of the microscopic and macroscopic susceptibilities imply the identification

$$\chi_{ab}(\omega) = \frac{1}{V} \sum_n \alpha_{ab}(\omega). \tag{2.66}$$

Using this crude smearing function results in the PSD

$$S_{ab} \equiv S_{M^a M^b} = \frac{i}{2V} \left[\chi_{ab}^* - \chi_{ba}\right] \coth\left[\frac{\beta\omega}{2}\right], \tag{2.67}$$

which (as stated above) should be used on scales where individual spins are completely unresolvable. Changing the smearing function such that there is manifest position dependence results in a different coefficient which could be computed or determined through calibration. In identifying the PSDs we have implicitly assumed that the spins are not correlated with each other. Note that in using Bloch's equations of the form given in Eq. (2.51), we have effectively ignored any spatial dependence in $\mathbf{M}$, so we are already implicitly assuming that we can ignore this information.

Using the causality properties enforces the conditions $\chi_{xx} = \chi_{yy}$ and $\chi_{xy} = -\chi_{yx}$, which themselves imply

$$S_{xx} = \frac{1}{V} \mathrm{Im}\left(\chi_{xx}\right) \coth\left[\frac{\beta\omega}{2}\right] = S_{yy}, \qquad S_{xy} = \frac{i}{V} \mathrm{Re}\left(\chi_{xy}\right) \coth\left[\frac{\beta\omega}{2}\right] = -S_{yx}\,. \tag{2.68}$$

In the previous analysis the problem was studied not in the Cartesian basis but in the $\pm$ basis. We can also convert these results to that basis by noting that $\chi_{++} = \chi_{xx} - i\chi_{xy}$ and $\chi_{--} = \chi_{xx} + i\chi_{xy}$. We then see

$$S_{++} = S_{--} = 0, \qquad S_{-+} = \frac{1}{V}\coth\left[\frac{\beta\omega}{2}\right]\mathrm{Im}\left(\chi_{++}\right), \qquad S_{+-} = \frac{1}{V}\coth\left[\frac{\beta\omega}{2}\right]\mathrm{Im}\left(\chi_{--}\right). \tag{2.69}$$

To recover Eq. (2.7), we must take the high spin-temperature limit and further we have the following form of the imaginary part of the susceptibility,

$$\mathrm{Im}\left(\chi_{++}\right) = \frac{M_0 T_2 \gamma}{1 + \left(\omega - \omega_0\right)^2 T_2^2}. \tag{2.70}$$

Note that the expression derived here differs from that of App. SII in Ref. [228] by a J-dependent factor. The correction arises from a more careful treatment here of taking the macroscopic limit.

Chapter 3

Dark Matter Constraints from Earth

3.1 Chapter overview

This chapter points out that there are many ways to find constraints in DM parameter space using well-known properties of the Earth. First we give some details for why the non-observation of anomalous heating of the Earth's core can be taken as a very robust and conservative constraint for DP DM. There are various interesting technicalities involved in such a calculation which are worth exploring in their own right. For example, the presence of a medium changes the propagating degrees of freedom when there is kinetic mixing with a massive DP.

We will then describe an experimental proposal to search for the resonant conversion of DP DM or axion DM into radio-waves in the ionosphere. This takes inspiration from astrophysics research, whereby ultralight DM resonantly converts in astrophysical plasma. There are proposals to search for signals associated with this conversion. The ionosphere is very well studied and continuously monitored, meaning that there is much less theoretical uncertainty associated to it than there would be for a typical astrophysical environment. In what follows below, we will cover the conversion of the DM into radio waves, the typical noise sources that must be accounted for and a very simple proposal for an antenna.

3.2 Anomalous heating of the Earth

Consider the kinetically mixed DP system of (1.23). It is clear that the propagating degrees of freedom within a medium will not be the same as those in vacuum, due to the presence of the electromagnetic currents. The basis rotations required to diagonalise to the propagating combinations have been calculated, see for example [287, 288]. A simple method to compute the heat dumped into a system by a DP background is to look for the presence of Ohmic heating. This is the determined by the power density: $Q = \mathbf{E} \cdot \mathbf{J}$, where $\mathbf{E}$ is the electric field corresponding to the visible photon and $\mathbf{J}$ is the current.

Very robust constraints on the DP kinetic mixing parameter can be inferred considering the Earth's interior. There are known constraints on the power generated in the Earth's interior through measurements of the Earth's surface heat flux [289]. The total power emanating from the interior is 47 ± 2 TW. Most of this power has a known origin, generated by the radioactive decay of isotopes in the mantel and crust. One can still place robust bounds on the kinetic mixing parameter and mass of the DP, by requiring that the Ohmic heating of the Earth's core does not exceed the inferred heat output of the core. Based on analysis of heat flux at the core-mantle boundary [290], one can infer that the power being pumped out of the core alone falls between $4 - 15$ TW. The electrical conductivity of the core has been determined to be of the order of ~ 100 eV [291].

To simplify the calculation, it is assumed that the Earth is surrounded by vacuum. This allows one to choose the mass eigenstate basis as the propagating basis outside the Earth. Additionally, we do not consider the gravitational capture of the DPs which will only increase the number density in the core and therefore

increase the rate of heating. As is usual in any electromagnetism problem, enforcing the boundary conditions is of particular importance. The easiest way to see what the relevant boundary conditions are, is to derive the analogue of the macroscopic Maxwell equations, involving the kinetically mixed DP. This can be done in whichever basis is most natural.

Because the interaction and mass eigenstates do not align, it is somewhat non-trivial to map from the microscopic degrees of freedom to the macroscopic ones. In standard electromagnetism auxiliary fields $\mathbf{D}$ and $\mathbf{H}$ are introduced to account for the aggregate behaviour of microscopic charges and currents in whatever medium is being considered. In principle, one introduces the notion of a smearing function, which allows one to perform a multipole expansion for bound charges and currents. This results in a macroscopic charge density, polarisation vector, quadrupole density etc. The auxiliary fields $\mathbf{D}$ and $\mathbf{H}$ then act as a bookkeeping device to absorb these terms. This is still perfectly fine, even when including the DP mixing. A potential problem arises in introducing *constitutive relations* of a medium, for example $\mathbf{D} = \varepsilon\,\mathbf{E}$ or $\mathbf{H} = \mu^{-1}\,\mathbf{B}$. One imposes a physical bias on which field combination that materials reacts with. An incorrect choice of this combination can lead to incorrect analyses at the $\mathcal{O}(\epsilon)$ level. It seems natural to enforce the constitutive relations only in the interaction basis, as this will be the local combination of fields imparting a force on any given charge.

In the interaction eigenstate basis the relevant inhomogeneous equations read

$$\begin{aligned}
&\nabla\cdot\mathbf{D} = \rho - \epsilon\, m_{A'}^2\, A'^0\,, \quad \nabla\times\mathbf{H} - \partial_t\mathbf{D} = \mathbf{J} - \epsilon\, m_{A'}^2\mathbf{A}'\,,\\
&\nabla\cdot\mathbf{E}' = -m_{A'}^2\, A'^0 - \epsilon\, m_{A'}^2\, A^0\,, \quad \nabla\times\mathbf{B}' - \partial_t\mathbf{E}' = -m_{A'}^2\,\mathbf{A}' - \epsilon\, m_{A'}^2\,\mathbf{A}\,,
\end{aligned} \tag{3.1}$$

to leading order in ϵ. It is important to recognise that the $U(1)$ gauge symmetry still exists here, it is the choice of basis that makes it appear as though there are unphysical gauge potentials in the equations. Integrating these equations over vanishingly small surfaces one can read off the required boundary conditions, where we assume that there is no singular behaviour on the boundary. We obtain the usual boundary conditions for Maxwell's equations; the normal components of $\mathbf{D}$ are conserved and the tangential components of $\mathbf{H}$, but we also see that the normal components of $\mathbf{E}'$ and the tangential components of $\mathbf{B}'$ are conserved. One can obtain additional boundary conditions from the homogeneous equations.

Returning to the Earth's core, we can solve for the propagating modes as in [287]. We impose Ohm's law in frequency space, then using a Helmholtz decomposition we find dispersion relations for the transverse and longitudinal fields. The dispersion for the transverse modes then reads

$$\begin{aligned}
k_{T,1}^2 &= \omega^2 + i\sigma\omega - \epsilon^2\frac{im^2\sigma\omega}{m^2+i\sigma\omega}\,,\\
k_{T,2}^2 &= \omega^2 - m^2 - \epsilon^2\frac{m^4}{m^2+i\sigma\omega}\,,
\end{aligned} \tag{3.2}$$

to second order in ϵ. It is clear which of the modes corresponds to the photon and DP in the limit of no mixing. The corresponding dispersion relations for the longitudinal modes are

$$\begin{aligned}
k_{L,1}^2 &= \omega^2\,,\\
k_{L,2}^2 &= \omega^2 - m^2 - \epsilon^2\frac{m^2\omega^2}{\sigma^2+\omega^2} + i\epsilon^2\frac{m^2\sigma\omega}{\sigma^2+\omega^2}\,.
\end{aligned} \tag{3.3}$$

The gapless mode does not correspond to a physical degree of freedom which fixes a constraint, as seen in the interaction basis as,

$$\mathbf{A}_{L,1} = 0 \quad\Rightarrow\quad \mathbf{A} = \epsilon\frac{\omega}{\omega+i\sigma}\mathbf{A}'\,. \tag{3.4}$$

Combining the above information, we can solve for the power density Q in the Earth's core. In the low frequency regime we may justify the conductivity being frequency independent by appealing to the Drude model. The collision frequency in the plasma of the Earth's core is incredibly high, such that this is typically not relevant. The general form for Q computed is not particularly illuminating, it accounts for all the mixing

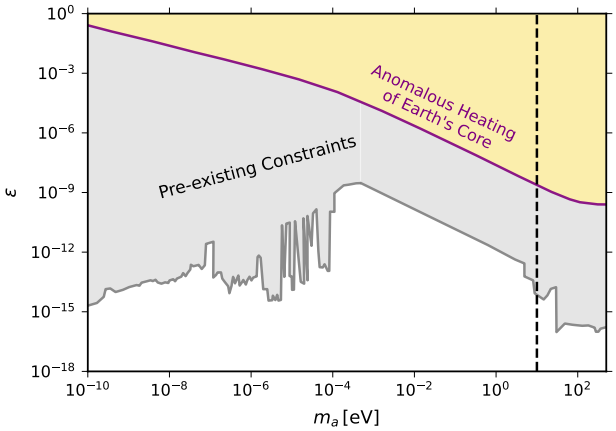

Figure 3.1: The conservative constraint coming from the lack of observation of anomalous heating of the Earth's core in yellow is compared with pre-existing experimental bounds and astrophysical constraints shown in grey. We see that it is subsumed by the other bounds. The dashed black line at $\sim 10\,\mathrm{eV}$ denotes where the fully classical description starts failing to capture the behaviour of the DM properly.

between the bases at the boundaries as well as the finite size effects coming from the Earth's core. We see that limiting cases of [292] are reproduced. In the low mass limit we see that

$$Q \simeq \epsilon^2 \frac{m^2}{\sigma} \rho_{\mathrm{DM}} \,, \tag{3.5}$$

where we have omitted the numeric prefactor. Interestingly, if we look at very low masses a different scaling behaviour emerges, when the ratio $m/\sigma \lesssim v^2$. Here the scaling is approximated by

$$Q \simeq \epsilon^2 \left(\frac{m}{\sigma}\right)^{1/2} (mv)\, \rho_{\mathrm{DM}} \,. \tag{3.6}$$

Formally, in the very large mass limit we recover the behaviour

$$Q \simeq \epsilon^2 \nu_{\mathrm{col}}^2 \frac{\sigma}{m^2} \rho_{\mathrm{DM}} \,. \tag{3.7}$$

Taking this limit is purely academic as the description of DP DM as a classical wave breaks down before this. The constraint 3.1 comes from demanding that the full value of Q is less than that which is observed.

3.3 Resonant Conversion in the Earth's Ionosphere

We consider a possible signal due to resonant conversion of wave-like DM into radio waves in the Earth's ionosphere which is common to both ALPs and DPs. For the DP signal to exist, the presence of a plasma is sufficient, while for ALPs, a background magnetic field must also be present. Both conditions are met in the weakly-ionised plasma of the Earth's ionosphere, where the Earth's small magnetic field ($B \sim 0.1\,\mathrm{G}$) is present. Non-resonant signatures using the Earth and its ionosphere at lower masses have been studied previously [287, 305–307].

The structure of the interactions between DPs/ALPs and the SM photon are such that in a medium the mass eigenstates no longer correspond to the vacuum mass eigenstates as described above in the case of the Earth's core. When the plasma frequency of the medium and the vacuum mass of the DM are degenerate, resonant level crossing between one state and the other can occur. For DPs, this condition has been exploited to study resonant conversion in various astrophysical environments such as the solar

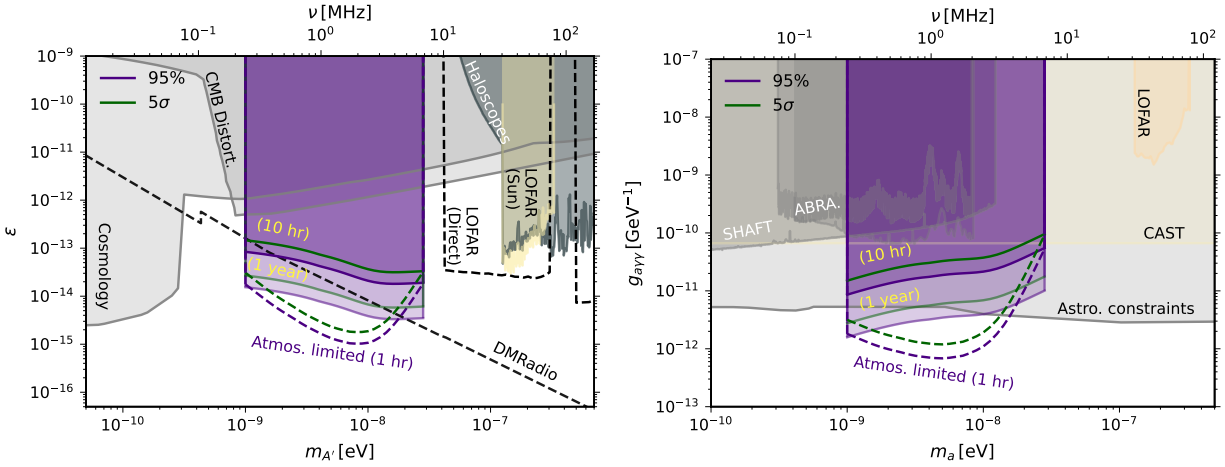

Figure 3.2: (Left) Prospective reach in the DP kinetic mixing ϵ by considering a broadband search with integration time of 10 hours and 1 year (solid curves), for both a 95% (purple) and 5σ (green) discovery potential. The dashed curves indicates the reach of 1 hour of observation when measurements are limited by atmospheric noise rather than anthropogenic noise. The light grey region is excluded by cosmological probes [94, 293, 294], the dark grey region by Haloscopes, while the light gold region is excluded by LOFAR observation of the solar corona [241]. The dashed black lines indicate possible future reach of LC-resonator DM-radio [295], as well as LOFAR reach for DP *direct* detection in the antenna [296]. (Right) Projections for the axion to photon coupling $g_{a\gamma\gamma}$, with the same experimental set-up used for the DP. The light gray region is excluded by astrophysical probes [297–301], the dark grey regions by terrestrial DM experiments ABRA[302] and SHAFT[303], while the light yellow region is excluded by CAST [304]. The limit from LOFAR observation of the solar corona[241] are shown in light orange.

corona [241, 308], neutron star magnetospheres [309], or the intergalactic medium [293, 294, 310, 311]. For ALPs, this effect has also been studied in a variety of astrophysical environments [312–321].

In the remainder of this chapter we propose searching for the conversion of DM in the Earth's own ionosphere. This approach has two advantageous properties: the ionosphere is well-studied and monitored (see [322] and references therein), allowing for a precise understanding of the conversion and propagation of the resulting radio waves; the peak plasma frequency in the ionosphere is $\omega_{\rm pl} \sim 10^{-8}$ eV, such that the mass range that can be probed is complementary to existing searches. Furthermore, galactic noise is reflected by the ionosphere, such that the dominant noise source is of anthropogenic or atmospheric origins, both of which can be monitored or even partially mitigated. Several features of the ionosphere might allow for an improved ability to distinguish true signals from spurious ones. For example, there is a daily modulation due to solar irradiation varying the free-electron number density, introducing a spectral feature in the true signal that would be absent for certain spurious signals. Finally, for ALP searches, the dependence on the transverse component of the magnetic field makes the amplitude of the signal latitude-dependent. Such variations are the subject of constant monitoring [323], and would have to be accounted for when analysing collected data.

The idea to resonantly convert DPs into photons in the Earth's ionosphere was roughly sketched in Ref. [324]. However, these authors used an unsuitable approach to estimate the signal and introduced a somewhat arbitrary boost from gravitational focusing to enhance it. Additionally they did not conduct an accurate noise analysis, which as we show, is crucial and thus did not produce a compelling sensitivity curve. Furthermore, a different measurement technique using a stratospheric balloon was proposed whereas we will discuss a ground based antenna. Finally, this other work did not consider axion conversion.

3.3.1 DM conversion to electromagnetic waves

The DP-photon system is described by the Lagrangian

$$\mathcal{L} \supset -\frac{1}{4}\left(F_{\mu\nu}F^{\mu\nu} - 2\epsilon F'_{\mu\nu}F^{\mu\nu} + F'_{\mu\nu}F'^{\mu\nu}\right) + \frac{1}{2}m_{A'}^2 A'_\mu A'^\mu - A_\mu \mathcal{J}^\mu \,, \tag{3.8}$$

where primed quantities are associated to the DP, while the axion Lagrangian is

$$\mathcal{L} \supset -\frac{1}{4}\Big(F_{\mu\nu}F^{\mu\nu} - 2\,\partial_\mu a\,\partial^\mu a + g_{a\gamma\gamma}aF_{\mu\nu}\tilde{F}^{\mu\nu}\Big) - \frac{1}{2}m_a^2 a^2 - A_\mu \mathcal{J}^\mu \,. \tag{3.9}$$

The parameter ϵ is the kinetic mixing between the photon and the DP, $g_{a\gamma\gamma}$ is the axion-photon coupling, while $m_{A'}$ and m_a are the masses of DPs and axions, respectively. For convenience, we define the effective DM-photon coupling $g_{\rm eff} = \epsilon$ for DPs and $g_{\rm eff} = g_{a\gamma\gamma}|\mathbf{B}_T|/m_a$ for axions[1].

The evolution of the photon and DM system can be modelled as a two-state system of equations. While in vacuum the photon and DM are mass eigenstates, so no mixing can occur, in a medium such as a weakly-coupled plasma, the equations of motion of the two states become coupled through their interaction strength $g_{\rm eff}$. The form of the coupled equations implies that as long as $g_{\rm eff}$ is non-zero, resonant two-level crossing can occur when the effective photon mass (i.e. the plasma mass) and the DM mass are equivalent. If the spatial variations of the plasma frequency occur on scales much larger than the de Broglie wavelength of the DM[2], then the conversion probability is well approximated by the Landau-Zener formula [241, 328–331]

$$P_{\alpha\to\gamma} \simeq (f_{\rm pol}\,\pi)\frac{g_{\rm eff}^2\, m_\alpha}{v_r}\left|\frac{\partial \ln \omega_{\rm pl}^2}{\partial r}\right|^{-1}_{r_c} \,, \tag{3.10}$$

where $\alpha = A'$, a depends on the DM candidate being considered. The polarisation fraction is $f_{\rm pol} = 2/3,\ 1$ for the DP and axion respectively. The probability is evaluated at the conversion radius r_c where $\omega_{\rm pl}(r_c) = m_\alpha$. The velocity factor $v_r \sim v_0$ is the radial component of the DM velocity, with $v_0 \simeq 220\,{\rm km/s}$ the galactic dispersion velocity of DM [332].

Unfortunately, for the Earth's ionosphere, which we model in what follows using a Chapman profile [333, 334] and for the DM masses of interest, the plasma frequency varies on a scale similar to or smaller than the de Broglie wavelength of the DM. As a result, the WKB approximation used in the derivation of the simplified formula in Eq. (3.10) does not hold, and the full second-order differential equations must be solved. We use the fact that the ionosphere plasma density has a strong gradient only along the z-direction to model the problem as a *driven one-dimensional cavity filled with plasma*, where the driver is the DM field. This is a very good approximation due to Snell's law [335]: light rays in the ionosphere naturally experience *strong refraction towards the z-direction* as they propagate downwards. Therefore, considering only vertical propagation with respect to the ground is good up to corrections which we expect to be suppressed by the ratio $h/R_\oplus \sim 10^{-2}$ (with h being the width of the ionosphere), which sets the difference between the gradients along the parallel and orthogonal directions to the ground. Thus, the equation to be studied reduces to

$$\left[\partial_z^2 + \omega^2 - \frac{\omega^2\omega_{\rm pl}^2(z)}{\omega^2 + i\nu_c\omega}\right]\mathbf{E}_T(z) = i\omega\, g_{\rm eff}\, m_\alpha^2\, \mathbf{V}(z) \,, \tag{3.11}$$

where $\mathbf{E}_T$ is the sourced electric field, $\mathbf{V} = \mathbf{A}'_T$ $(a\,\hat{\mathbf{B}}_T)$ for the DP (axion), ν_c is the electron-ion collision frequency in the ionosphere, and z is the height into the ionosphere as measured from the Earth's surface.

[1] In this chapter we will take $|\mathbf{B}_T| \sim 0.4\,{\rm G}$ and assume it is homogeneous (a good approximation over the scales relevant for the ionosphere) [325].

[2] The spatial coherence length of the DM waves is set by its de Broglie wavelength [326], this is the intuitive reason why this (and not other scales, such as the Compton length) is the important quantity to compare with the density gradient. At the mathematical level, when one studies the EOM for the two-level system of interest (photons/DM waves) and passes to Fourier space, it is the *momentum* k_a of the particle which appears in the wave equations to be solved and $1/k_a$ is the quantity to be compared with the plasma characteristic length scale [293, 327].

The form of Eq. (3.11) shows the salient aspects of the problem. When $(\partial_z^2 + \omega^2)\mathbf{E}_T = m_\alpha^2 \mathbf{E}_T = \omega_{\rm pl}^2 \mathbf{E}_T$, we see that there is a resonance as expected. Meanwhile, when $\omega_{\rm pl}^2 \ll \omega^2$, we obtain the evolution of the transverse electric field as a function of z, subject to the appropriate boundary conditions. For the wavelengths of interest, the Earth acts as a good conductor [287], so that the field will vanish within one skin depth of the surface. Similarly, the plasma of the ionosphere behaves as a conductor for frequencies below $\omega_{\rm pl}$, imposing that the field should also vanish once deep inside the plasma. In the above, we are neglecting effect of the Earth's magnetic field on the motion of the electrons in the plasma. Including it does introduce modifications of the equation of motion by the cyclotron frequency, $\Omega_{\rm B} \sim 10^{-9}\left(\frac{B}{0.1{\rm Gauss}}\right){\rm eV}$. While this frequency is similar to the DM masses we consider, we have numerically verified that its impact is limited. Particularly, it does not affect the magnitude of the signal strength. However, for specific DM masses (depending on the detector's location), cyclotron motion suppresses one polarization of the signal fields. This effect could possibly aid in detection, so it is important to account for it properly when analysing experimental data.

This 1D model breaks down if we consider DM waves with de Broglie wavelengths comparable to the Earth's radius, i.e. for $m_\alpha \lesssim 10^{-10}\,{\rm eV}$. In practice, for DM masses below $m_\alpha \lesssim 10^{-9}\,{\rm eV}$, our model of the ionosphere is a poor approximation of the real data [336] which we show in the following subsection, so we restrict ourselves to only considering masses above this value.

3.3.2 Ionosphere modelling: the Chapman profile

A very simple parametrisation of the ionosphere electron density is the so-called Chapman model [333, 334]. The model has three parameters that must be provided as input: the maximal free electron density $n_{\rm max}$, the scale height H and the maximal height $z_{\rm max}$. In terms of these three parameters, the free electron number density as a function of height can be expressed as

$$n_e(z) = n_{\rm max} \exp\left[\frac{1}{2}\left(1 - \frac{z - z_{\rm max}}{H}\right) - \exp\left(-\frac{z - z_{\rm max}}{H}\right)\right], \tag{3.12}$$

where z is the distance from the Earth's surface, and we have set $n_{\rm max} = 10^6\,{\rm cm}^{-3}$, $H = 100\,{\rm km}$ and $z_{\rm max} = 300\,{\rm km}$. In Fig. 3.3 we plot the corresponding plasma frequency (red curve), $\omega_{\rm pl}(z) = \sqrt{4\pi\, n_e(z)\alpha/m_e}$, where m_e is the electron mass and α the electromagnetic structure constant. In the same figure we also

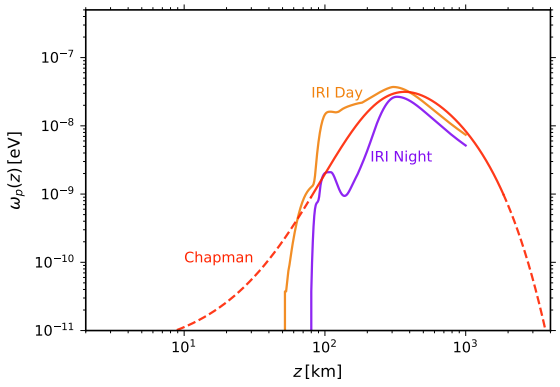

Figure 3.3: A simple Chapman profile for the plasma frequency in the ionosphere as a function of the distance from the Earth surface. The profile is compared with midday and midnight data from the 1st January 2023 at the location of the EDGES radio telescope at the Murchison Radio-astronomy Observatory in Western Australia, from the International Reference Ionosphere [336]. The salient features of the ionosphere are well-modelled within the shaded grey region.

show two real plasma frequency profiles as monitored at midday and midnight on the 1st January 2023

at the location of the EDGES radio-telescope at the Murchison Radio-astronomy Observatory in Western Australia (data from the International Reference Ionosphere [336]). As discussed in the main text, this model is a reasonable approximation to the daytime free electron number density for plasma frequencies $10^{-9}\,\mathrm{eV} \lesssim \omega_{\rm pl}(z) \lesssim 3\times10^{-8}\,\mathrm{eV}$ only.

3.3.3 Electromagnetic field and energy density at detector

In this subsection, we describe the method we use to solve for the electromagnetic fields and energy density that arrives at the detector. For the mass range under consideration, the phase-space density of the DM particles is high, such that it is appropriate to treat the system classically. We consider the DM field to constitute the full local DM abundance, such that we may write it as follows [238, 326]

$$\left\{ \begin{array}{c} \mathbf{A}'\left(\mathbf{x},t\right) \\ a\left(\mathbf{x},t\right) \end{array} \right\} = \frac{\sqrt{2\rho_{\rm DM}}}{m_\alpha} \sum_l f_l \left\{ \begin{array}{c} \mathbf{n}_l \\ 1 \end{array} \right\} \exp\left(-i\omega_l t + i\mathbf{k}_l\cdot\mathbf{x} + i\phi_l\right), \tag{3.13}$$

where m_α is the mass of $\alpha = A',\ a$ where appropriate, and f_l is the combination of the velocity distribution in a local frame and a random variable drawn from a Rayleigh distribution. The quantity ϕ_l is a random phase, while $\mathbf{n}_l$ specifies the polarisation of the vector field in the case of the DP. The dispersion of the DM wave oscillation frequency ω_l (discussed in greater detail below) is such that there is a natural coherence time $\tau_c \sim 2\pi/m_\alpha v^2$ where $v \sim 200\,\mathrm{km/s}$. For the masses of interest, this coherence time is about one second. The expected data-taking campaign will involve recording data for much longer timescales, such that we can approximate the DM wave as having a fixed amplitude $\sqrt{\rho_{\rm DM}}/m_\alpha$.

As before we can treat the presence of wave-like DM as leading to an additional *effective* current density $j^\mu_{\rm eff} = (\rho_{\rm eff},\ \mathbf{j}_{\rm eff})$ in Maxwell's equations

$$\begin{aligned} &\nabla\cdot\mathbf{D} = \rho - \rho_{\rm eff},\ \ \nabla\times\mathbf{H} - \partial_t\mathbf{D} = \mathbf{j} - \mathbf{j}_{\rm eff}, \\ &\nabla\cdot\mathbf{B} = 0, \qquad\qquad \nabla\times\mathbf{E} + \partial_t\mathbf{B} = 0\ . \end{aligned}$$

The effective charge density is $\rho_{\rm eff} = \epsilon\, m_{A'}^2 A'^0$ for the DP and $\rho_{\rm eff} = g_{a\gamma\gamma}\mathbf{B}\cdot\nabla a$ for the axion. The effective 3-current density can be written in terms of the effective coupling and a vector $\mathbf{V}$ defined in the main text, $\mathbf{j}_{\rm eff} = g_{\rm eff}\, m_\alpha^2 \mathbf{V}$. We remind the reader that $\mathbf{V} = \mathbf{A}'_T$ for the DP, and $\mathbf{V} = a\,\hat{\mathbf{B}}_T$ for the axion, where the subscript T refers to transverse modes. Furthermore, we recall the definition $g_{\rm eff} = \epsilon$ for DPs and $g_{\rm eff} = g_{a\gamma\gamma}|\mathbf{B}_T|/m_a$ for axions.

The Drude model allows for a simplified characterisation of the motion of electrons in the plasma in the presence of EM fields. The model combines the Lorentz force law with a collision term that accounts for electron-ion collisions. The model allows us to solve in frequency space for the motion of the electrons, and thereby derive the physical EM current $\mathbf{j}$ entering in Maxwell's equations. Neglecting the Earth's magnetic field, we can solve for the average momentum of electrons

$$\langle\mathbf{p}\rangle \simeq -\frac{i\,e}{\omega + i\nu_c}\mathbf{E}\ . \tag{3.14}$$

This is not always a good approximation in the parameter space we consider. As mentioned above, the main effect of including the magnetic field would be that the resulting EM radiation gets polarised. However, without detailed knowledge of the antenna type and its placement, any inclusion of magnetic field effects on the resulting EM radiation is premature. The average current density can then be found

$$\mathbf{J} = -e\langle\mathbf{p}\rangle\frac{n_e}{m_e}\frac{i\omega_{\rm pl}^2}{\omega+i\nu_c}\mathbf{E}\ , \tag{3.15}$$

where we have used the definition of the plasma frequency in the second equality. Here m_e and e are the electron mass and charge respectively, ω is the frequency of the driver and ν_c is the electron-ion collision frequency. We model ν_c as arising due to Thomson scattering of electrons and ions [337]:

$$\nu_c = \frac{4\sqrt{2\pi}\alpha^2\, n_e}{3m_e^{1/2}T_e^{3/2}}\ \log\Lambda_c\,. \tag{3.16}$$

In general this quantity will depend on the position in the ionosphere as a result of the varying electron number density and temperature. For our mass range of interest $\nu_c/\omega \lesssim 10^{-4}$ [338], we see that it is negligible compared with other effects (even on resonance), but we include it for completeness. This is also verified numerically.

The current density can be related to the charge density by the continuity equation in frequency space. Assuming the entirety of the effect of charged or polarised matter is contained in $\mathbf{j}$, ρ, we can further simplify Maxwell's equations by setting $\mathbf{H} = \mathbf{B}$ and $\mathbf{D} = \mathbf{E}$. This approach is equivalent to setting up the problem with both a conductivity and a polarization tensor and assuming no free charges or currents are present. Unless otherwise stated, from here on, we are working in frequency space.

One can keep track of the relevant degrees of freedom in the problem by performing a Helmholtz decomposition,

$$\mathbf{E} = \mathbf{E}_T + \mathbf{E}_L \;\text{ such that }\; \nabla \cdot \mathbf{E}_T = 0 \;\text{ and }\; \nabla \times \mathbf{E}_L = \mathbf{0}\,. \tag{3.17}$$

We will only consider transverse modes, as these will be the ones relevant to detection on Earth. The second order differential equation governing their evolution is obtained by combining Ampére's and Faraday's laws, yielding

$$\nabla^2 \mathbf{E}_T + \omega^2 \left(1 - \frac{\omega_p^2}{\omega^2 + i\,\nu\,\omega}\right) \mathbf{E}_T = i\, g_{\rm eff}\, m_{\rm DM}^2\, \omega\, \mathbf{V}, \tag{3.18}$$

which is the 3D generalisation of Eq. (3.11) in the main text. In order to make further progress some information about the plasma needs to be specified.

One natural approximation to make in the case of the ionosphere is that the number density of electrons is primarily a function of height from the surface of the Earth. For the masses under consideration, we are justified in ignoring effects coming from the curvature of the Earth; they will contribute at most $\mathcal{O}(1/m_{\rm DM}\, v\, R_\oplus)$ corrections which are at the percent level for the smallest masses we consider. The combination of these assumptions leads us to work in a 1D approximation where the only relevant variation is in the z-direction, defined as the height above the surface of the Earth. One can now see that there is a good translational symmetry in the transverse directions, implying conservation of momentum in these directions. An immediate consequence of this will be the significant refraction of light rays towards the z-direction as they propagate downwards. A photon near the Earth's surface should approximately satisfy the dispersion relation: $\omega^2 \approx \mathbf{k}^2$. Given that the photon produced as a result of the DM effective current should inherit both the frequency *and* transverse momentum of the DM, the only way this relation can be satisfied is if the momentum in the z-direction is of order m_α, which is $\sim 10^3$ times larger than the value in the transverse directions. An alternative, but equivalent, way to see the same effect is by considering the relation between the plasma frequency and the refractive index of the ionosphere and using Snell's law as explained before.

It is now very natural to decompose the fields of Eq. (3.18) into plane waves in the transverse directions and some generic function of the z-direction, resulting in:

$$\left[\partial_z^2 + \omega^2 - \frac{\omega^2}{\omega^2 + i\nu\omega}\,\omega_p^2\,(z)\right] \mathbf{E}_T\,(z) = i\, g_{\rm eff}\, m_{\rm DM}^2\, \omega\, \mathbf{V}\,(z)\,. \tag{3.19}$$

The problem has now been reduced to finding the form of these modes. For a totally generic plasma frequency profile this is still not a trivial problem, as the gradient and any possible turning points of the plasma will influence the amplitude of a wave arriving at the detector. For the radio wavelengths of interest, the surface of Earth is effectively a perfect conductor, thereby imposing an important boundary condition on the problem. The boundary conditions imposed are that the electric field is zero by the time that the wave gets to the Earth's mantle and similarly that the electric field is zero deep into the bulk of the ionospheric plasma.

In order to solve Eq. (3.19) we adopt a finite difference method. We first discretise the equation as

$$\frac{E_{i-1} - 2E_i + E_{i+1}}{\Delta z^2} + E_i\left(\omega^2 - \frac{\omega^2 \omega_{\rm pl,i}^2}{\omega^2 + i\nu_i\omega}\right) = i\, g_{\rm eff}\, \omega\, m_{\rm DM}^2 V_i, \tag{3.20}$$

where the subscript i indicates the ith position on a grid along the z-axis. We are then left with an algebraic system of the type

$$A_i\, E_{i-1} + B_i\, E_i + C_i\, E_{i+1} - D_i = 0, \tag{3.21}$$

where $A_i = C_i = 1/\Delta z^2$, $B_i = -\frac{2}{\Delta z^2} + \left(\omega^2 - \frac{\omega^2}{\omega^2 + i\nu_i\omega}\omega_{\rm pl,i}^2\right)$ and $D_i = i\, g_{\rm eff}\, \omega\, m_{\rm DM}^2 V_i$. We thus have to solve a tridiagonal system of equations, and to do so employ the well-known Thomas algorithm. Our formalism automatically takes into account all the wave propagation phenomena, including reflection, absorption and refraction of the electromagnetic (EM) waves that ultimately arrive at the detector. In fact, because of these propagation effects, the amplitude of the wave at detection point is expected to be different than the amplitude at the resonance point, as we now show.

Fig. 3.4 shows the EM energy density in natural units as a function of the ionosphere height for a fixed effective coupling, $g_{\rm eff} = 10^{-10}$. Different colours correspond to different DM masses; the solid curves are our numerical results, while the horizontal dashed lines show the result of applying Eq. (3.10). We notice that the resonant peak of each of our curves never deviates too much from the naïve calculation. However, the energy density near the Earth's surface, which is the quantity relevant for detection, is typically suppressed with respect to the peak. This is a particularly important effect for large masses, $\sim 10^{-8}\,$eV, whose resonant conversion condition is only satisfied for the largest electron densities near the peak of the Chapman profile. An EM wave produced at that height undergoes many reflections as it propagates through the plasma, and its amplitude is therefore attenuated before it reaches the detector. The effect is less evident for smaller masses, where reflection plays only a minor role. The EM energy density near the Earth's surface is approximated to within $\sim 10\,\%$ by the following sigmoid function

$$\rho_{\rm EM} \simeq \frac{3\times 10^{-23}\,{\rm eV}^4 \left(\frac{g_{\rm eff}}{10^{-10}}\right)^2}{1+\exp\left[-\left(\frac{m_\alpha}{2.3\times 10^{-9}{\rm eV}} - 3.8\right)\right]}\,, \tag{3.22}$$

which is valid for masses in the range $10^{-9} \leq m_\alpha/{\rm eV} \lesssim 3\times 10^{-8}$. The lower boundary is defined by the aforementioned issues with the validity of our calculation, while the upper bound is defined by the peak values of the free electron number density. Ultimately, a detailed analysis taking into account the detector location and time could be performed using real ionosphere data [336], and could extend our sensitivity to much smaller masses.

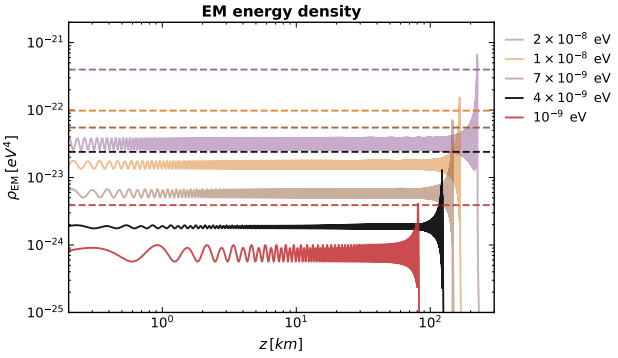

Figure 3.4: EM energy density in natural units as a function of the distance z from the Earth surface. Different colours correspond to different DM masses, while the effective coupling is always fixed to $g_{\rm eff} = 10^{-10}$. The solid curves are our full numerical solutions, while the horizontal dashed lines correspond to the Landau-Zener conversion probability from Eq. (3.10).

3.4 Signal detection

The EM radiation incident on the Earth's surface has a characteristic wavelength $\lambda \gg 1\,$m, and can therefore be detected with an electrically-small antenna [339]. The signal approximated by Eq. (3.22) is the total integrated energy density. For detection, the more relevant quantity is the spectral density (SD) of the

EM radiation $\mathcal{S}_{\rm sig}(\omega) \sim \rho_{\rm EM} f(\omega)$. The function $f(\omega)$ is approximately a Maxwell-Boltzmann distribution [332, 340], normalised as $\int d\omega f(\omega) = 1$, which describes the frequency dispersion of the signal inherited from the DM velocity distribution. The signal is spread between frequencies $\omega \in m_\alpha[1, 1+\sigma^2/2]$, where $\sigma \sim 200\,{\rm km/s}$ is the DM dispersion velocity. The bandwidth of the signal is thus narrow, and can be approximated as having an effective quality factor of $Q_{\rm sig} \sim 10^6$. Full details are given in the later section 3.5.

The dominant noise at the relevant frequencies is from processes external to the receiver antenna. It is primarily a combination of atmospheric and anthropogenic radiation. As a fiducial noise level, we adopt the anthropogenic noise expected at a quiet rural location given by the International Telecommunication Union (ITU), see for example curve C of Fig. 2 of Ref. [341]. This can be characterised by the characteristic temperature of the Gaussian component of the noise

$$T_{\rm N}(\nu) \simeq 6.1 \times 10^7 \left(\frac{\rm MHz}{\nu}\right)^{2.75} {\rm K}\,. \tag{3.23}$$

Under the assumption of an equivalent loss-free receiving antenna, this temperature can then be converted to a noise SD (see *e.g* Ref. [339] for a pedagogical derivation)

$$\mathcal{S}_{\rm N}(\nu) \simeq \frac{32}{3}\pi^2\,\nu^2\,T_{\rm N}(\nu)\,. \tag{3.24}$$

A real device might contend not only with this typical anthropogenic noise, but also with impulsive components at particular frequencies. Furthermore, atmospheric noise leads to a temperature that can vary significantly depending on weather conditions, sometimes exceeding typical anthropogenic noise by many orders of magnitude [341].

Both the signal and the noise are external to the antenna, and are filtered by the same transfer function determining the antenna response, which therefore does not enter the signal-to-noise ratio (SNR). As a result, the optimal SNR is given by [326, 342]

$${\rm SNR} = \left[t_{\rm int}\int_0^\infty d\nu \left(\frac{\mathcal{S}_{\rm Sig}}{\mathcal{S}_{\rm N}}\right)^2\right]^{1/2}\,, \tag{3.25}$$

where $t_{\rm int}$ is the integration time of our measurement (assumed to be larger than the DM coherence time). If the receiver antenna is critically coupled, it will have a narrow bandwidth owing to the small radiation resistance. As a result, it is optimal to couple the antenna to an additional in-series resistance. In section 3.7 we provide a simple model for an RLC circuit that allows to broaden the frequency response up to $\Delta\nu \sim$ MHz. The circuit we describe, and the value of its parameters, are similar to those of very old radio missions [343, 344]. The result of this broad frequency response is that in order to scan an e-fold in DM mass t_e, an integration time at a given frequency of $t_{\rm int} \sim t_e \min\left(1, 2\,\pi\,\Delta\nu/m_\alpha\right)$ is required.

Fig. 3.2 shows our fiducial prospects (solid purple lines) for a broadband search with 1 MHz bandwidth, for 10 hours and one year of e-fold time, for both DPs (left panel) and axions (right panel). In both panels light grey regions are excluded by cosmological and astrophysical probes [94, 293, 294, 297–301]. Observations by LOFAR of the solar corona are shown in light orange [241] in both panels. For the DP panel the dark grey region is excluded by Haloscopes. The dashed black lines indicate possible future sensitivity of DM Radio [295], as well as LOFAR sensitivity to *direct* absorption by the antenna. For the axion panel, the dark grey regions are excluded by terrestrial DM experiments ABRA [302] and SHAFT [303], while the light yellow region is excluded by CAST [304].

In case anthropogenic noise can be mitigated, we also show a dashed purple curve corresponding to the typical atmospheric noise in Western Australia around midday on a winter day (see Fig. 18 of Ref. [341]), assuming *a single hour* of e-fold time.

3.5 Frequency spread of the DM

In this section we give some details about the DM energy distribution entering the signal PSD in the main text. We make the simplifying approximation that the DM is well-described by a gas of non-relativistic particles and is thus characterised by the following momentum distribution:

$$f(\mathbf{p}) = \frac{1}{\left(\frac{2\pi}{3} m^2 \langle v^2 \rangle\right)^{3/2}} \exp\left[-\frac{\mathbf{p}^2}{\frac{2}{3} m^2 \langle v^2 \rangle}\right] , \tag{3.26}$$

where we have fixed the normalisation such that the distribution integrates to one and the rms momentum is given by $\langle \mathbf{p}^2 \rangle = m^2 \langle v^2 \rangle$. Here $\langle v^2 \rangle$ denotes the mean-square velocity, which in the case of isotropic distribution is related to the velocity dispersion by $\langle v^2 \rangle = 3\,\sigma^2$, where $\sigma = \sqrt{3/2}\, v_c$, with $v_c = 220\,\mathrm{km/s}$ being the circular velocity for the Milky Way [332, 342]. We then make the identification $f(\omega)\,\mathrm{d}\omega = f(\mathbf{p})\,\mathrm{d}^3 p$ to find the distribution in frequency space, namely:

$$f(\omega) = \frac{1}{\sqrt{\pi}} \frac{\sqrt{|\omega| - m}}{\left(\frac{1}{3} m \langle v^2 \rangle\right)^{3/2}} \exp\left[-\frac{|\omega| - m}{\frac{1}{3} m \langle v^2 \rangle}\right] \theta\left(|\omega| - m\right) . \tag{3.27}$$

We see that this is the same as previously found in the literature [340]. As mentioned above, the signal should inherit this frequency spread. The PSD of the signal E-field may then be constructed from the EM energy density ρ_{EM} as:

$$\mathcal{S}_{\mathrm{sig}}(\omega) = 4\pi \left(\frac{\omega}{m}\right)^2 f(\omega)\, \rho_{\mathrm{EM}} . \tag{3.28}$$

A straightforward calculation shows that this PSD is peaked at $\omega \approx m\left(1 + \frac{1}{6}\langle v^2 \rangle\right)$; assuming that the signal energy density varies more slowly in ω than $f(\omega)$. From here we may find the bandwidth of this PSD by the usual FWHM criterion, where we see that it given by the expected: $\Delta\omega \approx m \langle v^2 \rangle$.

3.6 Comparison with direct detection

The same antenna used to detect radiation resulting from the resonant conversion of wave-like DM in the ionosphere can also be sensitive to the non-resonantly-converted signal that is present on Earth anyway. In the case of DP DM, this is especially straightforward to understand: if there is a non-zero A' amplitude in the vicinity of the antenna, it can couple to charges in the antenna and generate a current. The signal PSD associated to this effect is

$$\mathcal{S}_{\mathrm{sig,\,DD}}(\omega) \simeq \epsilon^2 \rho_{\mathrm{DM}} f(\omega) , \tag{3.29}$$

and would enter Eq. (3.25) as an additional contribution to the signal PSD in the numerator. We notice that this PSD and the resonant conversion signal PSD share the same spread in frequency space, $f(\omega)$, such that the comparison between the two signals amounts to a comparison between ρ_{DM} and Eq. (3.22). For $g_{\mathrm{eff}} = \epsilon = 10^{-10}$, we find that $\epsilon^2 \rho_{\mathrm{DM}} \sim 3 \times 10^{-26}\,\mathrm{eV}^4$, and is therefore between 2 and 3 orders of magnitude smaller than the EM energy density due to resonant conversion given in Eq. (3.22) for the mass range considered.

For axion DM, the analogous effect can be estimated by arguing that axions can convert into an electric field parallel to the Earth's magnetic field of a magnitude $E_a \sim g_{a\gamma\gamma} a B$, such that the direct detection signal PSD is approximately

$$\mathcal{S}_{\mathrm{sig,\,DD}}(\omega) \simeq g_{a\gamma\gamma}^2 B_\oplus^2 \frac{\rho_{\mathrm{DM}}}{m_a^2} f(\omega) . \tag{3.30}$$

The prefactor without the frequency spread function can be compared with Eq. (3.22). This is the same comparison as for the DP above, indicating that once again, the resonant conversion EM signal PSD is between 2 and 3 orders of magnitude larger than the direct absorption PSD.

3.7 Modelling of transfer function in a simple antenna circuit

Here we provide a simple description of a small linear antenna that could be used for detection of the DM signal. This is not intended to be exhaustive of the list of possibilities to detect our signal, but it gives an idea of the simplicity of a possible detector.

The antenna and read-out circuit combined are treated as a simple, in-series RLC-circuit, where the driving voltage is provided by the antenna. There is a characteristic impedance $Z_A = R_A + X_A$ for the antenna element, determined primarily by its geometry and material properties. We consider a linear antenna of length h, cross-sectional area A, resistance $R_A \equiv R_{\rm Ohm} + R_{\rm rad}$ and reactance $X_A(\lambda)$. In this case, we are working in the "electrically small" limit for the antenna meaning that the radiation resistance reads:

$$R_{\rm rad} = \frac{2\pi\, Z_0}{3}\left(\frac{h}{\lambda}\right)^2 \simeq 0.05\,\Omega\,\left(\frac{h}{\rm m}\right)^2\left(\frac{m_\alpha}{10^{-8}{\rm eV}}\right)^2\,, \tag{3.31}$$

where we identified $\lambda = 2\pi/m_\alpha$ and the reactance of the antenna is largely dominated by its effective capacitance:

$$X_A(\lambda) \approx -\frac{Z_0}{2\pi}\frac{\lambda}{C_A} \approx -\frac{Z_0}{\pi^2}\left(\frac{\lambda}{2\,h}\right)\ln\left(\frac{h}{\sqrt{A/\pi}}\right)\,. \tag{3.32}$$

The remaining circuit elements are well-modelled by a resistive load element 'R_L' and an inductive element 'L'.

The power dissipated across the load may be computed by finding the voltage across it using Kirchhoff's laws and the standard relation for power in a circuit element. We see that the current flowing through any given element is:

$$I\,(\omega) = \frac{i\,\omega}{L\,(\omega^2 - \omega_0^2 + i\,\omega\,\Delta\nu)}\,V_d\,(\omega)\,, \tag{3.33}$$

where the circuit resonant frequency is $\omega_0^2 \equiv 1/\,(C_A L)$ and the bandwidth is $\Delta\nu \equiv (R_A + R_L)\,/L$. The result is that the power dissipated is

$$P_L = \int {\rm d}\omega\,\frac{\omega^2\,h^2}{R_L\,L^2\,\left[\left(\omega^2-\omega_0^2\right)^2 + \omega^2\,\Delta\nu^2\right]}S_E\,(\omega)\,, \tag{3.34}$$

where S_E is the PSD of the electric field incident on the antenna, consisting of the signal and any external noise sources. We note that the bandwidth is dominated by a constant $R_L > R_A$ for resistive elements easily available for purchase by amateurs, leading to a broadband detector response. As discussed in the previous analysis, by far the dominant noise source is extrinsic to the detector, and therefore is filtered by the same detector response as the signal. This transfer function of the antenna, i.e. the prefactor of $S_E(\omega)$ in the integrand above, therefore factorises out of the integrand of the SNR, Eq. (3.25). However, the bandwidth of the receiver $\Delta\nu$ affects the scan rate, which enters the expression for the integration time $t_{\rm int}$ in Eq. (3.25). In Fig. 3.5 we show the signal flux spectral density for three different DM masses, fixing $g_{\rm eff} = 10^{-10}$ and showing three choices for the detector bandwidth. This demonstrates how the detector response affects the signal as a function of frequency and bandwidth.

3.8 Estimates of uncertainties in the analysis

In this section we quantify some of the uncertainties in our sensitivity estimates. In our analysis we make certain assumptions, for example on the typical value of the Earth's magnetic field, the effect of losses and reflection, or that we can treat the problem as being 1-dimensional. We must further assume a benchmark noise level. Below, we address various assumptions in turn, and attempt to quantify the level of uncertainty this leads to in our sensitivity projections.

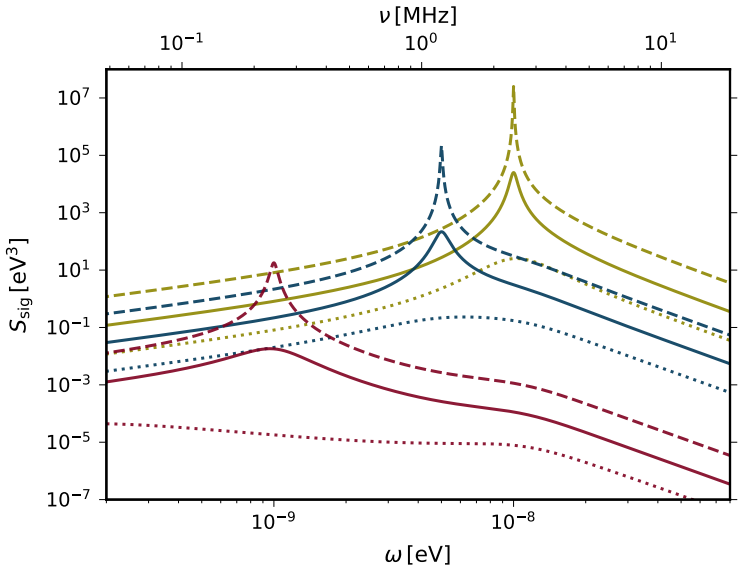

Figure 3.5: The value of the signal PSD fed through the transfer function of the antenna circuit assuming the signal is peaked at frequency ω, for all curves we take $g_{\rm eff} = 10^{-10}$. The value of ω_0 is $1 \cdot 10^{-9}$eV for red curves, $5 \cdot 10^{-9}$eV for blue and $1 \cdot 10^{-8}$eV for golden curves. The bandwidth of the circuit is 10MHz for dotted lines, 1MHz for solid and 100kHz for dashed lines.

- Non-inclusion of magnetic field in plasma modelling: as discussed in the main text, this assumption only affects our result at the $\mathcal{O}(1)$ level numerically, but can have an important qualitative impact. In particular, including cyclotron motion of electrons in the plasma leads to polarisation of the signal, which we have not accounted for in our sensitivity projections. As this is a feature of the signal that might not be shared of all noise sources, omitting this effect is conservative. Inclusion of this plasma effect might allow us to overcome certain noise sources, possibly improving the expected sensitivity, and will be the subject of detailed analysis when considering actual data.

- Magnitude of Earth's magnetic field: this is primarily a concern for the sensitivity to axion DM, which requires the background magnetic field for conversion to occur. The magnetic field of the Earth varies by $\mathcal{O}(1)$ depending on location, and its orientation is also subject to similar variation due to e.g. solar activity. This variability corresponds to an uncertainty on the sensitivity to $g_{a\gamma\gamma}$ of the same magnitude.

- Losses in propagation: as discussed throughout, a key finding we made is that the signal fields experience attenuation from their peak at the location of resonant conversion to the surface of the Earth. This attenuation is typically due to multiple reflections undergone by a photon as it propagates from the conversion region to the Earth, and is accounted for in our numerical results. Uncertainty in this result is therefore carried over from uncertainty in our modelling of the profile of the plasma (see above discussion on "ionosphere modelling". As shown in Fig. 3.3, our use of the Chapman profile is a reasonable approximation to real ionosphere profiles. For small masses, our approach is likely conservative, in that our profile is shallower than a true ionospheric profile, such that photons will undergo more losses in propagation. For larger masses, our approach is likely optimistic when compared with a daytime profile (orange curve in Fig. 3.3, which is shallower than the Chapman profile), but conservative when compared with a nighttime profile (purple curve, steeper than Chapman). Since typical losses in the mass range under consideration vary between a factor of 2 and 10 in the energy density, this leads to $\mathcal{O}(1)$ variability in the sensitivity to the effective coupling $g_{\rm eff}$.

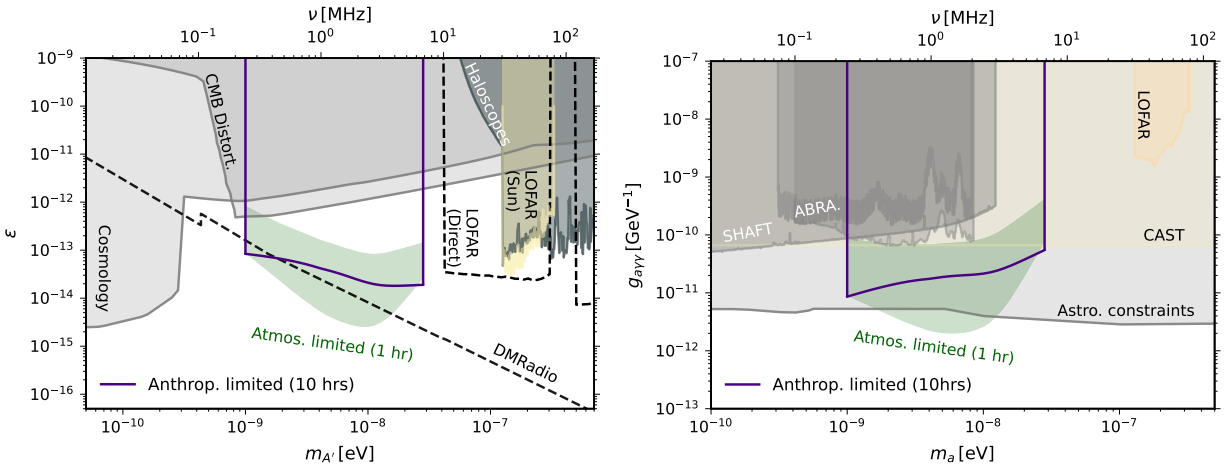

Figure 3.6: The sub-figures show the typical variation in the reach when limited by atmospheric noise, given one hour of integration time. The noise levels vary over eight hours during the winter in Western Australia.

- 1-dimensional approximation: as discussed above, this assumption is most likely to affect the smallest masses we consider, as the de Broglie wavelength of the DM approaches the Earth's radius. However, the smallest mass we consider corresponds to a typical de Broglie wavelength of $\mathcal{O}(0.03\,R_\oplus)$, such that corrections are likely to be small. The low-velocity component of the Maxwell-Boltzmann distribution should in principle be treated as 3-dimensional, since individual k-modes can have very long wavelengths. However, only a tiny sliver of the DM phase space has wavelengths greater than $R_\oplus$, even for $m = 10^{-9}$ eV. As such, this is unlikely to be more than an $\mathcal{O}(\%)$-level effect.

- Typical noise levels: this is the main source of uncertainty in our sensitivity estimates. From Ref. [341], it is clear that the effective temperature of anthropogenic noise can vary over orders of magnitude. This can be mitigated by performing observations in radio-quiet environments, and is already done by many experimental collaborations. Therefore, a greater source of uncertainty comes from atmospheric noise, whose effective temperature can also vary by orders of magnitude. As this noise cannot be controlled, we must account for this variability in our estimated sensitivity. In Fig. 3.6, we show as a green band the typical variability in atmospheric noise levels over an 8-hour period at a radio-quiet site in Western Australia, taken from Ref. [341]. Compared with the anthropogenic noise-limited sensitivity (solid purple line), we see that when atmospheric noise is large, it can lead to a loss in sensitivity of an order of magnitude in $g_{\rm eff}$. This effect can be mitigated by e.g. not using data taken during storms, or by cross-correlating detectors separated by less than a DM coherence length $\sim 1/mv$, but greater than the coherence length of the noise (set by the typical size of the atmospheric perturbation).

Chapter 4

Quadratic Coupling of the Axion to Photons

4.1 Chapter overview

In this chapter, we explore the quadratic coupling of axions to photons. We provide a heuristic explanation as to why the coupling is larger than might initially be anticipated. Following this is an explicit calculation for the QCD axion, using Chiral Perturbation Theory (χPT) to show how the operator of Eq. (4.6) *is* generated at one-loop order, verifying the heuristic. We then identify a sufficient condition to achieve such a large coupling for more generic ALPs and motivate this discussion with toy constructions. We also explore where this effect might become phenomenologically relevant.

4.2 Motivation for the coupling

Originally introduced to explain the non-detection of the electric dipole moment (EDM) of the neutron [111–113], it has since garnered much interest as a candidate for DM [70, 101, 102]. The incarnation of the axion that explains the (so far) unobservably small neutron EDM is often called the "QCD axion", while a generic pseudo-scalar particle with an additional explicit mass term (then giving up solving the strong CP puzzle) is often referred to as an "axion-like particle" (ALP). Many experimental searches are directed at discovering an axion, a large number of which assume it to make up all of the DM of the universe. Many of these searches rely on the coupling between the axion and photons [345],

$$\mathcal{L} \supset -\frac{g_{a\gamma\gamma}}{4} a F_{\mu\nu}\tilde{F}^{\mu\nu} \ , \tag{4.1}$$

to generate observable signals from axion-photon conversion. This interaction and that of the QCD axion with nuclei are the subject of extensive experimental and theoretical work (see e.g. [67, 79] for reviews).

The axion field, being odd under parity-conjugation (P) and charge-parity-conjugation (CP), does not couple to the kinetic term of the photon and therefore does not lead to a shift in the fine-structure constant α to leading order. Likewise, it can be shown through simple helicity arguments, symmetry prevents the operator of Eq. (4.1) from generating a quadratic axion-photon amplitude. There are both t- and u-channel contributions to the amplitude. The axion-photon-photon vertex is associated to the structure:

$$g_{a\gamma\gamma}\epsilon_{\mu\nu\alpha\beta}\varepsilon_1^{*,\mu}\varepsilon_2^{*,\nu}p_1^{\alpha}p_2^{\beta}, \tag{4.2}$$

where the subscripts label the distinct outgoing photon momenta and their corresponding polarisation vectors. We may construct a 4-point vertex by gluing two of these vertices together, choosing opposite helicities

for the outgoing states such that this contributes to the same amplitude as the a^2F^2 operator. We see that the t-channel diagram contribution is:

$$\mathcal{M}_{t;\,+,-} = \frac{g_{a\gamma\gamma}^2}{t}\left[\left(\varepsilon_1^+\cdot\varepsilon_2^-\right)(p_1\cdot q) - \left(\varepsilon_1^+\cdot q\right)\left(\varepsilon_2^-\cdot p_1\right)\right](p_2\cdot q)\,, \tag{4.3}$$

where $p_{1,2}$ are the momenta of the outgoing photons and q is the transferred momentum. One can now easily verify that a gauge choice exists where this is zero. A nice way to see an appropriate gauge choice is by using the spinor-helicity formalism and the Fierz identities for spinors. For example, take the following product in Eq. (4.3):

$$\varepsilon_2^-\cdot p_1 \to \left(-\frac{1}{\sqrt{2}}\frac{\langle 2|\,\gamma_\mu|s]}{[2s]}\right)\left(\frac{1}{2}\,\langle 1|\,\gamma^\mu|1]\right) = -\frac{1}{\sqrt{2}}\frac{\langle 21\rangle\,[s1]}{[2s]}\,. \tag{4.4}$$

We have used Fierz identities to go from the first to the second line. The label 's' corresponds to a light-like reference momentum we are free to choose; this encodes our choice of gauge. Choosing the reference momentum to be that of the other photon's momentum:'$s = 1$', is a good choice as the spinor-helicity brackets are antisymmetric in their arguments, so the product is zero. Having chosen $s = 1$, the same now occurs for the product of polarisation vectors:

$$\varepsilon_1^+\cdot\varepsilon_2^- \to \frac{1}{2}\left(\frac{\langle r|\,\gamma_\mu|1]}{\langle r1\rangle}\frac{\langle 2|\,\gamma^\mu|1]}{[21]}\right) = \frac{\langle r2\rangle\,[11]}{\langle r1\rangle\,[21]} = 0. \tag{4.5}$$

The u-channel diagram calculation follows similarly, making the whole contribution zero. Note that the result could be anticipated by seeing that parity forbids the process [346].

However, we show for the QCD axion, and generalise to ALPs, that an operator of the form

$$\mathcal{L}_{a^2F^2} \supset c_{_{F^2}}\,\frac{\alpha}{16\pi^2}\left(\frac{a}{f_a}\right)^2 F_{\mu\nu}F^{\mu\nu}\,, \tag{4.6}$$

is generated at one loop. This operator does not respect the UV shift symmetry of the axion and originates in dynamics that are explicitly symmetry-breaking, with $c_{_{F^2}}$ encoding the origin. In the case of the QCD axion, $c_{_{F^2}}$ arises from the same dynamics that generates the potential, which preserves a discrete $\mathbb{Z}_n$ shift symmetry for a, such that $c_{_{F^2}} \sim \mathcal{O}(10^{-1})$. Crucially, when expressed as a function of m_a, the coupling above scales as $\sim m_a^2/\Lambda_{\rm QCD}^4$, so that $c_{_{F^2}} \sim \mathcal{O}(10^{-1})$ is not further suppressed by m_a or f_a. For ALPs, we present two constructions that lead to non-zero $c_{_{F^2}}$, one QCD-like and one invoking an explicit symmetry-breaking operator. In the latter, $c_{_{F^2}}$ directly depends on the explicit symmetry breaking parameter, emphasising the fact that the quadratic operator only exists when the axion shift symmetry is broken. However, for ALPs some degree of model-building is required to generate this coupling[1].

The operator of Eq. (4.6) leads to time-variation of the fine-structure constant α if the axion has a time-varying field value, as expected for DM axions:

$$\alpha(t) \simeq \alpha\left(1 + c_{_{F^2}}\,\frac{\alpha}{4\pi^2}\left(\frac{a(t)}{f_a}\right)^2\right). \tag{4.7}$$

Such a variation in the fine-structure constant is severely constrained by both cosmological and lab-based experiments [68, 350, 351], and is currently the subject of an intense experimental program (see, e.g., [68] for a recent review). We demonstrate that these constraints also apply to axions, QCD or otherwise. In particular, we consider constraints from cosmology, violations of the weak equivalence principle and direct searches for ultralight DM. Our results are summarised in Fig. 4.1 for the QCD axion, and in Fig. 4.4 for ALPs.

[1] Populating the parameter space where ALPs have a larger coupling to $F\tilde{F}$ than the QCD axion also requires model-building [347–349].

4.3 Generating the quadratic axion-photon coupling

In the standard lore, the shift symmetry of the axion implies that a basis can be found such that it is derivatively-coupled to SM fields. In this case, the naive expectation is that the first order at which a quadratic axion-photon coupling is generated will be $\mathcal{O}((\partial_\mu a)^2 f_a^{-4})$, and will therefore be vanishingly small. However, since axions have a small mass due to a breaking of the shift symmetry, a much larger quadratic axion-photon coupling can be generated. Below we will explore this coupling, first for the QCD axion, and subsequently for an ALP.

4.4 The QCD Axion

The coupling of the QCD axion to SM fields can be consistently treated in Chiral Perturbation Theory (χPT) associated to the breaking of the approximate $SU(N_f)_L \times SU(N_f)_R$ flavour symmetry of the N_f light SM quarks[2]. Our guide to understanding the coupling of axions to SM fields is then the neutral pion, which shares the same quantum numbers as the axion[3].

In χPT, the first order at which an operator appears leading to a tree-level coupling of neutral pions to $F^2 \equiv F_{\mu\nu}F^{\mu\nu}$ is $\mathcal{O}(p^6)$. However, the process $\gamma\gamma \to \pi^0\pi^0$ is experimentally observed to have a cross-section that is only $\sim$ 100 times smaller than that of $\gamma\gamma \to \pi^+\pi^-$, a tree-level $\mathcal{O}(p^2)$ effect, at $\sqrt{s} \sim 0.4\,\text{GeV}$ [353, 354]. In χPT, the large $\gamma\gamma \to \pi^0\pi^0$ cross-section is explained by the observation that unitarity requires it to be generated at one-loop order involving $\mathcal{O}(p^2)$ operators, and is thus $\mathcal{O}(p^4)$ in the χPT power-counting. Importantly, as there is no tree-level $(\pi^0)^2F^2$ operator in the $\mathcal{O}(p^4)$ χPT Lagrangian, there can be no counterterm and the amplitude for $\gamma\gamma \to \pi^0\pi^0$ is finite [346, 355].

The same arguments apply to the QCD axion, which couples to $\pi^+\pi^-$ at tree-level in the $\mathcal{O}(p^2)$ Lagrangian, and therefore couples to $\gamma\gamma$ at one loop. In the following subsection, we derive the coupling of two axions to two photons, whose size is approximately

$$\begin{aligned}\mathcal{L}_{a^2F^2} &\simeq \frac{\alpha}{16\pi^2}\frac{m_u\,m_d}{(m_u+m_d)^2}\frac{\pi}{3}\left(\frac{a}{f_a}\right)^2 F_{\mu\nu}F^{\mu\nu} + \mathcal{O}(p^6) \\ &\simeq \frac{\alpha}{16\pi^2}\frac{\pi}{3}\frac{m_a^2}{\epsilon\, m_\pi^2 f_\pi^2}\, a^2\, F_{\mu\nu}F^{\mu\nu} + \mathcal{O}(p^6)\,. \end{aligned} \tag{4.8}$$

We identify $c_{F^2} = \pi\, m_u\, m_d/3\,(m_u+m_d)^2 \sim 0.2$ when comparing with the form of Eq. (4.6). In the second line of Eq. (4.8) we have written the coupling in terms of the axion mass

$$m_a^2 \simeq \epsilon \frac{m_u m_d}{(m_u+m_d)^2}\frac{m_\pi^2 f_\pi^2}{f_a^2}\,, \tag{4.9}$$

where ϵ encodes possible deviations from the usual QCD prediction [356–358] and is typically taken to be $\epsilon \lesssim 1$, but it may also account for large tunings of the potential. We see the expected result that any non-derivative coupling is suppressed by the shift-symmetry breaking parameter, the axion mass, and goes to zero when the shift symmetry is restored. Crucially, the denominator has no powers of f_a when the numerator is expressed in terms of m_a, and therefore the suppression is not as small as might have been anticipated on dimensional grounds. Indeed, since the operator is generated through the same dynamics as the axion potential at Λ, the naive power counting should have been that $c_{F^2} \sim (m_\pi f_\pi)^2/\Lambda^4$, which is confirmed in the more detailed computation. Given the size of $c_{F^2} \sim \mathcal{O}(1)$ one anticipates a variation of α, and could exploit the precision of non-measurements of variations of the fine structure constant to place bounds on axion-photon coupling.

[2] We will take $N_f = 2$ for simplicity, but our results hold for $N_f = 3$.

[3] In a particular axion coupling parametrisation, there is tree-level mixing between a and π^0. Since observables should not be parametrisation-dependent, we should already conclude that the axion will have all the same couplings as a π^0. Due to its transformation properties under the chiral symmetry, the $\eta^{(\prime)}$ is an even better guide, and also possesses a quadratic coupling to photons [352].

Higher-order one-loop and tree-level corrections to Eq. (4.8) appear at $\mathcal{O}(p^6)$ in the χPT power-counting scheme, and can safely be neglected.

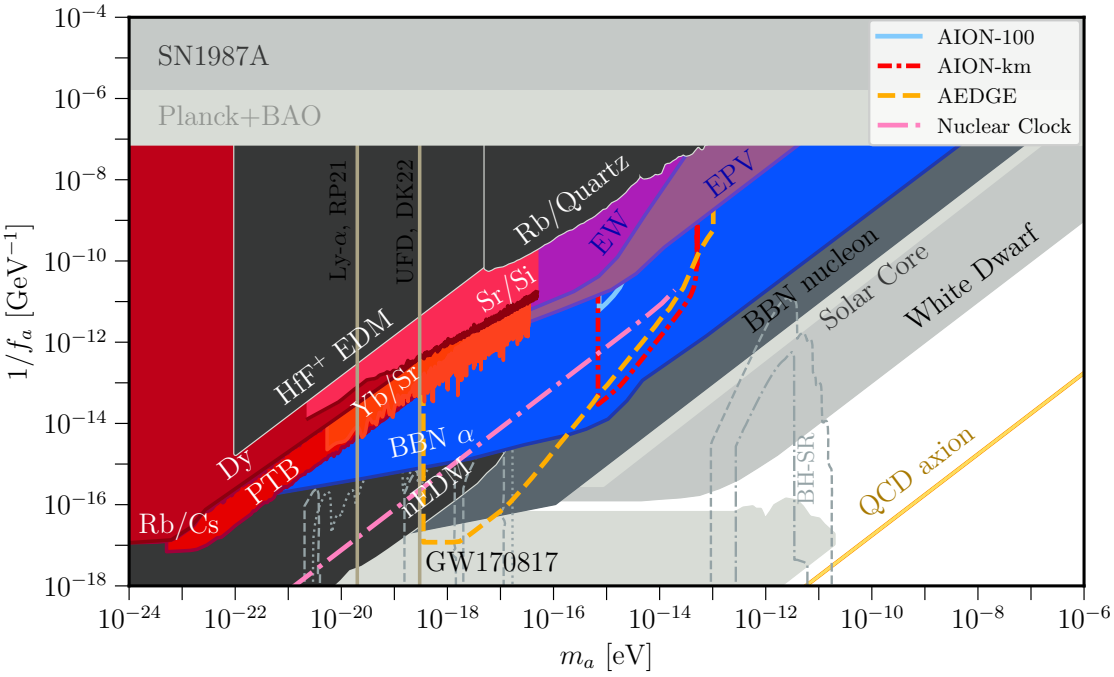

Figure 4.1: New constraints on the decay constant f_a as a function of the mass m_a for axion DM, which rely on the existence of the quadratic coupling, are shown in a variety of colours. Pre-existing constraints (relying on axion-photon linear coupling and axion-nucleon coupling) are given in grey with dark shades indicating DM axion and lighter shades indicating that the bound does not rely on the axion being DM. The new constraints from atomic clocks are shown in shades of red [359–364], as well as from Eöt-Wash (EW) [365, 366] and MICROSCOPE (labelled by EPV) [366, 367] in shades of purple, which search for fifth forces and violations of the equivalence principle respectively. Finally, new constraints from BBN [368] are shown in blue. In addition to these new constraints, we show projections for future atom interferometer experiments AION-100/MAGIS, AION-km and AEDGE [369–371], as well as from a Nuclear clock [372] with sensitivity $|\delta\alpha|/\alpha = 10^{-22}$, as coloured lines. Also shown are existing constraints on tuned QCD axions, such as searches for EDMs (HfF^+ [373] and n [374]), Rb clocks [360], BBN from to the coupling to nucleons [375], in-medium effects on the tuned QCD axion potential from the Sun [376] and White Dwarfs [377], SN1987A [378], cosmology [379] and from GW170817 [380]. We also show exclusions from black hole superradiance [381–383] as dashed grey lines. Analysis of ultra-faint dwarf (UFD) galaxies [384] and of the Lyman-α forest [385] exclude wave-like DM with very low masses.

4.4.1 Axion-Photon Couplings in Chiral Perturbation Theory

We derive the non-derivative axion-photon couplings from the Chiral Lagrangian, showing that they first appear at $\mathcal{O}(p^4)$. This is analogous to the couplings between the neutral pions and photons, which also appear at this order [346, 355]. After performing a rotation of the light quark fields to remove the anomaly-induced coupling of the axion to gluons, the axion enters the Chiral Lagrangian through the light quark mass matrix,

$$M_a = e^{i(a/2f_a)Q_a} \begin{pmatrix} m_u & 0 \\ 0 & m_d \end{pmatrix} e^{i(a/2f_a)Q_a} , \tag{4.10}$$

where Q_a is a matrix whose trace is unity, following the notation of Ref. [386]. At $\mathcal{O}(p^2)$, this matrix gives rise to the QCD axion mass through the mixing with the neutral pion,

$$\mathcal{L}_{p^2} = \frac{f_\pi^2}{4}\mathrm{Tr}\left[D_\mu U (D^\mu U)^\dagger\right] + 2B_0\frac{f_\pi^2}{4}\mathrm{Tr}\left[U M_a^\dagger + M_a U^\dagger\right] , \tag{4.11}$$

where $U \equiv e^{i\Pi/f_\pi}$, $\Pi = \begin{pmatrix} \pi^0 & \sqrt{2}\pi^+ \\ \sqrt{2}\pi^- & -\pi^0 \end{pmatrix}$ and we define $B_0 \equiv m_\pi^2/(m_u + m_d)$. Choosing the charge assignment of Ref. [387], $Q_a = M_q^{-1}/\mathrm{Tr}(M_q^{-1})$, which removes the tree-level mixing between the axion and pion, we find the usual relation for the axion-pion potential,

$$V(a) = -m_\pi^2 f_\pi^2 \left(1 - \frac{4m_u m_d}{(m_u+m_d)^2}\sin^2\left(\frac{a}{2f_a}\right)\right)^{1/2} , \tag{4.12}$$

We make this choice in order to simplify the calculation, but note that the final results should be parametrisation-independent [388][4].

Expanding Eq. (4.11) to second order in both the axion and the pion fields, we find that it contains terms coupling the charged pions to the photon, which is contained in the covariant derivative D_μ, as well as a term that goes as $a^2\,\pi^+\,\pi^-$. Therefore, at one loop we can construct an a^2-photon coupling. The relevant Feynman rules are given in Fig. 4.2, which lead to three one-loop diagrams contributing to the axion-photon coupling shown in Fig. 4.3. These loop diagrams, made of two insertions of p^2 operator, are $\mathcal{O}(p^4)$ in the usual χPT power-counting scheme.

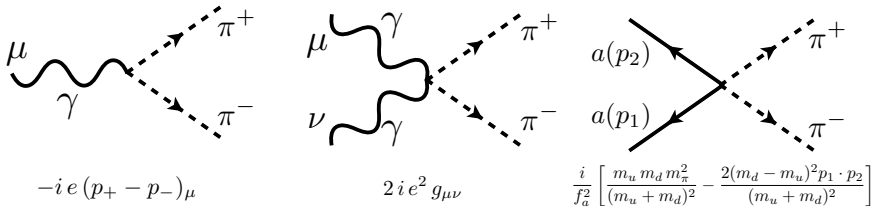

Figure 4.2: Feynman rules for the vertices from the $\mathcal{O}(p^2)$ chiral Lagrangian leading to a loop-induced a^2F^2 coupling.

It can be shown that the sum of the three one-loop diagrams of Fig. 4.3 is finite. Indeed, they must be, since the $\mathcal{O}(p^4)$ χPT Lagrangian contains no tree-level a^2F^2 coupling to absorb any eventual counterterm. The amplitude for $\gamma\gamma \to aa$ is

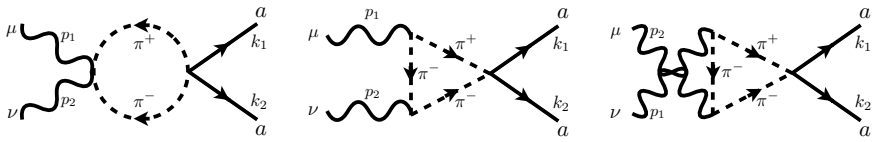

Figure 4.3: Three diagrams contributing to $\gamma\gamma \to aa$ at $\mathcal{O}(p^4)$ in the χPT Lagrangian.

$$\mathcal{A}(\gamma\gamma \to aa) = \epsilon_\mu(p_1)\epsilon_\nu(p_2)M^{\mu\nu} , \tag{4.13}$$

where the tensor multiplying the polarisation vectors is

$$\begin{aligned} iM^{\mu\nu} = {} & \frac{e^2}{f_a^2\,(m_u+m_d)^2}\left(m_u m_d m_\pi^2 + 2(m_d-m_u)^2(k_1\cdot k_2)\right) \\ & \times \int \frac{d^4l}{(2\pi)^4}\frac{g^{\mu\nu}(l^2-m_\pi^2) - (2l+p_1)^\mu(2l-p_2)^\nu}{(l^2-m_\pi^2)((l+p_1)^2-m_\pi^2)((l-p_2)^2-m_\pi^2)} . \end{aligned} \tag{4.14}$$

[4]This choice doesn't avoid a kinetic mixing term, but as it is suppressed by $\sim m_a^2/m_\pi^2$, it will be a sub-dominant effect.

The possibly divergent terms appear as $g^{\mu\nu}l^2 - 4l^\mu l^\nu$, and will therefore cancel in four dimensions after dimensional regularisation, leaving a finite result. Unsurprisingly, this scattering amplitude looks precisely like that of $\gamma\gamma \to \pi^0\pi^0$, which was calculated long ago [346, 355], albeit with a different prefactor. The amplitude also has a structure that is manifestly gauge-invariant, and contains a part proportional to the combination $g^{\mu\nu}p_1\cdot p_2 - p_2^\mu p_1^\nu$, which is characteristic of renormalisation of the coupling α:

$$\begin{aligned} iM^{\mu\nu} = &\left(\frac{-i}{8\pi^2}\right)\frac{e^2}{f_a^2\,(m_u+m_d)^2}\left(m_u m_d m_\pi^2 + 2(m_d-m_u)^2(k_1\cdot k_2)\right)\left(\frac{g^{\mu\nu}(p_1\cdot p_2) - p_2^\mu p_1^\nu}{p_1\cdot p_2}\right) \\ &\times\left[1 - \frac{2\,m_\pi^2}{s}\left(\mathrm{Li}_2\left(\frac{2\sqrt{s}}{\sqrt{s}-\sqrt{s-4\,m_\pi^2}}\right) + \mathrm{Li}_2\left(\frac{2\sqrt{s}}{\sqrt{s}+\sqrt{s-4\,m_\pi^2}}\right)\right)\right] . \end{aligned} \tag{4.15}$$

In the $s \equiv p_1 + p_2 \to 0$ limit, this gives

$$M^{\mu\nu} = (g^{\mu\nu}(p_1\cdot p_2) - p_2^\mu p_1^\nu)\,\Pi(0) \ , \quad \Pi(0) \simeq \frac{e^2\,m_u\,m_d}{48\,\pi^2\,f_a^2\,(m_u+m_d)^2} \ . \tag{4.16}$$

The result is that α is modified from its initial value α_0 as

$$\alpha \simeq \alpha_0\left(1 + \frac{\alpha_0\,m_u\,m_d\,a^2}{12\,\pi\,f_a^2\,(m_u+m_d)^2}\right) \ , \tag{4.17}$$

where a in the case of DM axions has a vacuum expectation value, $\langle a(t)^2\rangle \equiv \rho_{\rm DM}/m_a^2$, so that the shift will be non-zero. The same shift in α can be obtained by writing a quadratic axion-photon operator as in Eq. (4.6).

4.5 Axion-like Particles

ALPs are often characterised as possessing a mass m_a and decay constant f_a that are unrelated. This is a convenient way of considering the phenomenology of ALPs as an effective field theory (EFT) while setting aside unknown UV dynamics. However, given this ignorance of the UV, one must be careful about consistently building the EFT and including all possible operators (for recent discussions see [389, 390]). As we saw in the preceding discussion of the QCD axion, the dynamics that breaks the axion shift symmetry also generates the quadratic axion-photon coupling. Similar arguments can be applied to an ALP.

A simple QCD-like model for an ALP with a quadratic coupling to photons is an $SU(N)\otimes U(1)'$ sector where $SU(N)$ instantons break the ALP shift symmetry, and there are chiral fermions charged under both $SU(N)$ and $U(1)'$. If the chiral fermion masses are $\mathcal{O}$(GeV), they can have an effective charge under EM of $q_{\rm eff} \lesssim 0.1e$ through kinetic mixing of the $U(1)'$ with $U(1)_{\rm EM}$. The dynamics of the $SU(N)$ sector ensure that the ALP couples to the kinetic term of the $U(1)'$, while the kinetic mixing induces a corresponding coupling to $U(1)_{\rm EM}$ with a suppression from the effective charge. The resulting quadratic ALP-photon operator assuming $N_f = 2$ with degenerate $SU(N)$ quark masses is

$$\mathcal{L}_{a^2F^2} \simeq \frac{(q_{\rm eff})^2\,\alpha}{16\pi^2}\frac{\pi}{12}\left(\frac{a}{f_a}\right)^2 F_{\mu\nu}F^{\mu\nu} \ . \tag{4.18}$$

We can relate this coupling to the ALP mass as in the case of the QCD axion, with $m_a^2 f_a^2 \simeq \epsilon_{\rm ALP}\,m_{\pi'}^2\,f_{\pi'}^2$. The scale $\Lambda' \sim 4\pi f_{\pi'}$ of the $SU(N)$ sector must be sufficiently heavy compared with the light quark mass scale, such that the price to pay for having a light ALP is that $\epsilon_{\rm ALP}$ must be very small. Explicit computation in a later section shows that for this construction of the ALP-photon coupling, we have $c_{_{F^2}} \simeq q_{\rm eff}^2(\pi/12)$ which can be $\mathcal{O}(10^{-2})$ for $\Lambda' \sim$ TeV.

An alternative construction of the quadratic operator starts from a UV Lagrangian in which the complex scalar field containing the radial (ρ) and ALP fields couples to fermions charged under $U(1)_{\rm EM}$, similar to the

KSVZ model [72, 73][5]. Without an explicit shift-symmetry breaking operator, no quadratic coupling of the ALP to photons is generated upon integrating out the fermions. However, an operator of the form $(\rho/f_a)FF$ *is* generated. Since the radial mode mass is $M_\rho \sim \mathcal{O}(f_a)$, one might think this operator is never relevant for the ALP. However, the potential typically contains a term of the form $V(\rho, a) \supset S[a]\,\rho + \text{h.c.}$ such that upon integrating out ρ, the operator $(\rho/f_a)FF \to (S[a]/f_a M_\rho^2)FF$. For the canonical potential with no symmetry breaking, $S[a] \sim (\partial a)^2/f_a$, so that the original intuition that the first quadratic axion-photon operator is $\mathcal{O}((\partial a)^2/f_a^4)$ appears to be confirmed. However, if the UV does not respect the full ALP shift symmetry but only the milder $a \to a + 2n\pi f_a$ $\mathbb{Z}_n$ symmetry, e.g., $S[a] \sim g^2 f_a \cos(a/f_a)$ with g a dimensionful parameter, integrating out ρ leads to an operator $\sim (g^2 a^2/f_a^2 M_\rho^2)FF$. A precise calculation is given in the later section 4.7, yielding $c_{F^2} = (4\pi/3)Q^2(g/M_\rho)^2$, where Q is the charge of the fermions integrated out in the UV. While the potential we give in 4.7 does not lead to a new contribution to the ALP mass, the symmetry-breaking removes some of the protection of the small mass. Significant tuning could therefore be required for the ALP mass to remain small in the IR.

In a sense, the two constructions above reflect the same overarching result: dynamics that breaks the full axion shift symmetry (possibly to the smaller $\mathbb{Z}_n$ symmetry) at a certain scale leads to an a^2F^2 operator with a coefficient given by a ratio of some power of the shift-breaking parameter over the scale of the breaking. For the QCD-like model, this ratio is $\sim (m_\pi f_\pi)^2/\Lambda^4 \sim 1$, while for the UV-driven model this ratio is $(g/M_\rho)^2$.

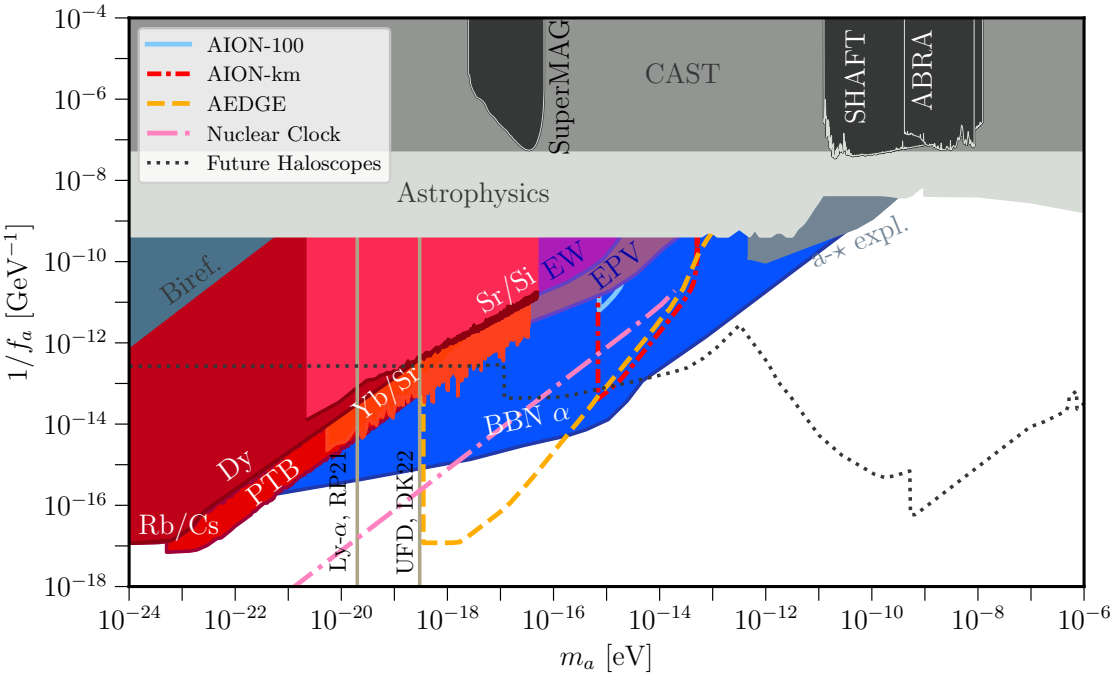

Figure 4.4: ALP parameter space excluded by considering only ALP-photon coupling. The colour scheme is the same as in Fig. 4.1. We have compared with existing and future constraints on linear ALP-photon couplings as discussed in the main text. We have set $c_{F^2} = 0.2$, and constraints from variations of α scale as $(c_{F^2})^{1/2} f_a$. Existing constraints on the linear coupling to photons shown here are from CAST [304], Astrophysics [297, 391], Birefringence [392–397], SHAFT [398], ABRA [399, 400] and axion star explosions [401]. Future haloscopes aimed at ALP DM in this mass range include [402–408]. Analysis of ultra-faint dwarf (UFD) galaxies [384] and of the Lyman-α forest [385] exclude wave-like DM with very low masses. To compare with constraints on the linear coupling, we use $g_{a\gamma\gamma} \equiv \alpha/(2\pi f_a)$.

[5] A DFSZ-like model [71, 74] would result in tree-level couplings to QCD.

4.6 Phenomenology of the Quadratic Coupling.

The quadratic axion-photon coupling leads to a shift in the fine-structure constant in the presence of a non-zero background field value of the axion. For DM axions near a spherically-symmetric, homogeneous body of mass M and radius R with dilaton charge Q_e [409], the background field value is [366]

$$a(t) \simeq \frac{\sqrt{2\rho_{\rm DM}}}{m_a} \cos(m_a t + \varphi) X(r)\,, \tag{4.19}$$

$$X(r) = \left(1 - s_C(Q_e) \frac{c_{F^2}\,\alpha\, M}{16\,\pi^3 f_a^2}\frac{1}{r}\right)\,, \tag{4.20}$$

where r is the distance between the centre of the homogeneous body and a detector. The function $s_C(Q_e) \sim Q_e \min\left[1,\, 3/x^2\right]$, accounts for the screening of the scalar near the macroscopic object, and

$$x = \sqrt{3 Q_e \frac{c_{F^2}\,\alpha\, M}{16\,\pi^3 f_a^2\, R}}\,. \tag{4.21}$$

The resulting shift in α is given by

$$\frac{\Delta\alpha}{\alpha} \simeq c_{F^2}\frac{\alpha}{4\pi^2}\frac{2\rho_{\rm DM}}{m_a^2 f_a^2}\cos^2(m_a t + \varphi) X(r)^2\,, \tag{4.22}$$

with φ an arbitrary phase. The form of Eq. (4.22) implies that there is a static shift in α, since $\langle \cos^2 x\rangle = 1/2$, and that the time-varying part oscillates at a frequency $\omega \simeq 2m_a$.

The constraints from a quadratic scalar-photon coupling have previously been considered in, e.g., Refs. [350, 351, 368, 410, 411]. There is a far more extensive literature considering a linear scalar-photon coupling, which has recently been summarised in Ref. [68]. To facilitate comparison between constraints on f_a arising from the a^2F^2 coupling and constraints on the linear axion-photon coupling, Eq. (4.1), we use $g_{a\gamma\gamma} \equiv \alpha/2\pi f_a$.

4.6.1 Big Bang Nucleosynthesis (BBN)

Variations of the fine-structure constant would impact the predictions of standard BBN, as has been discussed previously [350, 351, 368, 412]. The most sensitive BBN observable is the yield of ^{4}He, measured to be $Y_p^{\rm exp}(^4{\rm He}) = 0.245 \pm 0.003$ [413], which agrees extremely well with the theoretical prediction in the Standard Model, $Y_p^{\rm th}(^4{\rm He}) = 0.2467 \pm 0.0002$ [414]. A careful analysis of the impact of a quadratically-coupled ultralight scalar DM candidate on BBN was recently performed in Ref. [368], which we recast as a limit on axions through Eq. (4.22) with $X(r) = 1$. We take the "zero-T" result from their analysis, but caution that the true constraint on f_a could be be up to a factor of ~ 3 weaker due to thermal loops contributing to the mass of the axion [368]. Changes to the primordial ^{4}He abundance are given schematically by [351]

$$\frac{\Delta Y_p(^4{\rm He})}{Y_p(^4{\rm He})} \simeq \frac{\Delta(n/p)_{\rm weak}}{(n/p)_{\rm weak}} - \Delta(\Gamma_n t_{\rm BBN})\,, \tag{4.23}$$

where $(n/p)_{\rm weak}$ is the neutron-to-proton ratio when the weak interaction freezes out, Γ_n is the neutron decay rate, and $t_{\rm BBN}$ is the end-time of BBN. The neutron-proton mass difference enters the calculation, and is affected by a variation in α as

$$\frac{\Delta(m_n - m_p)}{(m_n - m_p)} = \frac{b\alpha\Lambda_{\rm QCD}}{(m_n - m_p)}\, c_{F^2}\frac{\alpha}{16\pi^2}\left(\frac{a}{f_a}\right)^2\,, \tag{4.24}$$

where $b\alpha\Lambda_{\rm QCD} \simeq -0.76$ MeV [412].

For the QCD axion, the resulting constraints are weaker than those arising from the axion-nucleon coupling [375]. This is expected, since the nucleon coupling appears at tree level, while the photon coupling is a one-loop effect. The EM effect should translate into constraints on f_a that are a factor $\sim 4\pi/\sqrt{\alpha} \sim 10^2$ weaker than the nucleon coupling, an estimate which is confirmed in Fig. 4.1. For an ALP, however, the nucleon coupling is model-dependent such that the BBN α constraint might be the most stringent in much of the ALP parameter space, as seen in Fig. 4.4.

4.6.2 Fifth Forces and the Weak Equivalence Principle

The effects of ultralight scalar DM quadratically-coupled to photons on searches for fifth forces and violations of the weak equivalence principle were considered in Ref. [366]. These results apply to the quadratically-coupled axion also, and therefore appear in Figs. 4.1 and 4.4. The strongest constraints are from the MICROSCOPE experiment [367] searching for violations of the weak equivalence principle, and the Eöt-Wash torsion balance experiments [365].

4.6.3 Ultra-light DM Searches

Experiments looking for ultra-light *scalar* DM with a coupling to photons are sensitive to the resulting shift in α. The axion-induced oscillation of α leads to a change in atomic energy transitions, allowing strong constraints from very precise clocks [359–364]. These constraints are shown in Figs. 4.1 and 4.4. We also show projections for atomic interferometers AION and AEDGE [369][6], and from a nuclear clock [372]. Notice that some constraints have abrupt endpoints, ranging from $m_a \sim 10^{-17}\,\text{eV}$ for Dy clocks to $m_a \sim 10^{-13}\,\text{eV}$ for AION-km. This is a result of screening by the Earth [366, 410], which occurs for $f_a \lesssim (c_{F^2})^{1/2} \times 10^{11}\,\text{GeV}$, as can be computed from Eqs. (4.20), (4.21).

4.6.4 Other Phenomenology

A quadratic axion-photon coupling can have profound implications for experiments looking for axion DM on Earth due to the screening of the axion field at large coupling to matter. On Earth, the screening effect reduces the amplitude of the axion field drastically if f_a is too small. This affects not only the observables associated to the quadratic axion coupling, but the linear axion couplings as well.

It has been shown that the polar cap regions of neutron stars (NSs) have large $\boldsymbol{E} \cdot \boldsymbol{B}$ and can therefore source non-DM axions [297, 416]. The quadratic coupling to $\boldsymbol{B} \cdot \boldsymbol{B}$ leads to an effective mass for the axion of order

$$\omega_a \sim \left(c_{F^2} \frac{\alpha}{4\pi^2} \left(\frac{|\boldsymbol{B}|}{f_a} \right)^2 \right)^{1/2} \sim 10^{-9}\,\text{eV} \times \left(\frac{|\boldsymbol{B}|}{10^{12}\,\text{G}} \right) \left(\frac{g_{a\gamma\gamma}}{5 \times 10^{-12}\,\text{GeV}^{-1}} \right) .$$

This "plasma" mass for the axion coincides with the lower end of the range of bare axion masses to which the analysis of Ref. [297] is sensitive. A careful re-analysis taking into account this effect is therefore motivated. More generally, the plasma mass from the magnetic field around the NS exceeds the bare mass for $g_{a\gamma\gamma} \gtrsim 7 \times 10^{-9}\ \text{GeV}^{-1} \times (m_a/\mu\text{eV})\,(10^{12}\,\text{G}/|\boldsymbol{B}|)$.

4.7 ALP couplings to Photons

We discuss the generation of the quadratic coupling of an ALP to photons, fleshing out the arguments made in the previous section. Two approaches are possible: IR dynamics similar to that which generates the a^2F^2 coupling for the QCD axion also apply to the ALP; the ALP shift symmetry is broken, leading to a^2F^2 operators being generated by UV dynamics. For the quadratic coupling to be phenomenologically relevant, some level of tuning of the ALP mass will likely be required in both cases.

[6] In Figs. 4.1, 4.4 we have re-interpreted Fig. 4 of Ref. [369]. However, as shown in Ref. [415], the sensitivity of atom interferometers to a scalar with linear couplings is likely slightly weaker. Depending on the specific design of the experiment, the signal amplitude is refined by a correction factor, which might take the values ~ 0.98 for AION-km and $\sim [0.8, 0.95]$ for AION-100. These correction factors are taken into account on the bounds of quadratic coupling.

4.7.1 QCD-like Dynamics

A simple model for realising QCD-like dynamics for the ALP-photon coupling consists of a sector with gauge symmetry $SU(N_c) \times U(1)'$. Instantons of the $SU(N_c)$ sector will generate a potential for the ALP,

$$V(a) \sim m^{N_f} \Lambda'^{4-N_f} \cos\left(\frac{a}{f_a}\right) , \tag{4.25}$$

where m is the mass scale of the N_f 'quarks' which remain light at the condensation scale of the $SU(N_c)$ sector, Λ', in analogy with QCD. Assuming $N_f = 2$, with both fermions having equal mass, we can use χPT to refine our estimate to

$$V(a) = -m_{\pi'}^2 f_{\pi'}^2 \cos\left(\frac{a}{2f_a}\right) \simeq -\frac{1}{2} m_a^2 a^2 , \tag{4.26}$$

with $m_a^2 f_a^2 = m_{\pi'}^2 f_{\pi'}^2/4$.

Let us now consider the $U(1)'$, which we will take to be unbroken. The couplings of the ALP to the dark photon will have exactly the same structure as those of the QCD axion to photon, so that we have

$$\alpha' \simeq \alpha'_0 \left(1 + \frac{\alpha'_0\, a^2}{48\,\pi\, f_a^2}\right) , \tag{4.27}$$

assuming equal light quark masses. In order to transmit this shift in the dark photon gauge coupling to the regular photon, we can invoke a kinetic mixing χ of the two photons,

$$\mathcal{L}^K_{\gamma,\gamma'} = -\frac{1}{4}\left(F_{K,\mu\nu}F_K^{\mu\nu} + F'_{K,\mu\nu}F'_K{}^{\mu\nu} - 2\chi F_{K,\mu\nu}F'_K{}^{\mu\nu}\right) - e\, j^\mu A_{K,\mu} - e'\, j'^\mu A'_{K,\mu} , \tag{4.28}$$

where the subscript K indicates that these quantities are associated to the kinetic mixing basis, and j and j' denote the SM and hidden sector currents respectively. For a massless dark photon, the kinetic mixing basis quantities can be rotated as $A_{K,\mu} \to A_\mu$, $A'_{K,\mu} \to A'_\mu + \chi A_\mu$ to leading order in χ, such that the photon now couples to the dark current j'^μ

$$\mathcal{L}_{\gamma,\gamma'} = -\frac{1}{4}\left(F_{\mu\nu}F^{\mu\nu} + F'_{\mu\nu}F'^{\mu\nu}\right) - A_\mu\left(e\, j^\mu + \chi\, e'\, j'^\mu\right) - e'\, j'^\mu A'_\mu + \mathcal{O}(\chi^2) . \tag{4.29}$$

We see that the dark current couples directly to the photon with a strength $\chi\, e'$. As a result, in the χPT analysis of the couplings to external vector fields, the covariant derivative acting on the U' contains not only the dark photon A', but also the regular photon A. The dark sector therefore has the same Feynman rules as in Fig. 4.2, only with $m_u = m_d$ and $e \to \chi e'$. Therefore, the shift in e is the same as the shift in e', moderated by the kinetic mixing factor χ,

$$\alpha \simeq \alpha_0 \left(1 + \chi^2 \alpha'_0 \frac{a^2}{48\,\pi\, f_a^2}\right) . \tag{4.30}$$

Above we considered a massless dark photon, for which $\chi \sim 1$ is allowed until we account for the dark fermions. The dark pions will have an effective milli-charge of $q_{\text{eff}} = \chi e'/e$ under EM, and are therefore subject to constraints from collider searches [417–421] and stellar cooling [418, 422]. The latter require $\chi \lesssim 10^{-15}$ for $e' \sim 1$, which would make the shift in α so small that it could not be observed for reasonable values of f_a. If the dark pions have masses $m_{\pi'} \gtrsim$ MeV (GeV), then $\chi \lesssim 10^{-4}$ (0.1) is allowed, such that the shift in α can be substantial for reasonable f_a.

If the dark photon is massive, the rotation to obtain the mass eigenstate basis is different from above, and results in

$$\mathcal{L}_{\gamma,\gamma'} = -\frac{1}{4}\left(F_{\mu\nu}F^{\mu\nu} + F'_{\mu\nu}F'^{\mu\nu}\right) - \frac{1}{2}m_{A'}^2 A'_\mu A'^\mu - e\, j^\mu A_\mu - A'_\mu\left(e'\, j'^\mu + \chi\, e\, j^\mu\right) + \mathcal{O}(\chi^2) . \tag{4.31}$$

A_μ is now an admixture $A_{K,\mu} - \chi A'_{K,\mu}$, so that an ALP-induced shift of e' translates into an ALP-induced shift of e at $\mathcal{O}(\chi)$. This follows from the fact that e' is defined in the kinetically mixed basis through the dark current interaction, so that the shift in e' due to the ALP can be absorbed by a shift in $A'_{K,\mu}$, which then enters A_μ at $\mathcal{O}(\chi)$. The resulting shift in α is the same as in Eq. (4.30) above.

4.7.2 Shift Symmetry-breaking EFT

For our EFT analysis, let us consider an ALP with a coupling to vector-like (VL) fermions similar to a KSVZ model [72, 73]. In order to couple to photons, the fermions should have electric charge. The UV Lagrangian is

$$\mathcal{L}_{\rm UV} = -\frac{1}{4}F_{\mu\nu}F^{\mu\nu} + \bar{\psi}_L i\not{D}\psi_L + \bar{\psi}_R i\not{D}\psi_R + \left(y\phi\bar{\psi}_L\psi_R + \text{h.c.}\right) + \partial_\mu\phi^\dagger\partial^\mu\phi - V(\phi^\dagger\phi)\,, \tag{4.32}$$

with ϕ being the complex scalar field containing both the radial field and the axion. As written, the Lagrangian is invariant under a global $U(1)$ transformation, and the potential can be written as

$$V(\phi^\dagger\phi) = \lambda\left(\phi^\dagger\phi - \frac{f_a^2}{2}\right)^2\,. \tag{4.33}$$

The field ϕ admits two commonly used and equivalent representations, one linear with $\phi_l = \frac{1}{\sqrt{2}}(\sigma + f_a + i\alpha)$, and one polar with $\phi_p = \frac{1}{\sqrt{2}}(\rho + f_a)\exp(ia/f_a)$. The polar representation makes the shift symmetry that acts on the axion field a evident, while the linear representation obscures it. There exists a map between the two representations and to leading order, $\rho \sim \sigma$ and $a \sim \alpha$.

The a^2F^2 operator is not generated from the Lagrangian of Eq. (4.32) upon integrating out the VL fermions $\psi_{L,R}$, as expected given the shift-invariance of the Lagrangian. In order to see how such an operator is generated if the shift-symmetry is broken, it is instructive to examine this result.

It is straightforward to calculate in the polar representation, where the Yukawa interaction of ϕ with the VL fermions is $\mathcal{L} \supset (1/\sqrt{2})\,y(\rho + f_a)e^{ia/f_a}\bar{\psi}_L\psi_R + \text{h.c.}$ We can then demonstrate that the coefficient of the operator a^2F^2 is zero in two ways. In the first, we can expand the Yukawa interaction in powers of a/f_a, leading to two diagrams contributing to the operator: a box containing two vertices linear in a and a triangle containing one vertex quadratic in a. Integrating out ψ using the universal structures of the fermionic Universal One-Loop Effective Action (UOLEA) of Ref. [27] we obtain

$$\mathcal{L}^{\text{1-loop}}_{a^2F^2} = \frac{i^2}{16\pi^2}\frac{1}{3M_\psi^2}\left[M_\psi^2\frac{a^2}{f_a^2}\right](iQ_\psi e)^2F_{\mu\nu}F^{\mu\nu} + \frac{i^2}{16\pi^2}\frac{2}{3M_\psi}\left[M_\psi\frac{(ia)^2}{2f_a^2}\right](iQ_\psi e)^2F_{\mu\nu}F^{\mu\nu} = 0\,, \tag{4.34}$$

where Q_ψ is the EM charge of the VL fermion in units of e, and $M_\psi = y\,f_a/\sqrt{2}$. The first term in Eq. (4.34) corresponds to the box diagram, while the second corresponds to the triangle. They precisely cancel each other, as indeed they should. A more elegant way of obtaining the same result is to make use of the symmetries of the UV Lagrangian, and perform a chiral rotation of the fermion field $\psi \to \exp(-ia\gamma_5/2f_a)\psi$ to remove the a-dependent phase in the Yukawa interaction in favour of a manifestly shift-symmetric derivative coupling $\mathcal{L} \supset -\frac{\partial_\mu a}{2f_a}\bar{\psi}\gamma^\mu\gamma_5\psi$. Using the fermionic UOLEA we find that the coefficient of the operator $\mathcal{O}((\partial a)^2A^2)$, which can map to a^2F^2, is zero as expected. Both approaches demonstrate that the symmetry structure of the Lagrangian is responsible for ensuring that symmetry-breaking operators are not generated.

In the above analysis, we have neglected the radial mode ρ. It has a linear coupling to the fermions, such that upon integrating them out, we obtain a $\rho F^2/f_a$ operator with a non-zero Wilson coefficient. Integrating out the ρ at tree level, from the Lagrangian of Eq. (4.32) we find that this leads to an operator $\sim (\partial a)^2F^2/f_a^4$, since the classical background field value of ρ is $\rho_c \simeq (\partial_\mu a)^2/(f_a\,M_\rho^2)$, with $M_\rho^2 = 2\lambda f_a^2$. However, this also means that if the potential for ϕ contains non-shift-symmetric terms, ρ_c could be the origin of an a^2F^2 operator. For example, adding a shift-symmetry-breaking potential that preserves CP and a $\mathbb{Z}_n$ symmetry for a,

$$V(a,\rho)_{\text{s.b.}} = g^2\left(\phi^\dagger\phi - \frac{f_a^2}{2}\right)\left(1 - \cos\left(\frac{a}{f_a}\right)\right)\,, \tag{4.35}$$

where g is a dimensionful parameter, leads to $\rho_c = (\partial_\mu a)^2/(f_a\,M_\rho^2) + a^2g^2/2f_aM_\rho^2$, and therefore both the $(\partial a)^2F^2/f_a^4$ and a^2F^2 operators. We do not specify the origin of this potential, but merely point out that it is possible to generate the a^2F^2 coupling without generating a mass for a, without violating CP, and retaining the residual $\mathbb{Z}_n$ symmetry for a. Integrating out first the fermions with the UOLEA, and then

integrating ρ out by setting it to its classical background field value, we find

$$\mathcal{L}^{1-\text{loop}}_{a^2F^2} \supset \frac{i^2}{16\pi^2}\frac{2}{3M_\psi}\left[M_\psi\frac{\rho}{f_a}\right](iQ_\psi e)^2 F_{\mu\nu}F^{\mu\nu}\Big|_{\rho=\rho_c(a)} \tag{4.36}$$

$$= \frac{1}{48\pi^2}(Q_\psi e)^2\frac{g^2}{f_a^2M_\rho^2}a^2F_{\mu\nu}F^{\mu\nu} + \frac{1}{24\pi^2}(Q_\psi e)^2\frac{1}{f_a^2M_\rho^2}(\partial_\mu a)^2F_{\nu\sigma}F^{\nu\sigma}\,. \tag{4.37}$$

In the second line, we have replaced $\rho \equiv \rho_c = \dfrac{(\partial a)^2}{f_aM_\rho^2} + \dfrac{a^2g^2}{2f_aM_\rho^2}$. Comparing with Eqs. (4.6), (4.7) one can identity the value of c_{F^2} and $\alpha(a)$ as,

$$c_{F^2} = \frac{4\pi}{3}Q_\psi^2\frac{g^2}{M_\rho^2}\,, \quad \alpha(a) = \alpha\left(1 + \frac{Q_\psi^2\alpha}{3\pi}\frac{g^2a^2}{M_\rho^2f_a^2}\right)\,. \tag{4.38}$$

More generally, the condition for the a^2F^2 operator to be generated by a symmetry-breaking potential is that the potential takes the form

$$V_{\text{s.b.}} \supset S[a]\rho + \text{h.c.}\,, \tag{4.39}$$

where we can further impose that $S[a]$ be an even function of a to preserve CP, and that it be a trigonometric function of a/f_a in order for a to possess a residual $\mathbb{Z}_n$ symmetry. In this case, we should expect the coefficient of the a^2F^2 operator and the corresponding shift in alpha to obey

$$c_{F^2} \propto \frac{Q_\psi^2 f_a}{M_\rho^2}\frac{\partial^2 S[a]}{\partial a^2}\,, \quad \alpha(a) \sim \alpha\left(1 + Q_\psi^2\alpha\frac{S[a]}{M_\rho^2f_a}\right)\,, \tag{4.40}$$

where the leading term is $S[a] \propto a^2/f_a^2$.

4.8 Scaling of constraints with c_{F^2}

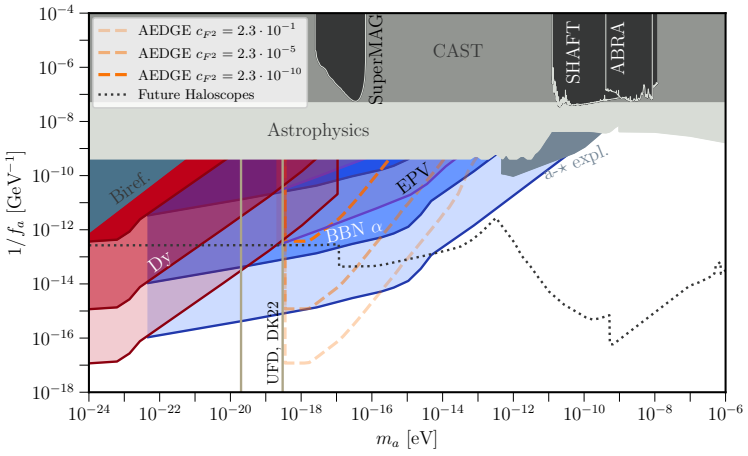

Figure 4.5: ALP parameter space, showing how a subset of constraints change with a rescaling of c_{F^2}. The colour scheme remains the same as in Figs. 4.1 and 4.4. We have chosen to show how the constraints of Dy, MICROSCOPE, BBN α and AEDGE change; although the behaviour of the rescaling should be generic. Three values of c_{F^2} are chosen: $2.3\cdot10^{-1}$, $2.3\cdot10^{-5}$ and $2.3\cdot10^{-10}$, where the increasing colour intensity denotes the smaller value of c_{F^2}.

We also present a subset of the expected bounds and future experimental sensitivities for axion-like particles while allowing the coupling coefficient c_{F^2} to vary. The results are shown in Fig. 4.5.

Chapter 5

Consistent Positivity at Finite-t

5.1 Chapter overview

This chapter introduces the problems associated with deriving dispersion relations for theories which have divergences in the forward limit. Time is spent developing the notion of smeared dispersion relations in section 5.2, which can be used to rectify these issues. We then propose a procedure to obtain positivity bounds, which *completely avoids the forward limit*. The procedure can be consistently used to derive bounds in any theory (including gravity) beyond the strictly tree-level case. There may be problems in obtaining Wilson coefficients from smeared dispersion relations, due to the Müntz-Szász theorem, related to the non-uniqueness of the parametrisation of distributions. The necessary implicit assumptions required to circumvent this theorem are discussed in section 5.3. Results are then presented which we claim are robust under the inclusion of loop effects in section 5.4.

5.2 Dispersion relations

Here we focus on EFT positivity bounds, as derived by dispersion relations for the $2 \to 2$ scattering amplitude for spin-0 particles, in the Mandelstam variable s and for fixed t, where the analyticity and boundedness properties of amplitudes are best understood. The bounds stem from writing this quantity in an IR representation, where it can be computed within the EFT as a function of the Wilson coefficients, and a UV representation, where unitarity implies positivity. In the forward limit $t = 0$, these UV/IR relations are effectively completely understood, see e.g. [145, 147] In this context, several approaches have been proposed to extract bounds, by including information about the finite t behaviour. The simplest method involves a Taylor-expansion at $t = 0$ [145, 146, 150], and as such, is only applicable when the amplitude is analytic in $t = 0$. This fails to be true in physically relevant theories containing massless particles. As an example, in the presence of dynamical gravity, not only is there a Coulomb pole $\sim su/t$, but also loop effects which diverge in the forward limit. Because the effects are not analytic in s they will appear in all dispersion relations, meaning that the dispersion relations are all contaminated by this divergent behaviour in the forward limit.

We are interested in the $2 \to 2$ scattering amplitude for spin-0 massless particles, i.e. Goldstone bosons, and study this amplitude in the complex Mandelstam variable $s \in \mathbb{C}$ plane, for fixed $t < 0$. The Lorentz-invariant causal structure implies that the only non-analyticities are confined to the real s axis and are associated with physical phenomena [142] (see Figure 5.1). We define arcs in their *IR representation* as contour integrals in s,

$$a_n(t) \equiv \int_{\frown} \frac{\mathrm{d}\,\mathrm{s}}{2\pi \mathrm{i}\ \mathrm{s}} \frac{\mathcal{M}(\mathrm{s},t)}{[\mathrm{s}\,(\mathrm{s}+t)]^{n+1}}\,, \quad n \geq 0\,. \tag{5.1}$$

As shown in Figure 5.1, the contour of integration '$\frown$' is given by the union of two semi-circles of radius

$|\,\mathrm{M}^2+t/2|$, centred at $-t/2$. Notice that the measure and subtraction is manifestly s-u crossing symmetric. Arcs probe the theory at finite energy, and are particularly appropriate in the presence of massless particles, where the branch cut extends all the way to the origin in s [147, 423]. An assumption that is often made in the literature is that below the mass-gap of the EFT $s \leq M^2$, the theory is weakly coupled and the discontinuity along this branch cut is negligible. In this situation, arcs would reduce to the residues of the n-subtracted amplitude at $s=0$ and $s=-t$. In this chapter we develop a tool that is suitable to deal with the IR effects, and therefore we keep the arc as defined above, although in practice we will often work with the tree-level formulae as well.

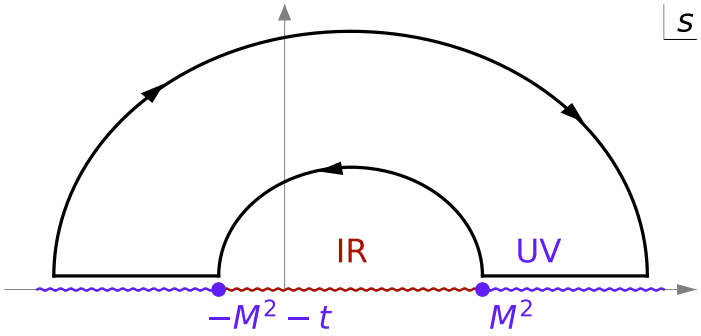

Figure 5.1: *The $2\to 2$ scattering amplitude is analytic in the upper (and by crossing, lower) half plane in s. The inner semi-circular contour is the IR arc Eq. (5.1) that runs within the EFT validity region, whereas the horizontal contour denotes the arc in the UV Eq. (5.3). In red the IR part of the branch cut, due to loops in the EFT, in violet its UV part, associated also to particle exchange in the unknown UV theory.*

Exploiting the analyticity properties of the amplitude in the complex s-plane, the integration contour $\circlearrowleft$ can be deformed into another contour that encompasses the discontinuities on the positive $\mathrm{s}\geq \mathrm{M}^2$ and negative $\mathrm{s}\leq -\mathrm{M}^2-t$ real axis, as well as a pair of semicircles at infinity enclosing the upper and lower-half planes (Figure 5.1). Assuming that the latter contributions vanish, as implied by generalisations of the Froissart-Martin bound [214, 215, 424] to theories involving gravity in $d>4$ [185, 216], corresponds to the asymptotic behaviour

$$\lim_{|s|\to\infty} \mathcal{M}(s,t)/s^2 = 0\,. \tag{5.2}$$

Moreover, the property of s-u crossing symmetry of both the amplitude $\mathcal{M}(\mathrm{s},t)=\mathcal{M}(-\mathrm{s}-t,t)$ and the measure in Eq. (5.1), combined with real analyticity $\mathcal{M}(\mathrm{s},t)=\mathcal{M}^*(\mathrm{s}^*,t)$, allows us to relate the integrals along the positive and negative real axis, obtaining,

$$a_n(t) = \frac{1}{\pi}\int_{\mathrm{M}^2}^{\infty} \mathrm{d\,s}\,\frac{(2\,\mathrm{s}+t)}{[\mathrm{s}(\mathrm{s}+t)]^{n+2}}\,\mathrm{Im}\,\mathcal{M}(\mathrm{s},t)\,. \tag{5.3}$$

At this point, unitarity in the forward $t=0$ limit directly translates into $\mathrm{Im}\,\mathcal{M}(\mathrm{s},0)\geq 0$, and the condition $a_n(s,0)\geq 0$. For theories including massless particles the forward limit may be divergent. As mentioned in the introduction, to exploit unitarity away from the forward limit, we can project the amplitude onto partial waves,

$$\mathcal{M}(\mathrm{s},t) = \sum_{\ell=0}^{\infty} \mathcal{M}_\ell(\mathrm{s})\,\mathcal{P}_\ell\Big(1+\frac{2\,t}{\mathrm{s}}\Big)\,, \tag{5.4}$$

where $\mathcal{P}_\ell(\cos\theta) = {}_2F_1\left(-\ell,\ell+d-3,(d-2)/2,(1-\cos\theta)/2\right)$ are the Gegenbauer polynomials in d space-time dimensions, which reduce to Legendre polynomials in $d=4$. The appeal of using this basis is that S-matrix unitarity is diagonal in the partial waves, and directly implies $\mathrm{Im}\,\mathcal{M}_\ell(\mathrm{s})>0$. In Eq. (5.4) we absorb

any normalisation factors into the definition of $\mathcal{M}_\ell(\mathrm{s})$. For identical scalars, the amplitude is symmetric under $\cos\theta \to -\cos\theta$ and the partial waves expansion has support on only even ℓ's. By projecting the right hand side of Eq. (5.4) onto partial waves, we are also expressing the arcs in a *UV representation*

$$\begin{aligned} a_n(t) &= \frac{1}{\pi}\int_{\mathrm{M}^2}^{\infty} \mathrm{d}\,\mathrm{s} \sum_{\ell=0}^{\infty} \rho_\ell(\mathrm{s})\, \frac{(2\,\mathrm{s}+t)}{[\mathrm{s}(\mathrm{s}+t)]^{n+2}}\, \mathcal{P}_\ell\Big(1+\frac{2\,t}{\mathrm{s}}\Big) \\ &\equiv \left\langle \frac{(2\,\mathrm{s}+t)}{[\mathrm{s}(\mathrm{s}+t)]^{n+1}}\, \mathcal{P}_\ell\Big(1+\frac{2\,t}{\mathrm{s}}\Big)\right\rangle , \end{aligned} \tag{5.5}$$

where we have defined the average

$$\Big\langle \cdots \Big\rangle = \frac{1}{\pi}\int_{\mathrm{M}^2}^{\infty} \frac{\mathrm{d}\,\mathrm{s}}{\mathrm{s}} \sum_{\ell=0}^{\infty} \rho_\ell(\mathrm{s})\,(\cdots)\,, \tag{5.6}$$

and $\rho_\ell(s) \equiv \mathrm{Im}\,\mathcal{M}_\ell > 0$ is the spectral density, which provides a positive measure for the average $\langle\cdots\rangle$. This positivity implies constraints for the UV representation of arcs of Eq. (5.5), which are inherited by the IR representation (5.1), implying bounded coefficients within the EFT.

5.2.1 IR arcs

In this section, we explicitly compute the arcs in their IR representations, for the $2 \to 2$ scattering of massless Goldstone bosons interacting among themselves and gravitationally in a theory with a mass gap M. As usual, at sufficiently low energy $E \ll M$ the theory is weakly coupled and well described by an effective Lagrangian with interactions ordered by a derivative expansion. We organise the amplitude as,

$$\mathcal{M} = \mathcal{M}^{\mathrm{tree}}_{\mathrm{EFT}} + \mathcal{M}^{\mathrm{loops}}\,. \tag{5.7}$$

The tree-level contribution includes graviton exchange and higher order contact interactions,

$$\mathcal{M}^{\mathrm{tree}}_{\mathrm{EFT}} = \kappa^2\left(\frac{u\,t}{s}+\frac{s\,u}{t}+\frac{s\,t}{u}\right) + \sum_{p\geq 1}\sum_{q=0}^{p} g_{2p+q,q}\left(\frac{s^2+t^2+u^2}{2}\right)^{p-q}(stu)^q\,, \tag{5.8}$$

with $\kappa^2 \equiv \frac{1}{M_{\mathrm{P}}^{d-2}}$ denoting the gravitational constant in d-dimensions, where M_{P} is the Planck scale $M_{\mathrm{P}}^{-2} = 8\pi G$ in $d=4$ dimensions.[1] The coefficients $g_{n,q}$ scale as $1/M^{2n}$ in units of the mass gap. We will refer to an amplitude with $\mathcal{M}^{\mathrm{loops}} = 0$ as "strictly tree-level". This is equivalent to taking the limit $\kappa, g_{n,q} \to 0$ while keeping ratios $g_{n,q}/\kappa^2$ fixed.

Strictly tree-level. The tree-level part of the amplitude is analytic in both s and t away from the origin and the arcs reduce to the sum of residues at $s=0$ and $s=-t$. From Eq. (5.8) we can then find an all-order expression for the arcs,

$$\begin{aligned} a_n^{\mathrm{tree}}(t) &= (\mathrm{Res}\,|_{\mathrm{s}=0} + \mathrm{Res}\,|_{\mathrm{s}=-t})\frac{\mathcal{M}(\mathrm{s},t)}{\mathrm{s}[\mathrm{s}(\mathrm{s}+t)]^{n+1}} \\ &= -\frac{\kappa^2}{t}\,\delta_{n,0} + \sum_{p=1}^{\infty}\sum_{q=0}^{p} g_{2p+q,q}(-t)^{2(p-n-1)+q}\binom{p-q}{n+1-q}. \end{aligned} \tag{5.9}$$

[1] A constant term in the amplitude Eq. (5.8), as well as a pole associated with the scalar exchange are forbidden by the Goldstone Boson shift symmetry. Furthermore, the contribution from gravity is limited to the amplitude emerging from minimal coupling because 3-point interactions between massless particles are completely fixed up to field redefinitions.

Notice that the gravity pole only appears in the zeroth arc,

$$\begin{aligned} a_0^{\text{tree}}(t) &= -\frac{\kappa^2}{t} + \sum_{n=1}^{\infty} [\, n\, t^{2n-2}\, g_{2n,0} - t^{2n-1}\, g_{2n+1,1}] \\ &= -\frac{\kappa^2}{t} + g_{2,0} - g_{3,1} t + 2\, g_{4,0} t^2 + \cdots , \end{aligned} \tag{5.10}$$

while all of the other arcs are polynomials in t, for example:

$$\begin{aligned} a_1^{\text{tree}}(t) &= g_{4,0} - t g_{5,1} + 3t^2 g_{6,0} + t^2 g_{6,2} + \cdots \\ a_2^{\text{tree}}(t) &= g_{6,0} - t g_{7,1} + 4t^2 g_{8,0} + t^2 g_{8,2} + \cdots \end{aligned} \tag{5.11}$$

Without gravity and in the strictly tree-level limit, these IR arcs are all polynomials in t. Then one can expand both the IR and UV arcs in t using a Taylor series, which provides a set of equations for the EFT coefficients in terms of UV averages Eq. (5.6). For instance, from Eq. (5.3) and Eq. (5.9) at $t = 0$ we may read

$$g_{2,0} = \left\langle \frac{1}{\mathrm{s}} \right\rangle , \quad g_{4,0} = \left\langle \frac{1}{\mathrm{s}^3} \right\rangle \quad \text{and} \quad g_{6,0} = \left\langle \frac{1}{\mathrm{s}^5} \right\rangle . \tag{5.12}$$

Since $\mathrm{s} \geq M^2$ and the measure in the average is positive, the Wilson coefficients surviving in the forward limit must monotonically decrease in units of M^2, and must also satisfy two-sided bounds $g_{2,0} \geq g_{4,0} M^4 \geq g_{6,0} M^8 \geq 0$ [147].

Moreover, there is a redundancy in these equations because many EFT coefficients $g_{n,q}$ appear in multiple arcs, multiplying different powers of t. Indeed, from Eq. (5.10) and Eq. (5.11), we observe that $g_{2,0}$ and $g_{3,1}$ appear only in a_0, while $g_{4,0}$ and $g_{5,1}$ also appear in a_1. On the other hand the coefficient $g_{6,2}$ appears uniquely in a_1, while there are none in a_2. This redundancy implies the existence of "null constraints": non-trivial relations between UV representations of different arcs. For instance, from Eq. (5.10) (with $\kappa = 0$) and Eq. (5.11), we see that for the IR arcs,

$$(\partial_t^2 a_0^{\text{tree}} - 4 a_1^{\text{tree}})\big|_{t=0} = 0 . \tag{5.13}$$

These relations can be thought as constraints on the UV measure $\rho_\ell(s)$ appearing in the average. Using them, one finds two-sided bounds also for the coefficients that vanish in the forward limit, such as $g_{3,1}$ [149, 150].

With gravity, the first arc Eq. (5.10) is singular at $t = 0$, so the approach based on the Taylor expansion fails. There will be more on this in the next section. On the other hand, gravity at tree level does not enter any other arc a_n with $n \geq 1$, all of which are still polynomials. Therefore, in the strictly tree-level limit, it is still possible to build null constraints using these higher arcs.

Loop-level. The 1-loop effects in $\mathcal{M}^{\text{loops}}$ are known, see e.g. [178, 222, 425, 426] in the context of positivity. Since, by construction, the EFT is weakly coupled in the far IR, these effects have small coefficients, of the order $g^2/16\pi^2$ or $\kappa^4/16\pi^2$ in the case of gravity. For this reason, they are mostly neglected in the EFT positivity literature, where one works in the strictly tree-level limit. We will comment on this further in the next chapter.

Despite the small coefficients, loop effects qualitatively modify the analytic structure of amplitudes, and therefore play an important role in dispersion relations, see Eq. (1.64). For instance, at order κ^4 in $d = 5$ dimensions, where the computation is particularly well-defined, the amplitude develops features such as,

$$\mathcal{M}^{\text{loops}} \propto \sqrt{-t}\, s^2 \log s , \tag{5.14}$$

which is clearly no longer analytic. Because of the non analyticity in s, such effects appear in *all* arcs. Then, the non-analyticity in t prevents the dispersion relations from being Taylor expanded. This also implies that all null constraints obtained using arcs a_n with $n \geq 1$ are singular. These facts force us to rethink both dispersion relations and null constraints, while entirely avoiding the $t = 0$ limit.

5.3 Positivity at finite t

When equating the IR and UV representations of the arcs (Eq. (5.1) and Eq. (5.5)), it is important to understand in what sense the partial wave expansion correctly reproduces the amplitude. Pointwise convergence (convergence at each point in t) is not always guaranteed. Indeed, in the presence of gravity or loop effects, it is of course impossible to reproduce non-analytic structures, such as the $1/t$ pole or branch cuts, using only polynomials. Instead, the series might converge in a weaker sense, meaning that given appropriate measures $\mathrm{d}\mu(t) \equiv f(t)\mathrm{d}t$, the integrals,

$$\int_{-t_{\rm max}}^{0} \mathrm{d}\mu(t)\, a_n(t), \tag{5.15}$$

with $0 < t_{\rm max} < 1$, will converge both in the IR and UV representations. The arcs $a_n(M^2, t)$ are therefore treated as distributions. Hence, rather than Taylor expanding dispersion relations and comparing different powers of t (as illustrated above), we shall project (smear) dispersion relations against an appropriate basis of functions $f_i(t)$. The projected dispersion relations shall shape the allowed space of EFT parameters [185].

5.3.1 Improving arcs to circumvent the Müntz-Szász theorem

There is a crucial difference between the Taylor expansion method and using the smeared relations that we should first discuss. Indeed, the Taylor expansion is in one-to-one correspondence with the EFT approach, and the t-expanded arcs directly imply conditions on the EFT coefficients. Does a suitable basis of functions $f_i(t)$ exist, such that the smeared IR arcs are also projected directly onto the EFT coefficients?

To answer this question we rely on the fact that the space of continuous functions in $t \in [-t_{\rm max}, 0]$ constitutes a vector space, albeit an infinite dimensional one. While many of the properties of finite dimensional vector spaces extend to infinite dimensional ones, the Müntz-Szász theorem [427, 428] represents a striking difference between the two cases. The monomials $\{1, t, t^2, t^3, \cdots\}$ are a basis of continuous functions on an interval. The Müntz-Szász theorem states that the same is true for the generic basis,

$$\{t^{\lambda_0}, t^{\lambda_1}, t^{\lambda_2}, \cdots\} \tag{5.16}$$

with parameters $0 = \lambda_0 < \lambda_1 < \cdots$, iff

$$\sum_{i=1} \frac{1}{\lambda_i} \to \infty\,. \tag{5.17}$$

Notice that it is a necessary condition that $\lambda_0 = 0$. In other words, this theorem quantifies how many "missing terms" a basis of monomials is allowed to have to still approximate a function or distribution arbitrarily well. For instance, it implies that any basis missing a few monomials, such as the set $\{1, t, t^3, t^4, t^5, \cdots\}$ that does not contain t^2, is still a basis.

In a Taylor expansion it makes sense to expand two equal expressions (such as the UV and IR representations of the arcs) in powers of t and then compare their coefficients. Instead, when we talk about distributions under a measure, there is no absolute meaning associated with the coefficient of a particular power of t, because it can just be re-written in terms of the other powers. For instance a function $g_{2,0} - g_{3,1}t + 2g_{4,0}t^2 + \cdots$ like the one appearing in a_0, may be re-written as $\tilde{g}_{2,0} + 2\tilde{g}_{4,0}t^2 + \cdots$ as well, without the linear term in t, but instead with some new coefficients $\tilde{g}_{n,q}$. Therefore, without extra assumptions or information, it is not possible to extract unique coefficients of an infinite Taylor series from integrated distributions.

To understand what type of information might be needed, it is interesting to see how the Müntz-Szász theorem works in practice. For instance, in the above example, how large would the coefficients $\tilde{g}_{n,q}$ have to be relative to $g_{n,q}$ in order to be able to accurately describe the same function? In the following subsection, this question is discussed in detail and some extra examples are provided.

5.3.2 Müntz-Szász in practice

The Müntz-Szász theorem provides a fundamental obstruction to reconstruct the individual coefficients in a Taylor expansion when all the information at our disposal is in the form of its integrals against test measures.

While the fundamental obstruction is indeed there, in this section we want to make its implications more quantitative. Given a series expansion $\sum_n g_n\, t^n$, we ask how would the "Müntz-Szász alternative solution" $\sum_{\lambda_n} \tilde{g}_n\, t^{\lambda_n}$ look if the basis were missing one or more of the monomials? For instance if $\lambda_n \notin [n_-, n_+]$ for some $n_+ \geq n_- \geq 0$ were missing. More explicitly, we want to approximate the function t, with higher powers from $t^{2\,N}$ to some other $t^{N_{\rm max}}$, to some precision ϵ,

$$\left| t - \sum_{n=2N}^{N_{\rm max}} \tilde{g}_n\, t^n \right| < \epsilon\,, \quad t \in [0,1]\,. \tag{5.18}$$

This is exactly the situation we are focusing on, where the function t is associated to the coefficient $g_{3,1}$ which we want to bound, and we have removed all terms up to $t^{2\,N}$ in the partially improved arc; $t^{N_{\rm max}}$ would be the highest term that can be resolved by the computer.

In figure 5.2 we show the minimum (absolute) value for the last coefficient in the series $|\tilde{g}_N|$, as a function of N, in two cases. In the first we demand $\epsilon = 1/10$ and allow $N_{\rm max} = 4\,N$ (red dots). In the second (blue dots) we take $\epsilon = 1/20$: in this case the previous value of N was not enough to approximate the function to the desired accuracy, and we had to take more terms in the series: $N_{\rm max} = 6\,N$. Even then, for $N > 22$ the problem Eq. (5.18) has no solution, and a higher N should have been taken. Ref. [429]

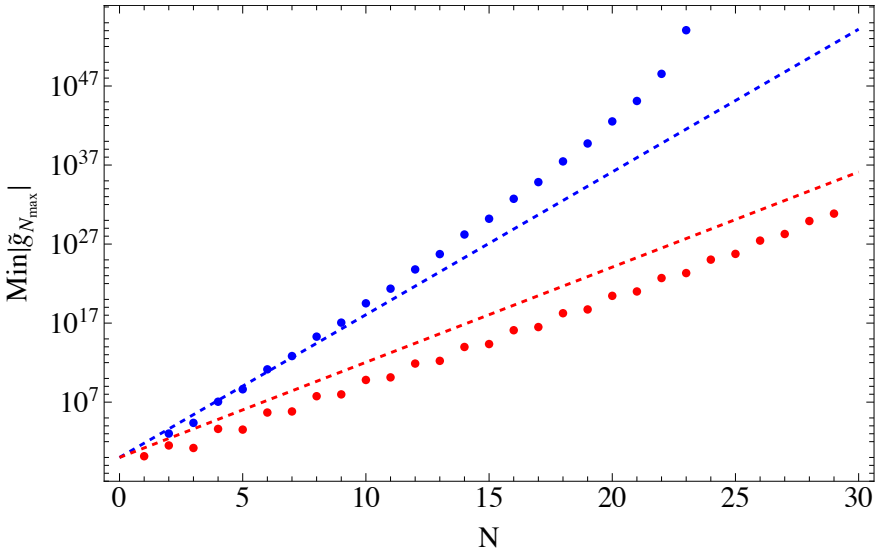

Figure 5.2: The size of the smallest possible coefficient $g_{N_{\rm max}}$ in order to fulfil Eq. (5.18), with $N_{\rm max} = 4\,N$ and $\epsilon = 1/10$ (red) or $\epsilon = 1/20$ and $N_{\rm max} = 6\,N$ (blue). The minimal coefficient was found solving a simple linear programming algorithm in `Mathematica`, by discretising t over 100 points in the interval $[0,1]$ and imposing Eq. (5.18) in each point. The dashed red (blue) line corresponds to $g_{N_{\rm max}} \sim 2^{N_{\rm max}}$ for $N_{\rm max} = 4\,N(6\,N)$.

studied a similar problem, the approximation of $|t|$ in $t \in [0,1]$ with a basis of even-power monomials t^{2k}, with $k = 1, \cdots, n$. The author showed that for the approximation to be valid with precision ϵ, the series requires at least $2n = 1/(20\epsilon)$ terms, and the coefficients are as big as $(0.75\,\epsilon)\, 2^{1/(40\epsilon)}$, implying coefficients as large as $10^{107'000}$ for an $\epsilon = 10^{-6}$ precision.

These results tell us two things about how the Müntz-Szász theorem is realised in practice. First of all, the coefficients can become so large, that it is plausible that in numerical studies the "Müntz-Szász alternative solution" discussed in the main text cannot be found numerically with current machine precision. Secondly, and most importantly, it also tells us that even the weakest assumptions on the behaviour of the coefficients as n grows, are enough to avoid the solution taking over. For reference, the dashed lines in Fig. 5.2 correspond to coefficients that grow as $g_{N_{\rm max}} \sim 2^{N_{\rm max}}$ in the two scenarios above (where $N_{\rm max} = 4N(6N)$). These would be the coefficients in an EFT with ordinary power-counting if the ratios of energy versus cutoff were of order

2, rather than being much smaller than one. Furthermore, from a physical point of view, it is reasonable to assume that after a certain order, the coefficients start decreasing, otherwise the whole idea of EFT loses its appeal. This assumption would be enough, by far, to prevent the higher coefficients from playing the role of the smaller ones and invalidating the bounds.

To summarise, the coefficients $\tilde{g}_{n,q}$ would need to grow exponentially fast in n w.r.t. the original coefficients to appear as the lower coefficients. Both on numerical and physical grounds, very mild assumptions about the convergence of the EFT coefficients is enough to prevent the low coefficients from being expressible in terms of higher ones. For instance, the underlying assumption behind every EFT that after a certain order the coefficients start becoming smaller in units of the energy, would be enough to limit the impact of the Müntz-Szász theorem. On the other hand, without making use of such an assumption, even implicitly, one might wonder if it even makes sense to talk about bounds on the coefficients of the EFT from smearing, as the tree-level approximation is identical to a Taylor expansion.

Even without this assumption, in the case of dispersion relations, extra information *is* available. Full crossing symmetry implies that the same EFT coefficients appear in different dispersion relations. The most straightforward way to see how this information can be used is to algorithmically use dispersion relations themselves to subtract off all of the higher coefficients. It is indeed possible to find coefficients $c_{n,k}$ to build an '*improved arc*',

$$a_0^{\rm imp}(t) = \sum_{n,k} c_{n,k} \frac{t^{2n+k}}{k!} \partial_t^k a_n(t)\,, \tag{5.19}$$

such that in the IR representation, only a finite number of terms appear. For instance, in the strictly tree-level limit, the first arc can be improved to

$$a_0^{\rm imp}(t) = -\frac{\kappa^2}{t} + g_{2,0} - g_{3,1} t\,, \tag{5.20}$$

removing any higher order term. The improved arc lacks the freedom to reproduce the monomial t with other coefficients and the Müntz-Szász theorem, as used above, does not apply. The resulting dispersion relations can be projected on test functions to unambiguously extract bounds on $g_{2,0}$ and $g_{3,1}$ in terms of κ. Similarly, an improved arc,

$$a_0^{\rm imp}(t) = -\frac{\kappa^2}{t} + g_{2,0} - g_{3,1} t + 2 g_{4,0} t^2\,, \tag{5.21}$$

allows one to include also $g_{4,0}$ in the projected dispersion relations, and so on.

The idea of improved arcs has been introduced in Ref. [185], where an improved a_0 arc of the form Eq. (5.20) was achieved via the following linear combination,

$$a_0(t) - \sum_{n\geq 1} t^{2n} \left(n\, a_n(0) - t\, \partial_t a_n(t) \Big|_{t=0} \right). \tag{5.22}$$

Crucially, this expression uses higher arcs and their first derivatives at $t = 0$.

Outside of the strictly tree-level regime, when loop effects are introduced, there will be corrections to this formula when evaluated in the IR representation. In particular, all couplings $g_{n,q}$ re-appear in a non-linear way, at all orders in the perturbative expansion. They multiply each other so that their effect cannot be removed by a simple algebraic operation on the arcs. In principle, one could take a perturbative approach and ignore these contributions,[2] were it not for the fact that Eq. (5.22) is evaluated at $t = 0$ where the loop effects entering into higher arcs, such as Eq. (5.14), diverge. Therefore, a finite t improvement procedure in the form of Eq. (5.19) or similar is qualitatively necessary to ensure the bounds survive at finite coupling rather than Eq. (5.22).

[2]By ignoring loops one is assuming that the EFT is infinitely perturbative in the sense that any loop is smaller than even the most irrelevant EFT operator. On the other hand, in this approximation, one still keeps all orders in the EFT expansion. This approximation is correct only in the exact $g_{n,q} \to 0$ limit as we have commented on.

5.3.3 Improvement at finite t

For the reasons outlined in the previous subsection, in what follows we introduce a procedure to improve arcs while not exploiting the information at $t = 0$. This will eventually enable a consistent perturbative derivation of bounds in theories with any IR structure $\mathcal{M}^{\text{loop}} \neq 0$. Indeed, if we improve the strictly tree-level arc of Eq. (5.22) using only relations at $t \neq 0$, the $\mathcal{M}^{\text{loop}}$ entering the improved arc will not be infinite when evaluated at $t \neq 0$, but small in perturbation theory. It will then provide a genuinely small correction to the bounds, rather than compromising them.

It is useful to express derivatives of arcs in the form,

$$\frac{1}{k!}\partial_t^k\, a_n(t) = \sum_{p=1}^{\infty}\sum_{q=0}^{p} \binom{p-q}{n+1-q}\binom{2\,(p-n-1)+q}{k}\, t^{2\,(p-n-1)+q-k}\, g_{2p+q,q}\,. \tag{5.23}$$

While this result seems opaque, it is easy to show that it is true using some basic complex analysis. In the strictly tree-level approximation and without gravity $\kappa \to 0$, the IR representation of arcs can be written in a compact form via Eq. (5.8),

$$\begin{aligned} a_n(t) &= \oint \frac{\mathrm{d}s}{2\pi\mathrm{i}}\, \frac{\mathcal{M}^{\text{tree}}_{\text{EFT}}(s,t)}{(s)^{n+2}(s+t)^{n+1}} = \sum_{p\geq 1}\sum_{q\geq 0} g_{2p+q,q}(-t)^q \oint \frac{\mathrm{d}s}{2\pi\mathrm{i}}\, \frac{\left[s^2+t^2+st\right]^{p-q}}{s^{n-q+2}(s+t)^{n-q+1}} \\ &= \sum_{p\geq 1}\sum_{q\geq 0} g_{2p+q,q}(-t)^{2(p-n-1)+q}\alpha_{p-q,\,n-q+1}. \end{aligned} \tag{5.24}$$

In the last step, we have pulled an overall t-dependent factor outside of the integral and have used that,

$$\alpha_{n,m} = \oint \frac{\mathrm{d}z}{2\pi\mathrm{i}}\, \frac{(z^2-z+1)^n}{z^{m+1}(z-1)^m} = \binom{n}{m}. \tag{5.25}$$

The integral is easily solved using the binomial and residue theorems. Using this, we can then take k derivatives in t and obtain Eq. (5.23).

We insert this expression into the definition of the improved arc given in Eq. (5.19), and require it to match the improved $a_0^{\text{imp.}}$ of Eq. (5.20). The result provides relations between the coefficients $c_{n,k}$. For instance a partial improvement,

$$a_0^{\text{tree}}(t) - 2t^2 a_1^{\text{tree}}(t) + t^3\partial_t a_1^{\text{tree}}(t) - 3t^4 a_2^{\text{tree}}(t) = -\frac{\kappa^2}{t} + g_{2,0} - g_{3,1}t + 4g_{8,0}t^6 + \cdots \tag{5.26}$$

eliminates the coefficients $g_{4,0}, g_{5,1}, g_{6,0}, g_{7,1}$ from the 0th arc. For each further $g_{2p+q,q}$ coefficient that we wish to cancel from $a_0^{\text{imp.}}$, there exists an additional constraint. The collection of these constraints leads to the following system of equations for the $c_{n,k}$'s:

$$\sum_{n\geq 0}\sum_{k\geq 0} \binom{p-q}{n+1-q}\binom{2(p-n-1)+q}{k}\, c_{n,k} = 0, \quad \forall g_{2p+q,q} \notin \mathcal{S} \tag{5.27}$$

where $\mathcal{S}$ is the set of indices we wish to keep in the improved arc. For instance, in order to improve the arc to the form of Eq. (5.20), the relevant set $\mathcal{S}$ is $\mathcal{S} = \{g_{2,0}, g_{3,1}\}$, which is equivalent to setting $c_{0,0} = 1$ and $c_{0,1} = 0$ in the system of equations. On the other hand, for Eq. (5.21) $\mathcal{S} = \{g_{2,0}, g_{3,1}, g_{4,0}\}$, such that $c_{0,0} = 1$, $c_{0,1} = 0$ and $c_{1,0} = 0$. In both cases $c_{0,0} = 1$ provides the correct normalisation because we start with the zeroth arc. In particular, the first n arcs contain $(n^2+3n)/2$ couplings not appearing in higher arcs. Generically, solutions for some improved arc exist if there are at least $k \leq n+1$ derivatives per arc included in Eq. (5.19). This expectation does not hold in special cases, such as the improvement of Eq. (5.26), where we require only $k \leq n$ derivatives per arc, due to accidental cancellations. We can think of the solution with $k \leq n$ as the *minimal one*, while solutions for higher k are redundant, since they can be repackaged in the form of null constraints, as we show in the following subsection.

5.3.4 Null constraints and higher-arcs

There is a general procedure for improvement and to find null constraints algorithmically, without using arcs (or their derivatives) in the forward limit. It consists of gradually removing all the coefficients $g_{n,q}$ from an initial object, using higher arcs. The coefficients have dimension, and they always multiply the same powers of t when grouped into dimensionless objects. For simplicity we neglect gravity in this subsection. Its inclusion is trivial.

The starting point is to identify an object to be improved. In subsection 5.3.3 this is $a_0(t)$, but we may as well start from $a_1(t)$ to improve the first arc, or we could start from $\partial_t^4 a_1(t)$: in this case we could use higher arcs to remove all coefficients, and we would obtain genuine null constraints.[3] Here we will follow the example of a_0, in a way that will make its generalisation straightforward. Using Eq. (5.24), the object to improve is,

$$a_0(t) = \sum_{p\geq 1}^{N}\sum_{q\geq 0}^{N-n}\binom{p-q}{1-q} g_{2p+q,q}(-t)^{2(p-1)+q}\,, \tag{5.28}$$

where we highlighted that, although the original arc has infinitely many terms, the procedure is constructed to cancel a finite number of them, up to N. We make the choice to truncate in both the number of arcs used and also at some order in t; in practice we choose these to be the same, but this is not required.

To improve this object, we can subtract combinations of arcs a_n, with $n \geq 1$, and their derivatives $\partial_t^k a_n$, where $0 \leq k \leq n+1$ is in principle necessary to find a solution:

$$a_0^{\text{imp},N} = \sum_{n=1}^{N}\sum_{k=0}^{N-n} c_{n,k}\sum_{p\geq 1}\sum_{q=0}^{n+1}\binom{p-q}{n+1-q}\binom{2(p-n-1)+q}{k} t^{2(p-1)+q} g_{2p+q,q}\,, \tag{5.29}$$

which is simply Eq. (5.19) combined with Eq. (5.23) for the arc's k-th derivatives. The sum of these two expressions Eq. (5.28) and Eq. (5.29), must give the improved arc $g_{2,0} - g_{3,1}t$. We can phrase this in matrix notation by defining a vector

$$\vec{g} \equiv \{g_{2,0}, g_{3,1}t, g_{4,0}t^2, g_{5,1}t^3, \ldots, g_{2N,0}\,t^{2N-2}\}, \tag{5.30}$$

of all coefficients multiplied by the appropriate powers of t to endow them all with the same dimension. We can then write the right-hand side of Eq. (5.28) as $\vec{a}_0 \cdot \vec{g}$, the improved arc as $\vec{a}_{\text{imp}} \cdot \vec{g}$ (with $\vec{a}_{\text{imp}} = \{1, -1, 0, 0, 0, \cdots\}$), and Eq. (5.29) as $\vec{c} \cdot A \cdot \vec{g}$, with $\vec{c}$ a vector collecting the $c_{n,k}$ coefficients and A a square matrix of size $(N^2+5N)/2$, defined by Eq. (5.29). With this definition the improvement formula becomes,

$$\vec{a}_0 \cdot \vec{g} + \vec{c} \cdot A \cdot \vec{g} = \vec{a}_{\text{imp}} \cdot \vec{g} \qquad \Rightarrow \qquad \vec{c} = (\vec{a}_{\text{imp}} - \vec{a}_0).A^{-1}\,, \tag{5.31}$$

since the formula must be valid for all values of $\vec{g}$. This algorithm can be implemented for different N.

To find null constraints, the procedure is very similar, but with $\vec{a}_{\text{imp}} \to \vec{0}$, since all coefficients must be cancelled. For instance, in the case without gravity, we could cancel all coefficients order by order in $\partial_k^2 a_0$ using higher arcs. The associated coefficients $\tilde{c}_{n,k}$ are $\vec{\tilde{c}} = \overrightarrow{\partial_k^2 a_0} \cdot A^{-1}$, where the A matrix is the same as above, while $\overrightarrow{\partial_k^2 a_0}$ is the vector of coefficients of $\vec{g}$ in $\partial_k^2 a_0(s,t)$.

We do not use these null constraints since smearing the improved arc with high Legendre polynomials gives zero on the IR side and something non-trivial on the UV side, thus automatically delivering null UV conditions.

The resulting algorithm is infinite, meaning that in order to cancel the infinitely many coefficients, we need a series containing infinitely many arcs. In practice, we will solve the system algorithmically after *truncating* Eq. (5.27) at some value $n \leq N$, which is equivalent to setting $c_{n,k} = 0$ for $n \geq N$. Then Eq. (5.27) becomes a linear system of equations with unique solution,

$$c_{1,0} = -2, \quad c_{1,1} = 1, \quad c_{1,2} = 0,$$

[3] Null constraints can also be obtained trivially by taking $m+1$ derivatives in t of an arc $a_{n\geq 1}(t)$ improved up to order m.

$$
\begin{aligned}
&c_{2,0} = -3, \quad c_{2,1} = 0, \quad c_{2,2} = 1, \quad c_{2,3} = 0, \\
&c_{3,0} = -8, \quad c_{3,1} = -2, \quad c_{3,2} = 2, \quad c_{3,3} = 1, \quad c_{3,4} = 0 \\
&\dots
\end{aligned}
\tag{5.32}
$$

satisfying the recursion relation,

$$
c_{n+1,\,k} = c_{n,\,k-1} + 2\,c_{n,\,k} + c_{n,\,k+1}\,. \tag{5.33}
$$

Alternatively, this solution can be expressed using the generating function,

$$
G(x,y) \equiv \frac{x\left(1+\sqrt{1-4x}-6x\right)}{\sqrt{1-4x}\left[2x+y\left(2x-1+\sqrt{1-4x}\right)\right]}\,, \tag{5.34}
$$

as

$$
c_{n,k} = \frac{\partial_x^n\,\partial_y^k}{n!k!}\,G(x,y)\bigg|_{x\,=\,y\,=\,0}\,. \tag{5.35}
$$

Importantly, the improvement presented here is only ever partially implemented: if we include arcs only up to N, we cannot cancel coefficients such as $g_{2N+2,0}$, which require the arc $a_N(s,t)$. Following the discussion on the Müntz-Szász theorem, the use of this expression only makes sense by postulating that the coefficients $g_{n,p}$ with $n > N$ are bounded in some way. This way they can not reproduce the effects of the lower coefficients as implied by the Müntz-Szász theorem. This assumption is further justified by two facts that will be discussed in the next subsection. Firstly, we will see that $|t|$ is limited by an upper value $t_{\max} \ll s$, implying that the neglected terms are exponentially small in N. Secondly the bounds derived with this algorithm converge very quickly with N, and asymptotically approach the ideal situation with no additional assumptions on the coefficients.

5.3.5 Partial improvement in the UV

Now that the problem is well posed, we can apply the same improvement algorithm to the UV representation of the arcs. This means substituting the UV arcs Eq. (5.5) in the sum Eq. (5.19), obtaining,

$$
a_0^{\text{imp}}(t) = \langle I_\ell\,(\mathrm{s},t)\rangle\,, \tag{5.36}
$$

with

$$
I_\ell\,(\mathrm{s},t) = \sum_{n,k} c_{n,k}\,\frac{t^{2\,n+k}}{k!}\,\partial_t^k\,\frac{1}{[\mathrm{s}(\mathrm{s}+t)]^{n+1}}\,\frac{(2\,\mathrm{s}+t)}{\mathrm{s}(\mathrm{s}+t)}\mathcal{P}_\ell\left(1+\frac{2\,t}{\mathrm{s}}\right)\,, \tag{5.37}
$$

where the coefficients $c_{n,k}$ are given by Eq. (5.35). To our knowledge (and dismay) this function cannot be re-summed, unlike the improved arc in Eq. (5.22) taken from Ref. [185]. Using a simple trick, we may nevertheless write it in such a way that some of its convergence properties are manifest. We introduce the additional variable $\tilde{t}$ and bring the t^{2n} factors in Eq. (5.36) inside the partial derivative by the replacement,

$$
t^{2\,n}\partial_t^k\,(\cdots) = \partial_t^k\,\tilde{t}^{\,2\,n}\,(\cdots)\,\Big|_{\tilde{t}=t}\,. \tag{5.38}
$$

The sum in n can then be carried out explicitly. The result is the kth order in y of the generating function Eq. (5.34), with $x = \tilde{t}^2/s(s+t)$:

$$
\begin{aligned}
a_0^{\text{imp}}(t) = \Big\langle \sum_k \frac{t^k}{k!}\partial_t^k \Bigg(&\frac{2}{\sqrt{1-\frac{4\,\tilde{t}^2}{s(s+t)}}+1}-1\Bigg)^k \\
&\times \frac{(2\,s+t)\left(s(s+t)\left(\sqrt{1-\frac{4\,\tilde{t}^2}{s(s+t)}}+1\right)-6\,\tilde{t}^2\right)}{2(s(s+t))^{3/2}\sqrt{s(s+t)-4\,\tilde{t}^2}}\Bigg|_{\tilde{t}=t}\mathcal{P}_\ell\left(1+\frac{2t}{\mathrm{s}}\right)\Big\rangle\,.
\end{aligned}
\tag{5.39}
$$

By inspecting the improved arc in this form, it is clear that the formula cannot converge if the expression appearing under all of the square roots is negative, which puts a bound on the values of t for which it can be used,

$$-t_* \leq t \leq 0 \quad \text{with} \quad \frac{t_*}{M^2} \equiv \frac{1}{8}\left(\sqrt{17}-1\right) \approx 0.39\,. \tag{5.40}$$

This is an important result, since it limits the range, $t_{\max} \leq t_*$, over which the dispersion relations can be smeared against the measure appearing in Eq. (5.15). The existence of this upper bound is supported by numerical results.

5.3.6 Projection on basis functions

Integrating both the IR improved arcs Eq. (5.20) and their corresponding UV representations Eq. (5.36) against a complete set of basis functions $f_i(t)$ (as in Eq. (5.15)), we obtain the most general set of IR-UV relations in algebraic form. In the absence of gravity ($\kappa \to 0$), arcs are continuous functions of t. For continuous functions, the space of polynomials provide a complete basis by the Weierstrass theorem. Moreover, orthogonal polynomials, in particular Legendre polynomials P_j, are useful as they provide a countable set for this goal. Indeed, they are orthogonal with respect to the flat $\mathrm{d}t$ integration measure and therefore are the most natural choice of basis.

We consider a smearing function of the form,

$$f(t) = \sum_{j=0}^{j_{\max}} b_j P_j\left(1+\frac{2t}{t_{\max}}\right) \tag{5.41}$$

where in principle $j_{\max} \to \infty$, but in practice it will be taken to be finite. Notice that when integrated against the IR representation of the arcs at tree-level,

$$\kappa \to 0: \quad \int_{-t_{\max}}^{0} \mathrm{d}t\, f(t)\, a_0^{\text{imp}}(t) = b_0\left(g_{2,0}\, t_{\max} + g_{3,1}\frac{t_{\max}^2}{2}\right) - b_1\, g_{3,1}\,\frac{t_{\max}^2}{6}\,, \tag{5.42}$$

only the first two polynomials have support. As the constant and linear terms in t can be expressed entirely in terms of the first two Legendre polynomials, all P_j with $j \geq 2$ integrate to zero on the IR side. Then, in a sense, the $j \geq 2$ polynomials provide all of the null constraints: when integrated against the UV representation of the arcs, the corresponding expression has to vanish. For the improvement of Eq. (5.21), which includes $g_{4,0}$, the same holds true for $j \geq 3$ and so on.

In the presence of gravity, the IR arcs are clearly no longer analytic in $t \in [\,-t_{\max}, 0\,]$, due to the pole. Nevertheless, by modifying the integration measure to

$$\mathrm{d}\mu(t) \equiv (-t/t_{\max})^{\alpha} f(t)\,, \quad \text{with} \quad \alpha > 0\,, \tag{5.43}$$

the arcs become integrable. Continuous functions span the set of integrable functions on an interval. Therefore polynomials, which are themselves a basis of continuous functions, again provide a complete basis. In this work we take $\alpha = 1$, in order to preserve the property that, at tree-level, higher Legendre polynomials integrate to 0 in the IR and provide null constraints. On the other hand, the small j terms have support in the IR leading to,

$$\begin{aligned}\kappa \neq 0: \quad \int_{-t_{\max}}^{0} \mathrm{d}t\ (-t/t_{\max})\, f(t)\, a_0^{\text{imp}}(t) = \ & b_0\left(\kappa^2 + g_{2,0}\,\frac{t_{\max}}{2} + g_{3,1}\,\frac{t_{\max}^2}{3}\right) \\ & - b_1\, t_{\max}\left(\frac{g_{2,0}}{6} + g_{3,1}\,\frac{t_{\max}}{6}\right) + b_2\, g_{3,1}\,\frac{t_{\max}^2}{30}\,.\end{aligned} \tag{5.44}$$

Notice that in this expression the integral with $j = 2$ is non-vanishing, as opposed to the case without gravity of Eq. (5.42).

Now we need to compute the integrals on the UV side, as in Eq. (5.36). We express the smeared Eq. (5.36) as

$$\int_{-t_{\max}}^{0} \mathrm{d}t\ (-t/t_{\max})^{\alpha}\ f(t)\ a_0^{\mathrm{imp}}(t) = \int_{-t_{\max}}^{0} \mathrm{d}t\ (-t/t_{\max})^{\alpha}\ f(t) \left\langle I_\ell(s,t) \right\rangle , \tag{5.45}$$

where we can take $\alpha = 0$ in the absence of gravity, and $\alpha = 1$ otherwise. We then assume convergence and exchange the various orders of integration and sums. It turns out that for all fixed values of k and n for the coefficient $c_{n,k}$, and for each value of ℓ, the integrals in t can be performed analytically.

In summary, the equalities between UV expressions (5.45), and smeared IR arcs (which in the strictly tree-level approximation look like Eq. (5.42), or Eq. (5.44) with gravity) allow one to extract bounds on Wilson coefficients. This means that we can access the information contained in dispersion relations at finite t, through the space of basis functions spanned by the coefficients b_j in Eq. (5.41). In the next section these results will be implemented to find the constraints on various Wilson coefficients.

5.4 Bounds on Wilson coefficients

The finite t dispersion relations obtained in the previous section 5.3 imply bounds on the IR Wilson coefficients deriving from the positivity properties of the average $\langle \cdots \rangle$ of Eq. (5.6). In the forward limit the bounds can be obtained analytically and at all orders by expressing the UV integrals as moments [147]. As for the smeared dispersion relations discussed above, there is no similar formulation, but the problem can be recast as a linear or semi-definite optimisation problem and solved numerically, as proposed in Ref. [185]. We take this numerical approach in what follows.

We have the freedom to choose the parameters b_j of the smearing function $f(t)$ to ensure that the projected UV representation is positive. Assuming convergence, we take the t integral inside the other sums and integrals, where it is computed explicitly. We then demand positivity of the integrand for all values of ℓ, s:

$$\text{UV:}\ \int_{-t_{\max}}^{0} \mathrm{d}\mu(t)\, I_\ell^N(s,t) \geq 0,\ \ \forall\ \mathrm{s} \text{ and } \ell\ \Rightarrow\ \text{IR:}\ \int_{-t_{\max}}^{0} \mathrm{d}\mu(t)\, a_0^{\mathrm{imp},N}(t) \geq 0, \tag{5.46}$$

where we use the notation I_ℓ^N and $a_0^{\mathrm{imp},N}(t)$ to refer to the truncated sum and arc used for numerical applications. Here, $a_0^{\mathrm{imp},N}(t)$ is the truncated, improved arc Eq. (5.19) in the IR representation (as in Eq. (5.20) or Eq. (5.21)).

Therefore, if the positivity of the t integrals of each individual $I_\ell^N(s,t)$ can be ensured, it implies a positivity statement for the IR improved arc. Practically, we truncate various parameters: the maximum order in $t_{\max}$ by which the arc is improved, the maximum order in the partial wave expansion, and the maximum order of the smearing polynomials. This introduces three parameters that are scanned over: N, $\ell_{\max}$, and $j_{\max}$, respectively.

On the other hand, to ensure positivity in s, differently from Ref. [185], we approximate the integrand in s with a polynomial, for every ℓ. Such an approximation follows naturally by expanding in $t_{\max}/\mathrm{s}$ as a Taylor series, because $\mathrm{s}/M^2 > 1$ from the integral range and $t_{\max}/M^2 \ll 1$ from kinematics. For consistency with truncation, we keep terms up to order $2N$ in $t_{\max}$. This approach is advantageous because positive polynomials are more simple to characterise than positive functions: every positive polynomial can be written as a sum of squares of polynomials, which have a straightforward characterisation in terms of semi-definite positive matrices. Furthermore, for every fixed ℓ, it captures all values of s.

5.4.1 Numerical implementation

In the following subsection some technical details of how this procedure is implemented are given. There is a review of Ref. [185] and the differences are highlighted. A first difference w.r.t. Ref. [185] is that we use polynomials in t rather than p, with $t = -p^2$. In terms of building functionals, both approaches are equivalent, we opted for t to preserve the property described below Eq. (5.42). The constraints in impact

parameter space described in Ref. [185] can still be added to our procedure, but we found that they have little impact on the results.

To define a semi-definite optimisation problem we start by writing $f(t)$ as in Eq. (5.41). We can explicitly integrate the single functions both in the UV as in Eq. (5.45), defining the vectors $\vec{W}$ and $\vec{V}$ in the space spanned by the P_j's

$$W_{j,\,\ell}(s') = \int_{-t_{\max}}^{0} \mathrm{d}t \, \left(\frac{t}{t_{\max}}\right) \, P_j\left(\frac{t}{t_{\max}}\right) I_\ell^N(s,t), \tag{5.47}$$

and in the IR

$$V_j = \int_{-t_{\max}}^{0} \mathrm{d}t \, \left(\frac{t}{t_{\max}}\right) \, P_j\left(\frac{t}{t_{\max}}\right) a_0^{\mathrm{imp},N}(t) \tag{5.48}$$

such that the positivity requirement is written as

$$\sum_{j=0}^{j_{\max}} b_j W_{j,\,\ell}(s) \geq 0, \quad \forall\, s,\, \ell, \implies \sum_{j=0}^{j_{\max}} b_j V_i \geq 0. \tag{5.49}$$

Having complete freedom on the choice of $f(t)$ and therefore b_j, we can try to find a function which makes the bound evident.

This is a semi-definite optimisation problem, where we have a target vector V_j and a vector we want to optimise b_j to get $b_j V_j \geq 0$, subject to some constraints $W_{j,\,\ell}(s) \succcurlyeq 0$.

Writing the form of V_j reveals the details of the numerical procedure involved, because the IR arc contains information about g_2, g_3 and g_4 for the 2D bound, depending on which coefficient we want to target. For example,

$$V_j = \int_{-t_{\max}}^{0} \mathrm{d}t \, \left(\frac{t}{t_{\max}}\right) \, P_j\left(\frac{t}{t_{\max}}\right) \left(2g_2 - g_3 t + 8 g_4 t^2\right) . \tag{5.50}$$

We can then ask to optimise the value of g_3/g_2 for a fixed value of g_4/g_2, for example. Furthermore the boundary of the allowed region is found when the inequality is saturated. Therefore we can implement an additional bisection algorithm, where we choose a value of g_4/g_2 and multiple values of g_3/g_2. If the optimisation problem results in a positive value for $b_j V_j$ then the value is allowed, otherwise it is prohibited.

In Figure 5.3 we show how the $g_{3,1}s/g_{2,0}$ bounds behave as functions of the algorithm's parameters $\ell_{\max}$ and $j_{\max}$. For small $\ell_{\max}$ and a large basis of polynomials $j_{\max}$, the bounds might be too strong (non conservative), since not enough conditions have been imposed. For larger values of both parameters, they asymptotically approach the correct values (dashed black lines).

To set up the problem numerically and ensure positivity for every s we performed an expansion in s as described in Sec. 5.4.

In the UV, we can change variables to $x = t/t_{\max}$,

$$W_{j,\,\ell}(s) = t_{\max} \int_{-1}^{0} \mathrm{d}x \; x \; P_j(x) I_\ell^N(s, (x\, t_{\max})). \tag{5.51}$$

Inspecting the function I_ℓ^N reveals that it can be written as an overall dimension $1/s^k$ times a function of the variable $x t_{\max}/s$. Because $t_{\max}/s \ll 1$ and $x \in [-1, 0]$, we can expand with a Taylor series the function in the integral, giving

$$s^k I_\ell^N(s, (x\, t_{\max})) = g\left(\frac{x\, t_{\max}}{s}\right) = \sum_{j=0}^{M} a_j \left(\frac{x\, t_{\max}}{s}\right)^j + \left(\partial_x^{M+1} g\Big|_{t=\zeta}\right) \left(\frac{\zeta\, t_{\max}}{s}\right)^{(M+1)}, \tag{5.52}$$

where the second piece is the rest of the Taylor expansion and gives us an estimate of the error. Therefore, we can expand the whole partially improved arc I_ℓ^N as a polynomial in $t_{\max}/s$, up to a certain order O.

The parameter O is chosen such that $O \approx 2N$, i.e. we require consistency in the size of the terms we omit, since the improvement omits terms of order $t_{\max}^{2N+2}$, and the Taylor expansion omits terms of order $t_{\max}^{O+1}$. For

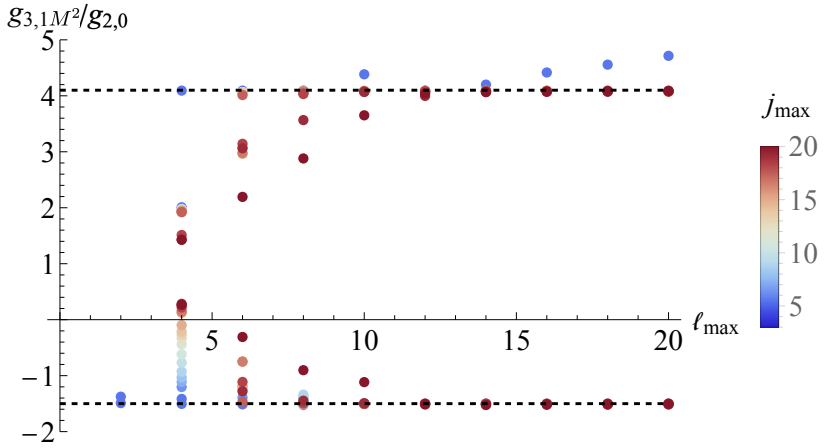

Figure 5.3: *Convergence of the 1D bound for $g_{3,1}s/g_{2,0}$ for various values of $\ell_{\max}$. The colour bar refers to the number of elements of the polynomial basis used, $j_{\max}$. For fixed $\ell_{\max}$, a large enough basis is needed to obtain a better bound. For small $\ell_{\max}$ the bound is not conservative, since too few conditions have been imposed in the UV. For large enough values of both $\ell_{\max}$ and $j_{\max}$, bounds converge to the correct value (dashed black line).*

all our bounds, we consistently discard higher powers of $t_{\max}$ if the leftover terms in the improvement and the Taylor expansion are of order 10^{-9}. Table 5.1 shows some of the various consistent choices we make.

$t_{\max}$	N	O	$(t_{\max}/s)^O$	first discarded term in the improvement
$0.5t_*$	6	12	3×10^{-9}	$2\times10^{-8}g_{14,0}$
$0.8t_*$	8	16	8×10^{-9}	$7\times10^{-8}g_{18,0}$
$0.99t_*$	12	20	5×10^{-9}	$1.6\times10^{-9}g_{26,0}$

Table 5.1: *Consistent parameter choices for the partial improvement and Taylor expansion of the arcs, such that the discarded pieces are of similar order. These are the choices we use throughout.*

This expansion in $t_{\max}/s$ serves two purposes. Firstly it speeds up the numerical calculation because now $W_{j,\ell}$ after the expansion is written as a polynomial in s with a global pre-factor $1/s^{O+1}$ and can be easily integrated analytically. Secondly it allows us to require positivity for a generic polynomial in s, for $s\in[1,\infty]$. Without the expansion we require to optimise a generic function for all values of s and the only way is by taking a discrete grid of values for it. This discretisation not only makes the numerical problem harder but it also weakens the bound, as argued in Ref. [185].

Given that we require positivity for each

$$\sum_{j=0}^{j_{\max}} b_j W_{j,\,\ell}(s)\geq 0 \tag{5.53}$$

we can solve now the equivalent problem expanded in $t_{\max}$

$$s^{O+1}\sum_{j=0}^{j_{\max}} b_j W_{j,\,\ell}(s)\geq 0. \tag{5.54}$$

To obtain the various bounds found in this work we set up the problem as above and we use the numerical optimisation algorithm `sdpb` [430, 431]. We used the constraint as input for multiple values of ℓ, optimising a polynomial in s. We built a matrix with rows made from 1×1 matrices for the discrete values of ℓ, and

a column for each j of the basis chosen for $f(t)$. While setting up the problem we are free to choose a normalisation for the target vector b_j. We choose to always take the following normalisation condition,

$$\sum_{j=0}^{j_{\max}} b_j \int_{-t_{\max}}^{0} \mathrm{d}t \, \left(\frac{t}{t_{\max}}\right) P_j\left(\frac{t}{t_{\max}}\right) \, t = \pm 1, \tag{5.55}$$

which corresponds to the "vector" associated with g_3, giving for example the bound with the + sign in the normalisation,

$$2\left(\sum_{j=0}^{j_{\max}} b_j \int_{-t_{\max}}^{0} \mathrm{d}t \, \left(\frac{t}{t_{\max}}\right) P_j\left(\frac{t}{t_{\max}}\right)\right) + 8\frac{g_4}{g_2}\left(\sum_{j=0}^{j_{\max}} b_j \int_{-t_{\max}}^{0} \mathrm{d}t \, \left(\frac{t}{t_{\max}}\right) P_j\left(\frac{t}{t_{\max}}\right) t^2\right) \geq \frac{g_3}{g_2}, \tag{5.56}$$

or, choosing the other normalisation, a lower bound.

For the bounds with gravity, we find it useful to restrict the parameters b_j to be at most of order 10^6 in absolute value. This facilitates numerical convergence and avoids any fake solutions. We implement this in `sdpb` by adding rows and columns to the positive matrix for each j, forcing $\pm b_j \geq -10^6$. We include typical values used in the Table 5.2. The algorithm for `sdpb` taken from Ref. [430, 431] is set up with the default parameters except the maximum number of iterations that has been increased for the case with gravity from 500 to 1000.

	Fig. 5.4	Fig. 5.5	Fig. 5.7
$j_{\max}$	7	10	4, 6, 8
$\ell_{\max}$	14	100	400
N	3, 8	6	6, 8, 12

Table 5.2: Values of the parameters of the improvement algorithm for all the plots in this article.] Refer to Table 5.1 for the choices of N, O, and $t_{\max}$.

Now that the numerical procedure has been fleshed out, we can move onto the bounds that can be found.

5.4.2 Bounds at $\kappa = 0$

In Section 5.3.5, we pointed out that our partial improvement algorithm has a finite radius of convergence, which requires smearing over $-t_* < t \leq 0$, see Eq. (5.40). In order to compare with previous literature, in this section we present results using both our approach and the one of Ref. [185], for different smearing windows $-t_{\max} \leq t \leq 0$.

We first work in the $\kappa \to 0$ limit and $d = 6$ for easier comparison with the next section. Bounds in $d = 4$ share the same qualitative features, although the numerical values for the lower bound vary slightly.

In Fig. 5.4 we show upper and lower bounds on the ratio $g_{3,1}/g_{2,0}$ in units of the arc energy scale M^2, for different values of $t_{\max}$, fixing the parameters $j_{\max} = 7$, $\ell_{\max} = 14$ used in the bound derivation. The blue line is obtained using the algorithm of Ref. [185], but expanded in the UV side in powers of $t_{\max}/M^2$ (hence the plot ranging only to $t_{\max} = 0.7\, M^2$). In purple/orange, instead, our approach for $N = 3, 8$ respectively, limited to $t_{\max} < t_*$ (dashed black line). As discussed previously, these correspond to neglecting terms of order $O(t_{\max}^7)$ and $O(t_{\max}^{17})$.

From Fig. 5.4 we conclude that our algorithm correctly reproduces the 1-dimensional bounds without gravity, despite the limit on the smearing range $t_{\max} < t_*$. Furthermore, we notice that it rapidly converges with N. In particular, for $N = 8$ the obtained bounds are indistinguishable from the exact results. Finally, for fixed $j_{\max}, \ell_{\max}$, the bounds become unreliable as $t_{\max} \to 0$.

In Figure 5.5 we present a similar analysis, extended to bounds on the ratio of coefficients $g_{3,1}M^2/g_{2,0}$ and $g_{4,0}M^4/g_{2,0}$, using $\ell_{\max} = 100$, $j_{\max} = 10$.

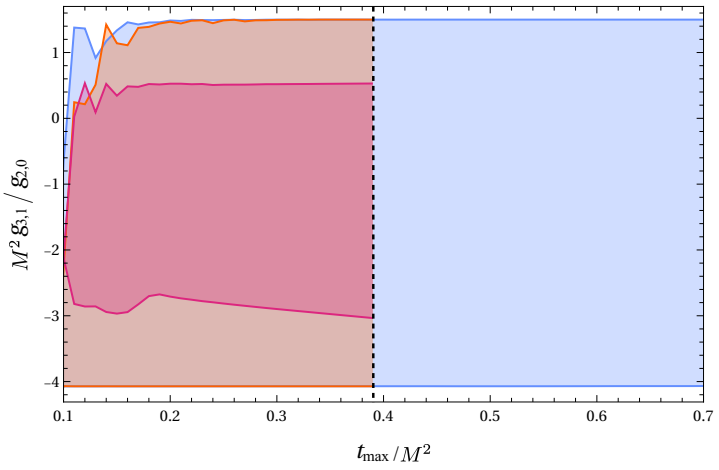

Figure 5.4: Bounds on the ratio $g_{3,1}M^2/g_{2,0}$ as a function of $t_{\rm max}$, the maximum value of t in the smearing integral. All curves are derived with fixed $j_{\rm max} = 7$, $\ell_{\rm max} = 14$. In blue the improvement approach of Ref. [185] where positivity is obtained expanding the integrand at order $O(t_{\rm max}^{16})$. In purple (orange), our improvement at order $N = 3$ ($N = 8$). The dashed vertical line delimits the applicability of our improvement formula, $t_{\rm max} \leq t_*$. As N is increased, the algorithm at finite t of Section 5.3 rapidly converges to the value of Ref. [185].

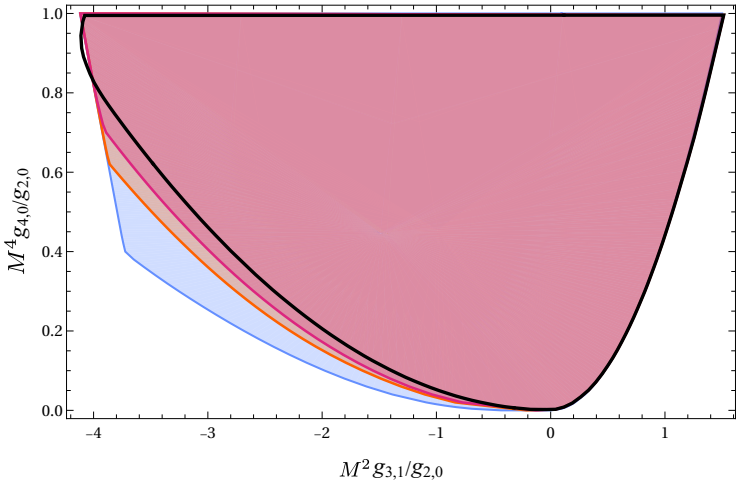

Figure 5.5: *Positivity bounds on the ratio of coefficients $g_{4,0}/g_{2,0}$ and $g_{3,1}/g_{2,0}$ in units of M^2, for $d = 6$, using $\ell_{max} = 100$ and $j_{max} = 10$. In blue the bounds using our partial improvement Eq. (5.36) with $N = 6$ and $t_{max} = t_*/2 \approx 0.2M^2$. The approach of Ref. [185] is shown for comparison in black for $t_{max} = M^2$, in red for $t_{max} = 0.8\, M^2$ and orange for $t_{max} = 0.5\, M^2$.*

First, we explore how changing the lower bound of integration Eq. (5.15) affects the bounds in the approach of Ref. [185]. The black line, the orange and the red areas are smeared over $-t_{\rm max} < t \leq 0$ with $t_{\rm max} = M^2$ in black, $t_{\rm max} = 0.5M^2$ in orange, and $t_{\rm max} = 0.8M^2$ in purple. For $t_{\rm max} = M^2$ the figure coincides with the forward limit bounds [150, 432]. We observe that constraints corresponding to the algorithm of Ref. [185] become weaker as we take smaller values of $t_{\rm max}$.

The blue area shows instead our approach, with the smearing range $t_{\rm max} = 0.2M^2$. Our partial improve-

ment goes up to order $N = 6$, meaning we neglect terms of order $O(t_{\rm max}^{12})$ in the improvement, which, given the value of t_*, are of order $10^{-8} \times g_{2n,q} M^{4n}$. We checked that the results are stable for larger values of N, meaning that the truncated algorithm has converged.

In Figure 5.5, for both algorithms, we observe a feature that develops as soon as $t_{\rm max} < M^2$: a kink in the lower bound. The fact that for large values of $g_{4,0}M^4/g_{2,0}$ the $t_{\rm max} < M^2$ bounds are slightly more stringent than the $t_{\rm max} = M^2$ ones, makes us think that this feature is some numerical artifact. Were this not the case, one would expect that even for $t_{\rm max} = M^2$ the test polynomials would arrange to (almost) vanish at large $|t|$, to obtain a more stringent result. On the other hand, we have tried several approaches to improve the bounds in this region. We have explored values as large as $\ell_{\rm max} = 600$ and introduced the $\ell \to \infty$ constraints discussed in Ref. [185]. Moreover, we have produced the red curve by employing two different methods. In the first we have followed exactly the procedure detailed in Ref. [185], where positivity of Eq. (5.46) is ensured by discretising s and requiring that the integrand be positive at each discrete value. In the second we have used the expansion of the integrand in $t_{\rm max}$, and its polynomial approximation in s, as described above. Despite having explored various approaches and increased numerical precision, the kink on the left hand side of Figure 5.5 survives. Regardless of this feature, the results of our algorithm are qualitatively consistent with those obtained from the approach of [185].

5.4.3 Bounds at $\kappa \neq 0$

In this section we work in the presence of gravity, at $\kappa \neq 0$, and in $d = 5, 6$ dimensions, where the partial wave expansion converges and the $2 \to 2$ amplitude is well defined w.r.t. soft graviton emission.

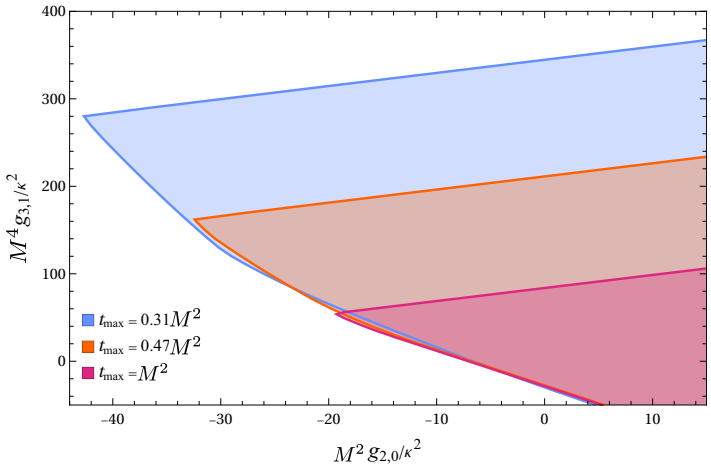

Figure 5.6: *Bounds in the presence of gravity on the ratios $g_{2,0}M^2/\kappa^2$ and $g_{3,1}M^4/\kappa^2$, in $d = 6$, for different values of $t_{\rm max}$. All bounds in this figure are derived using the improvement of Ref. [185]. The blue (orange) line uses $j_{max} = 6$ (9), and is expanded up to order 16 (25) in t_{max}.*

In Figures 5.6 and 5.7 we show the bounds on the coefficients $g_{2,0}$ and $g_{3,1}$ in units of the gravitational coupling κ^2 and the arc energy scale M^2. Both figures are derived in $d = 6$ dimensions and use $\ell_{\rm max} = 400$, and up to $j_{\rm max} = 9$. Figure 5.6 uses the method of Ref. [185], but for different values of $t_{\rm max}$. Figure 5.7 uses our method Eq. (5.45), where the smearing polynomials involve the overall $(-t)^\alpha$ factor, with $\alpha = 1$, in order to make the EFT amplitudes integrable.

In Figure 5.8, we show the t dependence of the functionals $f(t)$ that optimize our bounds, for different extremal points, defined by the colours in the top left-hand corner plot. Gravity plays the most important role for small values of the couplings. Interestingly, the functionals exhibit a distinctive peak at finite values of t, far from the maximum allowed value $t_{\rm max}$, while staying away from $t = 0$ to avoid the gravity pole. The existence of a scale associated with this feature provides an explanation of why the bounds become weaker

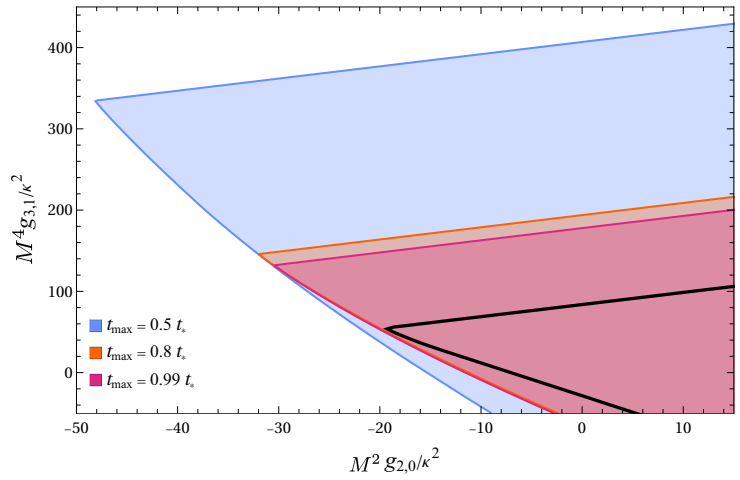

Figure 5.7: *Same as Figure 5.6, but using our improvement formula Eq. (5.36) up to order $N = 12$ (refer to Table 5.1 and 5.2 for the exact choices of parameters we make). All the bounds are computed with $\ell_{max} = 400$, and up to j_{max}=8. Here $t_{\max}$ is expressed in units of the maximum allowed smearing range $t_* \approx 0.39M^2$. For reference, in black we show the bounds from Ref. [185].*

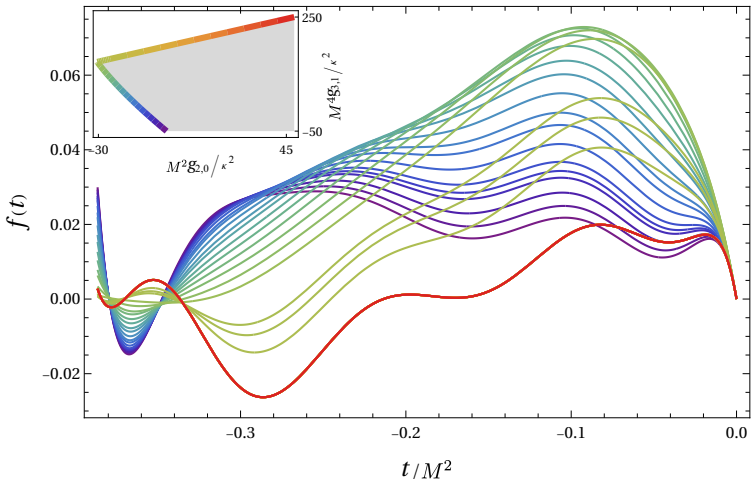

Figure 5.8: In the top left-hand corner, the $d = 6$ bound of Figure 5.7 for $t_{\max} = 0.99t_*$, with each extremal point colour-coded. In the main figure, for each extremal point, the corresponding smearing functions $f(t)$ as a function of t. The functions are normalised as $\sum_{j=0}^{j_{\max}} b_j = 1$. Here, we use $j_{\max} = 8$.

as the smearing range to $t_{\max} < s$ is reduced. For larger values of the couplings, the functionals morph into oscillatory functions, which are less impacted by the $t_{\max}$ cut. Indeed the asymptotic upper and lower slopes $g_{3,1}/g_{2,0}$ are almost insensitive to $t_{\max}$, as already observed in Figure 5.4.

It seems as though our bounds are less stringent than those of [185], they are in a sense more robust as they will be stable against the introduction of IR loop effects. Moreover, as discussed above, they are penalised by the $t_{\max} < M^2$ constraint. It is plausible that a variation of our algorithm exists that possesses a larger radius of convergence, and which re-sums to all orders. An example of such a method are the crossing symmetric dispersion relations that will be introduced in the following chapter.

Chapter 6

Positivity Bounds and Gravity Loops

6.1 Chapter overview

Most efforts to map the allowed parameter space of EFTs have assumed a *tree-level* framework, where the amplitude's non-analytic features arise solely from high-energy exchanges above the EFT cutoff. This approach neglects calculable non-analyticities within the EFT. In this chapter, we systematically examine the infrared structure of EFT amplitudes at one-loop order, focusing on $2 \to 2$ scattering of massless scalar particles interacting via gravity in various spacetime dimensions. Now that we have seen how to self-consistently find positivity bounds, for theories which have a divergent forward limit, it is time to check that the procedures are robust against loop effects as claimed. A simple argument is provided to show that at sufficiently low energies the loop effects must dominate over the less relevant operators. This must impact the positivity bounds. We find that in scalar-gravity systems, the dominant gravitational IR effects scale as $\kappa^4 s^3\sqrt{-t}$ or $\kappa^4 s^3 \log(-t)$ in $d = 5, 6$, where the calculation is particularly well defined. In this chapter we compute the scattering amplitude of shift symmetric scalars to one-loop, including EFT-vertices and the exchange of internal gravitons in section 6.2. This is done by using on-shell methods. We then compute the arc variables used in the previous chapter and introduce another kind of dispersion relation called a crossing symmetric dispersion relation in section 6.3. We find the modified bounds on the couplings using both types of dispersion relation and comment on the differences that we find in section 6.4.

6.2 The Structure of EFT Amplitudes

6.2.1 Tree-Level

We remain focused on the $2 \to 2$ scattering amplitude for exact (massless) Goldstone bosons in generic d-dimensions in a theory with a mass-gap M, such that at sufficiently small energy $E \ll M$ the theory is weakly coupled and well described by an effective Lagrangian with interactions organised in a derivative expansion. We insist on the Goldstone nature of the spin-0 particles to naturally justify their lack of mass that we assume throughout. At tree-level, the $2 \to 2$ amplitude can be written as $\mathcal{M}_{\text{tree}} = \mathcal{M}^{\text{EFT}}_{\text{tree}} + \mathcal{M}^{\text{grav}}_{\text{tree}}$ with one part associated with contact interactions,

$$\mathcal{M}^{\text{EFT}}_{\text{tree}} = \sum_{n\geq 2, q\geq 0} g_{n,q} \left(\frac{s^2+t^2+u^2}{2}\right)^{\frac{n-3q}{2}} \cdot (stu)^q \tag{6.1}$$

and one mediated by gravity,

$$\mathcal{M}^{\text{grav}}_{\text{tree}} = \kappa^2 \left(\frac{tu}{s} + \frac{us}{t} + \frac{st}{u}\right), \quad \text{where } \kappa^2 \equiv \frac{1}{M_{Pl}^{d-2}} \tag{6.2}$$

denotes the gravitational constant in d-dimensions, and M_{Pl} the Planck scale.[1]

It is illustrative to keep track of the size of the various terms in situations where the EFT is dominated by a single scale M and a dimensionless coupling g, such that,

$$g_{n,m} \sim \frac{g^2}{M^{2n+d-4}} \,. \tag{6.3}$$

This relation holds in simply weakly coupled UV models, but also captures important features at strong coupling [433]. This expression helps to separately keep track of the EFT energy expansion controlled by $E/M \ll 1$ and the EFT loop expansion, controlled by $g^2/(4\pi)^{d/2} \ll 1$. For gravity instead it's roughly controlled by $\kappa^4 M^{2d-4}/(4\pi)^{d/2}$.

Gravity is always more relevant than all other EFT interactions and dominates at sufficiently small energies. Moreover, even loops of gravity can dominate over certain EFT interactions. This was alluded to in the previous chapter and can be quantified as follows. Comparing the contributions to the amplitude, we see that an irrelevant EFT operators with $n \geq d/2$ contributes less to the amplitude than a one-loop diagram from gravity, at energies

$$\frac{E}{M} \lesssim \frac{E_*}{M} \equiv \left[((4\pi)^{d/2}\, g)^{-2} \left(\frac{M}{M_{Pl}}\right)^{2(d-2)} \right]^{\frac{1}{2n-d}} \,. \tag{6.4}$$

Therefore the tree-level EFT is a good approximation only within a window at sufficiently high energy where gravity loops are negligible, but with energies sufficiently small that the EFT description holds, $E_*/M \ll E/M \ll 1$. For larger n, this window shrinks and disappears, meaning that for statements on $n \gg d/2$ couplings, loops are always important. Furthermore dispersion relations, by construction, are sensitive to the amplitude at all energies, in particular also in the region of Eq. (6.4), where loops dominate. In the rest of this section we compute these effects more precisely and study how they appear in dispersion relations.

6.2.2 IR Effects

We are interested in how higher order effects modify the structure of Eq. (6.1) by altering the analytic structure in both s and t, as well as how this impacts dispersion relations. The inclusion of long-range interactions has different consequences in the study of scattering amplitudes [434–436]. First of all, it is well known that IR divergences in diagrams with a fixed number of external legs cancel against divergences in the real IR radiation, when appearing in the total (inclusive) cross section. The contribution to the total cross-section from the real emission of gravitons diverges in $d \leq 4$ due to collinear/soft effects, which also implies that the amplitude is not well-defined for any exclusive process (e.g. $2 \to 2$ scattering). To make this more concrete, we study the case of $d > 4$, where the problem is absent and the phase-space integral of collinear radiation is finite. We will discuss the case $d = 4$ separately in sec. 6.2.4. Technically, the study of $d > 4$ in the context of gravity is made possible by the convergence of the partial wave expansion, which diagonalises the unitary property of the S-matrix. Its coefficients are given by the integrals,

$$f_\ell(s) = \mathcal{N}_d \int_{-s}^{0} \frac{dt}{s} \left(4\,tu/s^2\right)^{(d-4)/2} \mathcal{P}_\ell\left(1+2t/s\right) \mathcal{M}(s,t)\,, \qquad \text{with} \quad \mathcal{N}_d = \frac{(16\pi)^{\frac{2-d}{2}}}{\Gamma\left(\frac{d-2}{2}\right)}\,, \tag{6.5}$$

where $\mathcal{P}_\ell(x) = {}_2F_1\left(-\ell, \ell+d-3, (d-2)/2, (1-x)/2\right)$ are Gegenbauer polynomials, and $u = -s-t$. This allows us to write the amplitude in the partial wave expansion as,

$$\mathcal{M}(s,t) = \sum_{\ell=0}^{\infty} n_\ell^{(d)}\, \mathcal{P}_\ell\left(1+\frac{2t}{s}\right) f_\ell(s)\,, \quad \text{where} \quad n_\ell^{(d)} = \frac{(4\pi)^{\frac{d}{2}}(d+2\ell-3)\Gamma(d+\ell-3)}{\pi\,\Gamma\left(\frac{d-2}{2}\right)\Gamma(\ell+1)}\,, \tag{6.6}$$

[1] A constant term in the amplitude Eq. (6.1) and a pole associated with the scalar exchange are forbidden by the Goldstone-Boson shift-symmetry.

and ℓ runs over even integers for identical scalars.

For gravity in $d = 4$ this expansion does not converge due to the pole of the amplitude $\sim 1/t$. In $d \geq 5$ it converges, but only as a distribution [216, 437] appearing within integrals over given measures. In other words, the amplitude and the dispersion relations that follow will have to be *smeared* with weight-functions in t as in the previous chapter, rather than being thought of as functions of t.

After the above IR ambiguities have been addressed, massless particles still leave their imprint via finite computable loop effects. These are physical predictions of the theory, they also exist in $d > 4$ and would plausibly survive in an IR safe definition of the S-matrix. We are interested in the ones that modify the analytic structure of the amplitude as $s, t \to 0$, since these have an impact on how dispersion relations can be used. We refer to these generically as *IR effects*, and we seek to identify the most relevant ones.

6.2.3 Finite IR Effects in the theory of a scalar and gravity

For our purpose, the most important IR effects arise at 1-loop, because they represent the first qualitative modification of the amplitude analytic structure compared to at tree-level. As discussed above 1-loop effects can in principle be relatively large in certain circumstances, without necessarily implying a breakdown of the perturbative expansion. Indeed, higher loops introduce more powers of energy and soften the $s, t \to 0$ behaviour, thus playing less of an important role in the context of positivity bounds. In this section we compute these 1-loop effects. Although parts of these already appear in the literature, we present a systematic study in general d and including EFT couplings. We work in dimensional regularisation $d = D - 2\epsilon$ for integer D, which is recovered by assuming that all couplings are defined in integer dimensions.

The 1-loop contribution to the amplitude can be divided into three pieces,

$$\mathcal{M}_{\text{1-loop}} = \mathcal{M}^{\text{EFT-EFT}}_{\text{1-loop}} + \mathcal{M}^{\text{grav-EFT}}_{\text{1-loop}} + \mathcal{M}^{\text{grav-grav}}_{\text{1-loop}}, \tag{6.7}$$

where the subscripts denote the power counting both in terms of gravitational and EFT couplings. Each piece can be projected onto a basis of scalar one-loop integrals [438, 439]. As we are looking at the $2 \to 2$ amplitude, they are limited to bubble, triangle and box integrals. Because all states are massless the contribution from all triangle integrals can themselves be projected onto bubble integrals using integration by parts (IBP) identities [440–442]. This leaves,

$$\mathcal{M}_{\text{1-loop}} = \sum_{i=\bigcirc,\square} c_i \, \mathcal{I}_i \, . \tag{6.8}$$

where the c_i are rational functions of the kinematic variables and,

$$\mathcal{I}_{\bigcirc}(t) = \mu^{2\epsilon} \int \frac{d^d l}{(2\pi)^d} \frac{1}{l^2} \frac{1}{(l + p_1 + p_3)^2} = \frac{\mathrm{i}\, \mu^{2\epsilon}\, \Gamma\left(2 - \frac{d}{2}\right) \Gamma\left(\frac{d}{2} - 1\right)^2}{(4\pi)^2\, \Gamma(d-2)} \left(-\frac{t}{4\pi}\right)^{d/2-2}, \tag{6.9}$$

$$\begin{aligned} \mathcal{I}_{\square}(s,t) &= \mu^{2\epsilon} \int \frac{d^d l}{(2\pi)^d} \frac{1}{l^2} \frac{1}{(l+p_1)^2} \frac{1}{(l+p_1+p_3)^2} \frac{1}{(l-p_2)^2} = -\frac{\mathrm{i}\, \mu^{2\epsilon}\, \Gamma\left(2-\frac{d}{2}\right) \Gamma\left(\frac{d}{2}-2\right)^2}{(4\pi)^2\, st\, \Gamma(d-4)} \\ &\quad \times \left[\left(-\frac{s}{4\pi\mu^2}\right)^{\frac{d}{2}-2} {}_2F_1\left(1, \frac{d}{2}-2, \frac{d}{2}-1, 1+\frac{s}{t}\right) + (s \leftrightarrow t) \right]. \end{aligned} \tag{6.10}$$

These expression are most often found in the literature having applied dimensional regularisation in the $d = 4$ case [443, 444], or in generic dimension d [445]. The hypergeometric function in Eq. (6.10) will play an important role for us because of its analytic structure; explicitly,

$${}_2F_1\left(1, \frac{d}{2}-2, \frac{d}{2}-1, 1+\frac{s}{t}\right) = \begin{cases} 1 & d = 4 \\ \frac{\tanh^{-1}\left(\sqrt{1+s/t}\right)}{\sqrt{1+s/t}} & d = 5 \\ -\frac{\log(-s/t)}{1+s/t} & d = 6 \end{cases} . \tag{6.11}$$

To determine the factors c_i in Eq. (6.8) we use reverse unitarity [446–449]. Unitarity dictates that the 1-loop integrand discontinuity is given by the product of two tree-level amplitudes and by projecting said discontinuity onto that of the above 1-loop scalar integrals in Eq. (6.9) and Eq. (6.10), we can then extract $\mathcal{M}_{\text{1-loop}}$. In any specific number of dimensions, this type of procedure determines the 1-loop amplitude only up to possible rational terms that do not have the above-mentioned singularities. However, since we consider general d-dimensional integrands, these rational terms are also uniquely determined; they contribute to non-analytic behaviour in other dimensions and are therefore picked up by our procedure [450]. IBP identities are applied with the help of the 'LiteRed' package [451, 452].

The 1-loop amplitude is then reduced to a weighted sum of box and bubble diagrams of the form,

$$\begin{aligned} \mathrm{i}\mathcal{M}_{1-\text{loop}} = & f_1(s,t)\,\mathcal{I}_{\square}(s,t) + f_2(u,s)\,\mathcal{I}_{\square}(u,s) + f_3(t,u)\,\mathcal{I}_{\square}(t,u) \\ & + g_1(u,s)\,\mathcal{I}_{\bigcirc}(t) + g_2(s,t)\,\mathcal{I}_{\bigcirc}(u) + g_3(t,u)\,\mathcal{I}_{\bigcirc}(s)\,, \end{aligned} \tag{6.12}$$

where f_i and g_i are functions of d and of the external momenta. They are in principle independent of one another. However, since the particles scattered are identical scalars, we can use crossing symmetry to see that the functions in Eq. (6.12) are related by,

$$\begin{aligned} f_1(x,y) = f_2(x,y) = f_3(x,y) \equiv f_d(x,y)\,, \\ g_1(x,y) = g_2(x,y) = g_3(x,y) \equiv g_d(x,y)\,, \end{aligned} \tag{6.13}$$

and are reduced to two independent functions f_d, g_d. This also implies that it is sufficient to match the discontinuities of an individual cut, which we choose to be the t-channel cut, as illustrated in Fig. 6.1. The discontinuities in the other channels will then be reproduced by the identities Eq. (6.13). As shown in the figure, there are two contributions to this cut, one obtained by cutting internal scalar legs and another by cutting internal graviton legs.

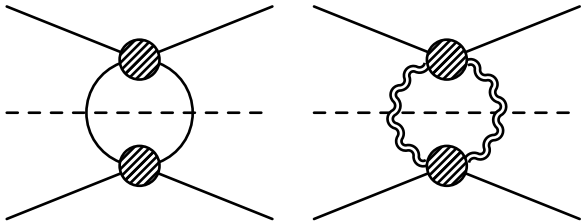

Figure 6.1: *Non-trivial cuts used for the matching in Eq. (6.8). LEFT: cuts for* 1*-loop diagrams with scalar propagators in the 't-channel'. RIGHT: cuts for* 1*-loop diagrams with gravitons. The grey blobs denote all possible tree-level interactions associated with either graviton exchange or insertion of an EFT* 4*-point interaction.*

EFT interactions

First we focus on the interactions without gravity, $\mathcal{M}_{\text{1-loop}}^{\text{EFT-EFT}}$. The tree-level EFT has only 4-point contact interactions Eq. (6.1). Because of this it is clear that at 1-loop level, there can only be a projection onto scalar bubble integrals, implying $f_d = 0$. At small enough energies, the leading effects within the EFT should come from the couplings $g_{n,m}$'s in Eq. (6.1) that are labelled by the smallest integers, and dominated by the term $\propto g_{2,0}^2$, followed by less relevant terms from the mixing of $g_{2,0}$ and other Wilson coefficients.

Performing the t-channel cut on the scalar legs and counting the powers of Wilson coefficients allows us to isolate some of the contributions; the others will be reproduced via crossing symmetry. Loops involving arbitrary EFT coefficients share a common, dimension dependent factor, which stems from the scalar bubble integral $\mathcal{I}_{\bigcirc}(t)$. The most relevant contributions are written as,

$$\mathrm{i}\mathcal{M}_{\text{1-loop}}^{\text{EFT-EFT}} = \frac{t^2}{2^4\,(d^2-1)}\mathcal{I}_{\bigcirc}(t)\left[g_{2,0}^2\left(4su - \frac{3}{2}d\,(3d+2)t^2\right)\right. \tag{6.14}$$

$$+g_{2,0}\,g_{3,1}\,t\left(((2-3d)d+8)t^2-8su\right)+g_{3,1}^2\,\frac{t^2}{2}\left(8su-(d-2)dt^2\right)$$
$$-g_{2,0}\,g_{4,0}\,\frac{3t^2\left(\left(9d\,(d+2)^2+32\right)t^2-16(d+4)su\right)}{4(d+3)}+\cdots\Bigg]+(t\leftrightarrow s,u)\,.$$

This matches Ref. [425] in the $d\to 4$ limit. Polynomial pieces in Eq. (6.14) are resorbed into the definitions of the renormalised EFT coefficients. Higher order terms, denoted by dots in Eq. (6.14), become less and less relevant but are systematically calculable.

For $\mathcal{M}_{\text{1-loop}}^{\text{EFT-EFT}}$, the function $\mathcal{I}_{\bigcirc}(t)$, and its crossed counterparts $\mathcal{I}_{\bigcirc}(s),\mathcal{I}_{\bigcirc}(u)$, are responsible for the amplitude's non-analyticities. These are associated entirely to the factor $(-t)^{d/2}$ in Eq. (6.9), multiplied by a polynomial in the crossing symmetric combinations su,t^2, and similarly for the other channels. In even dimensions these will lead to logarithmic discontinuities, while in odd dimensions to square-root ones.

Mixed EFT-Gravity Interactions

Loops involving both gravity and EFT interactions, also have the property that they project onto scalar bubble integrals only; because of this, they have a structure similar to EFT-EFT effects. The most relevant pieces are,

$$\begin{aligned}\mathrm{i}\mathcal{M}_{\text{1-loop}}^{\text{grav-EFT}} \;=\; & \kappa^2\frac{t^2}{2^4\,(d^2-1)}\mathcal{I}_{\bigcirc}(t)\Bigg[g_{2,0}\,\frac{6\left((d-2)\left(9(d-2)d^2+32\right)t^2-8(d(5d+2)-8)su\right)}{(d-4)(d-2)t}\\
&+g_{3,1}\,6\left(\frac{8(d(5d+2)-8)su}{(d-4)(d-2)}+d\,(3d+2)t^2\right)\\
&+g_{4,0}\Bigg[\frac{3\left((d-2)d(3d+4)\left(9d^3-36d+128\right)t^4+2048(d+1)(d+3)s^2u^2\right)}{2(d-4)(d-2)d(d+3)t}\\
&\quad+\frac{3\left(-16d(d(3d(5d+22)+64)-32)st^2u\right)}{2(d-4)(d-2)d(d+3)t}\Bigg]+\cdots\Bigg]+(t\leftrightarrow s,u)\end{aligned}\tag{6.15}$$

The analytic structure of these effects is similar to that of EFT-EFT diagrams discussed above. Notice that in $d>2$ dimensions, the apparent $1/t$ pole in the first line is cancelled by positive powers of t in $\mathcal{I}_{\bigcirc}(t)$. At low enough energy, these effects dominate over the ones in the previous paragraph, since gravity is a more relevant interaction.

Gravity Only

The largest loop effects in the IR are associated with diagrams involving only gravitational interactions. An example of such diagrams is shown in Fig. 6.2, which contributes to the cut represented in Fig. 6.1.

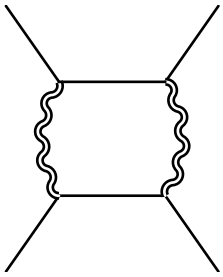

Figure 6.2: *One of many diagrams contributing to the* 1*-loop amplitude at order* κ^4.

To compute the effects from diagrams of this class using reverse unitarity, we must cut the internal graviton legs in the t-channel and sum over the different graviton polarisations. For this we need the tree-level scattering amplitude of spin-0 particles and gravitons in generic dimension d [453]. This can be compactly written as,

$$\mathcal{M}_{\phi h\to\phi h} = \frac{\kappa^2}{stu}\left[2s\,(\epsilon_1\cdot p_4)\,(\epsilon_3\cdot p_2) + 2u\,(\epsilon_1\cdot p_2)\,(\epsilon_3\cdot p_4) + su\,(\epsilon_1\cdot\epsilon_3)\right]^2, \tag{6.16}$$

which in $d=4$ can be recast in spinor-helicity language, simplifying to

$$\mathcal{M}_{\phi h\to\phi h}\Big|_{d=4} = \frac{\kappa^2}{stu}\,[1|2|3\rangle^4. \tag{6.17}$$

The sum over graviton helicities is given by the full momentum-dependent graviton propagator, suitable to be employed with this tree-level amplitude [454]:

$$\sum_\lambda \epsilon^{\mu\nu}_\lambda(\ell)\epsilon^{\rho\sigma}_\lambda(-\ell) = \frac{1}{2}\left(P^{\mu\rho}P^{\nu\sigma} + P^{\mu\sigma}P^{\nu\rho} - \frac{2}{d-2}P^{\mu\nu}P^{\rho\sigma}\right), \tag{6.18}$$

where,

$$P^{\mu\nu} = \eta^{\mu\nu} - \frac{\ell^\mu q^\nu + \ell^\nu q^\mu}{\ell\cdot q}, \tag{6.19}$$

and q is a reference momentum.

Repeating the matching procedure for the one-loop gravity corrections allows us to write $\mathcal{M}^{\text{grav-grav}}_{1-\text{loop}}$ in the form of Eq. (6.12) with,

$$f_d\,(x,y) \equiv \kappa^4(x^4+y^4)\,, \qquad g_d\,(x,y) \equiv \kappa^4\left(x^2+y^2\right)r_1\,(d) + \kappa^4\,x\,y\,r_2\,(d)\,. \tag{6.20}$$

The dimension specific rational functions are themselves given by,

$$\begin{aligned} r_1\,(d) &\equiv \frac{d^6-11d^5-562d^4+2820d^3-2792d^2-2848d+3584}{64\,(d-4)\,(d-2)\,(d^2-1)}, \\ r_2\,(d) &\equiv \frac{d^6-27d^5+74d^4-232d^3+648d^2+496d-576}{32(d-4)(d-2)(d^2-1)}. \end{aligned} \tag{6.21}$$

Contrary to loops involving EFT interactions, here we inherit the non-analyticities of the box integral $\mathcal{I}_\square$. The hypergeometric function ${}_2F_1\left(1,\frac{d}{2}-2,\frac{d}{2}-1;1+z\right)$, with $z=s/t$ in the box integral Eq. (6.10) has a branch cut which extends from $z=0$ to real infinity, see Eq. (6.11), but is otherwise analytic everywhere. Therefore, at fixed-t, the amplitude contains a branch cut on the real axis. As we will review in section 6.3, the coefficient of such a discontinuity enters dispersion relations with an *arbitrary number of subtractions*, when the contour of integration is taken across the $\mathcal{I}\text{m}\,[s]=0$ axis. In turn, this coefficient has $t\to 0$ singularities. We find that the most singular such pieces are[2],

$$\text{Disc}\left[\text{i}\mathcal{M}^{\text{grav-grav}}_{1-\text{loop}}\right] \underset{t\ll s}{\sim} \kappa^4\,(-t)^{\frac{d-6}{2}}\,s^3\begin{cases}\log(-t) & d \text{ is even},\\ 1 & d \text{ is odd}\end{cases} \tag{6.22}$$

where we have regulated the integrals using the dimensional regularisation in the $\overline{\text{MS}}$ scheme, which we employ throughout. This is an important result that reveals how beyond-tree-level dispersion relations can be employed. In particular it shows that in dimensions $d\leq 6$ all dispersion relations diverge in the forward limit, while in $d\leq 8$ the dispersion relations' first derivative in t will diverge.

Lastly, from the non-analyticities of the one-loop amplitudes reported above, we can easily extract the running of the Wilson coefficients. In particular, we observe that $g_{4,0}$ runs for $d\leq 8$, $g_{3,1}$ for $d\leq 6$ and $g_{2,0}$ for $d\leq 4$, as expected by naive dimensional analysis arguments [459].

[2] In the Regge limit $\frac{t}{s}\ll 1$, this leading contribution arises from the box diagram, and is consistent with the first iteration of the tree-level graviton exchange relevant in the eikonal approximation, see e.g. [455–458].

6.2.4 4 dimensions

As mentioned above, S-matrix elements in $d = 4$ are affected by IR divergences when massless particles are considered. After regularisation, these divergences can be cancelled by considering inclusive observables or different notions of asymptotic states, see e.g. [460–463], or resummed when the IR cutoff has a physical meaning, in the case of IR sensitive observables, see e.g. [464–466].

In this section, we compute the $d = 4$ IR divergences that appear for generic kinematic configurations and we compare them with the $t \to 0$ singularities of Eq. (6.22). This comparison makes it clear that the $t \to 0$ singularities affecting the dispersion relations are not captured by kinematic-independent IR divergences that might be resorbed by redefinition of the asymptotic states. Rather, the contributions in Eq. (6.22) are the result of the dynamical properties of gravitational scattering in $t = 0$.

To see this we can explicitly compute the kinematic-independent one-loop IR divergences of a scattering amplitude in the presence of gravity. In dimensional regularisation, $d = 4 - 2\epsilon$, the IR divergences take the form of poles around $\epsilon = 0$ whose residues are non-polynomial functions of the Mandelstam invariants. At 1-loop, these divergences will be of two kinds. The first kind of kinematic-independent divergences are those corresponding to massless bubble loops on external legs, contributing to the so-called collinear anomalous dimension. Since the on-shell computation of the 1-loop amplitude uses connected tree-level amplitudes as building blocks (see for example Sec. 6.2.3), the result of Eq. (6.22) is not affected by these bubble loops on the external legs. The second kind of kinematic-independent IR divergences are those corresponding to the exchange of one soft particle between two external legs, contributing to the Sudakov double logs and to the so-called cusp anomalous dimension, see e.g. [467–470]. Indeed, aside from bubble loops on the on-shell legs, kinematic-independent IR divergences can only arise when three consecutive propagators are on-shell. In this case the loop will be of the form:

$$\frac{d^4p}{p^2(k_1+p)^2(k_2-p)^2} \sim \frac{d^4p}{p^2\, p\cdot k_1\, p\cdot k_2}\,, \tag{6.23}$$

which gives a divergent integral when $p^2 = k_1^2 = k_2^2 = 0$, regardless of the direction of k_1 and k_2. The only case in which the three legs are on-shell regardless of the kinematics will be when the loop arises from the exchange of a soft particle between two external legs. Therefore, we only have to compare the $t \to 0$ singularity of Eq. (6.22) to the contributions from exchanges of soft particles between external legs of a tree-level amplitude.

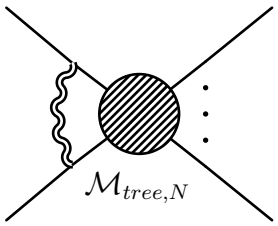

Figure 6.3: *Example of one-loop diagram contributing to the cusp anomalous dimension in an N-point scattering amplitude. The graviton internal line is taken to have soft momentum. External particles are taken to be on-shell.*

In the case of scattering of shift-symmetric scalars coupled to gravity, at 1-loop only a graviton can be exchanged between external legs, as there are no three-point scalar self-interactions. The 1-loop IR divergence will be proportional to the tree-level scalar $N-$point amplitude $\mathcal{M}_{\text{tree},N}$ and will have the following form in

dimensional regularisation, see for example [471]:

$$\frac{ir_\Gamma}{(4\pi)^{2-\epsilon}}\frac{\kappa^2}{4\epsilon^2}\left(\sum_{i\neq j}^{N}(-s_{ij})^{1-\epsilon}\right)\mathcal{M}_{\text{tree},N}\,, \tag{6.24}$$

where $r_\Gamma=\Gamma^2(1-\epsilon)\Gamma(1+\epsilon)/\Gamma(2-\epsilon)$ and the sum is performed on the Mandelstam invariants for N particle scattering in the unphysical region $s_{ij}<0\ ,\ \forall i,j$. Expanding at leading order for small ϵ, for $N=4$ particles, we find:

$$\left(\frac{1}{\epsilon}\frac{-s\log(-s)}{(4\pi)^2}+\frac{s\log(-s)}{32\pi^2}\left(\log\left(\frac{-s}{(4\pi)^2}\right)-2\right)+\{s\leftrightarrow t,u\}\right)\mathcal{M}_{\text{tree},4}\,, \tag{6.25}$$

where $\{s\leftrightarrow t,u\}$ indicates two contributions equal to the $s-$dependent one, but evaluated in t and u respectively. This result makes clear that the $\log s\log t$ contributions found in Eq. (6.22) are not captured by kinematic-independent IR divergences. Therefore, such contributions cannot be eliminated by re-dressing the one-particle states, or by redefining the asymptotic Hamiltonian that evolves the single-particle states. Rather, the $t\to 0$ singularities of Eq. (6.22) signal the IR kinematic dependence of gravitational scattering as provided by the Coulomb interaction.

6.3 IR effects in Dispersion Relations

The IR loop effects that we have computed in section 6.2.2 define the analytic structure in the IR, and therefore also contribute to the IR integrals. In this section we discuss how these dispersion relations are affected by the IR loops.

We consider two different approaches, dispersion relations at fixed-t (FT), as developed in Ref. [226] and covered in detail in the previous chapter, and crossing symmetric dispersion relations (CS) [148, 152, 472–476], which will be covered in an upcoming subsection. We assume that the amplitude is analytic in both s and t up to the physical cuts: maximal analyticity. Then dispersion relations can be developed on any hyper-slice of the s,t complex planes: FT and CS dispersion relations make different choices for these slices. For clarity, we present the results specifically in $d=6$, and we set the renormalisation scale $\mu=M$, so that our results will involve (running) Wilson coefficients evaluated at that scale.

6.3.1 Fixed-t dispersion relations

For fixed values of $t<0$, the discontinuity associated with physical scattering implies the existence of a branch-cut along the entire real axis in the s plane, but the amplitude is analytic elsewhere (see Section 6.2.2). For $n\geq 0$, we again define arcs in their *IR representation* as integrals in s that probe the theory at finite energy M^2 and momentum transfer $q^2=-t$, and are suited to study amplitudes with the discontinuities associated to massless particles,

$$\text{IR:}\qquad a_n^{FT}(t)\equiv\int_{\frown}\frac{ds}{2\pi i s}\mathcal{K}_n^{FT}(s,t)\mathcal{M}(s,t)\,, \tag{6.26}$$

where the integral is performed along the contour $\frown$: the circle with radius $\mathrm{M}^2+t/2$ and centred at $-t/2$ (minus its interception with the real axis), see Fig. 5.1. The idea is now to exploit s-analyticity of the amplitude to deform the contour $\frown$ into a contour that encompasses the discontinuities on positive $s\geq \mathrm{M}^2$ and negative $s\leq -\mathrm{M}^2-t$ real axis, together with the semicircle at infinity. Then, IR-UV relations follow if the kernel $\mathcal{K}_n^{FT}$ satisfies a number of conditions:

- it has poles in $|s|\leq M^2$ such that the IR arc is non-trivial even for analytic amplitudes,

- it is s,u–symmetric, allowing to easily combine the s and u non-analyticities,
- it must decrease sufficiently fast at $s \to \infty$, $|\mathcal{K}_n^{FT}| \leq 1/s^2$.

The last condition allows us to neglect the integration contour at complex infinity for amplitudes that satisfy $\lim_{|s|\to\infty} \mathcal{M}(s,t)/s^2 = 0$. For gapped theories, this is a result of unitarity and it is guaranteed by the Froissart-Martin bound [214, 215, 424]. For gravitational theories a similar result applies to dispersion relations when smeared over compact impact parameter [185, 216], which is also required for convergence of the partial-wave expansion in gravity, as discussed in section 6.2.2. Kernels that satisfy all of these conditions can be built from

$$\mathcal{K}_n^{FT}(s,t) = \frac{1}{[s(s+t)]^{n+1}}\,. \tag{6.27}$$

Crossing symmetry in $s-u$ leads to $\mathcal{M}(s,t) = \mathcal{M}(-s-t,t)$. It is also manifest in the denominator with subtractions in $s=-t$ and $s=0$. Together with real-analyticity $\mathcal{M}(s,t) = \mathcal{M}^*(s^*,t)$ it allow us to relate the integrals along the positive and negative real axis and write,

$$a_n^{FT}(t) \quad = \quad \frac{1}{\pi}\int_{\mathrm{M}^2} \frac{ds}{s}\frac{2s+t}{s+t}\mathcal{K}_n^{FT}(s,t)\,\mathrm{Im}\mathcal{M}(s,t)\,. \tag{6.28}$$

The partial wave projection Eq. (6.6) allows us to rewrite arcs in a *UV representation*

$$\begin{aligned}\text{UV:}\qquad a_n^{FT}(t) &= \frac{1}{\pi}\int_{\mathrm{M}^2}\frac{ds}{s}\frac{2s+t}{s+t}\sum_{\ell=0}^{\infty} n_\ell^{(d)}\,\mathrm{Im}f_\ell(s)\,\mathcal{K}_n^{FT}(s,t)\,\mathcal{P}_\ell\left(1+\frac{2t}{s}\right)\\ &\equiv \left\langle \frac{2s+t}{s+t}\,\mathcal{K}_n^{FT}(s,t)\,\mathcal{P}_\ell\left(1+\frac{2t}{s}\right)\right\rangle_{FT}\,.\end{aligned} \tag{6.29}$$

Positivity of the integration measure $\mathrm{Im}f_\ell(s) \geq 0$ implied by S-Matrix unitarity, leads to a number of constraints on the UV representation of arcs, which will be interpreted as consistency conditions on the calculable IR representation of arcs.

These constraints can be extracted by smearing both arcs in the UV Eq. (6.29) and in the IR Eq. (6.26) with appropriate functions $f(q)$ of $q^2=-t$, as described in the previous chapter. Functions that evaluate to a positive value in the UV imply positivity conditions in the IR [185],

$$\begin{aligned}&\int_0^{q_{max}} dq\, f(q)\frac{2s-q^2}{s-q^2}\mathcal{K}_n^{FT}(s,-q^2)\,\mathcal{P}_\ell\left(1-\frac{2q^2}{s}\right) > 0 \quad \forall s,\ell\\ &\qquad\qquad \Rightarrow \quad \int_0^{q_{max}} dq f(q)\; a_n^{FT}(-q^2)\big|_{IR} > 0\,.\end{aligned} \tag{6.30}$$

For such smearing functions $f(q)$ to give useful results, they must integrate to a finite quantity in the IR too, in particular on the Coulomb pole, requiring that for small q, $f(q) \sim q^{1+\delta}$, with $\delta > 0$. On the other hand, as nicely remarked in Ref. [185], at large ℓ and large s (but fixed impact parameter $b = 2\ell/\sqrt{s}$) we have $\mathcal{P}_\ell \to \Gamma(d/2-1)J_{d/2-2}(bp)/(bp/2)^{d/2-2}$, with $J_{d/2-2}$ the Bessel function. In this limit, therefore, the UV part of Eq. (6.30) becomes proportional to the $d-2$ dimensional Fourier transform of $F(q) = f(q)/q^{d-3}$.

Now, Bochner's theorem [477] requires that functions 'F' with positive Fourier transforms must be such that the matrix $b_{ij} \equiv F(q_i - q_j)$, for all $q_{i,j} \in [0, q_{max}]$ be positive definite. Taking only two values $q_i = 0$ and $q_j = q$, this condition implies that $|F(q)| \leq |F(0)|$, which translates into $4 - d + \delta \leq 0$. This is incompatible in $d = 4$ with the positivity of δ required by the Coulomb singularity, but provides a necessary condition to build the functions f in higher dimensions.

IR arcs

The IR representation of arcs instead can be computed within the EFT via Eq. (6.26) as was done in the previous chapter, and then confronted with the UV bounds. At tree-level the EFT amplitude is analytic

when $s < M^2$ and, along with the kernels of Eq. (6.27), finding the IR arc reduces to computing the sum of residues at $s = 0$ and $s = -t$ as previously described. From Eqs. (6.1) and (6.2) we find the arcs [226],

$$\text{Tree-level:} \qquad a_n^{FT}(t) = (\text{Res}|_{s=0} + \text{Res}|_{s=-t}) \frac{\mathcal{M}(s,t)}{s[s(s+t)]^{n+1}}$$
$$= -\frac{\kappa^2}{t}\delta_{n,0} + \sum_{p\geq 1}\sum_{q\geq 0} g_{2p+q,q}(-t)^{2(p-n-1)+q}\binom{p-q}{n-q}\,. \tag{6.31}$$

The gravity pole appears only in the first arc,[3] $a_0^{FT}(t) = -\frac{\kappa^2}{t} + \sum_{n=1}^{\infty}[nt^{2n-2}g_{2n,0} - t^{2n-1}g_{2n+1,1}]$, while all higher arcs are infinite polynomials in t.

As discussed in Ref. [226] and the previous chapter, an important aspect of Eq. (5.34) (the generating function for these coefficients) is that it contains an intrinsic upper limit on

$$|t| \leq t_{\text{max}} \equiv M^2\frac{(\sqrt{17}-1)}{8}\,, \tag{6.32}$$

which limits the range on which dispersion relations can be smeared, affecting the bounds.

Loop effects in IR arcs

It is at this step that the IR effects computed above play a rôle. The different pieces in the amplitude in Eq. (6.7) give different contributions to the arcs. The computation of the IR arcs and their derivatives, even when containing the loops, is conceptually straightforward, but the expressions eventually obtained tend to be rather complex. Using Eq. (6.26) we compute the contour integral explicitly by introducing an angular variable θ such that,

$$s = -\frac{t}{2} + \left(M^2 + \frac{t}{2}\right)e^{i\theta}\,,$$

which is integrated from 0 to π and from π to 2π. For simplicity we perform a series expansion $|t/M^2| \ll 1$ when integrating against these kernels, justified in particular by the upper bound Eq. (6.32) which implies $t \lesssim 0.39\,M^2$. The leading terms for the first three arcs in $d = 6$ dimensions (which we assume in most of the following) are,

$$\delta a_0^{FT} = \kappa^4\left(\frac{\left(49000\pi^2 - 310049\right)t + 70\log(-t)(1829t + 1050t\log(-t) + 840) + 90020}{1881600\pi^3}\right)$$
$$+g_{2,0}\kappa^2\left(-M^2\frac{83}{4480\pi^3} + t\frac{29}{640\pi^3}\right) + \ldots, \tag{6.33}$$
$$\delta a_1^{FT} = \kappa^4\left(\frac{-653t + 420(7t-4)\log(-t) + 788}{53760\pi^3}\right)$$
$$+g_{2,0}\kappa^2\left(M^2\frac{56017}{470400\pi^3} - t\frac{369}{4480\pi^3}\right) + \ldots\,, \tag{6.34}$$
$$\delta a_2^{FT} = \kappa^4\left(\frac{477t + 210(27t-8)\log(-t) - 332}{161280\pi^3}\right)$$
$$+g_{2,0}\kappa^2\left(M^2\frac{83}{4480\pi^3} - t\frac{107}{2688\pi^3}\right) + \ldots \tag{6.35}$$

where the dots contain contributions from all combinations of EFT coefficients as well as higher powers in t. We show these results, for the gravity-only contribution, in Figure 6.4.

[3] This is due to the graviton having spin-2, which forces the residue of the $t-$channel pole in the amplitude to be s^2, regardless of which interactions beyond minimal coupling are considered.

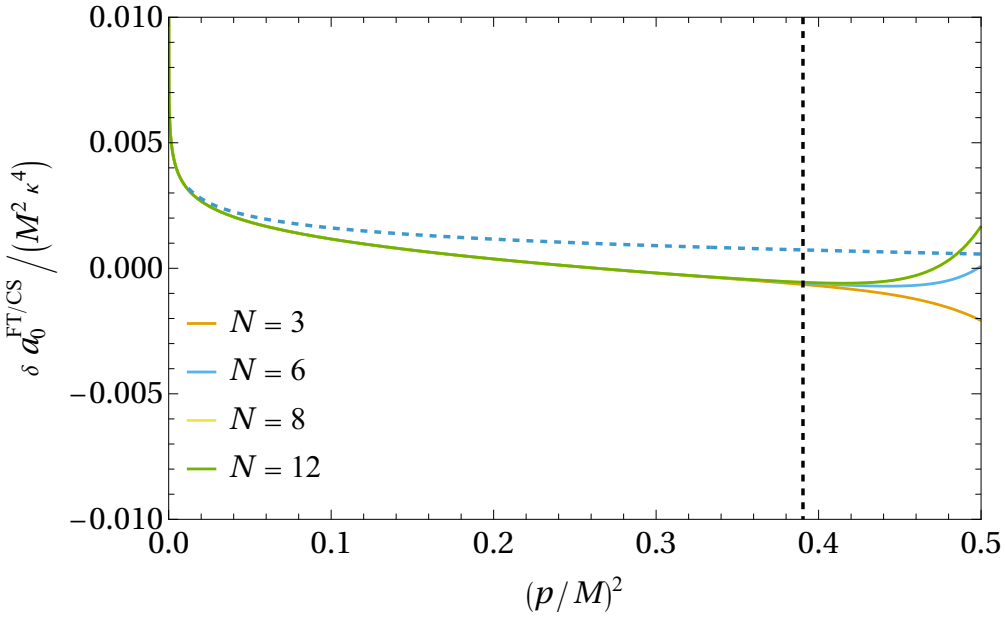

Figure 6.4: *Solid lines: 1-loop contributions to the fixed-t arc a_0^{FT} from the $O(\kappa^4)$ terms, for various values of N in Eq. (5.19), in $d = 6$. The dashed vertical line shows the radius of convergence of our expressions Eq. (6.32). The dashed blue line shows the same contribution to the crossing-symmetric arc a_0^{CS}, where we identify $-t = p^2$. Despite the discrepancy at large p, the two methods give bounds on Wilson coefficients that are in agreement with one another, see Fig. 6.14*

We see that any discontinuity in s induced by loop effects in the amplitude, appears in *every* arc $a_n^{FT}(t)$. So, contrary to the tree-level idealisation where the t-pole appears only in the first arc, here the non-analytic functions like $\log(-t/s)$ propagate to all arcs. The most important such pieces are associated with the gravitational interaction only. In the $|t| \ll M^2$ limit these are easy to identify in any dimension, and contribute to the arcs as,

$$\delta a_n^{FT} \underset{|t|\ll M}{\sim} \frac{\kappa^4 M^{d-8n-2} t^{\frac{d-6}{2}}}{2n-1} \begin{cases} \log\left(-t/M^2\right) & d \text{ is even}, \\ 1 & d \text{ is odd}\,. \end{cases} \tag{6.36}$$

6.3.2 Crossing Symmetric Dispersion Relations

Naive fixed-t dispersion relations have the inconvenience that already at tree-level, they contain infinitely many EFT coefficients in the IR. The reason behind the appearance of infinitely many coefficients is that dispersion relations correspond at tree-level to n-residues in $su = 0$; these are not aligned with the crossing-symmetric expansion of the amplitude Eq. (6.1), where $(stu)^m$ and infinitely many terms $(s^2+t^2+u^2)^n = 2^n(su+st+tu)^n$ contain the same powers of su. For this *not* to be the case, only $(stu)^m$ and $(s^2+t^2+u^2)^m$ must appear in the same dispersion relation, and nowhere else.[4] The simplest way to realise this is to choose new variables with the property

$$\frac{2stu}{(s^2+t^2+u^2)} = p^2 \tag{6.37}$$

[4]Similarly, it might also be possible to obtain finitely many terms if $(stu)^m$ and $(s^2+t^2+u^2)^{m'}$, with $m \neq m'$ appear in the same dispersion relation.

where $p^2 > 0$ is held fixed in dispersion relations. Crossing symmetric dispersion relations[5] are developed along variables with the property Eq. (6.37).

For maximally analytic amplitudes, dispersion relations can be developed on any slice of the s, t complex planes. In particular the slice of constant p in Eq. (6.37) is what we are interested in. Following [473], we change variables from (s, t) to (z, p),

$$s(z,p) = -\frac{3p^2 z}{1+z+z^2}\,, \quad t(z,p) = s(z\,\xi, p)\,, \quad u(z,p) = s(z\,\xi^2, p)\,, \tag{6.38}$$

with $\xi = e^{i2\pi/3}$ and $0 < p^2$ satisfying Eq. (6.37). The amplitude is analytic in $z \in \mathbb{C}$, up to the physical cuts corresponding to real positive values of s, t, u. These are located on the unit circle, where all Mandelstam variables are real (e.g. $s = -3p^2/[1 + 2\cos\theta]$), and on the lines that span from the origin in the directions $-1, -\xi, -\xi^2$, see the left panel of Fig. 6.5.

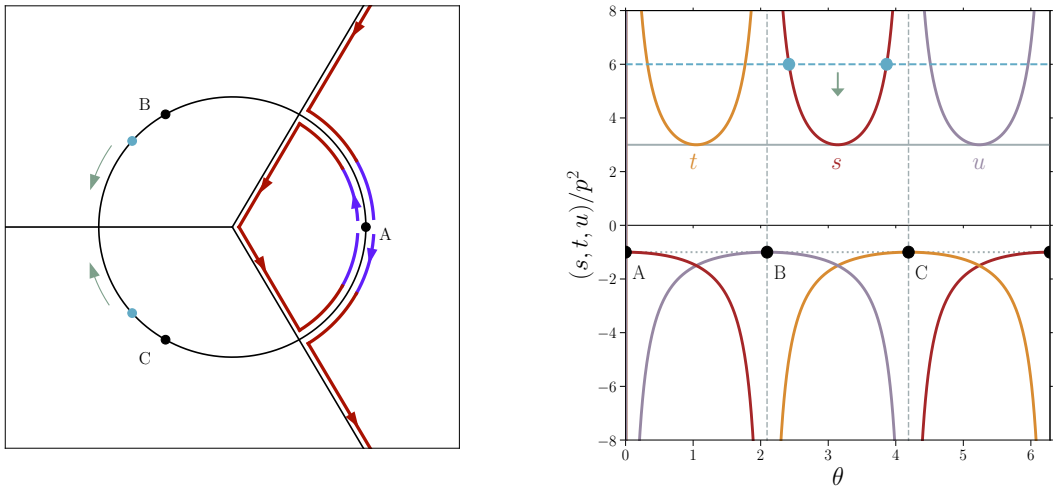

Figure 6.5: *LEFT: Analytic structure of the amplitude in the $z \in \mathbb{C}$ plane, with branch-cuts on the unit circle and the radial directions $-1, -\xi, -\xi^2$. In blue(red) the UV(IR) contours of integration $C_{\rm UV}$ ($C_{\rm IR}$) from Eq. (6.42) (which include the analog around the points B and C). On the unit circle the amplitude is real; points and arrows help translating to the right panel. RIGHT: Values of s, t, u along the unit circle as a function of the angle θ. At the black points A,B,C two of the Mandlestam variables diverge, with the third asymptoting to $-p^2$. On the positive side we have $s, t, u > 3p^2$ and on the negative $s, t, u < -p^2$. In blue, points of fixed $s = M^2 > 3p^2$; as M is lowered the points move closer to the radial directions, as shown by the arrows.*

As illustrated in the right panel of Fig. 6.5, the points $z = 1, \xi, \xi^2$ correspond to infinities in one of the (real) Mandelstam variables; for instance approaching $z = \xi^2$ from above corresponds to $s \to \infty$, $t = -p^2$. We build dispersion relations starting from knowledge of the amplitude's behaviour in these limits. Along the discussion below Eq. (6.26), we assume that amplitudes *smeared in* p grow slower than s^2 at large $|s|$,

$$\lim_{s\to\infty} \int_0^{p_{max}} dp f(p) \frac{\mathcal{M}(z,p^2)}{s^2} = 0\,. \tag{6.39}$$

where $\mathcal{M}(z,p^2) = \mathcal{M}(s(z,p), t(z,p))$. From Eq. (6.39) we can write,

$$\oint_{z=1,\xi,\xi^2} \frac{dz}{4\pi i}\, \mathcal{K}_n^{CS}(z) \mathcal{M}(z,p^2) \equiv 0\,, \tag{6.40}$$

[5] Which might be equally well referred to as fixed-p relations.

where it is implicitly assumed that these relations will be smeared in p. The kernel $\mathcal{K}_n^{CS}$ is built according to the following criteria: it is invariant under $z \to \xi z$ and $z \to \xi^2 z$, as imposed by crossing symmetry. Then, in the Regge limits $z = (1, \xi^2, \xi^{-2})$ it contains enough subtractions to ensure convergence as assumed in Eq. (6.39), which is explicitly realised by a $(1-z^3)^{2n+1}$ factor. Finally, the kernel contains a low energy symmetric pole at $z = 0$, i.e. $s = t = u = 0$, in order to capture the EFT contributions. We then consider the kernel

$$\mathcal{K}_n^{CS}(z) = (-1)^n \frac{\left(z^3+1\right)\left(1-z^3\right)^{2n+1}}{3^{3(n+1)} p^{4n+4} z^{3n+4}}\,, \tag{6.41}$$

with $n \geq 0$.

The contour in Eq. (6.40) can be deformed and separated into two (equivalent) pieces, as illustrated in the left panel of Fig. 6.5, where the separation is defined by the value $s = M^2$, $t = M^2$ and $u = M^2$ on the unit circle (see green dots in left and right panels),

$$a_n^{CS}(p) \equiv \oint_{C_{\rm IR}} \frac{dz}{4\pi i}\, \mathcal{K}_n^{CS}(z) \mathcal{M}(z, p^2) = -\oint_{C_{\rm UV}} \frac{dz}{4\pi i}\, \mathcal{K}_n^{CS}(z) \mathcal{M}(z, p^2)\,. \tag{6.42}$$

Now the UV representation of a_n^{CS} is equivalent to the integral along the (positive) amplitude discontinuity, and can be rewritten in terms of a more familiar integral in s,

$$a_n^{CS}(p) = \int_{M^2}^{\infty} \frac{ds}{2\pi} s^{-3n-4} \left(3p^2 + 2s\right)\left(p^2+s\right)^n \text{Disc}\mathcal{M}(s, p^2)\,. \tag{6.43}$$

where t (and u) read,

$$t = -\frac{s(p^2 + s - \sqrt{s-3p^2}\sqrt{s+p^2})}{2(s+p^2)}\,, \quad u = -\frac{s(p^2 + s + \sqrt{s-3p^2}\sqrt{s+p^2})}{2(s+p^2)}\,. \tag{6.44}$$

So, in contrast to fixed-t dispersion relation here t changes with s: for $s \to \infty$ we have $t \to -p^2$, while for $s \to 3p^2$ (the minimum value on the unit circle) $t \to -3p^2/2$. Moreover, since we need $M^2 \geq 3p^2$ (see the dashed line in the left panel of Fig. 6.5), this implies that $|t| \leq \frac{M^2}{2}$, while for values larger than this the rôle of t is taken by u, as shown in the figure. This implies that CS dispersion relations also have a naturally built-in upper bound on the allowed smearing range

$$p^2 \leq \frac{M^2}{3}\,, \tag{6.45}$$

which translates into $t_{max} = \frac{M^2}{2}$.

In the tree-level approximation, the IR contour has no non-analyticities and the only contributions come from poles at $z = 0$ and $z = \infty$. In more realistic amplitudes like the ones computed in section 6.2.3, the IR contour involves a complicated sum over non-analyticities in z across the unit circle and the radial directions. We circumvent this problem with a trick. The EFT series expansion converges in the IR $s \lesssim M^2$ where the amplitude can be well approximated by finitely many terms, including the tree-level polynomial part and the non-polynomial loop contributions described above. The *truncated function* has non-analyticities associated only with the discontinuities of the loop contributions and the subtraction. These are known a priori in the whole complex plane and they consist of the regions already illustrated in Fig. 6.5 but also include *extra* poles in the points $z \in \mathcal{D} = \{1, \xi, \xi^2\}$. We will use this analytic continuation to compute the IR arcs along the UV contours plus the poles in $\mathcal{D}$. Importantly, this is different from the actual, more-refined UV amplitude which receives further contributions to the discontinuities from UV states and has vanishing residues at infinity. Therefore the IR integrals can be written as,

$$a_n^{CS}(p) \equiv \oint_{C_{\rm UV+\mathcal{D}}} \frac{dz}{4\pi i}\, \mathcal{K}_n^{CS}(z) \mathcal{M}^{\rm EFT}(z, p^2) \tag{6.46}$$

as illustrated in Fig. 6.6. As it is clear from Eq. (6.43), the integral of the EFT amplitude along the UV contour diverges, for instance a $s\log(-s)$ term has a πs discontinuity that diverges quadratically. However,

this divergence is cancelled by an equal and opposite contribution from the poles at $z = 1, \xi, \xi^2$, leaving only finite pieces, as it should. With this method we compute below the IR part of CS dispersion relations, see section 6.3.2.

Meanwhile, the bounds will come from the UV representation, after writing it in terms of partial waves via Eq. (6.6),

$$a_n^{CS}(p) = \sum_{\ell=0}^{\infty} n_\ell^{(d)} \int_{M^2}^{\infty} \frac{ds}{2\pi} \frac{\text{Im} f_\ell(s)}{s^{3n+4}} \left(3p^2+2s\right)\left(p^2+s\right)^n \mathcal{P}_\ell\left(\sqrt{\frac{s-3p^2}{s+p^2}}\right), \tag{6.47}$$

which can also be expressed in the form $a_n^{CS}(p) = \left\langle I_{\ell,n}^{CS}(s,p)\right\rangle_{CS}$, with the definitions,

$$\langle \dots \rangle_{CS} = \sum_{\ell=0}^{\infty} n_\ell^{(d)} \int_{M^2}^{\infty} \frac{ds}{2\pi} \frac{\text{Im} f_\ell(s)}{s^4} (\dots), \quad I_{\ell,n}^{CS}(s,p) = \frac{3p^2+2s}{s^{3n}\left(p^2+s\right)^{-n}} \mathcal{P}_\ell\left(\sqrt{\frac{s-3p^2}{s+p^2}}\right). \tag{6.48}$$

At tree level, using the explicit form of the amplitude Eqs. (6.1) and (6.2), we obtain the following IR-UV relation for $n = 0$,

$$a_0^{CS}(p) = \frac{\kappa^2}{p^2} + g_{2,0} + g_{3,1}p^2 = \left\langle (2s+3p^2)\mathcal{P}_\ell\left(\sqrt{\frac{s-3p^2}{s+p^2}}\right)\right\rangle_{CS}. \tag{6.49}$$

Notably, on the IR part only a finite number of terms appear, as discussed above Eq. (6.37).

We can now perform the same procedure used for the fixed-t case and smear the IR and UV sides, now in $p \in [0,\, M/\sqrt{3}]$, which gives (for $n = 0$),

$$\int_0^{M/\sqrt{3}} \text{d}p\, f(p) \left(\frac{\kappa^2}{p^2} + g_{2,0} + g_{3,1}p^2\right) = \int_0^{M/\sqrt{3}} \text{d}p\, f(p) \left\langle I_{\ell,0}^{CS}(s,p)\right\rangle. \tag{6.50}$$

Exploiting convergence of the partial wave expansion in the UV and finiteness of the dispersion relations, we swap the order of integrations ds and dp. Then, *if* each element of the UV sum in ℓ is positive for each value of s after being integrated in dp, *then* the integral on the IR side is positive,

$$\int_0^{M/\sqrt{3}} \text{d}p\; f(p)\; I_{\ell,n}^{CS}(s,p) > 0,\; \forall s \text{ and } \forall\, \ell \implies \int_0^{M/\sqrt{3}} \text{d}p\; f(p)\; a_{n,\text{IR}}^{CS} > 0. \tag{6.51}$$

Loop Effects in Crossing Symmetric Dispersion Relations

Following the approach described in Fig. 6.6, we compute the contribution of loop effects on the IR CS dispersion relations. The leading EFT interactions give,

$$\begin{aligned}
\delta a_0^{CS} \;=\; & -\frac{g_{2,0}^2}{107520\pi^3}\left[60 + 133\bar{p}^2 - 2\left(\bar{p}^2\right)^2 + 2\left(\bar{p}^2\right)^3 \log\left(1+\frac{1}{\bar{p}^2}\right)\right] \\
& -\frac{g_{2,0}g_{3,1}}{161280\pi^3}\left[33 + 70\bar{p}^2 + 3\left(\bar{p}^2\right)^2 - 6\left(\bar{p}^2\right)^3 + 6\left(\bar{p}^2\right)^4 \log\left(1+\frac{1}{\bar{p}^2}\right)\right] \\
& +\frac{g_{2,0}g_{4,0}}{4838400\pi^3}\left[-2616 - 4755\bar{p}^2 + 100\left(\bar{p}^2\right)^2 - 150\left(\bar{p}^2\right)^3 + 300\left(\bar{p}^2\right)^4 - 300\left(\bar{p}^2\right)^5 \log\left(1+\frac{1}{\bar{p}^2}\right)\right] \\
& +\frac{g_{3,1}^2}{3225600\pi^3}\left[-72 - 105\bar{p}^2 + 20\left(\bar{p}^2\right)^2 - 30\left(\bar{p}^2\right)^3 + 60\left(\bar{p}^2\right)^4 - 60\left(\bar{p}^2\right)^5 \log\left(1+\frac{1}{\bar{p}^2}\right)\right] \\
& +\dots,
\end{aligned} \tag{6.52}$$

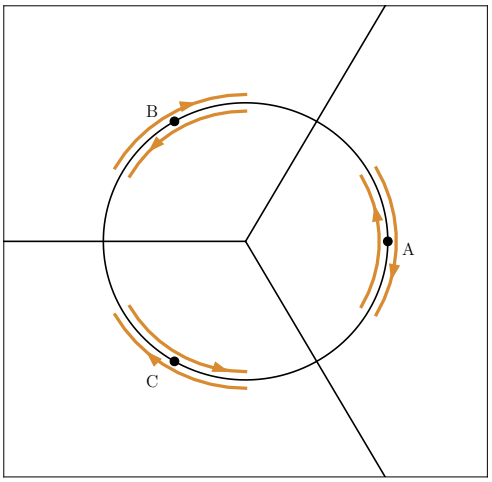

Figure 6.6: *Alternative contour of integration for the IR EFT amplitude. The contour includes the integrals along the discontinuity and the poles around A, B and C, both of which independently diverge. We regularise them by integrating at a finite distance from the poles and the singularities cancel out.*

while mixed EFT-gravity effects give,

$$\begin{aligned}\delta a_0^{CS} \;=\; & \kappa^2\Bigg[\frac{g_{2,0}}{4480\pi^3}\left(83+203\bar{p}^2-23\left(\bar{p}^2\right)^2\log\left(1+\frac{1}{\bar{p}^2}\right)\right)\\ & +\frac{g_{3,1}}{4480\pi^3}\left(10+\frac{91}{2}\bar{p}^2+23\left(\bar{p}^2\right)^2-23\left(\bar{p}^2\right)^3\log\left(1+\frac{1}{\bar{p}^2}\right)\right)\\ & +\frac{g_{4,0}}{241920\pi^3}\left(\frac{1914+4250\bar{p}^2+1721\left(\bar{p}^2\right)^2+1119\left(\bar{p}^2\right)^3+2238\left(\bar{p}^2\right)^4}{1+\bar{p}^2}\right.\\ & \left.-2238\left(\bar{p}^2\right)^4\log\left(1+\frac{1}{\bar{p}^2}\right)\right)+\dots\Bigg]\,.\end{aligned} \tag{6.53}$$

where we define $\bar{p}=p/M$. In pure gravity, we instead obtain a long expression which we report in a later section 6.5, to try to have a level of readability. Figure 6.4 provides a graphical representation of these results, and also compares it with the FT approach.

It is instructive to isolate the leading effects at small p/M, which can be computed using the leading discontinuity across the unit circle in $z\in\mathbb{C}$ (i.e. real kinematics) from the box diagram in Eq. (6.22). Similarly to what was found for arcs at fixed t in Eq. (6.36), this discontinuity will contribute to all arcs. Following Eq. (6.43), we are able to find a compact expression in all dimensions,

$$\delta a_n^{CS}\underset{|t|\ll M}{\sim}\frac{\kappa^4 M^{d-4(n+2)}p^{d-6}}{n}\begin{cases}\log\left(\bar{p}^2\right) & d \text{ is even},\\ 1 & d \text{ is odd}\,.\end{cases} \tag{6.54}$$

6.3.3 Impact on Dispersion Relations

From the above discussion we see that IR loops affect dispersion relations in several ways. Firstly, they introduce non-analyticities, which exhibit certain singular behaviours in dispersion relations. These effects can be classified into two categories. The first involves contributions that grow as $t\to 0$, such as those described in Eq. (6.36), or their crossing-symmetric counterparts as $p\to 0$, see Eq. (6.54). These contributions impose limitations on how dispersion relations can be applied to extract bounds. Specifically, they affect dispersion

relations with any number of subtractions, unlike tree-level dispersion relations where even in the presence of gravity, non-analyticity arises only in a_0, as shown in Eq. (6.31). The gravitational effects highlighted in Eq. (6.36) lead to divergent FT arcs at $t = 0$ for $d \leq 5$, with their derivatives diverging for $d \leq 8$. By contrast, in $d \geq 3$, EFT-only interactions result in arcs and their first derivatives that remain regular as $t \to 0$, as also discussed in [145, 425]. This remains true also for the CS case.

This distinction shows the necessity of moving beyond the improvement procedure of Ref. [185], which relies on higher arcs and their derivatives in the forward limit. Instead, the methodology of Ref. [226], which is fully defined away from $t = 0$, provides a more suitable framework to address such problems.

On the other hand, divergences in $M^2 \to 0$ are the reflection of the fact that the running induced by more relevant operators sooner or later dominates over that induced by the less relevant ones, as discussed in section 6.2.1 and detailed in the context of dispersion relations in Ref. [147]. As discussed in this reference, the first operators that exhibit running is crucial for the following reason: at small M, the bounds on the leading running operator are modified by $\log M$ corrections. However, by dimensional analysis, the bounds on less relevant coefficients are influenced by terms proportional to powers of $1/M$, which are much larger at small M. In $d \geq 5$, the bounds on $\{\kappa, g_{2,0}, g_{3,1}\}$ are impacted solely by $\log M$ effects along $g_{3,1}$ as $M \to 0$. Polynomial effects would instead enter the bounds of the more irrelevant coefficients, like $g_{4,0}$ etc, which can now violate tree-level positivity and become negative by amounts that are polynomial in $1/M$ [147].

Another very important aspect of loop effects is that they imply that *all* dispersion relations contain *all* couplings. This stems from the fact that the discontinuity is proportional to the entire amplitude, involving all of the coefficients. This is also in sharp contrast with the strictly tree-level limit. There, when in the vanishing coupling limit ($g, \kappa M^{d-2} \to 0$ in sec. 6.2.1), the boundedness of the EFT expansion parameter $E/M \lesssim 1$ emerges as a result of dispersive bounds, [147, 150]. At finite coupling, it becomes unfeasible to derive sharp results because arcs involve infinitely many couplings, appearing linearly and quadratically. To extract quantitative results we will have to make *a priori assumptions* about the size of the higher coefficients.

Finally, an intriguing implication of loop effects is that, as discussed at the beginning of this paragraph, they require consistent dispersion relations without forward limits. The two such examples, at fixed-t [226] and in crossing-symmetric dispersion relations [148, 473], operate within a naturally compact range in t. This range, determined by the smearing procedure, is restricted to at most $|t| < M^2/2$. The size of this range will have an important effect on the bounds, even at tree-level.

6.4 Bounds on Gravitational Amplitudes

The arcs defined in dispersion relations are non-perturbative objects. When computed in the IR at tree-level they take the simple form like Eq. (6.49), in terms of the Lagrangian couplings and when computed at loop-level they also involve the corrections that we have computed, like Eq. (6.60). At stronger coupling higher loops will also appear in the IR expression. The UV expression, on the other hand, remains the same.

To answer the question of how loop effects impact the bounds, one would like to define non-perturbative objects that in the limit of weak coupling match to $\kappa, g_{2,0}, g_{3,1}$, etc. Unfortunately there are infinitely many such combinations, because there are infinitely many functionals $f(p)$ that integrate to the same quantity in the IR Eq. (6.50) [6]. Therefore we take the following approach. We first compute the *tree-level* bounds on ratios of the most relevant couplings $g_{2,0}/\kappa^2$ and $g_{3,1}/\kappa^2$. For every point on the boundary there will be an associated functional $f(p)$. We then evaluate this functional on the loop contributions to derive the modification of the bounds. In section 6.6.1 we will also compare this approach to that of exploring more generic loop-level functionals, and verify that this only leads to a small change in the bounds – see Fig. 6.12.

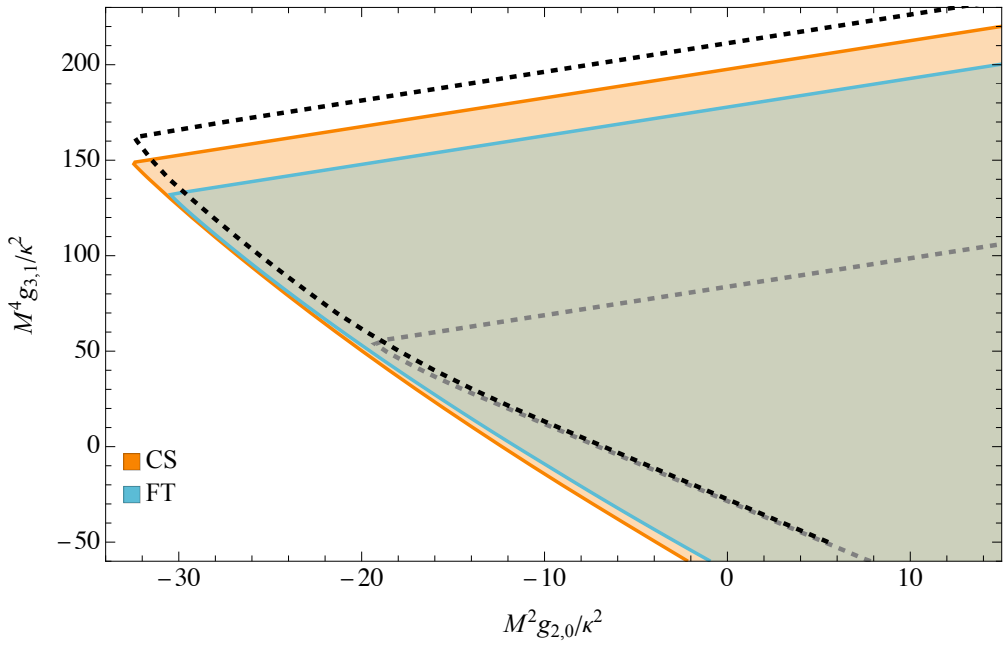

Figure 6.7: *Bounds on $g_{2,0}$ and $g_{3,1}$ in units of κ^2, for CS dispersion relations and the FT with the improvement of Ref. [226], in $d = 6$ dimensions. In grey (black) dashed the results from Ref. [185] with smearing up to $t_{max} = M^2$ ($t_{max} = M^2/2$). The bound from CS dispersion relations is obtained with $\ell_{max} = 30$, a basis of 20 functionals and 10 values of s as described in Appendix 6.6. The bound from FT was computed with $\ell_{max} = 400$ and a basis of 8 functionals and degree of improvement $N = 12$ consistently with Ref. [226].*

6.4.1 Tree-level Bounds

We derive the bounds using different methods, based on FT and CS dispersion relations, as described in Eq. (6.30) and Eq. (6.51). We begin by examining the tree-level bounds and later show how loop effects alter them. Using only the tree-level amplitude, in Fig. 6.7 we show the bounds on the first two EFT coefficients $g_{2,0}$ and $g_{3,1}$, normalised by the strength of gravity κ^2, in units of the EFT cutoff M. The different lines compare results obtained with CS (orange) and FT (blue) dispersion relations. For comparison, in black (grey) the results obtained with the method of Ref. [185] for smearing in $-t_{\rm max} < t < 0$ with $t_{\rm max} = M^2/2$ ($t_{\rm max} = M^2$). The black line has the same upper limit on $|t|$ as the CS method discussed in this work, while the grey one extends to higher values, hence explaining the tighter constraints.

All methods exhibit the same asymptotic behaviour, with slope

$$\frac{M^2 g_{2,0}}{\kappa^2} \to \infty \quad \Rightarrow \quad -4.07 \lesssim \frac{M^4 g_{3,1}/\kappa^2}{M^2 g_{2,0}/\kappa^2} \leq \frac{3}{2}, \tag{6.55}$$

compatible with bounds in the absence of gravity [150] – this result is not obvious in Fig. 6.7 and is highlighted in Fig. 6.13 in a later section. In this limit gravity becomes negligible and the functionals can move closer to the near-forward region where Eq. (6.55) holds. Moreover, in all methods, the upper bound always saturates the asymptotic slope. This is consistent with the expectation in terms of UV models: exchange of a scalar of mass M provides a consistent UV completion and gives an EFT amplitude with $g_{3,1}M^2/g_{2,0} = 3/2$, corresponding to the steepness of the upper bound in Fig. 6.7.

[6] In the IR the 0-th tree-level arc contains only powers $1/p^2, p^0, p^2$: there are infinitely many functionals of the form $p^2 \times Pol(p)$, with $Pol(p)$ a polynomial, which are positive in the UV, but vanish in the IR. For instance, because of orthogonality of the Legendre polynomials, any $Pol(p) = \sum_{l>4} P_l(p)$ integrates to 0 in the IR of Eq. (6.50).

We believe the small difference in the upper bound observable in CS and FT results can be traced to numerics rather than a physical effect. In particular, the two methods have very different convergence properties, with CS involving heavier initial computations but converging faster, while FT needing more constraints to stabilize [226]. The results shown have converged within our computational abilities; we show more details of this in Fig. 6.11 of section 6.6. It is plausible however that including more values of ℓ as well as larger bases for the functionals $f(p)$, would bring the two methods to agree.

The situation is more interesting and more complicated for the lower bound, where the methods of Ref. [185] differ the most from the methods presented here. In principle, it is not surprising that the figures appear different since they are based on different assumptions about the analytic structure in s and t, with Ref. [185] extending to $t = 0$ in higher subtracted dispersion relations. The different methods also employ different kernels, reflecting the underlying assumptions on the amplitude, and these kernels have different behaviours. In particular, CS and FT relations are limited to $|t| < M^2/2$, while the dispersion relations of Ref. [185] can extend to larger values of $|t|$. The range $|t| \leq M^2/2$, corresponds to arcs limited to physical scattering angles $\theta \leq \pi/2$ and is motivated by crossing symmetry, which implies that larger values of $|t|$ would be redundant under $u \leftrightarrow t$ exchange.

It would be interesting to develop a sharper perspective on extremal UV amplitudes, to identify what theories – if any – satisfy our bound, but not the one of Ref. [185], smeared over larger values of t. It was already pointed out in Ref. [185] that for theories with only a finite number of UV weakly coupled particles of finite ℓ with masses $m_\ell \leq \tilde{M}$, the residues are finite polynomials in t and dispersion relations hold to $|t| \leq \tilde{M}$. Interestingly, the *stu*-model proposed in Ref. [150], with UV amplitude,

$$\mathcal{M} = \frac{1}{(s-M^2)(t-M^2)(u-M^2)}, \tag{6.56}$$

would appear to violate this, since the simultaneous poles in the s, t and u channels can be thought of as the exchange of infinitely many particles with all spins at $s = M^2$, thus implying possible non-analyticities as $P_\ell(1-2t/M^2)$ diverges with $\ell \to \infty$ for $|t| > M^2$. However, for $s = M^2$ and negative t, Eq. (6.56) becomes singular only at $t = -2M^2$, when the u-pole is hit. So, even the *stu* model, despite its accumulation point, has amplitudes that are smearable up to $|t| = 2M^2$. On the other hand, amplitudes in gravity including loops have a smaller cutoff. Indeed $\mathcal{I}_\square$, evaluated at $s = M^2$, is singular for $t < -M^2$, see Eq. (6.11) ($\mathcal{I}_\bigcirc$ instead depends only on one kinematic variable and does not pose any problem).

In summary, while tree-level amplitudes at fixed $s = M^2$ are smooth over a broad range in $t < 0$, gravity at finite coupling imposes $t > -M^2$. However, the dispersion relations that remain finite with gravity loops, imply the more stringent condition $t > -M^2/2$, possibly implied by crossing symmetry.

Higher Couplings at tree-level

At tree-level, higher arcs a_n with $n > 0$ don't have the graviton pole. Bounds between the higher couplings can therefore be derived with the simpler methods of Refs. [145, 147, 150]. In particular one finds that, starting from $g_{4,0}$, the coefficients are monotonically decreasing in units of M – up to computable $O(1)$ numbers that depend also on the coupling normalisation. For instance,

$$0 \leq M^4 \frac{g_{6,0}}{g_{4,0}} \leq 1\,, \tag{6.57}$$

and so on, for other coefficients. Moreover, there are also bounds on $g_{4,0}$ in units of κ.

This is an important result: qualitatively, higher coefficients respect dimensional analysis. Without gravity this convergence starts already at $g_{2,0}$ (e.g. $0 \leq M^4 g_{4,0}/g_{2,0} \leq 1$), but gravity changes this statement. With gravity it is possible to have $g_{2,0} = 0$ or $g_{3,1} = 0$, but $g_{4,0} > 0$, and then the coefficients respect monotonicity, as in Eq. (6.57). Indeed, this is the case for dilaton scattering in Type II String theory, where $g_{2,0} = g_{3,1} = 0$, despite gravitational effects and the other coefficients being sizeable.

6.4.2 Bounds with Finite Couplings

At finite coupling, the IR expressions of arcs in terms of Lagrangian parameters differ from the expressions at tree-level, although the UV arcs are always the same. Now the method of Ref. [185], which was not designed for handling loop corrections, diverges in the IR, because it involves $n \geq 1$ dispersion relations evaluated in the forward limit. For illustration, we could imagine regularising these with an IR cutoff $|t| > \mu_{IR}^2$ and we would find that gravity loops enter dispersion relations with effects of order $O(\kappa^4 M^{10}/\mu_{IR}^2)$ in $d = 6$ or even $O(\kappa^4 M^8/\mu_{IR}^4)$ in $d = 4$. In $d = 4$ this polynomial behaviour in μ_{IR} behaves much worse than the logarithmic "negativity" effects discussed in Refs. [185, 187]. So, in what follows we abandon the approach of Ref. [185].

Using FT and CS dispersion relations, we take a perturbative approach around the tree-level bounds discussed in the previous section 6.4.1. For this, we rely initially on the assumption that, in the leading approximation, the functionals $f(p)$ that extremise the couplings at tree-level are unchanged by loop effects — we discuss this in more detail in the later section 6.6.1. We integrate these functionals against the 1-loop contributions,

$$\int_0^{p_{max}} \mathrm{d}p\, f(p)\, \delta a_0^{CS/FT}(p) \tag{6.58}$$

and then add these to the tree-level result to obtain the 1-loop corrected result. In the FT case we have $p_{\rm max}^2 = M^2(\sqrt{17} - 1)/8$, while in the CS case we have $p_{max} = M/\sqrt{3}$.

The results of this analysis are shown in Fig. 6.8 for CS dispersion relations, with the FT approach providing similar results (see section 6.8). This figure shows the most relevant effects discussed in section 6.3, in particular effects of order $O(\kappa^4, \kappa^2 g_{2,0}, g_{2,0}^2, \kappa^2 g_{3,1}, g_{2,0} g_{3,1}, g_{3,1}^2)$, organised here in terms of relevance of their dimensionality. These effects are evaluated on a point in the boundary, labelled by the value of $g_{2,0}M^2/\kappa^2$ on the horizontal axis. The normalisation of the vertical axis differs from Fig. 6.7, because it carries units of the gravity loop. This means that, to obtain the relative shift in $g_{3,1}/\kappa^2$ we have to first choose the size of gravity loop effects. To guarantee that the loop expansion stays perturbative, these will have to be smaller than tree-level effects, $\kappa^4 M^8/(4\pi)^3 \ll \kappa^2 M^4$.

The inherently multi-scale nature of this problem makes the result non-trivial. While the overall magnitude of these effects is governed by the scale M and the size of the gravity loop, the smearing in p introduces a smaller scale. Loops involving different coefficients involve different powers of either scale and lead to effects of different sizes, as can be seen in Fig. 6.8.

The sum of all these effects is displayed in Fig. 6.14 in section 6.8, where we see that FT and CS methods produce very similar results: the small differences can be traced to the different position of the tree-level boundary as discussed above. This is an important test, given that the dispersion relations, their IR contributions, and the numerics follow completely different paths.

6.4.3 A Consistent Perturbative Approach

An important message conveyed by Fig. 6.8 is that contributions from less relevant operators, like $g_{3,0}$, appear comparable or even dominant over more relevant contributions like κ^4 in some points at the boundary. This is a rather generic consequence of the fact that we study loop effects around *extremal* tree-level amplitudes. As discussed already in Refs. [147, 150, 211], tree-level bounds tend to saturate the EFT expansion, meaning that on the boundary all the coefficients have comparable size, in units of the cutoff. This is not a problem for tree-level bounds, because each coefficient can be treated almost individually as appearing only in dispersion relations with a given number of subtractions. Beyond tree-level however, unitarity forces all couplings to enter the discontinuity, and also the arcs. So, for extremal amplitudes, it is possible that even though the loop expansion is perfectly under control, all coefficients would have to be taken into account: the EFT expansion fails and poses a problem for calculability.

Extra assumptions must be introduced to keep the EFT expansion under control, while still working at finite couplings. One such possibility, that preserves all physical properties of the amplitude and at the same time is in principle testable in IR experiments, is to focus on theories where the less relevant couplings are small, see Ref. [478] for a broader discussion of this aspect inspired by phenomenological requirements and

also Ref. [151] for application of a similar condition to non-perturbative amplitudes. Assuming a small value for $g_{2,0}M^2/\kappa^2$ allows for significant gravitational effects while suppressing contributions from $g_{2,0}$. Likewise, the smallness of $g_{3,1}$, $g_{4,0}$, and higher-order terms shall also be assumed. A key question is how to efficiently impose this assumption.

In the absence of gravity, assuming a small tree-level $g_{2,0}$ would be enough to ensure that all higher couplings are small. As discussed in section 6.4.1, however, with gravity $g_{2,0}$ or $g_{3,1}$ can vanish without implying an inconsistency. Instead, the first condition that we can impose leading to smallness of all higher order terms is,[7]

$$\frac{g_{4,0}M^6}{\kappa^2} \leq \epsilon\,, \tag{6.59}$$

with small enough ϵ. From the bounds of section 6.4.1, we know that Eq. (6.59) implies $g_{n,q}M^{2(n-1)}\kappa^{-2} \lesssim \epsilon$.[8] This in turn implies that loops involving all higher EFT coefficients will be negligible.

The condition Eq. (6.59) is in fact not satisfied by all points in the tree-level quadrant allowed by positivity in Fig. 6.7. In Fig. 6.9 we update this result to include the condition Eq. (6.59) with $\epsilon = 0.1$. It is immediately noticeable that the slope of the upper bound is different in this case, as expected from EFT results without gravity - we have checked that for large values of positive $g_{2,0}$ the curves asymptote to the slopes expected in the absence of gravity.

Now, the boundary of Fig. 6.9 provides a robust platform on which to discuss the size of loop effects, consistent with a perturbative loop expansion *and* a perturbative EFT expansion. On the boundary of this figures, loops are entirely dominated by effects involving only the couplings $\kappa^2, g_{2,0}$ and $g_{3,1}$, which we have computed above. We show their sum in Fig. 6.10 colour-coded in such a way to match the corresponding point on the tree-level bound, shown in the inset (notice that the axes are inverted with respect to Fig, 6.8, so that the entire boundary can be represented on the same figure). The kink in the size of loop effects is of course located at the same position of the kink of the tree-level boundary. Corrections to the lower bound are much smaller than the upper bound.

6.5 Gravitational Contribution to the Arcs

In this section we list the expression for the arcs' corrections from loops of order $O(\kappa^4)$, for the CS case of Sec. 6.3.2.

$$\begin{aligned}
\delta a_0^{\rm CS} =& -\frac{173\bar{p}^2\log(\mu)}{2240\pi^3} - \frac{3\bar{p}^2\mathrm{Li}_2\left(-\frac{1}{\bar{p}^2}\right)}{64\pi^3} + \frac{\log\left(\frac{1}{\bar{p}^2}+1\right)}{64\pi^3\bar{p}^2} \\
&+ \frac{1}{1881600\pi^3}\left(\bar{p}^2\left(-\frac{9800\bar{p}^2(\bar{p}^2(\bar{p}^2+3)+3)\log(8)\log(32)}{(\bar{p}^2+1)^3} + 34300\pi^2 - 76529\right) - 148820\right) \\
&- \frac{3\sqrt{\frac{4}{\bar{p}^2+1}-3}\tanh^{-1}\left(\sqrt{\frac{4}{\bar{p}^2+1}-3}\right)}{32\pi^3(\bar{p}^2+1)^3} - \frac{1409\bar{p}^2\coth^{-1}(2\bar{p}^2+1)}{13440\pi^3} \\
&+ \frac{1}{215040\pi^3\bar{p}^2(\bar{p}^2+1)^3}\left[875\sqrt{\frac{4}{\bar{p}^2+1}-3}\,\bar{p}^6\log(4\bar{p}^2(\bar{p}^2+1))\right. \\
&+ 2485\sqrt{\frac{4}{\bar{p}^2+1}-3}\,\bar{p}^6\log\left(\bar{p}^2-\sqrt{(1-3\bar{p}^2)(\bar{p}^2+1)}+1\right) \\
&\left.- 4235\sqrt{\frac{4}{\bar{p}^2+1}-3}\,\bar{p}^6\log\left(\bar{p}^2+\sqrt{(1-3\bar{p}^2)(\bar{p}^2+1)}+1\right)\right.
\end{aligned}$$

[7] To study theories with sizeable $g_{4,0}$ one could instead impose $g_{6,0}M^12/\kappa^2 = \epsilon$; a condition on $g_{5,1}$ would not be sufficient to ensure convergence of the higher order terms.

[8] Loop effects will introduce departures from monotonicity, see Ref. [147]. These will be of the size of a non-divergent loop factor, hence small. In turn, such departures propagate into loops of $g_{4,0}$ as a 2-loop effect.

$$
\begin{aligned}
&+3360\bar{p}^4\left[(\bar{p}^2+1)^3\left[\log^2\left(\bar{p}^2-\sqrt{(1-3\bar{p}^2)(\bar{p}^2+1)}+1\right)+\log^2\left(\bar{p}^2+\sqrt{(1-3\bar{p}^2)(\bar{p}^2+1)}+1\right)\right.\right.\\
&-7\log\left(\bar{p}^2+\sqrt{(1-3\bar{p}^2)(\bar{p}^2+1)}+1\right)\log\left(\bar{p}^2-\sqrt{(1-3\bar{p}^2)(\bar{p}^2+1)}+1\right)+5\log(4\bar{p}^2)\log(\bar{p}^2+1)\Big]\\
&\left.+\log(32)\log\left(\frac{2\bar{p}^2}{\bar{p}^2+1}\right)+5(\bar{p}^4(\bar{p}^2+3)+3\bar{p}^2)\log(2)\log\left(\frac{4\bar{p}^2}{\bar{p}^2+1}\right)\right]\\
&-1001\sqrt{\frac{4}{\bar{p}^2+1}-3}\bar{p}^4\log(4\bar{p}^2(\bar{p}^2+1))+11081\sqrt{\frac{4}{\bar{p}^2+1}-3}\bar{p}^4\log\left(\bar{p}^2-\sqrt{(1-3\bar{p}^2)(\bar{p}^2+1)}+1\right)\\
&-9079\sqrt{\frac{4}{\bar{p}^2+1}-3}\bar{p}^4\log\left(\bar{p}^2+\sqrt{(1-3\bar{p}^2)(\bar{p}^2+1)}+1\right)-3360\sqrt{\frac{4}{\bar{p}^2+1}-3}\log(2\bar{p}^2)\\
&+3360\sqrt{\frac{4}{\bar{p}^2+1}-3}\log\left(-\bar{p}^2-\sqrt{(1-3\bar{p}^2)\ (\bar{p}^2+1)}+1\right)\Big]\,. \qquad (6.60)
\end{aligned}
$$

There is no expansion in p, the above is the result in full.

6.6 Bounds from Smearing and Consistency Checks

Here we adapt the smearing algorithm to CS dispersion relations. We also explain details of how the semi-definite optimisation program is built and how we treat the logarithms appearing in IR arcs. In this section, for simplicity, we work in units of the cutoff, $M^2=1$.

We write a generic smearing function $f(p)$ as,

$$
f(p)=p^\alpha\sum_{j=0}^{j_{\max}}c_j p^j, \qquad (6.61)
$$

where a constant overall factor p^α is added to integrate to a finite value on the gravity pole – α will be fixed later in the procedure. We define the vector $\mathbf{W}$ in the UV as

$$
W_{j,\,\ell}(s)=\int_0^{1/\sqrt{3}}\mathrm{d}p\,p^{j+\alpha}\;I_{\ell,0}(s,p). \qquad (6.62)
$$

While in the IR, we define the vector $\mathbf{V}$ as

$$
V_j=\int_0^{1/\sqrt{3}}\mathrm{d}p\,p^{j+\alpha}\,a_0^{CS}(p). \qquad (6.63)
$$

Then, positivity bounds can be written as

$$
\sum_{j=0}^{j_{\max}}c_j W_{j,\,\ell}(s)\geq 0,\quad \forall\, s,\ \ell,\ \implies \sum_{j=0}^{j_{\max}}c_j V_j\geq 0. \qquad (6.64)
$$

The coefficients c_j can be varied, in search of an optimal function which minimises or maximises the bound. We therefore have a target vector V_j and a vector to optimise c_j tin order to obtain $\sum c_j V_j\geq 0$, subject to some constraints $W_{j,\,\ell}(s)\succcurlyeq 0$. This defines the semi-definite optimisation problem.

In principle positivity should be imposed for all values of ℓ. To reiterate, in practice, we work with a finite $\ell\leq\ell_{\max}$ and increasing its value until the bound stabilises.

The finite range $\ell\leq\ell_{\max}$ means fewer UV conditions and hence artificially stronger bounds. As described below Eq. (6.30) this can be complemented with $\ell\to\infty$ information, through the *finite impact parameter* limit to gather information at large values of ℓ. This corresponds to $s\to\infty$, $\ell\to\infty$ with $b=2\ell/\sqrt{s}$ fixed. In this limit the Gegenbauer polynomials give,

$$
\lim_{m\to\infty}\mathcal{P}_{mb/2}\left(\sqrt{\frac{m^2-3p^2}{m^2+p^2}}\right)=\frac{\Gamma\left(\frac{d-2}{2}\right)}{\left(\frac{bp}{2}\right)^{\frac{d-4}{2}}}J_{\frac{d-4}{2}}(bp)\,, \qquad (6.65)
$$

with $m \equiv \sqrt{s}$. In this limit the dispersion relations can be integrated exactly into fixed-impact-parameter relations,

$$W_j(b) = \Gamma\left(\frac{d-2}{2}\right)\int_0^{1/\sqrt{3}} \mathrm{d}p\, p^{j+\alpha}\frac{J_{\frac{d-4}{2}}(bp)}{(bp/2)^{\frac{d-4}{2}}} = \left(\frac{1}{3}\right)^{(j+\alpha+1)/2}\frac{{}_1F_2\left(\frac{j+\alpha+1}{2};\frac{d-2}{2},\frac{j+\alpha+3}{2};-\frac{b^2}{12}\right)}{j+\alpha+1}. \tag{6.66}$$

This leads to more constraints on the function f, complementary to fixed-ℓ. In particular we impose Eq. (6.66) at fixed values of b and following Ref. [185], we demand that it is positive for large values of b, where,

$$\frac{{}_1F_2\left(\frac{j+\alpha+1}{2};\frac{d-2}{2},\frac{j+\alpha+3}{2};-\frac{b^2}{12}\right)}{j+\alpha+1} \sim A(b) + B(b)\cos(\phi) + C(b)\sin(\phi), \tag{6.67}$$

with ϕ defined as the argument of the oscillatory terms, which depends on b, and A, B, C obtain at a certain order in the $1/b$ expansion. Positivity for all ϕ requires,

$$\begin{pmatrix} A(b)+B(b) & C(b) \\ C(b) & A(b)-B(b)\end{pmatrix} \succcurlyeq 0. \tag{6.68}$$

For these expressions to be polynomial in b and to satisfy the condition $4-d+\alpha \leq 0$ implied by Bochner's theorem (see below Eq. (6.30)), we demand $\alpha = \frac{d-3}{2}$. Then, up to an overall factor, we are left with a matrix of polynomials in b, which can be treated with the usual techniques of semi-definite optimisation.

For the bounds described in the main text, we have used,

$$V_j = \int_0^{1/\sqrt{3}} \mathrm{d}p\, p^{\alpha+j}\left(\frac{\kappa^2}{p^2} + g_{2,0} + g_{3,1}p^2 + \mathcal{O}(\log(p^2))\right), \tag{6.69}$$

and optimised the value of $g_{3,1}/\kappa^2$ for a fixed value of $g_{2,0}/\kappa^2$ using the software `sdpb` [430, 431]. We utilise multiple values of $\ell \leq \ell_{\max}$ and discretise in $\sqrt{s} \in [1,\infty]$ in the CS case, by defining $\sqrt{s} = \frac{1}{1-x}$ with $x \in [0, 1-\delta x]$ sampled in steps $\delta x = 0.1$. We have checked that smaller values of δx do not change quantitatively the results. Furthermore, we show how the plot changes when increasing $\ell_{\max}$ and $j_{\max}$ in Fig.6.11. Changing these parameters does not modify the plot qualitatively.

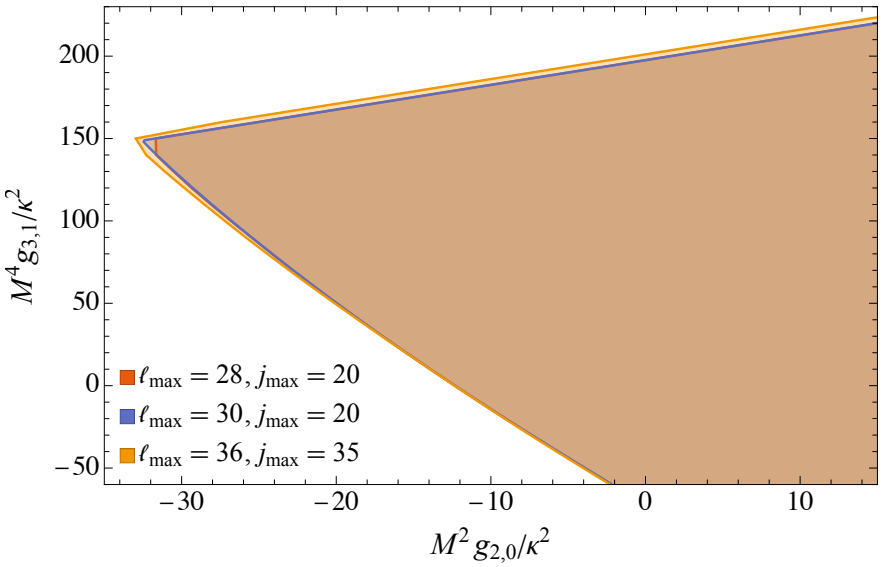

Figure 6.11: *Bounds in the CS case, for various values of $\ell_{\max}$, the number of spins, and $j_{\max}$, the number of elements in the basis. The bound becomes stable with $\ell_{\max} \sim 30$ and $j_{\max} \sim 30$.*

We built a matrix with rows made out of 1×1 matrices for each value of ℓ and x, and a column for each element of the basis of polynomials. For the optimisation procedure a normalisation choice for $f(p)$ is required.

$$\int_0^{1/\sqrt{3}} \mathrm{d}p\, f(p)\, p^2 = \sum_{j=0}^{j_{\max}} c_j \int_0^{1/\sqrt{3}} \mathrm{d}p\, p^{j+\frac{d+1}{2}} = \pm 1, \tag{6.70}$$

where the $-$ sign gives the upper bound and the $+$ the lower bound.

6.6.1 Loop order functionals

In our perturbative approach we have employed the tree-level extremal functionals $f(p)$ to compute the loop-level contributions via Eq. (6.58). In principle, dispersion relations with loop effects might be extremised by other "loop-level" functionals. Fig. 6.12 shows the difference between using tree-level and loop-level functionals, in the context of CS dispersion relations. For clarity we have limited the analysis to loops involving only gravity, with $\kappa^2/(4\pi)^3 = 0.1M^{-4}$.

The deviations are most notable near the kink, with the rest of the bound being unaffected. This difference can be explained by the fact that the $g_{3,1}$ position of the kink is not captured by the tree-level functionals.

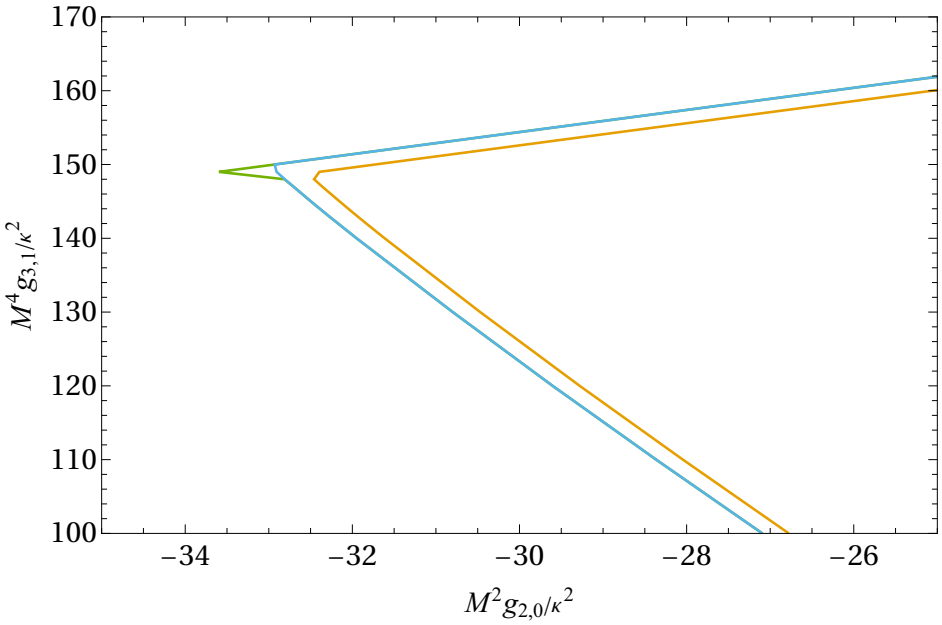

Figure 6.12: *Comparison, in the CS case, between the perturbative expansion used in Sec.6.4 (blue), and a direct approach of including the loops in the semidefinite optimisation problem (green) both for the gravitational loop only, with fixed* $\kappa^2/(4\pi)^3 = 0.1M^{-4}$. *In orange the tree-level bound.*

6.7 Bounds with fixed higher order Wilson coefficients

As described in section 6.4.3, to ensure control over the EFT expansion into loop effects, we demand the condition Eq. (6.59). This is reflected in Figs. 6.9 and 6.10. For practical reasons, it is simpler to impose, beside $M^6 g_{4,0}/\kappa^2 = \epsilon$, also $M^8 g_{5,1} = M^{10} g_{6,2} = \epsilon\kappa^2$, although smallness of $g_{5,1}, g_{6,2}$ is normally implied by the condition on $g_{4,0}$.

The reason for this is that we impose these conditions by adding a term $p^4 a_1^{\rm CS}$ to the 0-th CS arc $a_0^{\rm CS}$,

$$V_j = \int_0^{1/\sqrt{3}} {\rm d}p\, p^{j+\alpha} \left[a_0^{\rm CS}(p) + p^4 a_1^{\rm CS}(p)\right], \tag{6.71}$$

where the first arc in the IR reads,

$$a_1^{\rm CS}(p) = g_{4,0} + g_{5,1}p^2 + g_{6,2}p^4. \tag{6.72}$$

By entering specific values of each parameter in the objective function we fix their values. In this way we obtain Fig. (6.9). The lower bound and the kink are unchanged, while the slope of the upper bound changes from 3/2 to ~ 1.08. This is equally expected, since the scalar UV completion is excluded by our choice of Wilson coefficients. We use all the same parameters as for Fig. 6.7, with $\ell_{\rm max} = 30$, and 20 elements in the basis of polynomials.

This method of setting explicit values for $g_{4,0}$, $g_{5,1}$, and $g_{6,2}$ does not formally yield a bound for $M^6 g_{4,0} < \epsilon\kappa^2$. However, one expects that for smaller values of ϵ any bound will be contained within the region obtained by saturating Eq. (6.59). We have also verified this to be true by scanning several values of ϵ in our numerics.

6.8 FT versus CS Dispersion Relations

As referenced in section 6.4.1, in the region where the effects of gravity are small, $\kappa^2 \ll M^{2(n-1)}\,|g_{n,q}|$, the asymptote of the lower boundary reproduces a slope of ~ -4.07, which is indeed the lower bound on the ratio $M^2 g_{3,1}/g_{2,0}$ in the absence of gravity. We show this in Fig.6.13. The upper slope reaches the asymptotic value of 3/2 already quite close to the tip, therefore we do not show it here.

A further comparison between CS and FT methods is given by the correction to the bounds on $g_{2,0}$ and $g_{3,1}$ in the presence of gravity and all loops, which we show in Fig. 6.14. These corrections are displayed as a deviation $\delta g_{3,1}/(M^4\kappa^6)$ in terms of $g_{2,0}M^2/\kappa^4$ – the same as Fig. 6.8 but opposite than Fig. 6.10.

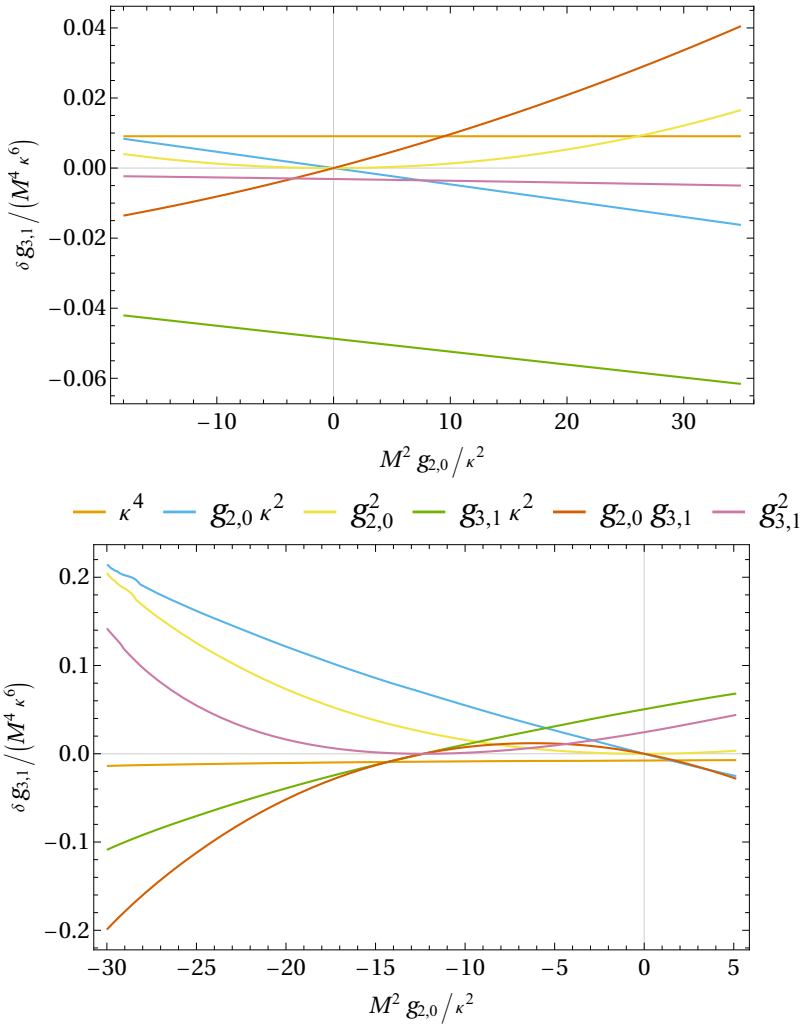

Figure 6.8: *Loop-correction to the tree-level bound, obtained with the CS method on $g_{3,1}$ varying $g_{2,0}$, for various loop contributions evaluated on the boundary of the allowed region, in $d = 6$. The vertical axis has the shift in $M^4 g_{3,1}/\kappa^2$ normalised to the $\kappa^4 M^8$ scaling of a gravity loop. The upper (lower) plot shows the correction to the upper (lower) bound.*

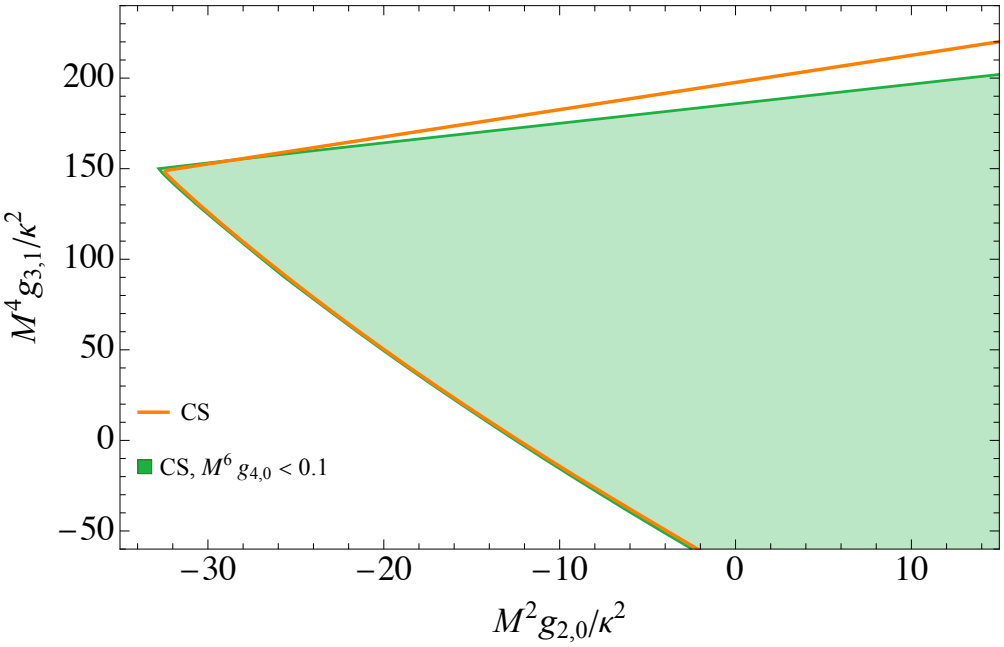

Figure 6.9: *The tree-level bound for CS dispersion relations in* $d = 6$. *In orange the same as in Fig. 6.7. In green, with the additional condition Eq. (6.59) with* $\epsilon = 0.1$, *with the procedure described in Appendix 6.7.*

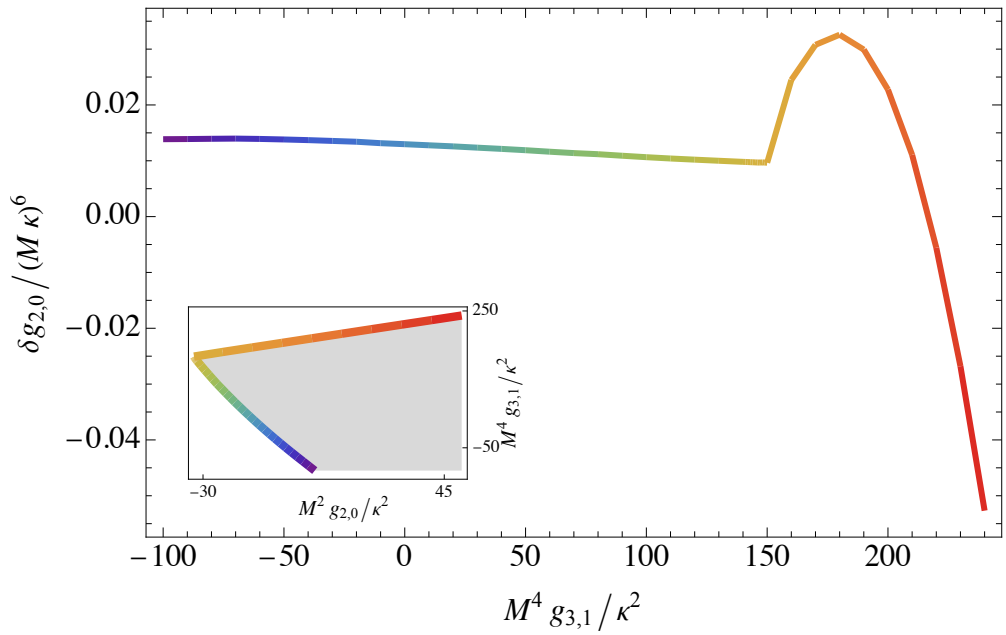

Figure 6.10: *Loop correction to the CS bounds on* $g_{2,0}M^2/\kappa^2$ *of Fig. 6.9, in units of gravity loops* $\kappa^4 M^8$, *at every point* $g_{3,1}M^4/\kappa^2$. *The colour scheme maps each point on the tree-level bound in the inset to the associated correction. We impose* $g_{4,0}M^6/\kappa^2 \leq 0.1$ *in order to suppress loops from higher Wilson coefficients.*

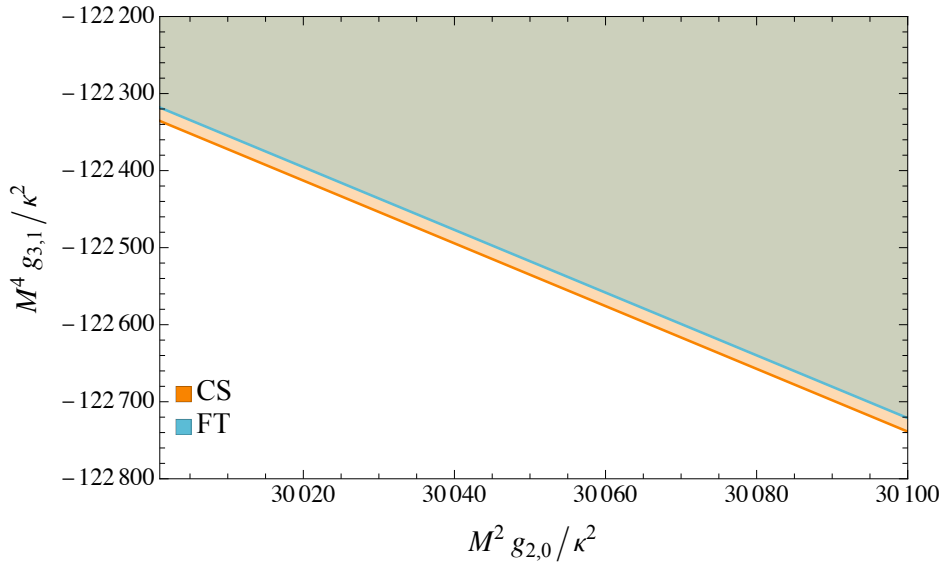

Figure 6.13: *Asymptotic behaviour of the lower bound in the regime where gravity is negligible, i.e.* $\kappa^2 \ll M^{2(n-1)}\,|g_{n,q}|$. *The slope here gives* $M^2 g_{3,1}/g_{2,0} \geq -4.07$, *which is consistent with the tree-level bound without gravity. Both CS and FT methods coincide with this slope value.*

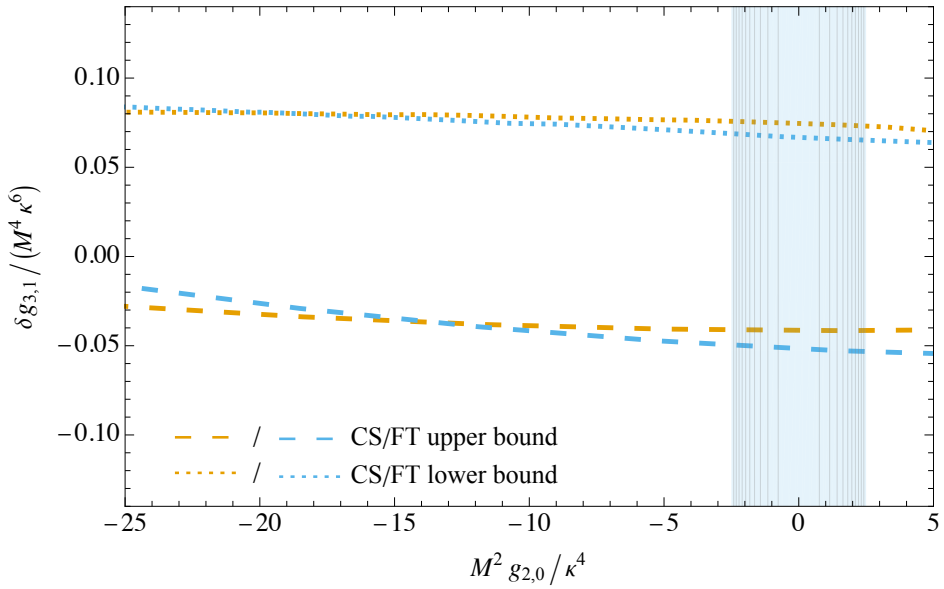

Figure 6.14: *Correction to* $\delta g_{3,1}$ *for each point of* $g_{2,0}$. *The CS (FT) method is plotted in orange (blue), while the upper (lower) bound is dashed (dotted). The upper bound gets corrected less than the lower bound.*

Chapter 7

Conclusions

Throughout the preceding thesis we have discussed a variety of topics relevant in contemporary particle physics. They are linked thematically in that they all address very low energy phenomenology. In the first two chapters after the introduction, 2 and 3, we explored experimental signatures that could be seen from ultralight DM particle candidates. The fourth chapter 4 dealt with the self-consistency of one of these DM models; namely the QCD-axion, where unitarity demanded a larger than expected quadratic coupling to photons. The final two chapters 5 and 6 sought to address theoretical questions involving the consistency of very low energy EFTs involving massless particles and gravity, with standard UV assumptions like unitarity, causality and locality.

7.1 Casting New Light on DM NMR

Axion NMR is a promising avenue to search for axion DM through its coupling to nucleons. This coupling generates an *effective* magnetic field that couples to a spin sample, causing it to precess in a measurable manner. Significant experimental efforts are underway by the CASPEr-Gradient collaboration [236, 237, 239, 479], and other proposals have been made to conduct similar experiments [480–483]. Axion NMR is also an active area of theoretical research aiming to refine the ultimate limits in sensitivity achievable with this technique [228, 484, 485].

In this chapter we quantified the sensitivity that axion NMR experiments have to alternative DM signals that produce *real* magnetic fields in the vicinity of the hyper-polarised spin sample. We demonstrated that CASPEr-Gradient can have world-leading sensitivity to DP DM as well as to the axion-photon coupling in the same experimental setup they use to search for the axion-nucleon coupling. Importantly, the three signals can be distinguished by virtue of their symmetry properties. The canonical signal induced by the axion-nucleon coupling is homogeneous throughout the electromagnetically-shielded volume in which the spin sample is placed. In contrast, the DP and axion-photon coupling generate inhomogeneous signals. We see by explicitly looking at the excited modes (for example Fig. 2.2) that the three signals can be differentiated by modifying the placement of the sample inside the shield.

The coming years promise revolutionary progress in the search for ultralight DM with masses below a μeV. In particular, as instruments like DMRadio [404, 486] or heterodyne SRF haloscopes [405, 406, 487] are increased in scale, the goal is to improve the sensitivity by many, many orders of magnitude beyond existing low-mass haloscopes [398–400, 488] to push towards the QCD-axion prediction. DM NMR represents a completely distinct experimental strategy to push towards that same goal, and as the present work has highlighted it can probe many forms of DM as it does so. For this reason it will be critical to determine how far the DM NMR approach can ultimately be scaled, in particular understanding the quantum mechanically-imposed limitations [484] and ways they can be evaded through the use of quantum resources [489].

7.2 Dark Matter Constraints from Earth

In this chapter we saw that it is possible to derive robust constraints in DM parameter space, by using natural features of the Earth. We also proposed a new way to detect bosonic DM with mass $m_\alpha \lesssim 3 \times 10^{-8}$ eV, *i.e* below the typical maximum ionosphere plasma frequency. When DM waves pass through the ionosphere of the Earth, they can get resonantly converted into radio waves that are detectable by a small meter-scale antenna. Our pessimistic projections suggest many decades of DP parameter space could be probed in just a few hours of observation time. The small magnetic field of the Earth affects the sensitivity to axions, but we nevertheless project that a similar setup can improve on the best laboratory constraints, and possibly the best current astrophysical constraints.

Fully characterising the electrical and physical properties of the antenna must be done. The location of the antenna can also be optimised, depending on anthropogenic and atmospheric noise, as well as the Earth's magnetic field for the axion. With a precise detector design and location in mind, the ionosphere's plasma properties require a more accurate treatment, for example using available data [336]. For example, one necessary feature to capture would be the diurnal variation, which can be used to look for modulations of the signal. This could be useful in discriminating it from backgrounds. Moreover, the signal can be characterized by the propagation of the signal radially towards the Earth's surface, $\mathbf{k} \propto \hat{\mathbf{r}}$, imprinted by the large plasma gradient in this direction.

Finally, given the simplicity, (small) size and low cost of the proposed antennae, one can easily envision the use of an array of antennae operating in an interferometric mode. Placing N antennae $\sim \mathcal{O}(10)$ km from each other can improve the signal to noise ratio by at least a factor $\sqrt{N}$. The coherence length of the DM signal would exceed the antenna separation, while anthropogenic noise varies more over these scales, thus the potential for improvement is greater if it enables the subtraction of anthropogenic noise sources.

7.3 Quadratic Coupling of the Axion to Photons

The dynamics that endows an axion with a mass, breaking its shift symmetry, can also lead to a non-shift-symmetric quadratic coupling of axions to photons. In the case of the QCD axion, we showed that the leading contribution to this operator arises at one-loop order. For a generic ALP, some model-building is required, but the quadratic coupling can still be generated. The result is that DM axions would induce temporal variation of the fine-structure constant α, an effect which is severely constrained. In the case of the QCD axion, other constraints are typically stronger, but the quadratic photon coupling offers a new way to independently rule out significant regions of parameter space. For ALPs, the quadratic photon coupling could be the strongest constraint in wide regions of parameter space, and offers a new way of probing regions that are inaccessible to traditional haloscope searches. Indeed, the existence of a quadratic coupling of axions to matter can have important implications for such searches due to screening near macroscopic objects [490]. Additionally, large magnetic fields found in astrophysical environments offer an interesting environment to study the inclusion of these effects.

The co-existence of the linear CP-odd and quadratic CP-even couplings of axions could lead to different phenomenology from that of ultralight scalars, which only have CP-even couplings at all orders in the scalar field. A thorough exploration of the implications of this admixture of couplings should be undertaken to study its effect.

7.4 Consistent Positivity at Finite-t

Positivity bounds help to discern swampland theories from those consistent with UV completions, whether weakly or strongly coupled. Despite the fact that most results in this field have been derived via Taylor expanding UV-IR dispersion relations in the vicinity of the forward limit, this approach fails for IR theories containing gravity or quantum effects associated with loops of massless particles [222, 425].

In this chapter we have presented a procedure that avoids the forward limit entirely, adding an important ingredient to Ref. [185]. A proof of principle has been provided to show that positivity bounds can be found in

all theories, independently of their IR structure, even in those theories where physical IR divergences appear in dispersion relations with any number of subtractions. It is based on a combination of arcs (dispersion relations with different subtractions), at $t \neq 0$. In the UV, this can be integrated in t against a weight function, demanding a manifestly positive quantity. In the IR this combination of arcs will have non-analyticities from gravity's poles and loop discontinuities, but it will integrate to a finite quantity.

In other words, we have seen how to open the door to treat loop effects as perturbative effects, rather than as an absolute obstruction to finding positivity bounds. Contrary to results in the strictly tree-level approximation, which can be packaged as relations among any finite numbers of coefficients or arcs, the results found here are based on approximating all infinite integrals and sums as finite ones. In this sense, the approach is rooted in the spirit of perturbation theory: it works at finite (albeit arbitrarily large) order in the EFT expansion and can work at any order in a perturbative loop expansion. Loop effects introduce infinitely many terms scaling with higher orders in t anyway. These cannot be removed by improvement. In light of this, partial improvement is qualitatively as good as it can be.

While discussed in the context of gravity, this approach is designed to work for any theory with massless particles. It would be interesting to study the IR structure of these theories in detail and evaluate their impact on positivity bounds quantitatively. In particular in gravity [179], spin-1 bosons [187, 205, 491] or pion physics [159, 188, 189, 492] to understand for instance the interplay between these effects and bounds on the chiral anomaly [190, 191].

It would be interesting to see if some of the results presented in this chapter can be re-summed into more compact expressions valid at all orders. Such expressions might reveal properties of the UV extreme amplitudes that saturate the bounds. The *partial improvement* procedure we proposed is only one of many possible treatments: it is based on identifying the smallest set of arcs needed to cancel all terms, but various combinations are also possible. Alternatively, adding the null constraints, as described in subsection 5.3.4, could lead to more compact forms for the improved arc. Manifestly crossing symmetric dispersion relations [148], provide a different take on this problem, as was discussed in the following chapter.

In this chapter, we also stressed the importance of the Müntz-Szász theorem, which highlights the tension between Taylor expanding an amplitude and their appearance in distributions. Besides the case of smeared positivity bounds, such a situation typically does arise in the context of EFTs. Indeed, the very idea of EFTs is based on Taylor expanding around small energies. The amplitude stemming from such an EFT construction is then used as a distribution in cross sections or other observables, where it is integrated over a finite energy range, or another certain measure. The Müntz-Szász theorem implies that to reverse-engineer this, i.e. to extract the coefficients from integrated distributions, we would need an infinite amount of extra information. As discussed, this can be in the form of assumptions about the convergence of the EFT, as is the case for phenomenological applications of EFTs [478], or in the form of null constraints as implied by full crossing symmetry at tree-level, as it is for positivity bounds. This problem could also potentially appear in the context of the non-perturbative S-Matrix bootstrap [493, 494], where one searches for a bound on the low-lying coefficients in the energy expansion of a generic function; it would be interesting to understand whether analyticity in both s and t provides a solution to this puzzle.

7.5 Positivity Bounds and Gravity Loops

In this chapter we discussed positivity bounds from dispersion relations in the EFT of a spin-0 particle coupled to gravity, including loop effects. We worked at finite IR couplings and focussed on effects coming from loops of the massless particles.

Amusingly, our most important result is that loop effects are calculable and small – under the right circumstances. The path to this conclusion, teaches us several lessons. Discontinuities from a box-diagram introduce singularities in dispersion relations at small fixed-t. We compared different methods to obtain the bounds from such dispersion relations, and found which ones are immune to these singularities: the approach of [226] and the manifestly crossing-symmetric one [148, 473]. The methods are completely different both in terms of their underlying hypothesis (such as analyticity and polynomial boundedness) and the methodology by which they are implemented (different slices in s, t complex planes). Thus, they offer us an important

check for our results, showing agreement within our computational abilities.

With these methods, we have addressed the question of how much loop effects modify tree-level bounds. Alas, tree-level extremal theories tend to saturate the validity of the EFT expansion. This is an important show-stopper given that at even 1-loop level *all* EFT couplings enter dispersion relations simultaneously. We have identified Eq. (6.59) as the simplest requirement which is physical, IR testable and guarantees that only a finite number of effects must be taken into account. The computation is robust, and loop-effects are indeed of the expected size, as shown in Fig. 6.10. Higher-loop effects will bear no surprises, beyond the obvious quantitative refinements of the perturbative expansion, as they should not qualitatively change the analytic properties of the amplitude as substantially as the first loop.

Regarding the addition of the initial loops, the effects may be small, but the changes needed to introduce them are significant. Indeed, the combination of the IR-safe approaches [148, 226] and the convergence condition Eq. (6.59), imply $O(1)$ changes in the bounds w.r.t. the original approach of Ref. [185]. Moreover, these changes are already evident when implemented at tree-level, as shown in Fig. 6.9.

The first running coefficients were identified: $g_{2,0}$ for $d \leq 4$, $g_{3,1}$ for $4 < d \leq 6$, and $g_{4,0}$ for $6 < d \leq 8$. This is significant as the running of a relevant operator dominates over less relevant ones at low energies. In bounds coming from dispersion relations, this implies that for $d = 5, 6$, the (running) coefficient $g_{4,0}(M)$, along with all less relevant terms, receives polynomially growing corrections at small M. For $d \geq 7$, this behaviour begins at $g_{6,0}(M)$. The constraints on these coefficients are determined by forward dynamics, and indicate that Wilson coefficients can become negative, as discussed in Ref. [147] – the sign-definiteness being a direct consequence of unitarity in the EFT.

There are many further questions left to be addressed as a result. It would also be satisfying to identify any non-trivial healthy UV completions involving gravity which sit in the allowed region. Are there any theories that satisfy these bounds and not those of Ref. [185]? In particular, understanding if the upper bound $|t| < M^2/2$ implied by the loop-resilient approaches bears any deeper meaning in terms of assumptions on the underlying theories that satisfy these dispersion relations. Conversely, can we exploit these different t-ranges to exclude unwanted theories from the UV spectrum? Smearing at values $|t| > 2M^2$ might rule out certain UV theories with accumulation points/double poles, like the *stu* amplitude of Eq. (6.56).

Again, the direct exploration of other theories using these methods would be interesting. Some of the aspects discussed here are expected to also arise in the theory of electromagnetism coupled to pions in single-subtracted dispersion relations [188, 189, 495]. In particular, it would be interesting to see how constraints involving anomalies [190, 191, 496] are impacted by the finite-N_c effects we discuss, given that the anomaly itself is loop generated.

More generally, it would be interesting to establish a solid bridge between the positivity program on weakly coupled gravitational theories, and fully non-perturbative approaches to the S-matrix bootstrap, as in [151, 227]. The work explored in this chapter constitutes an important step in this direction.

Bibliography

[1] N. Bohr, "On the Constitution of Atoms and Molecules," *Phil. Mag. Ser. 6* **26** (1913) 1–24.

[2] S. Weinberg, *The Quantum Theory of Fields. Vol. 1: Foundations*. Cambridge University Press, 6, 2005.

[3] K. G. Wilson, "The renormalization group and critical phenomena," *Rev. Mod. Phys.* **55** (1983) 583–600.

[4] I. Z. Rothstein, "TASI lectures on effective field theories," arXiv:hep-ph/0308266 [hep-ph].

[5] D. B. Kaplan, "Five lectures on effective field theory," arXiv:nucl-th/0510023.

[6] W. Buchmuller and D. Wyler, "Effective Lagrangian Analysis of New Interactions and Flavor Conservation," *Nucl. Phys. B* **268** (1986) 621–653.

[7] B. Grzadkowski, M. Iskrzynski, M. Misiak, and J. Rosiek, "Dimension-Six Terms in the Standard Model Lagrangian," *JHEP* **10** (2010) 085, arXiv:1008.4884 [hep-ph].

[8] R. Contino, M. Ghezzi, C. Grojean, M. Muhlleitner, and M. Spira, "Effective Lagrangian for a light Higgs-like scalar," *JHEP* **07** (2013) 035, arXiv:1303.3876 [hep-ph].

[9] B. Henning, X. Lu, and H. Murayama, "How to use the Standard Model effective field theory," *JHEP* **01** (2016) 023, arXiv:1412.1837 [hep-ph].

[10] F. Englert and R. Brout, "Broken Symmetry and the Mass of Gauge Vector Mesons," *Phys. Rev. Lett.* **13** (1964) 321–323.

[11] P. W. Higgs, "Broken Symmetries and the Masses of Gauge Bosons," *Phys. Rev. Lett.* **13** (1964) 508–509.

[12] G. S. Guralnik, C. R. Hagen, and T. W. B. Kibble, "Global Conservation Laws and Massless Particles," *Phys. Rev. Lett.* **13** (1964) 585–587.

[13] S. Weinberg, "A Model of Leptons," *Phys. Rev. Lett.* **19** (1967) 1264–1266.

[14] **Particle Data Group** Collaboration, S. Navas *et al.*, "Review of particle physics," *Phys. Rev. D* **110** no. 3, (2024) 030001.

[15] S. R. Coleman, J. Wess, and B. Zumino, "Structure of phenomenological Lagrangians. 1.," *Phys. Rev.* **177** (1969) 2239–2247.

[16] C. G. Callan, Jr., S. R. Coleman, J. Wess, and B. Zumino, "Structure of phenomenological Lagrangians. 2.," *Phys. Rev.* **177** (1969) 2247–2250.

[17] D. V. Volkov, "Phenomenological Lagrangians," *Fiz. Elem. Chast. Atom. Yadra* **4** (1973) 3–41.

[18] L. V. Delacrétaz, S. Endlich, A. Monin, R. Penco, and F. Riva, "(Re-)Inventing the Relativistic Wheel: Gravity, Cosets, and Spinning Objects," *JHEP* **11** (2014) 008, arXiv:1405.7384 [hep-th].

[19] S. Scherer, "Introduction to chiral perturbation theory," *Adv. Nucl. Phys.* **27** (2003) 277, arXiv:hep-ph/0210398.

[20] A. Pich, "Chiral perturbation theory," *Rept. Prog. Phys.* **58** (1995) 563–610, arXiv:hep-ph/9502366.

[21] J. Gasser and H. Leutwyler, "Chiral Perturbation Theory to One Loop," *Annals Phys.* **158** (1984) 142.

[22] M. C. Gonzalez-Garcia and M. Maltoni, "Phenomenology with Massive Neutrinos," *Phys. Rept.* **460** (2008) 1–129, arXiv:0704.1800 [hep-ph].

[23] F. Feruglio, "Pieces of the Flavour Puzzle," *Eur. Phys. J. C* **75** no. 8, (2015) 373, arXiv:1503.04071 [hep-ph].

[24] S. Das Bakshi, J. Chakrabortty, and S. K. Patra, "CoDEx: Wilson coefficient calculator connecting

SMEFT to UV theory," *Eur. Phys. J. C* **79** no. 1, (2019) 21, arXiv:1808.04403 [hep-ph].
[25] A. Carmona, A. Lazopoulos, P. Olgoso, and J. Santiago, "Matchmakereft: automated tree-level and one-loop matching," *SciPost Phys.* **12** no. 6, (2022) 198, arXiv:2112.10787 [hep-ph].
[26] J. Fuentes-Martín, M. König, J. Pagès, A. E. Thomsen, and F. Wilsch, "A proof of concept for matchete: an automated tool for matching effective theories," *Eur. Phys. J. C* **83** no. 7, (2023) 662, arXiv:2212.04510 [hep-ph].
[27] S. A. R. Ellis, J. Quevillon, P. N. H. Vuong, T. You, and Z. Zhang, "The Fermionic Universal One-Loop Effective Action," *JHEP* **11** (2020) 078, arXiv:2006.16260 [hep-ph].
[28] **2dFGRS** Collaboration, S. Cole *et al.*, "The 2dF Galaxy Redshift Survey: Power-spectrum analysis of the final dataset and cosmological implications," *Mon. Not. Roy. Astron. Soc.* **362** (2005) 505–534, arXiv:astro-ph/0501174.
[29] E. Corbelli and P. Salucci, "The Extended Rotation Curve and the Dark Matter Halo of M33," *Mon. Not. Roy. Astron. Soc.* **311** (2000) 441–447, arXiv:astro-ph/9909252.
[30] D. Clowe, A. Gonzalez, and M. Markevitch, "Weak lensing mass reconstruction of the interacting cluster 1E0657-558: Direct evidence for the existence of dark matter," *Astrophys. J.* **604** (2004) 596–603, arXiv:astro-ph/0312273.
[31] M. Markevitch, A. H. Gonzalez, D. Clowe, A. Vikhlinin, L. David, W. Forman, C. Jones, S. Murray, and W. Tucker, "Direct constraints on the dark matter self-interaction cross-section from the merging galaxy cluster 1E0657-56," *Astrophys. J.* **606** (2004) 819–824, arXiv:astro-ph/0309303.
[32] **Planck** Collaboration, N. Aghanim *et al.*, "Planck 2018 results. I. Overview and the cosmological legacy of Planck," *Astron. Astrophys.* **641** (2020) A1, arXiv:1807.06205 [astro-ph.CO].
[33] M. Milgrom, "A Modification of the Newtonian dynamics as a possible alternative to the hidden mass hypothesis," *Astrophys. J.* **270** (1983) 365–370.
[34] M. Milgrom, "A Modification of the Newtonian dynamics: Implications for galaxies," *Astrophys. J.* **270** (1983) 371–383.
[35] P. Natarajan and H. Zhao, "MOND plus classical neutrinos not enough for cluster lensing," *Mon. Not. Roy. Astron. Soc.* **389** (2008) 250, arXiv:0806.3080 [astro-ph].
[36] **SDSS** Collaboration, K. N. Abazajian *et al.*, "The Seventh Data Release of the Sloan Digital Sky Survey," *Astrophys. J. Suppl.* **182** (2009) 543–558, arXiv:0812.0649 [astro-ph].
[37] **WMAP** Collaboration, N. Jarosik *et al.*, "Seven-Year Wilkinson Microwave Anisotropy Probe (WMAP) Observations: Sky Maps, Systematic Errors, and Basic Results," *Astrophys. J. Suppl.* **192** (2011) 14, arXiv:1001.4744 [astro-ph.CO].
[38] D. Vadacchino, "A review on Glueball hunting," in *39th International Symposium on Lattice Field Theory*. 5, 2023. arXiv:2305.04869 [hep-lat].
[39] E. Witten, "Cosmic Separation of Phases," *Phys. Rev. D* **30** (1984) 272–285.
[40] **MACHO** Collaboration, K. Griest, "Baryonic dark matter and Machos," *Nucl. Phys. B Proc. Suppl.* **91** (2001) 393–397.
[41] **Macho** Collaboration, R. A. Allsman *et al.*, "MACHO project limits on black hole dark matter in the 1-30 solar mass range," *Astrophys. J. Lett.* **550** (2001) L169, arXiv:astro-ph/0011506.
[42] **MACHO** Collaboration, C. Alcock *et al.*, "The MACHO project: Microlensing results from 5.7 years of LMC observations," *Astrophys. J.* **542** (2000) 281–307, arXiv:astro-ph/0001272.
[43] S. Tremaine and J. E. Gunn, "Dynamical Role of Light Neutral Leptons in Cosmology," *Phys. Rev. Lett.* **42** (1979) 407–410.
[44] B. Dasgupta and J. Kopp, "Sterile Neutrinos," *Phys. Rept.* **928** (2021) 1–63, arXiv:2106.05913 [hep-ph].
[45] **XENON** Collaboration, E. Aprile *et al.*, "Dark Matter Search Results from a One Ton-Year Exposure of XENON1T," *Phys. Rev. Lett.* **121** no. 11, (2018) 111302, arXiv:1805.12562 [astro-ph.CO].
[46] **XENON** Collaboration, E. Aprile *et al.*, "WIMP Dark Matter Search using a 3.1 tonne $\times$ year Exposure of the XENONnT Experiment," arXiv:2502.18005 [hep-ex].
[47] **PandaX-4T** Collaboration, Y. Meng *et al.*, "Dark Matter Search Results from the PandaX-4T Commissioning Run," *Phys. Rev. Lett.* **127** no. 26, (2021) 261802, arXiv:2107.13438 [hep-ex].

[48] **LZ** Collaboration, J. Aalbers *et al.*, "First Dark Matter Search Results from the LUX-ZEPLIN (LZ) Experiment," *Phys. Rev. Lett.* **131** no. 4, (2023) 041002, arXiv:2207.03764 [hep-ex].
[49] **LZ** Collaboration, J. Aalbers *et al.*, "Dark Matter Search Results from 4.2 Tonne-Years of Exposure of the LUX-ZEPLIN (LZ) Experiment," arXiv:2410.17036 [hep-ex].
[50] A. Boveia and C. Doglioni, "Dark Matter Searches at Colliders," *Ann. Rev. Nucl. Part. Sci.* **68** (2018) 429–459, arXiv:1810.12238 [hep-ex].
[51] M. Cirelli, A. Strumia, and J. Zupan, "Dark Matter," arXiv:2406.01705 [hep-ph].
[52] **Fermi-LAT, DES** Collaboration, A. Albert *et al.*, "Searching for Dark Matter Annihilation in Recently Discovered Milky Way Satellites with Fermi-LAT," *Astrophys. J.* **834** no. 2, (2017) 110, arXiv:1611.03184 [astro-ph.HE].
[53] **VERITAS** Collaboration, S. Archambault *et al.*, "Dark Matter Constraints from a Joint Analysis of Dwarf Spheroidal Galaxy Observations with VERITAS," *Phys. Rev. D* **95** no. 8, (2017) 082001, arXiv:1703.04937 [astro-ph.HE].
[54] **IceCube** Collaboration, R. Abbasi *et al.*, "Search for GeV-scale dark matter annihilation in the Sun with IceCube DeepCore," *Phys. Rev. D* **105** no. 6, (2022) 062004, arXiv:2111.09970 [astro-ph.HE].
[55] **H.E.S.S.** Collaboration, H. Abdalla *et al.*, "Search for Dark Matter Annihilation Signals in the H.E.S.S. Inner Galaxy Survey," *Phys. Rev. Lett.* **129** no. 11, (2022) 111101, arXiv:2207.10471 [astro-ph.HE].
[56] K. Griest and M. Kamionkowski, "Unitarity Limits on the Mass and Radius of Dark Matter Particles," *Phys. Rev. Lett.* **64** (1990) 615.
[57] K. Schutz, "Subhalo mass function and ultralight bosonic dark matter," *Phys. Rev. D* **101** no. 12, (2020) 123026, arXiv:2001.05503 [astro-ph.CO].
[58] E. W. Kolb, D. J. H. Chung, and A. Riotto, "WIMPzillas!," *AIP Conf. Proc.* **484** no. 1, (1999) 91–105, arXiv:hep-ph/9810361.
[59] N. Blinov, M. J. Dolan, P. Draper, and J. Kozaczuk, "Dark matter targets for axionlike particle searches," *Phys. Rev. D* **100** no. 1, (2019) 015049, arXiv:1905.06952 [hep-ph].
[60] F. D'Eramo, E. Di Valentino, W. Giarè, F. Hajkarim, A. Melchiorri, O. Mena, F. Renzi, and S. Yun, "Cosmological bound on the QCD axion mass, redux," *JCAP* **09** (2022) 022, arXiv:2205.07849 [astro-ph.CO].
[61] R. T. Co, L. J. Hall, and K. Harigaya, "Axion Kinetic Misalignment Mechanism," *Phys. Rev. Lett.* **124** no. 25, (2020) 251802, arXiv:1910.14152 [hep-ph].
[62] M. Gorghetto, E. Hardy, and G. Villadoro, "Axions from Strings: the Attractive Solution," *JHEP* **07** (2018) 151, arXiv:1806.04677 [hep-ph].
[63] C. Eröncel, Y. Gouttenoire, R. Sato, G. Servant, and P. Simakachorn, "A New Source for (QCD) Axion Dark Matter Production: Curvature-Induced," arXiv:2503.04880 [hep-ph].
[64] M. Weber and W. de Boer, "Determination of the Local Dark Matter Density in our Galaxy," *Astron. Astrophys.* **509** (2010) A25, arXiv:0910.4272 [astro-ph.CO].
[65] D. Y. Cheong, N. L. Rodd, and L.-T. Wang, "Quantum description of wave dark matter," *Phys. Rev. D* **111** no. 1, (2025) 015028, arXiv:2408.04696 [hep-ph].
[66] J. Bonilla, I. Brivio, M. B. Gavela, and V. Sanz, "One-loop corrections to ALP couplings," *JHEP* **11** (2021) 168, arXiv:2107.11392 [hep-ph].
[67] C. B. Adams *et al.*, "Axion Dark Matter," in *Snowmass 2021*. 3, 2022. arXiv:2203.14923 [hep-ex].
[68] D. Antypas *et al.*, "New Horizons: Scalar and Vector Ultralight Dark Matter," arXiv:2203.14915 [hep-ex].
[69] C. Beadle *et al.*, "Quantum Sensing for Dark Matter and Gravitational Waves,".
[70] M. Dine and W. Fischler, "The Not So Harmless Axion," *Phys. Lett. B* **120** (1983) 137–141.
[71] M. Dine, W. Fischler, and M. Srednicki, "A Simple Solution to the Strong CP Problem with a Harmless Axion," *Phys. Lett. B* **104** (1981) 199–202.
[72] J. E. Kim, "Weak Interaction Singlet and Strong CP Invariance," *Phys. Rev. Lett.* **43** (1979) 103.
[73] M. A. Shifman, A. I. Vainshtein, and V. I. Zakharov, "Can Confinement Ensure Natural CP Invariance of Strong Interactions?," *Nucl. Phys. B* **166** (1980) 493–506.

[74] A. R. Zhitnitsky, "On Possible Suppression of the Axion Hadron Interactions. (In Russian)," *Sov. J. Nucl. Phys.* **31** (1980) 260.
[75] A. Caputo and G. Raffelt, "Astrophysical Axion Bounds: The 2024 Edition," *PoS* **COSMICWISPers** (2024) 041, arXiv:2401.13728 [hep-ph].
[76] B. R. Safdi, "TASI Lectures on the Particle Physics and Astrophysics of Dark Matter," *PoS* **TASI2022** (2024) 009, arXiv:2303.02169 [hep-ph].
[77] C. A. J. O'Hare, "Cosmology of axion dark matter," *PoS* **COSMICWISPers** (2024) 040, arXiv:2403.17697 [hep-ph].
[78] L. Di Luzio, M. Giannotti, E. Nardi, and L. Visinelli, "The landscape of QCD axion models," arXiv:2003.01100 [hep-ph].
[79] I. G. Irastorza and J. Redondo, "New experimental approaches in the search for axion-like particles," *Prog. Part. Nucl. Phys.* **102** (2018) 89–159, arXiv:1801.08127 [hep-ph].
[80] A. Caputo, A. J. Millar, C. A. J. O'Hare, and E. Vitagliano, "Dark photon limits: A handbook," *Phys. Rev. D* **104** no. 9, (2021) 095029, arXiv:2105.04565 [hep-ph].
[81] K. R. Dienes, C. F. Kolda, and J. March-Russell, "Kinetic mixing and the supersymmetric gauge hierarchy," *Nucl. Phys. B* **492** (1997) 104–118, arXiv:hep-ph/9610479.
[82] J. Giedt, "Completion of standard model like embeddings," *Annals Phys.* **289** (2001) 251, arXiv:hep-th/0009104.
[83] F. Gmeiner, R. Blumenhagen, G. Honecker, D. Lust, and T. Weigand, "One in a billion: MSSM-like D-brane statistics," *JHEP* **01** (2006) 004, arXiv:hep-th/0510170.
[84] K. R. Dienes, "Statistics on the heterotic landscape: Gauge groups and cosmological constants of four-dimensional heterotic strings," *Phys. Rev. D* **73** (2006) 106010, arXiv:hep-th/0602286.
[85] K. R. Dienes, M. Lennek, D. Senechal, and V. Wasnik, "Supersymmetry versus Gauge Symmetry on the Heterotic Landscape," *Phys. Rev. D* **75** (2007) 126005, arXiv:0704.1320 [hep-th].
[86] A. Arvanitaki, N. Craig, S. Dimopoulos, S. Dubovsky, and J. March-Russell, "String Photini at the LHC," *Phys. Rev. D* **81** (2010) 075018, arXiv:0909.5440 [hep-ph].
[87] A. Corti, M. Haskins, J. Nordström, and T. Pacini, "G_2-manifolds and associative submanifolds via semi-Fano 3-folds," *Duke Math. J.* **164** no. 10, (2015) 1971–2092, arXiv:1207.4470 [math.DG].
[88] W. Taylor and Y.-N. Wang, "A Monte Carlo exploration of threefold base geometries for 4d F-theory vacua," *JHEP* **01** (2016) 137, arXiv:1510.04978 [hep-th].
[89] B. S. Acharya, S. A. R. Ellis, G. L. Kane, B. D. Nelson, and M. J. Perry, "The lightest visible-sector supersymmetric particle is likely to be unstable," *Phys. Rev. Lett.* **117** (2016) 181802, arXiv:1604.05320 [hep-ph].
[90] J. Halverson and P. Langacker, "TASI Lectures on Remnants from the String Landscape," *PoS* **TASI2017** (2018) 019, arXiv:1801.03503 [hep-th].
[91] B. S. Acharya, A. Maharana, and F. Muia, "Hidden Sectors in String Theory: Kinetic Mixings, Fifth Forces and Quintessence," *JHEP* **03** (2019) 048, arXiv:1811.10633 [hep-th].
[92] B. Holdom, "Two U(1)'s and Epsilon Charge Shifts," *Phys. Lett. B* **166** (1986) 196–198.
[93] A. E. Nelson and J. Scholtz, "Dark Light, Dark Matter and the Misalignment Mechanism," *Phys. Rev. D* **84** (2011) 103501, arXiv:1105.2812 [hep-ph].
[94] P. Arias, D. Cadamuro, M. Goodsell, J. Jaeckel, J. Redondo, and A. Ringwald, "WISPy Cold Dark Matter," *JCAP* **06** (2012) 013, arXiv:1201.5902 [hep-ph].
[95] P. W. Graham, J. Mardon, and S. Rajendran, "Vector Dark Matter from Inflationary Fluctuations," *Phys. Rev. D* **93** no. 10, (2016) 103520, arXiv:1504.02102 [hep-ph].
[96] M. Bastero-Gil, J. Santiago, L. Ubaldi, and R. Vega-Morales, "Vector dark matter production at the end of inflation," *JCAP* **04** (2019) 015, arXiv:1810.07208 [hep-ph].
[97] R. T. Co, A. Pierce, Z. Zhang, and Y. Zhao, "Dark Photon Dark Matter Produced by Axion Oscillations," *Phys. Rev. D* **99** no. 7, (2019) 075002, arXiv:1810.07196 [hep-ph].
[98] J. A. Dror, K. Harigaya, and V. Narayan, "Parametric Resonance Production of Ultralight Vector Dark Matter," *Phys. Rev. D* **99** no. 3, (2019) 035036, arXiv:1810.07195 [hep-ph].
[99] P. Agrawal, N. Kitajima, M. Reece, T. Sekiguchi, and F. Takahashi, "Relic Abundance of Dark Photon Dark Matter," *Phys. Lett. B* **801** (2020) 135136, arXiv:1810.07188 [hep-ph].

[100] M. Bastero-Gil, J. Santiago, R. Vega-Morales, and L. Ubaldi, "Dark photon dark matter from a rolling inflaton," *JCAP* **02** no. 02, (2022) 015, arXiv:2103.12145 [hep-ph].
[101] L. F. Abbott and P. Sikivie, "A Cosmological Bound on the Invisible Axion," *Phys. Lett. B* **120** (1983) 133–136.
[102] J. Preskill, M. B. Wise, and F. Wilczek, "Cosmology of the Invisible Axion," *Phys. Lett. B* **120** (1983) 127–132.
[103] P. Fileviez Perez and H. H. Patel, "The Electroweak Vacuum Angle," *Phys. Lett. B* **732** (2014) 241–243, arXiv:1402.6340 [hep-ph].
[104] M. Pospelov and A. Ritz, "Electric dipole moments as probes of new physics," *Annals Phys.* **318** (2005) 119–169, arXiv:hep-ph/0504231.
[105] C. Abel *et al.*, "Measurement of the Permanent Electric Dipole Moment of the Neutron," *Phys. Rev. Lett.* **124** no. 8, (2020) 081803, arXiv:2001.11966 [hep-ex].
[106] M. Dine, L. Stephenson Haskins, L. Ubaldi, and D. Xu, "Some Remarks on Anthropic Approaches to the Strong CP Problem," *JHEP* **05** (2018) 171, arXiv:1801.03466 [hep-th].
[107] I. B. Khriplovich, "Quark Electric Dipole Moment and Induced θ Term in the Kobayashi-Maskawa Model," *Phys. Lett. B* **173** (1986) 193–196.
[108] J. R. Ellis and M. K. Gaillard, "Strong and Weak CP Violation," *Nucl. Phys. B* **150** (1979) 141–162.
[109] I. B. Khriplovich and A. I. Vainshtein, "Infinite renormalization of Theta term and Jarlskog invariant for CP violation," *Nucl. Phys. B* **414** (1994) 27–32, arXiv:hep-ph/9308334.
[110] **Flavour Lattice Averaging Group (FLAG)** Collaboration, Y. Aoki *et al.*, "FLAG Review 2024," arXiv:2411.04268 [hep-lat].
[111] R. D. Peccei and H. R. Quinn, "CP Conservation in the Presence of Instantons," *Phys. Rev. Lett.* **38** (1977) 1440–1443.
[112] S. Weinberg, "A New Light Boson?," *Phys. Rev. Lett.* **40** (1978) 223–226.
[113] F. Wilczek, "Problem of Strong P and T Invariance in the Presence of Instantons," *Phys. Rev. Lett.* **40** (1978) 279–282.
[114] M. Kamionkowski and J. March-Russell, "Planck scale physics and the Peccei-Quinn mechanism," *Phys. Lett. B* **282** (1992) 137–141, arXiv:hep-th/9202003 [hep-th].
[115] L. M. Carpenter, M. Dine, G. Festuccia, and L. Ubaldi, "Axions in Gauge Mediation," *Phys. Rev. D* **80** (2009) 125023, arXiv:0906.5015 [hep-th].
[116] K.-w. Choi, "A QCD axion from higher dimensional gauge field," *Phys. Rev. Lett.* **92** (2004) 101602, arXiv:hep-ph/0308024.
[117] P. Svrcek and E. Witten, "Axions in string theory," *JHEP* **06** (2006) 051, arXiv:hep-th/0605206.
[118] A. Arvanitaki, S. Dimopoulos, S. Dubovsky, N. Kaloper, and J. March-Russell, "String Axiverse," *Phys. Rev. D* **81** (2010) 123530, arXiv:0905.4720 [hep-th].
[119] N. Gendler, D. J. E. Marsh, L. McAllister, and J. Moritz, "Glimmers from the Axiverse," arXiv:2309.13145 [hep-th].
[120] M. Demirtas, N. Gendler, C. Long, L. McAllister, and J. Moritz, "PQ axiverse," *JHEP* **06** (2023) 092, arXiv:2112.04503 [hep-th].
[121] I. Broeckel, M. Cicoli, A. Maharana, K. Singh, and K. Sinha, "Moduli stabilisation and the statistics of axion physics in the landscape," *JHEP* **08** (2021) 059, arXiv:2105.02889 [hep-th]. [Addendum: JHEP 01, 191 (2022)].
[122] E. Witten, "Dynamical Breaking of Supersymmetry," *Nucl. Phys. B* **188** (1981) 513.
[123] S. Dimopoulos and H. Georgi, "Softly Broken Supersymmetry and SU(5)," *Nucl. Phys. B* **193** (1981) 150–162.
[124] N. Sakai, "Naturalness in Supersymmetric Guts," *Z. Phys. C* **11** (1981) 153.
[125] S. Weinberg, "Implications of Dynamical Symmetry Breaking," *Phys. Rev. D* **13** (1976) 974–996. [Addendum: Phys.Rev.D 19, 1277–1280 (1979)].
[126] L. Susskind, "Dynamics of Spontaneous Symmetry Breaking in the Weinberg-Salam Theory," *Phys. Rev. D* **20** (1979) 2619–2625.
[127] Z. Chacko, H.-S. Goh, and R. Harnik, "The Twin Higgs: Natural electroweak breaking from mirror symmetry," *Phys. Rev. Lett.* **96** (2006) 231802, arXiv:hep-ph/0506256.

[128] **Supernova Cosmology Project** Collaboration, S. Perlmutter *et al.*, "Measurements of Ω and Λ from 42 High Redshift Supernovae," *Astrophys. J.* **517** (1999) 565–586, arXiv:astro-ph/9812133.
[129] **SDSS** Collaboration, R. Kessler *et al.*, "First-year Sloan Digital Sky Survey-II (SDSS-II) Supernova Results: Hubble Diagram and Cosmological Parameters," *Astrophys. J. Suppl.* **185** (2009) 32–84, arXiv:0908.4274 [astro-ph.CO].
[130] D. Larson *et al.*, "Seven-Year Wilkinson Microwave Anisotropy Probe (WMAP) Observations: Power Spectra and WMAP-Derived Parameters," *Astrophys. J. Suppl.* **192** (2011) 16, arXiv:1001.4635 [astro-ph.CO].
[131] R. Durrer, "What do we really know about Dark Energy?," *Phil. Trans. Roy. Soc. Lond. A* **369** (2011) 5102–5114, arXiv:1103.5331 [astro-ph.CO].
[132] D. Bailin and A. Love, *Supersymmetric Gauge Field Theory and String Theory*. Taylor & Francis, 1994.
[133] S. Bahamonde, C. G. Böhmer, S. Carloni, E. J. Copeland, W. Fang, and N. Tamanini, "Dynamical systems applied to cosmology: dark energy and modified gravity," *Phys. Rept.* **775-777** (2018) 1–122, arXiv:1712.03107 [gr-qc].
[134] J. Martin, "Everything You Always Wanted To Know About The Cosmological Constant Problem (But Were Afraid To Ask)," *Comptes Rendus Physique* **13** (2012) 566–665, arXiv:1205.3365 [astro-ph.CO].
[135] S. Weinberg, "The Cosmological Constant Problem," *Rev. Mod. Phys.* **61** (1989) 1–23.
[136] G. 't Hooft, "Naturalness, chiral symmetry, and spontaneous chiral symmetry breaking," *NATO Sci. Ser. B* **59** (1980) 135–157.
[137] P. A. M. Dirac, "The Cosmological constants," *Nature* **139** (1937) 323.
[138] S. R. Coleman and R. Jackiw, "Why dilatation generators do not generate dilatations?," *Annals Phys.* **67** (1971) 552–598.
[139] D. M. Capper and M. J. Duff, "Trace anomalies in dimensional regularization," *Nuovo Cim. A* **23** (1974) 173–183.
[140] V. Agrawal, S. M. Barr, J. F. Donoghue, and D. Seckel, "Viable range of the mass scale of the standard model," *Phys. Rev. D* **57** (1998) 5480–5492, arXiv:hep-ph/9707380.
[141] A. G. Cohen, D. B. Kaplan, and A. E. Nelson, "Effective field theory, black holes, and the cosmological constant," *Phys. Rev. Lett.* **82** (1999) 4971–4974, arXiv:hep-th/9803132.
[142] J. Bros, H. Epstein, and V. J. Glaser, "Some rigorous analyticity properties of the four-point function in momentum space," *Nuovo Cim.* **31** (1964) 1265–1302.
[143] R. J. Eden, "Theorems on high energy collisions of elementary particles," *Rev. Mod. Phys.* **43** (1971) 15–35.
[144] A. Adams, N. Arkani-Hamed, S. Dubovsky, A. Nicolis, and R. Rattazzi, "Causality, analyticity and an IR obstruction to UV completion," *JHEP* **10** (2006) 014, arXiv:hep-th/0602178 [hep-th].
[145] N. Arkani-Hamed, T.-C. Huang, and Y.-t. Huang, "The EFT-Hedron," *JHEP* **05** (2021) 259, arXiv:2012.15849 [hep-th].
[146] C. de Rham, S. Melville, A. J. Tolley, and S.-Y. Zhou, "Positivity Bounds for Scalar Field Theories," *Phys. Rev.* **D96** no. 8, (2017) 081702, arXiv:1702.06134 [hep-th].
[147] B. Bellazzini, J. E. Miró, R. Rattazzi, M. Riembau, and F. Riva, "Positive moments for scattering amplitudes," *Phys. Rev. D* **104** (Aug, 2021) 036006. https://link.aps.org/doi/10.1103/PhysRevD.104.036006.
[148] A. Sinha and A. Zahed, "Crossing Symmetric Dispersion Relations in Quantum Field Theories," *Phys. Rev. Lett.* **126** no. 18, (2021) 181601, arXiv:2012.04877 [hep-th].
[149] A. J. Tolley, Z.-Y. Wang, and S.-Y. Zhou, "New positivity bounds from full crossing symmetry," *JHEP* **05** (2021) 255, arXiv:2011.02400 [hep-th].
[150] S. Caron-Huot and V. Van Duong, "Extremal Effective Field Theories," *JHEP* **05** (2021) 280, arXiv:2011.02957 [hep-th].
[151] J. Elias Miro, A. Guerrieri, and M. A. Gumus, "Bridging positivity and S-matrix bootstrap bounds," *JHEP* **05** (2023) 001, arXiv:2210.01502 [hep-th].
[152] S. D. Chowdhury, K. Ghosh, P. Haldar, P. Raman, and A. Sinha, "Crossing Symmetric Spinning

S-matrix Bootstrap: EFT bounds," *SciPost Phys.* **13** no. 3, (2022) 051, arXiv:2112.11755 [hep-th].
[153] T. N. Pham and T. N. Truong, "Evaluation of the Derivative Quartic Terms of the Meson Chiral Lagrangian from Forward Dispersion Relation," *Phys. Rev.* **D31** (1985) 3027.
[154] B. Ananthanarayan, D. Toublan, and G. Wanders, "Consistency of the Chiral Pion Pion Scattering Amplitudes with Axiomatic Constraints," *Phys. Rev. D* **51** (1995) 1093–1100, arXiv:hep-ph/9410302.
[155] M. R. Pennington and J. Portoles, "The Chiral Lagrangian Parameters, L1, L2, are Determined by the Rho Resonance," *Phys. Lett. B* **344** (1995) 399–406, arXiv:hep-ph/9409426.
[156] J. Bijnens, G. Colangelo, G. Ecker, J. Gasser, and M. E. Sainio, "Pion-Pion Scattering at Low Energy," *Nucl. Phys. B* **508** (1997) 263–310, arXiv:hep-ph/9707291. [Erratum: Nucl.Phys.B 517, 639–639 (1998)].
[157] B. Ananthanarayan, G. Colangelo, J. Gasser, and H. Leutwyler, "Roy Equation Analysis of Pi Pi Scattering," *Phys. Rept.* **353** (2001) 207–279, arXiv:hep-ph/0005297 [hep-ph].
[158] G. Colangelo, J. Gasser, and H. Leutwyler, "$\pi\pi$ scattering," *Nucl. Phys. B* **603** (2001) 125–179, arXiv:hep-ph/0103088.
[159] A. V. Manohar and V. Mateu, "Dispersion Relation Bounds for pi pi Scattering," *Phys. Rev. D* **77** (2008) 094019, arXiv:0801.3222 [hep-ph].
[160] V. Mateu, "Universal Bounds for $SU(3)$ Low Energy Constants," *Phys. Rev. D* **77** (2008) 094020, arXiv:0801.3627 [hep-ph].
[161] A. L. Guerrieri, J. Penedones, and P. Vieira, "Bootstrapping QCD Using Pion Scattering Amplitudes," *Phys. Rev. Lett.* **122** no. 24, (2019) 241604, arXiv:1810.12849 [hep-th].
[162] A. L. Guerrieri, J. Penedones, and P. Vieira, "S-matrix bootstrap for effective field theories: massless pions," *JHEP* **06** (2021) 088, arXiv:2011.02802 [hep-th].
[163] A. Zahed, "Positivity and Geometric Function Theory Constraints on Pion Scattering," *JHEP* **12** (2021) 036, arXiv:2108.10355 [hep-th].
[164] F. Figueroa and P. Tourkine, "Unitarity and Low Energy Expansion of the Coon Amplitude," *Phys. Rev. Lett.* **129** no. 12, (2022) 121602, arXiv:2201.12331 [hep-th].
[165] P. Bittar, S. Fichet, and L. de Souza, "Gravity-induced photon interactions and infrared consistency in any dimensions." 2024. https://arxiv.org/abs/2404.07254.
[166] X. O. Camanho, J. D. Edelstein, J. Maldacena, and A. Zhiboedov, "Causality Constraints on Corrections to the Graviton Three-Point Coupling," *JHEP* **02** (2016) 020, arXiv:1407.5597 [hep-th].
[167] B. Bellazzini, C. Cheung, and G. N. Remmen, "Quantum Gravity Constraints from Unitarity and Analyticity," *Phys. Rev.* **D93** no. 6, (2016) 064076, arXiv:1509.00851 [hep-th].
[168] Y. Hamada, T. Noumi, and G. Shiu, "Weak Gravity Conjecture from Unitarity and Causality," *Phys. Rev. Lett.* **123** no. 5, (2019) 051601, arXiv:1810.03637 [hep-th].
[169] J. Bonifacio and K. Hinterbichler, "Bounds on Amplitudes in Effective Theories with Massive Spinning Particles," *Phys. Rev. D* **98** no. 4, (2018) 045003, arXiv:1804.08686 [hep-th].
[170] B. Bellazzini, M. Lewandowski, and J. Serra, "Positivity of Amplitudes, Weak Gravity Conjecture, and Modified Gravity," *Phys. Rev. Lett.* **123** no. 25, (2019) 251103, arXiv:1902.03250 [hep-th].
[171] S. Melville and J. Noller, "Positivity in the Sky," *Phys. Rev.* **D101** no. 2, (2020) 021502, arXiv:1904.05874 [astro-ph.CO].
[172] J. Tokuda, K. Aoki, and S. Hirano, "Gravitational Positivity Bounds," *JHEP* **11** (2020) 054, arXiv:2007.15009 [hep-th].
[173] M. Herrero-Valea, R. Santos-Garcia, and A. Tokareva, "Massless Positivity in Graviton Exchange," *Phys. Rev. D* **104** no. 8, (2021) 085022, arXiv:2011.11652 [hep-th].
[174] J. D. Edelstein, R. Ghosh, A. Laddha, and S. Sarkar, "Causality constraints in Quadratic Gravity," *JHEP* **09** (2021) 150, arXiv:2107.07424 [hep-th].
[175] J. D. Edelstein, R. Ghosh, A. Laddha, and S. Sarkar, "Restoring Causality in Higher Curvature Gravity," arXiv:2409.16935 [hep-th].
[176] Z. Bern, D. Kosmopoulos, and A. Zhiboedov, "Gravitational effective field theory islands, low-spin

dominance, and the four-graviton amplitude," *J. Phys. A* **54** no. 34, (2021) 344002, arXiv:2103.12728 [hep-th].
[177] B. Bellazzini, G. Isabella, M. Lewandowski, and F. Sgarlata, "Gravitational Causality and the Self-Stress of Photons," *JHEP* **05** (2022) 154, arXiv:2108.05896 [hep-th].
[178] N. Arkani-Hamed, Y.-t. Huang, J.-Y. Liu, and G. N. Remmen, "Causality, unitarity, and the weak gravity conjecture," *JHEP* **03** (2022) 083, arXiv:2109.13937 [hep-th].
[179] S. Caron-Huot, Y.-Z. Li, J. Parra-Martinez, and D. Simmons-Duffin, "Causality constraints on corrections to Einstein gravity," *JHEP* **05** (2023) 122, arXiv:2201.06602 [hep-th].
[180] F. Serra, J. Serra, E. Trincherini, and L. G. Trombetta, "Causality constraints on black holes beyond GR," *JHEP* **08** (2022) 157, arXiv:2205.08551 [hep-th].
[181] T. Noumi and J. Tokuda, "Finite energy sum rules for gravitational Regge amplitudes," *JHEP* **06** (2023) 032, arXiv:2212.08001 [hep-th].
[182] M. Herrero-Valea, A. S. Koshelev, and A. Tokareva, "UV graviton scattering and positivity bounds from IR dispersion relations," *Phys. Rev. D* **106** no. 10, (2022) 105002, arXiv:2205.13332 [hep-th].
[183] L.-Y. Chiang, Y.-t. Huang, W. Li, L. Rodina, and H.-C. Weng, "(Non)-projective bounds on gravitational EFT," arXiv:2201.07177 [hep-th].
[184] B. Bellazzini, G. Isabella, and M. M. Riva, "Classical vs quantum eikonal scattering and its causal structure," *JHEP* **04** (2023) 023, arXiv:2211.00085 [hep-th].
[185] S. Caron-Huot, D. Mazac, L. Rastelli, and D. Simmons-Duffin, "Sharp boundaries for the swampland," *JHEP* **07** (2021) 110, arXiv:2102.08951 [hep-th].
[186] S. Caron-Huot, Y.-Z. Li, J. Parra-Martinez, and D. Simmons-Duffin, "Graviton partial waves and causality in higher dimensions," *Phys. Rev. D* **108** no. 2, (2023) 026007, arXiv:2205.01495 [hep-th].
[187] J. Henriksson, B. McPeak, F. Russo, and A. Vichi, "Bounding violations of the weak gravity conjecture," *JHEP* **08** (2022) 184, arXiv:2203.08164 [hep-th].
[188] J. Albert and L. Rastelli, "Bootstrapping pions at large N," *JHEP* **08** (2022) 151, arXiv:2203.11950 [hep-th].
[189] C. Fernandez, A. Pomarol, F. Riva, and F. Sciotti, "Cornering large-N_c QCD with positivity bounds," *JHEP* **06** (2023) 094, arXiv:2211.12488 [hep-th].
[190] J. Albert and L. Rastelli, "Bootstrapping Pions at Large N. Part II: Background Gauge Fields and the Chiral Anomaly," arXiv:2307.01246 [hep-th].
[191] T. Ma, A. Pomarol, and F. Sciotti, "Bootstrapping the chiral anomaly at large N_c," *JHEP* **11** (2023) 176, arXiv:2307.04729 [hep-th].
[192] C. de Rham, S. Jaitly, and A. J. Tolley, "Constraints on Regge behavior from IR physics," *Phys. Rev. D* **108** no. 4, (2023) 046011, arXiv:2212.04975 [hep-th].
[193] Z. Bern, E. Herrmann, D. Kosmopoulos, and R. Roiban, "Effective Field Theory islands from perturbative and nonperturbative four-graviton amplitudes," *JHEP* **01** (2023) 113, arXiv:2205.01655 [hep-th].
[194] C. Eckner, F. Figueroa, and P. Tourkine, "The Regge bootstrap, from linear to non-linear trajectories," arXiv:2401.08736 [hep-th].
[195] K. Häring and A. Zhiboedov, "The Stringy S-matrix Bootstrap: Maximal Spin and Superpolynomial Softness," arXiv:2311.13631 [hep-th].
[196] B. Bellazzini and F. Riva, "New phenomenological and theoretical perspective on anomalous ZZ and Z? processes," *Phys. Rev.* **D98** no. 9, (2018) 095021, arXiv:1806.09640 [hep-ph].
[197] C. Zhang and S.-Y. Zhou, "Positivity Bounds on Vector Boson Scattering at the Lhc," *Phys. Rev.* **D100** no. 9, (2019) 095003, arXiv:1808.00010 [hep-ph].
[198] G. N. Remmen and N. L. Rodd, "Flavor Constraints from Unitarity and Analyticity," *Phys. Rev. Lett.* **125** no. 8, (2020) 081601, arXiv:2004.02885 [hep-ph]. [Erratum: Phys.Rev.Lett. 127, 149901 (2021)].
[199] D. Karateev, J. Marucha, J. a. Penedones, and B. Sahoo, "Bootstrapping the a-anomaly in 4d QFTs," *JHEP* **12** (2022) 136, arXiv:2204.01786 [hep-th].
[200] K. Häring, A. Hebbar, D. Karateev, M. Meineri, and J. a. Penedones, "Bounds on photon scattering,"

arXiv:2211.05795 [hep-th].
[201] A. Hebbar, D. Karateev, and J. Penedones, "Spinning S-matrix bootstrap in 4d," *JHEP* **01** (2022) 060, arXiv:2011.11708 [hep-th].
[202] Q. Bonnefoy, E. Gendy, and C. Grojean, "Positivity Bounds on Minimal Flavor Violation," *JHEP* **04** (2021) 115, arXiv:2011.12855 [hep-ph].
[203] M. Riembau, "Full Unitarity and the Moments of Scattering Amplitudes," arXiv:2212.14056 [hep-th].
[204] F. Acanfora, A. Guerrieri, K. Häring, and D. Karateev, "Bounds on scattering of neutral Goldstones," *JHEP* **03** (2024) 028, arXiv:2310.06027 [hep-th].
[205] F. Bertucci, J. Henriksson, B. McPeak, S. Ricossa, F. Riva, and A. Vichi, "Positivity Bounds on Massive Vectors," arXiv:2402.13327 [hep-th].
[206] J. Elias Miro, A. Guerrieri, and M. A. Gumus, "Extremal Higgs couplings," arXiv:2311.09283 [hep-ph].
[207] M. McCullough, M. Riembau, and L. Ricci, "Boundaries of Universal Theories," arXiv:2312.03834 [hep-ph].
[208] D. Ghosh, R. Sharma, and F. Ullah, "Amplitude's positivity vs. subluminality: causality and unitarity constraints on dimension 6 & 8 gluonic operators in the SMEFT," *JHEP* **02** (2023) 199, arXiv:2211.01322 [hep-ph].
[209] Z. Komargodski and A. Schwimmer, "On Renormalization Group Flows in Four Dimensions," *JHEP* **12** (2011) 099, arXiv:1107.3987 [hep-th].
[210] D.-Y. Hong, Z.-H. Wang, and S.-Y. Zhou, "Causality bounds on scalar-tensor EFTs," *JHEP* **10** (2023) 135, arXiv:2304.01259 [hep-th].
[211] C. Englert, G. F. Giudice, A. Greljo, and M. Mccullough, "The $\hat{H}$-Parameter: An Oblique Higgs View," *JHEP* **09** (2019) 041, arXiv:1903.07725 [hep-ph].
[212] B. Bellazzini, F. Riva, J. Serra, and F. Sgarlata, "Massive Higher Spins: Effective Theory and Consistency," *JHEP* **10** (2019) 189, arXiv:1903.08664 [hep-th].
[213] B. Bellazzini, G. Isabella, S. Ricossa, and F. Riva, "Massive gravity is not positive," *Phys. Rev. D* **109** no. 2, (2024) 024051, arXiv:2304.02550 [hep-th].
[214] M. Froissart, "Asymptotic Behavior and Subtractions in the Mandelstam Representation," *Phys. Rev.* **123** (1961) 1053–1057.
[215] Y. S. Jin and A. Martin, "Number of Subtractions in Fixed-Transfer Dispersion Relations," *Phys. Rev.* **135** (1964) B1375–B1377.
[216] K. Häring and A. Zhiboedov, "Gravitational Regge bounds," *SciPost Phys.* **16** no. 1, (2024) 034, arXiv:2202.08280 [hep-th].
[217] M. F. Paulos, J. Penedones, J. Toledo, B. C. van Rees, and P. Vieira, "The S-Matrix Bootstrap. Part Iii: Higher Dimensional Amplitudes," *JHEP* **12** (2019) 040, arXiv:1708.06765 [hep-th].
[218] Y. He and M. Kruczenski, "S-matrix bootstrap in 3+1 dimensions: regularization and dual convex problem," *JHEP* **08** (2021) 125, arXiv:2103.11484 [hep-th].
[219] M. Correia, A. Sever, and A. Zhiboedov, "An Analytical Toolkit for the S-Matrix Bootstrap," arXiv:2006.08221 [hep-th].
[220] L. J. Dixon, "A brief introduction to modern amplitude methods," in *Theoretical Advanced Study Institute in Elementary Particle Physics: Particle Physics: The Higgs Boson and Beyond*, pp. 31–67. 2014. arXiv:1310.5353 [hep-ph].
[221] H. Elvang and Y.-t. Huang, "Scattering Amplitudes," arXiv:1308.1697 [hep-th].
[222] C. Beadle, G. Isabella, D. Perrone, S. Ricossa, F. Riva, and F. Serra, "The EFT Bootstrap at Finite M_{PL}," arXiv:2501.18465 [hep-th].
[223] C. Beadle, S. A. R. Ellis, J. M. Leedom, and N. L. Rodd, "Dark Matter Nuclear Magnetic Resonance is Sensitive to Dark Photons and the Axion-Photon Coupling," arXiv:2505.15897 [hep-ph].
[224] C. Beadle, A. Caputo, and S. A. R. Ellis, "Resonant Conversion of Wave Dark Matter in the Ionosphere," *Phys. Rev. Lett.* **133** no. 25, (2024) 251001, arXiv:2405.13882 [hep-ph].
[225] C. Beadle, S. A. R. Ellis, J. Quevillon, and P. N. Hoa Vuong, "Quadratic coupling of the axion to photons," *Phys. Rev. D* **110** no. 3, (2024) 035019, arXiv:2307.10362 [hep-ph].

[226] C. Beadle, G. Isabella, D. Perrone, S. Ricossa, F. Riva, and F. Serra, "Non-Forward UV/IR Relations," arXiv:2407.02346 [hep-th].
[227] A. Guerrieri, J. Penedones, and P. Vieira, "Where Is String Theory in the Space of Scattering Amplitudes?," *Phys. Rev. Lett.* **127** no. 8, (2021) 081601, arXiv:2102.02847 [hep-th].
[228] J. A. Dror, S. Gori, J. M. Leedom, and N. L. Rodd, "Sensitivity of Spin-Precession Axion Experiments," *Phys. Rev. Lett.* **130** no. 18, (2023) 181801, arXiv:2210.06481 [hep-ph].
[229] J. A. Dror, H. Murayama, and N. L. Rodd, "Cosmic axion background," *Phys. Rev. D* **103** no. 11, (2021) 115004, arXiv:2101.09287 [hep-ph]. [Erratum: Phys.Rev.D 106, 119902 (2022)].
[230] **ADMX** Collaboration, T. Nitta *et al.*, "Search for a Dark-Matter-Induced Cosmic Axion Background with ADMX," *Phys. Rev. Lett.* **131** no. 10, (2023) 101002, arXiv:2303.06282 [hep-ex].
[231] A. Berlin, D. Blas, R. Tito D'Agnolo, S. A. R. Ellis, R. Harnik, Y. Kahn, and J. Schütte-Engel, "Detecting high-frequency gravitational waves with microwave cavities," *Phys. Rev. D* **105** no. 11, (2022) 116011, arXiv:2112.11465 [hep-ph].
[232] A. Berlin, D. Blas, R. Tito D'Agnolo, S. A. R. Ellis, R. Harnik, Y. Kahn, J. Schütte-Engel, and M. Wentzel, "Electromagnetic cavities as mechanical bars for gravitational waves," *Phys. Rev. D* **108** no. 8, (2023) 084058, arXiv:2303.01518 [hep-ph].
[233] V. Domcke, C. Garcia-Cely, and N. L. Rodd, "Novel Search for High-Frequency Gravitational Waves with Low-Mass Axion Haloscopes," *Phys. Rev. Lett.* **129** no. 4, (2022) 041101, arXiv:2202.00695 [hep-ph].
[234] V. Domcke, C. Garcia-Cely, S. M. Lee, and N. L. Rodd, "Symmetries and selection rules: optimising axion haloscopes for Gravitational Wave searches," *JHEP* **03** (2024) 128, arXiv:2306.03125 [hep-ph].
[235] V. Domcke, S. A. R. Ellis, and N. L. Rodd, "Magnets are Weber Bar Gravitational Wave Detectors," arXiv:2408.01483 [hep-ph].
[236] P. W. Graham and S. Rajendran, "New Observables for Direct Detection of Axion Dark Matter," *Phys. Rev. D* **88** (2013) 035023, arXiv:1306.6088 [hep-ph].
[237] D. Budker, P. W. Graham, M. Ledbetter, S. Rajendran, and A. Sushkov, "Proposal for a Cosmic Axion Spin Precession Experiment (CASPEr)," *Phys. Rev. X* **4** no. 2, (2014) 021030, arXiv:1306.6089 [hep-ph].
[238] S. Chaudhuri, P. W. Graham, K. Irwin, J. Mardon, S. Rajendran, and Y. Zhao, "Radio for hidden-photon dark matter detection," *Phys. Rev. D* **92** no. 7, (2015) 075012, arXiv:1411.7382 [hep-ph].
[239] D. F. Jackson Kimball *et al.*, "Overview of the Cosmic Axion Spin Precession Experiment (CASPEr)," *Springer Proc. Phys.* **245** (2020) 105–121, arXiv:1711.08999 [physics.ins-det].
[240] H. An, S. Ge, J. Liu, and M. Liu, "In-situ Measurements of Dark Photon Dark Matter using Parker Solar Probe: Going beyond the Radio Window," arXiv:2405.12285 [hep-ph].
[241] H. An, X. Chen, S. Ge, J. Liu, and Y. Luo, "Searching for ultralight dark matter conversion in solar corona using Low Frequency Array data," *Nature Commun.* **15** no. 1, (2024) 915, arXiv:2301.03622 [hep-ph].
[242] P. Arias, D. Cadamuro, M. Goodsell, J. Jaeckel, J. Redondo, and A. Ringwald, "WISPy Cold Dark Matter," *JCAP* **06** (2012) 013, arXiv:1201.5902 [hep-ph].
[243] A. Caputo, H. Liu, S. Mishra-Sharma, and J. T. Ruderman, "Dark Photon Oscillations in Our Inhomogeneous Universe," *Phys. Rev. Lett.* **125** no. 22, (2020) 221303, arXiv:2002.05165 [astro-ph.CO].
[244] S. D. McDermott and S. J. Witte, "Cosmological evolution of light dark photon dark matter," *Phys. Rev. D* **101** no. 6, (2020) 063030, arXiv:1911.05086 [hep-ph].
[245] **ADMX** Collaboration, A. Wagner *et al.*, "A Search for Hidden Sector Photons with ADMX," *Phys. Rev. Lett.* **105** (2010) 171801, arXiv:1007.3766 [hep-ex].
[246] L. H. Nguyen, A. Lobanov, and D. Horns, "First results from the WISPDMX radio frequency cavity searches for hidden photon dark matter," *JCAP* **10** (2019) 014, arXiv:1907.12449 [hep-ex].
[247] S. Lee, S. Ahn, J. Choi, B. R. Ko, and Y. K. Semertzidis, "Axion Dark Matter Search around 6.7 μeV," *Phys. Rev. Lett.* **124** no. 10, (2020) 101802, arXiv:2001.05102 [hep-ex].

[248] **HAYSTAC** Collaboration, L. Zhong *et al.*, "Results from phase 1 of the HAYSTAC microwave cavity axion experiment," *Phys. Rev. D* **97** no. 9, (2018) 092001, arXiv:1803.03690 [hep-ex].
[249] **HAYSTAC** Collaboration, K. M. Backes *et al.*, "A quantum-enhanced search for dark matter axions," *Nature* **590** no. 7845, (2021) 238–242, arXiv:2008.01853 [quant-ph].
[250] B. Godfrey *et al.*, "Search for dark photon dark matter: Dark E field radio pilot experiment," *Phys. Rev. D* **104** no. 1, (2021) 012013, arXiv:2101.02805 [physics.ins-det].
[251] **CAPP** Collaboration, S. Ahn *et al.*, "Extensive Search for Axion Dark Matter over 1 GHz with CAPP'S Main Axion Experiment," *Phys. Rev. X* **14** no. 3, (2024) 031023, arXiv:2402.12892 [hep-ex].
[252] D. Alesini *et al.*, "Search for invisible axion dark matter of mass $m_a = 43$ μeV with the QUAX–$a\gamma$ experiment," *Phys. Rev. D* **103** no. 10, (2021) 102004, arXiv:2012.09498 [hep-ex].
[253] S. Ahyoune *et al.*, "RADES axion search results with a High-Temperature Superconducting cavity in an 11.7 T magnet," arXiv:2403.07790 [hep-ex].
[254] A. P. Quiskamp, B. T. McAllister, P. Altin, E. N. Ivanov, M. Goryachev, and M. E. Tobar, "Direct search for dark matter axions excluding ALP cogenesis in the 63- to 67-μeV range with the ORGAN experiment," *Sci. Adv.* **8** no. 27, (2022) abq3765, arXiv:2203.12152 [hep-ex].
[255] **CAST** Collaboration, V. Anastassopoulos *et al.*, "New CAST Limit on the Axion-Photon Interaction," *Nature Phys.* **13** (2017) 584–590, arXiv:1705.02290 [hep-ex].
[256] D. Noordhuis, A. Prabhu, S. J. Witte, A. Y. Chen, F. Cruz, and C. Weniger, "Novel Constraints on Axions Produced in Pulsar Polar-Cap Cascades," *Phys. Rev. Lett.* **131** no. 11, (2023) 111004, arXiv:2209.09917 [hep-ph].
[257] C. Dessert, D. Dunsky, and B. R. Safdi, "Upper limit on the axion-photon coupling from magnetic white dwarf polarization," *Phys. Rev. D* **105** no. 10, (2022) 103034, arXiv:2203.04319 [hep-ph].
[258] J. Davies, M. Meyer, and G. Cotter, "Constraints on axionlike particles from a combined analysis of three flaring Fermi flat-spectrum radio quasars," *Phys. Rev. D* **107** no. 8, (2023) 083027, arXiv:2211.03414 [astro-ph.HE].
[259] **MAGIC** Collaboration, H. Abe *et al.*, "Constraints on axion-like particles with the Perseus Galaxy Cluster with MAGIC," *Phys. Dark Univ.* **44** (2024) 101425, arXiv:2401.07798 [astro-ph.HE].
[260] **Fermi-LAT** Collaboration, M. Ajello *et al.*, "Search for Spectral Irregularities due to Photon–Axionlike-Particle Oscillations with the Fermi Large Area Telescope," *Phys. Rev. Lett.* **116** no. 16, (2016) 161101, arXiv:1603.06978 [astro-ph.HE].
[261] J. E. Kim, "Weak Interaction Singlet and Strong CP Invariance," *Phys. Rev. Lett.* **43** (1979) 103.
[262] R. T. Co, L. J. Hall, and K. Harigaya, "Predictions for Axion Couplings from ALP Cogenesis," *JHEP* **01** (2021) 172, arXiv:2006.04809 [hep-ph].
[263] C. O'Hare, "cajohare/axionlimits: Axionlimits," https://cajohare.github.io/AxionLimits/, July, 2020.
[264] D. Cyncynates and Z. J. Weiner, "Experimental targets for dark photon dark matter," arXiv:2410.14774 [hep-ph].
[265] W. E. East and J. Huang, "Dark photon vortex formation and dynamics," *JHEP* **12** (2022) 089, arXiv:2206.12432 [hep-ph].
[266] J. Walter, H. Bekker, J. Blanchard, D. Budker, N. L. Figueroa, A. Wickenbrock, Y. Zhang, and P. Zhou, "Fast shimming algorithm based on Bayesian optimization for magnetic resonance based dark matter search," arXiv:2309.11614 [astro-ph.CO].
[267] A. Berlin and K. Zhou, "Discovering QCD-coupled axion dark matter with polarization haloscopes," *Phys. Rev. D* **108** no. 3, (2023) 035038, arXiv:2209.12901 [hep-ph].
[268] E. U. Condon, "Forced oscillations in cavity resonators," *Journal of Applied Physics* **12** no. 2, (1941) 129–132.
[269] W. B. Smythe, *Static and dynamic electricity*. New York, NY (USA); Hemisphere Publishing, 1988.
[270] R. E. Collin, *Field theory of guided waves*. IEEE Press Series on Electromagnetic Wave Theory. John Wiley & Sons, Nashville, TN, 2 ed., 1990.
[271] A. Abragam, *The principles of nuclear magnetism*. International Series of Monographs on Physics. Clarendon Press, Oxford, England, 1983.

[272] N. G. Van Kampen, *Stochastic Processes in Physics and Chemistry*. Elsevier, 2007.
[273] J. Kowalewski and L. Maler, *Nuclear spin relaxation in liquids*. CRC Press, London, England, 2 ed., 2019.
[274] M. H. Levitt, *Spin dynamics*. Wiley-Blackwell, Hoboken, NJ, 2 ed., 2008.
[275] A. Redfield, *The Theory of Relaxation Processes*. Elsevier, 1965.
[276] C. P. Slichter, *Principles of Magnetic Resonance*. Springer Berlin Heidelberg, 1990.
[277] J. D. Jackson, *Classical Electrodynamics*. Wiley, 1998.
[278] C. Kittel, *Introduction to Solid State Physics*. Wiley, 8 ed., 2004.
[279] J. H. Simpson, "Chapter 2 - instrumental considerations," in *Organic Structure Determination Using 2-D NMR Spectroscopy (Second Edition)*, pp. 21–57. Academic Press, Boston, second edition ed., 2012.
[280] N. Bloembergen, E. M. Purcell, and R. V. Pound, "Relaxation effects in nuclear magnetic resonance absorption," *Phys. Rev.* **73** no. 7, (1948) 679.
[281] I. Solomon, "Relaxation processes in a system of two spins," *Phys. Rev.* **99** no. 2, (1955) 559.
[282] D. D. Traficante, "Relaxation. can t2, be longer than t1?" *Concepts in Magnetic Resonance* **3** no. 3, 171–177.
[283] N. Bloembergen and R. V. Pound, "Radiation damping in magnetic resonance experiments," *Phys. Rev.* **95** (1954) 8–12.
[284] H. B. Callen and T. A. Welton, "Irreversibility and generalized noise," *Phys. Rev.* **83** (1951) 34–40.
[285] R. Kubo, "The fluctuation-dissipation theorem," *Reports on Progress in Physics* **29** no. 1, (1966) 255.
[286] L. D. Landau and E. M. Lifshitz, "Chapter xii - fluctuations," in *Statistical Physics (Third Edition)*, vol. 5 of *Course of Theoretical Physics*, pp. 333–400. Pergamon, 1980.
[287] M. A. Fedderke, P. W. Graham, D. F. J. Kimball, and S. Kalia, "Earth as a transducer for dark-photon dark-matter detection," *Phys. Rev. D* **104** no. 7, (2021) 075023, arXiv:2106.00022 [hep-ph].
[288] G. G. Raffelt, *Stars as Laboratories for Fundamental Physics*. University of Chicago Press, 1996. http://wwwth.mpp.mpg.de/members/raffelt/mypapers/stars.pdf.
[289] J. H. Davies and D. R. Davies, "Earth's surface heat flux," *Solid Earth* **1** no. 1, (2010) 5–24. https://se.copernicus.org/articles/1/5/2010/.
[290] T. Lay, J. Hernlund, and B. A. Buffett, "Core–mantle boundary heat flow," *Nature Geoscience* **1** no. 1, (Jan., 2008) 25–32. http://dx.doi.org/10.1038/ngeo.2007.44.
[291] M. Pozzo, C. Davies, D. Gubbins, and D. Alfè, "Thermal and electrical conductivity of iron at earth's core conditions," *Nature* **485** no. 7398, (Apr., 2012) 355–358. http://dx.doi.org/10.1038/nature11031.
[292] S. Dubovsky and G. Hernández-Chifflet, "Heating up the Galaxy with Hidden Photons," *JCAP* **12** (2015) 054, arXiv:1509.00039 [hep-ph].
[293] A. Caputo, H. Liu, S. Mishra-Sharma, and J. T. Ruderman, "Dark Photon Oscillations in Our Inhomogeneous Universe," *Phys. Rev. Lett.* **125** no. 22, (2020) 221303, arXiv:2002.05165 [astro-ph.CO].
[294] S. D. McDermott and S. J. Witte, "Cosmological evolution of light dark photon dark matter," *Phys. Rev. D* **101** no. 6, (2020) 063030, arXiv:1911.05086 [hep-ph].
[295] S. Chaudhuri, P. W. Graham, K. Irwin, J. Mardon, S. Rajendran, and Y. Zhao, "Radio for hidden-photon dark matter detection," *Phys. Rev. D* **92** (Oct, 2015) 075012. https://link.aps.org/doi/10.1103/PhysRevD.92.075012.
[296] H. An, S. Ge, W.-Q. Guo, X. Huang, J. Liu, and Z. Lu, "Direct detection of dark photon dark matter using radio telescopes," arXiv:2207.05767 [hep-ph].
[297] D. Noordhuis, A. Prabhu, S. J. Witte, A. Y. Chen, F. Cruz, and C. Weniger, "Novel Constraints on Axions Produced in Pulsar Polar Cap Cascades," arXiv:2209.09917 [hep-ph].
[298] C. Dessert, D. Dunsky, and B. R. Safdi, "Upper limit on the axion-photon coupling from magnetic white dwarf polarization," *Phys. Rev. D* **105** no. 10, (2022) 103034, arXiv:2203.04319 [hep-ph].
[299] J. Davies, M. Meyer, and G. Cotter, "Constraints on axionlike particles from a combined analysis of three flaring Fermi flat-spectrum radio quasars," *Phys. Rev. D* **107** no. 8, (2023) 083027,

arXiv:2211.03414 [astro-ph.HE].
[300] **MAGIC** Collaboration, H. Abe *et al.*, "Constraints on axion-like particles with the Perseus Galaxy Cluster with MAGIC," *Phys. Dark Univ.* **44** (2024) 101425, arXiv:2401.07798 [astro-ph.HE].
[301] **Fermi-LAT** Collaboration, M. Ajello *et al.*, "Search for Spectral Irregularities due to Photon–Axionlike-Particle Oscillations with the Fermi Large Area Telescope," *Phys. Rev. Lett.* **116** no. 16, (2016) 161101, arXiv:1603.06978 [astro-ph.HE].
[302] C. P. Salemi *et al.*, "Search for Low-Mass Axion Dark Matter with ABRACADABRA-10 cm," *Phys. Rev. Lett.* **127** no. 8, (2021) 081801, arXiv:2102.06722 [hep-ex].
[303] A. V. Gramolin, D. Aybas, D. Johnson, J. Adam, and A. O. Sushkov, "Search for axion-like dark matter with ferromagnets," *Nature Physics* **17** no. 1, (Aug., 2020) 79–84. http://dx.doi.org/10.1038/s41567-020-1006-6.
[304] **CAST** Collaboration, V. Anastassopoulos *et al.*, "New CAST Limit on the Axion-Photon Interaction," *Nature Phys.* **13** (2017) 584–590, arXiv:1705.02290 [hep-ex].
[305] A. Arza, M. A. Fedderke, P. W. Graham, D. F. J. Kimball, and S. Kalia, "Earth as a transducer for axion dark-matter detection," *Phys. Rev. D* **105** no. 9, (2022) 095007, arXiv:2112.09620 [hep-ph].
[306] M. A. Fedderke, P. W. Graham, D. F. Jackson Kimball, and S. Kalia, "Search for dark-photon dark matter in the SuperMAG geomagnetic field dataset," *Phys. Rev. D* **104** no. 9, (2021) 095032, arXiv:2108.08852 [hep-ph].
[307] I. A. Sulai *et al.*, "Hunt for magnetic signatures of hidden-photon and axion dark matter in the wilderness," *Phys. Rev. D* **108** no. 9, (2023) 096026, arXiv:2306.11575 [hep-ph].
[308] H. An, F. P. Huang, J. Liu, and W. Xue, "Radio-frequency Dark Photon Dark Matter across the Sun," *Phys. Rev. Lett.* **126** no. 18, (2021) 181102, arXiv:2010.15836 [hep-ph].
[309] E. Hardy and N. Song, "Listening for Dark Photon Radio from the Galactic Centre," arXiv:2212.09756 [hep-ph].
[310] J. S. Bolton, A. Caputo, H. Liu, and M. Viel, "Comparison of Low-Redshift Lyman-α Forest Observations to Hydrodynamical Simulations with Dark Photon Dark Matter," *Phys. Rev. Lett.* **129** no. 21, (2022) 211102, arXiv:2206.13520 [hep-ph].
[311] A. Caputo, H. Liu, S. Mishra-Sharma, and J. T. Ruderman, "Modeling Dark Photon Oscillations in Our Inhomogeneous Universe," *Phys. Rev. D* **102** no. 10, (2020) 103533, arXiv:2004.06733 [astro-ph.CO].
[312] G. Raffelt and L. Stodolsky, "Mixing of the photon with low mass particles," *Phys. Rev. D* **37** (1988) 1237.
[313] M. S. Pshirkov and S. B. Popov, "Conversion of Dark matter axions to photons in magnetospheres of neutron stars," *J. Exp. Theor. Phys.* **108** (2009) 384–388, arXiv:0711.1264 [astro-ph].
[314] A. Hook, Y. Kahn, B. R. Safdi, and Z. Sun, "Radio Signals from Axion Dark Matter Conversion in Neutron Star Magnetospheres," *Phys. Rev. Lett.* **121** no. 24, (2018) 241102, arXiv:1804.03145 [hep-ph].
[315] G.-y. Huang, T. Ohlsson, and S. Zhou, "Observational Constraints on Secret Neutrino Interactions from Big Bang Nucleosynthesis," *Phys. Rev.* **D97** no. 7, (2018) 075009, arXiv:1712.04792 [hep-ph].
[316] S. J. Witte, D. Noordhuis, T. D. P. Edwards, and C. Weniger, "Axion-photon conversion in neutron star magnetospheres: The role of the plasma in the Goldreich-Julian model," *Phys. Rev. D* **104** no. 10, (2021) 103030, arXiv:2104.07670 [hep-ph].
[317] J. W. Foster *et al.*, "Green Bank and Effelsberg Radio Telescope Searches for Axion Dark Matter Conversion in Neutron Star Magnetospheres," *Phys. Rev. Lett.* **125** no. 17, (2020) 171301, arXiv:2004.00011 [astro-ph.CO].
[318] R. A. Battye, B. Garbrecht, J. I. McDonald, F. Pace, and S. Srinivasan, "Dark matter axion detection in the radio/mm-waveband," *Phys. Rev. D* **102** no. 2, (2020) 023504, arXiv:1910.11907 [astro-ph.CO].
[319] M. Leroy, M. Chianese, T. D. P. Edwards, and C. Weniger, "Radio Signal of Axion-Photon Conversion in Neutron Stars: A Ray Tracing Analysis," *Phys. Rev. D* **101** no. 12, (2020) 123003, arXiv:1912.08815 [hep-ph].

[320] R. A. Battye, J. Darling, J. McDonald, and S. Srinivasan, "Towards robust constraints on axion dark matter using psr j1745-2900." 2021.
[321] F. P. Huang, K. Kadota, T. Sekiguchi, and H. Tashiro, "Radio telescope search for the resonant conversion of cold dark matter axions from the magnetized astrophysical sources," *Phys. Rev. D* **97** no. 12, (2018) 123001, arXiv:1803.08230 [hep-ph].
[322] C. A. J. . S. S. Materassi M., Forte B., *The Dynamical Ionosphere: A Systems Approach to Ionospheric Irregularity*. Elsevier, 2019.
[323] I. Monitoring and P. Center, "Ionosphere monitoring and prediction," https://impc.dlr.de.
[324] G. Cantatore, S. A. Çetin, H. Fischer, W. Funk, M. Karuza, A. Kryemadhi, M. Maroudas, K. Özbozduman, Y. K. Semertzidis, and K. Zioutas, "Dark Matter Detection in the Stratosphere," *Symmetry* **15** no. 6, (2023) 1167, arXiv:2012.03353 [hep-ex].
[325] NCEI, "Magnetic field estimated values," https://www.ngdc.noaa.gov/geomag/calculators/magcalc.shtml#igrfwmm. Accessed: 2024-05-06.
[326] J. W. Foster, N. L. Rodd, and B. R. Safdi, "Revealing the Dark Matter Halo with Axion Direct Detection," *Phys. Rev. D* **97** no. 12, (2018) 123006, arXiv:1711.10489 [astro-ph.CO].
[327] N. Brahma, A. Berlin, and K. Schutz, "Photon-dark photon conversion with multiple level crossings," *Phys. Rev. D* **108** (Nov, 2023) 095045. https://link.aps.org/doi/10.1103/PhysRevD.108.095045.
[328] C. Zener, "Nonadiabatic crossing of energy levels," *Proc. Roy. Soc. Lond. A* **137** (1932) 696–702.
[329] L. D. Landau, "A theory of energy transfer. 2.," *Phys. Z. Sowjetunion* **2** (1932) 63–66.
[330] S. J. Parke, "Nonadiabatic Level Crossing in Resonant Neutrino Oscillations," *Phys. Rev. Lett.* **57** (1986) 1275–1278, arXiv:2212.06978 [hep-ph].
[331] T.-K. Kuo and J. T. Pantaleone, "Neutrino Oscillations in Matter," *Rev. Mod. Phys.* **61** (1989) 937.
[332] J. Herzog-Arbeitman, M. Lisanti, and L. Necib, "The Metal-Poor Stellar Halo in RAVE-TGAS and its Implications for the Velocity Distribution of Dark Matter," *JCAP* **04** (2018) 052, arXiv:1708.03635 [astro-ph.GA].
[333] S. Chapman, "The absorption and dissociative or ionizing effect of monochromatic radiation in an atmosphere on a rotating earth part ii. grazing incidence," *Proceedings of the Physical Society* **43** no. 5, (Sep, 1931) 483. https://dx.doi.org/10.1088/0959-5309/43/5/302.
[334] M. M. Hoque, L. Yuan, F. S. Prol, M. Hernández-Pajares, R. Notarpietro, N. Jakowski, G. Olivares Pulido, A. Von Engeln, and C. Marquardt, "A new method of electron density retrieval from metop-a's truncated radio occultation measurements," *Remote Sensing* **15** no. 5, (2023) 1424. https://www.mdpi.com/2072-4292/15/5/1424.
[335] M. Born and E. Wolf, *Principles of optics*. Cambridge Univ. Pr., 1999.
[336] C. on Space Research, "Iri 2016," https://kauai.ccmc.gsfc.nasa.gov/instantrun/iri.
[337] B. T. Draine, *Physics of the interstellar and intergalactic medium*. Princeton Series in Astrophysics. Princeton University Press, Princeton, NJ, Jan., 2011.
[338] M. Nicolet, "The collision frequency of electrons in the ionosphere," *Journal of Atmospheric and Terrestrial Physics* **3** no. 4, (1953) 200–211. https://www.sciencedirect.com/science/article/pii/002191695390110X.
[339] K. T. McDonald, "Power received by a small antenna," http://kirkmcd.princeton.edu/examples/power.pdf.
[340] L. Krauss, J. Moody, F. Wilczek, and D. E. Morris, "Calculations for cosmic axion detection," *Phys. Rev. Lett.* **55** (Oct, 1985) 1797–1800. https://link.aps.org/doi/10.1103/PhysRevLett.55.1797.
[341] I. R. Assembly, "Radio noise," https://www.itu.int/dms_pubrec/itu-r/rec/p/R-REC-P.372-8-200304-S!!PDF-E.pdf.
[342] S. Chaudhuri, K. Irwin, P. W. Graham, and J. Mardon, "Optimal Impedance Matching and Quantum Limits of Electromagnetic Axion and Hidden-Photon Dark Matter Searches," arXiv:1803.01627 [hep-ph].
[343] H. V. Cane, "Spectra of the non-thermal radio radiation from the galactic polar regions.," *Monthly Notices of the Royal Astronomical Society* **189** (Nov., 1979) 465–478.

[344] J. C. Novaco and L. W. Brown, "Nonthermal galactic emission below 10 megahertz.," *The Astrophysical Journal* **221** (Apr., 1978) 114–123.
[345] P. Sikivie, "Experimental Tests of the Invisible Axion," *Phys. Rev. Lett.* **51** (1983) 1415–1417. [Erratum: Phys.Rev.Lett. 52, 695 (1984)].
[346] J. Bijnens and F. Cornet, "Two Pion Production in Photon-Photon Collisions," *Nucl. Phys. B* **296** (1988) 557–568.
[347] M. Farina, D. Pappadopulo, F. Rompineve, and A. Tesi, "The photo-philic QCD axion," *JHEP* **01** (2017) 095, arXiv:1611.09855 [hep-ph].
[348] P. Agrawal, J. Fan, M. Reece, and L.-T. Wang, "Experimental Targets for Photon Couplings of the QCD Axion," *JHEP* **02** (2018) 006, arXiv:1709.06085 [hep-ph].
[349] P. Agrawal, M. Nee, and M. Reig, "Axion couplings in grand unified theories," *JHEP* **10** (2022) 141, arXiv:2206.07053 [hep-ph].
[350] K. A. Olive and M. Pospelov, "Environmental dependence of masses and coupling constants," *Phys. Rev. D* **77** (2008) 043524, arXiv:0709.3825 [hep-ph].
[351] Y. V. Stadnik and V. V. Flambaum, "Can dark matter induce cosmological evolution of the fundamental constants of Nature?," *Phys. Rev. Lett.* **115** no. 20, (2015) 201301, arXiv:1503.08540 [astro-ph.CO].
[352] S. J. Brodsky and G. P. Lepage, "Large Angle Two Photon Exclusive Channels in Quantum Chromodynamics," *Phys. Rev. D* **24** (1981) 1808.
[353] J. Boyer *et al.*, "Two photon production of pion pairs," *Phys. Rev. D* **42** (1990) 1350–1367.
[354] **Crystal Ball** Collaboration, H. Marsiske *et al.*, "A Measurement of $\pi^0\pi^0$ Production in Two Photon Collisions," *Phys. Rev. D* **41** (1990) 3324.
[355] J. F. Donoghue, B. R. Holstein, and Y. C. Lin, "The Reaction gamma Gamma —> pi0 pi0 and Chiral Loops," *Phys. Rev. D* **37** (1988) 2423.
[356] A. Hook, "Solving the Hierarchy Problem Discretely," *Phys. Rev. Lett.* **120** no. 26, (2018) 261802, arXiv:1802.10093 [hep-ph].
[357] L. Di Luzio, B. Gavela, P. Quilez, and A. Ringwald, "An even lighter QCD axion," *JHEP* **05** (2021) 184, arXiv:2102.00012 [hep-ph].
[358] A. Banerjee, J. Eby, and G. Perez, "From axion quality and naturalness problems to a high-quality $\mathbb{Z}_N$ QCD relaxion," arXiv:2210.05690 [hep-ph].
[359] K. Van Tilburg, N. Leefer, L. Bougas, and D. Budker, "Search for ultralight scalar dark matter with atomic spectroscopy," *Phys. Rev. Lett.* **115** no. 1, (2015) 011802, arXiv:1503.06886 [physics.atom-ph].
[360] X. Zhang, A. Banerjee, M. Leyser, G. Perez, S. Schiller, D. Budker, and D. Antypas, "Search for ultralight dark matter with spectroscopy of radio-frequency atomic transitions," arXiv:2212.04413 [physics.atom-ph].
[361] A. Hees, J. Guéna, M. Abgrall, S. Bize, and P. Wolf, "Searching for an oscillating massive scalar field as a dark matter candidate using atomic hyperfine frequency comparisons," *Phys. Rev. Lett.* **117** no. 6, (2016) 061301, arXiv:1604.08514 [gr-qc].
[362] C. J. Kennedy, E. Oelker, J. M. Robinson, T. Bothwell, D. Kedar, W. R. Milner, G. E. Marti, A. Derevianko, and J. Ye, "Precision metrology meets cosmology: Improved constraints on ultralight dark matter from atom-cavity frequency comparisons," *Phys. Rev. Lett.* **125** (Nov, 2020) 201302. https://link.aps.org/doi/10.1103/PhysRevLett.125.201302.
[363] M. Filzinger, S. Dörscher, R. Lange, J. Klose, M. Steinel, E. Benkler, E. Peik, C. Lisdat, and N. Huntemann, "Improved limits on the coupling of ultralight bosonic dark matter to photons from optical atomic clock comparisons," arXiv:2301.03433 [physics.atom-ph].
[364] N. Sherrill *et al.*, "Analysis of atomic-clock data to constrain variations of fundamental constants," arXiv:2302.04565 [physics.atom-ph].
[365] T. A. Wagner, S. Schlamminger, J. H. Gundlach, and E. G. Adelberger, "Torsion-balance tests of the weak equivalence principle," *Class. Quant. Grav.* **29** (2012) 184002, arXiv:1207.2442 [gr-qc].
[366] A. Hees, O. Minazzoli, E. Savalle, Y. V. Stadnik, and P. Wolf, "Violation of the equivalence principle from light scalar dark matter," *Phys. Rev. D* **98** no. 6, (2018) 064051, arXiv:1807.04512 [gr-qc].

[367] J. Bergé, P. Brax, G. Métris, M. Pernot-Borràs, P. Touboul, and J.-P. Uzan, "MICROSCOPE Mission: First Constraints on the Violation of the Weak Equivalence Principle by a Light Scalar Dilaton," *Phys. Rev. Lett.* **120** no. 14, (2018) 141101, arXiv:1712.00483 [gr-qc].
[368] T. Bouley, P. Sørensen, and T.-T. Yu, "Constraints on ultralight scalar dark matter with quadratic couplings," *JHEP* **03** (2023) 104, arXiv:2211.09826 [hep-ph].
[369] L. Badurina *et al.*, "AION: An Atom Interferometer Observatory and Network," *JCAP* **05** (2020) 011, arXiv:1911.11755 [astro-ph.CO].
[370] M. Abe *et al.*, "Matter-wave atomic gradiometer interferometric sensor (MAGIS-100)," *Quantum Science and Technology* **6** no. 4, (Jul, 2021) 044003. https://doi.org/10.1088%2F2058-9565%2Fabf719.
[371] L. Badurina, O. Buchmueller, J. Ellis, M. Lewicki, C. McCabe, and V. Vaskonen, "Prospective sensitivities of atom interferometers to gravitational waves and ultralight dark matter," *Phil. Trans. A. Math. Phys. Eng. Sci.* **380** no. 2216, (2021) 20210060, arXiv:2108.02468 [gr-qc].
[372] A. Banerjee, H. Kim, O. Matsedonskyi, G. Perez, and M. S. Safronova, "Probing the Relaxed Relaxion at the Luminosity and Precision Frontiers," *JHEP* **07** (2020) 153, arXiv:2004.02899 [hep-ph].
[373] T. S. Roussy, D. A. Palken, *et al.*, "Experimental constraint on axionlike particles over seven orders of magnitude in mass," *Phys. Rev. Lett.* **126** (Apr, 2021) 171301. https://link.aps.org/doi/10.1103/PhysRevLett.126.171301.
[374] C. Abel *et al.*, "Search for Axionlike Dark Matter through Nuclear Spin Precession in Electric and Magnetic Fields," *Phys. Rev. X* **7** no. 4, (2017) 041034, arXiv:1708.06367 [hep-ph].
[375] K. Blum, R. T. D'Agnolo, M. Lisanti, and B. R. Safdi, "Constraining Axion Dark Matter with Big Bang Nucleosynthesis," *Phys. Lett. B* **737** (2014) 30–33, arXiv:1401.6460 [hep-ph].
[376] A. Hook and J. Huang, "Probing axions with neutron star inspirals and other stellar processes," *JHEP* **06** (2018) 036, arXiv:1708.08464 [hep-ph].
[377] R. Balkin, J. Serra, K. Springmann, S. Stelzl, and A. Weiler, "White dwarfs as a probe of light QCD axions," arXiv:2211.02661 [hep-ph].
[378] G. Lucente, L. Mastrototaro, P. Carenza, L. Di Luzio, M. Giannotti, and A. Mirizzi, "Axion signatures from supernova explosions through the nucleon electric-dipole portal," *Phys. Rev. D* **105** no. 12, (2022) 123020, arXiv:2203.15812 [hep-ph].
[379] L. Caloni, M. Gerbino, M. Lattanzi, and L. Visinelli, "Novel cosmological bounds on thermally-produced axion-like particles," *JCAP* **09** (2022) 021, arXiv:2205.01637 [astro-ph.CO].
[380] J. Zhang, Z. Lyu, J. Huang, M. C. Johnson, L. Sagunski, M. Sakellariadou, and H. Yang, "First Constraints on Nuclear Coupling of Axionlike Particles from the Binary Neutron Star Gravitational Wave Event GW170817," *Phys. Rev. Lett.* **127** no. 16, (2021) 161101, arXiv:2105.13963 [hep-ph].
[381] V. M. Mehta, M. Demirtas, C. Long, D. J. E. Marsh, L. Mcallister, and M. J. Stott, "Superradiance Exclusions in the Landscape of Type IIB String Theory," arXiv:2011.08693 [hep-th].
[382] C. Ünal, F. Pacucci, and A. Loeb, "Properties of ultralight bosons from heavy quasar spins via superradiance," *JCAP* **05** (2021) 007, arXiv:2012.12790 [hep-ph].
[383] M. Baryakhtar, M. Galanis, R. Lasenby, and O. Simon, "Black hole superradiance of self-interacting scalar fields," arXiv:2011.11646 [hep-ph].
[384] N. Dalal and A. Kravtsov, "Excluding fuzzy dark matter with sizes and stellar kinematics of ultrafaint dwarf galaxies," *Phys. Rev. D* **106** (Sep, 2022) 063517. https://link.aps.org/doi/10.1103/PhysRevD.106.063517.
[385] K. K. Rogers and H. V. Peiris, "Strong bound on canonical ultralight axion dark matter from the lyman-alpha forest," *Phys. Rev. Lett.* **126** (Feb, 2021) 071302. https://link.aps.org/doi/10.1103/PhysRevLett.126.071302.
[386] G. Grilli di Cortona, E. Hardy, J. Pardo Vega, and G. Villadoro, "The QCD axion, precisely," *JHEP* **01** (2016) 034, arXiv:1511.02867 [hep-ph].
[387] H. Georgi, D. B. Kaplan, and L. Randall, "Manifesting the Invisible Axion at Low-energies," *Phys. Lett. B* **169** (1986) 73–78.
[388] M. Bauer, M. Neubert, S. Renner, M. Schnubel, and A. Thamm, "Consistent Treatment of Axions in

the Weak Chiral Lagrangian," *Phys. Rev. Lett.* **127** no. 8, (2021) 081803, arXiv:2102.13112 [hep-ph].
[389] H. Song, H. Sun, and J.-H. Yu, "Effective Field Theories of Axion, ALP and Dark Photon," arXiv:2305.16770 [hep-ph].
[390] C. Grojean, J. Kley, and C.-Y. Yao, "Hilbert series for ALP EFTs," arXiv:2307.08563 [hep-ph].
[391] J. S. Reynés, J. H. Matthews, C. S. Reynolds, H. R. Russell, R. N. Smith, and M. C. D. Marsh, "New constraints on light axion-like particles using Chandra transmission grating spectroscopy of the powerful cluster-hosted quasar H1821+643," *Mon. Not. Roy. Astron. Soc.* **510** no. 1, (2021) 1264–1277, arXiv:2109.03261 [astro-ph.HE].
[392] M. A. Fedderke, P. W. Graham, and S. Rajendran, "Axion Dark Matter Detection with CMB Polarization," *Phys. Rev. D* **100** no. 1, (2019) 015040, arXiv:1903.02666 [astro-ph.CO].
[393] T. Liu, X. Lou, and J. Ren, "Pulsar Polarization Arrays," *Phys. Rev. Lett.* **130** no. 12, (2023) 121401, arXiv:2111.10615 [astro-ph.HE].
[394] **BICEP/Keck** Collaboration, P. A. R. Ade *et al.*, "BICEP/Keck XIV: Improved constraints on axionlike polarization oscillations in the cosmic microwave background," *Phys. Rev. D* **105** no. 2, (2022) 022006, arXiv:2108.03316 [astro-ph.CO].
[395] A. Castillo, J. Martin-Camalich, J. Terol-Calvo, D. Blas, A. Caputo, R. T. G. Santos, L. Sberna, M. Peel, and J. A. Rubiño Martín, "Searching for dark-matter waves with PPTA and QUIJOTE pulsar polarimetry," *JCAP* **06** no. 06, (2022) 014, arXiv:2201.03422 [astro-ph.CO].
[396] **SPT-3G** Collaboration, K. R. Ferguson *et al.*, "Searching for axionlike time-dependent cosmic birefringence with data from SPT-3G," *Phys. Rev. D* **106** no. 4, (2022) 042011, arXiv:2203.16567 [astro-ph.CO].
[397] **POLARBEAR** Collaboration, S. Adachi *et al.*, "Constraints on axion-like polarization oscillations in the cosmic microwave background with POLARBEAR," arXiv:2303.08410 [astro-ph.CO].
[398] A. V. Gramolin, D. Aybas, D. Johnson, J. Adam, and A. O. Sushkov, "Search for axion-like dark matter with ferromagnets," *Nature Phys.* **17** no. 1, (2021) 79–84, arXiv:2003.03348 [hep-ex].
[399] J. L. Ouellet *et al.*, "First Results from ABRACADABRA-10 cm: A Search for Sub-μeV Axion Dark Matter," *Phys. Rev. Lett.* **122** no. 12, (2019) 121802, arXiv:1810.12257 [hep-ex].
[400] C. P. Salemi *et al.*, "Search for Low-Mass Axion Dark Matter with ABRACADABRA-10 cm," *Phys. Rev. Lett.* **127** no. 8, (2021) 081801, arXiv:2102.06722 [hep-ex].
[401] M. Escudero, C. K. Pooni, M. Fairbairn, D. Blas, X. Du, and D. J. E. Marsh, "Axion Star Explosions: A New Source for Axion Indirect Detection," arXiv:2302.10206 [hep-ph].
[402] I. Stern, "ADMX Status," *PoS* **ICHEP2016** (2016) 198, arXiv:1612.08296 [physics.ins-det].
[403] D. Alesini *et al.*, "KLASH Conceptual Design Report," arXiv:1911.02427 [physics.ins-det].
[404] **DMRadio** Collaboration, L. Brouwer *et al.*, "Projected sensitivity of DMRadio-m3: A search for the QCD axion below 1 μeV," *Phys. Rev. D* **106** no. 10, (2022) 103008, arXiv:2204.13781 [hep-ex].
[405] A. Berlin, R. T. D'Agnolo, S. A. R. Ellis, C. Nantista, J. Neilson, P. Schuster, S. Tantawi, N. Toro, and K. Zhou, "Axion Dark Matter Detection by Superconducting Resonant Frequency Conversion," *JHEP* **07** no. 07, (2020) 088, arXiv:1912.11048 [hep-ph].
[406] A. Berlin, R. T. D'Agnolo, S. A. R. Ellis, and K. Zhou, "Heterodyne broadband detection of axion dark matter," *Phys. Rev. D* **104** no. 11, (2021) L111701, arXiv:2007.15656 [hep-ph].
[407] I. Obata, T. Fujita, and Y. Michimura, "Optical Ring Cavity Search for Axion Dark Matter," *Phys. Rev. Lett.* **121** no. 16, (2018) 161301, arXiv:1805.11753 [astro-ph.CO].
[408] J. F. Bourhill, E. C. I. Paterson, M. Goryachev, and M. E. Tobar, "Twisted Anyon Cavity Resonators with Bulk Modes of Chiral Symmetry and Sensitivity to Ultra-Light Axion Dark Matter," arXiv:2208.01640 [hep-ph].
[409] T. Damour and J. F. Donoghue, "Equivalence Principle Violations and Couplings of a Light Dilaton," *Phys. Rev. D* **82** (2010) 084033, arXiv:1007.2792 [gr-qc].
[410] A. Banerjee, G. Perez, M. Safronova, I. Savoray, and A. Shalit, "The Phenomenology of Quadratically Coupled Ultra Light Dark Matter," arXiv:2211.05174 [hep-ph].
[411] P. Brax, C. Burrage, J. A. R. Cembranos, and P. Valageas, "Invisible dilaton," *Phys. Rev. D* **107** no. 9, (2023) 095015, arXiv:2303.14469 [hep-ph].

[412] A. Coc, N. J. Nunes, K. A. Olive, J.-P. Uzan, and E. Vangioni, "Coupled Variations of Fundamental Couplings and Primordial Nucleosynthesis," *Phys. Rev. D* **76** (2007) 023511, arXiv:astro-ph/0610733.
[413] **Particle Data Group** Collaboration, R. L. Workman *et al.*, "Review of Particle Physics," *PTEP* **2022** (2022) 083C01.
[414] T.-H. Yeh, K. A. Olive, and B. D. Fields, "The Neutron Mean Life and Big Bang Nucleosynthesis," arXiv:2303.04140 [astro-ph.CO].
[415] L. Badurina, D. Blas, and C. McCabe, "Refined ultralight scalar dark matter searches with compact atom gradiometers," *Phys. Rev. D* **105** no. 2, (2022) 023006, arXiv:2109.10965 [astro-ph.CO].
[416] A. Prabhu, "Axion production in pulsar magnetosphere gaps," *Phys. Rev. D* **104** no. 5, (2021) 055038, arXiv:2104.14569 [hep-ph].
[417] A. A. Prinz *et al.*, "Search for millicharged particles at SLAC," *Phys. Rev. Lett.* **81** (1998) 1175–1178, arXiv:hep-ex/9804008.
[418] S. Davidson, S. Hannestad, and G. Raffelt, "Updated bounds on millicharged particles," *JHEP* **05** (2000) 003, arXiv:hep-ph/0001179.
[419] **ArgoNeuT** Collaboration, R. Acciarri *et al.*, "Improved Limits on Millicharged Particles Using the ArgoNeuT Experiment at Fermilab," *Phys. Rev. Lett.* **124** no. 13, (2020) 131801, arXiv:1911.07996 [hep-ex].
[420] A. Ball *et al.*, "Search for millicharged particles in proton-proton collisions at $\sqrt{s} = 13$ TeV," *Phys. Rev. D* **102** no. 3, (2020) 032002, arXiv:2005.06518 [hep-ex].
[421] C. A. Argüelles Delgado, K. J. Kelly, and V. Muñoz Albornoz, "Millicharged particles from the heavens: single- and multiple-scattering signatures," *JHEP* **11** (2021) 099, arXiv:2104.13924 [hep-ph].
[422] J. H. Chang, R. Essig, and S. D. McDermott, "Supernova 1987A Constraints on Sub-GeV Dark Sectors, Millicharged Particles, the QCD Axion, and an Axion-like Particle," *JHEP* **09** (2018) 051, arXiv:1803.00993 [hep-ph].
[423] M. A. Luty, J. Polchinski, and R. Rattazzi, "The a-theorem and the Asymptotics of 4D Quantum Field Theory," *JHEP* **01** (2013) 152, arXiv:1204.5221 [hep-th].
[424] A. Martin, "Unitarity and High-Energy Behavior of Scattering Amplitudes," *Phys. Rev.* **129** (1963) 1432–1436.
[425] B. Bellazzini, M. Riembau, and F. Riva, "IR side of positivity bounds," *Phys. Rev. D* **106** no. 10, (2022) 105008, arXiv:2112.12561 [hep-th].
[426] S. Caron-Huot and J. Tokuda, "String loops and gravitational positivity bounds: imprint of light particles at high energies," arXiv:2406.07606 [hep-th].
[427] C. H. Müntz, "Über den approximationssatz von weierstraß," in *Mathematische Abhandlungen Hermann Amandus Schwarz*, C. Carathéodory, G. Hessenberg, E. Landau, and L. Lichtenstein, eds., pp. 303–312. Springer Berlin Heidelberg, Berlin, Heidelberg, 1914. https://doi.org/10.1007/978-3-642-50735-9_22.
[428] O. Szász, "Über die approximation stetiger funktionen durch lineare aggregate von potenzen," *Mathematische Annalen* **77** no. 4, (1916) 482–496. https://doi.org/10.1007/BF01456964.
[429] L. N. Trefethen, "Spectacularly large expansion coefficients in Müntz's theorem," *La Matematica* **2** no. 1, (2023) 31–36.
[430] D. Simmons-Duffin, "A Semidefinite Program Solver for the Conformal Bootstrap," *JHEP* **06** (2015) 174, arXiv:1502.02033 [hep-th].
[431] W. Landry and D. Simmons-Duffin, "Scaling the semidefinite program solver SDPB," arXiv:1909.09745 [hep-th].
[432] L.-Y. Chiang, Y.-t. Huang, W. Li, L. Rodina, and H.-C. Weng, "Into the EFThedron and UV constraints from IR consistency," *JHEP* **03** (2022) 063, arXiv:2105.02862 [hep-th].
[433] G. F. Giudice, C. Grojean, A. Pomarol, and R. Rattazzi, "The Strongly-Interacting Light Higgs," *JHEP* **06** (2007) 045, arXiv:hep-ph/0703164 [hep-ph].
[434] S. B. Giddings, "The Gravitational S-Matrix: Erice Lectures," *Subnucl. Ser.* **48** (2013) 93–147, arXiv:1105.2036 [hep-th].

[435] A. Strominger, "Lectures on the Infrared Structure of Gravity and Gauge Theory," arXiv:1703.05448 [hep-th].
[436] J. Ware, R. Saotome, and R. Akhoury, "Construction of an Asymptotic S Matrix for Perturbative Quantum Gravity," *JHEP* **10** (2013) 159, arXiv:1308.6285 [hep-th].
[437] P. Kravchuk, J. Qiao, and S. Rychkov, "Distributions in CFT. Part I. Cross-Ratio Space," *JHEP* **05** (2020) 137, arXiv:2001.08778 [hep-th].
[438] G. Passarino and M. J. G. Veltman, "One Loop Corrections for e+ e- Annihilation Into mu+ mu- in the Weinberg Model," *Nucl. Phys. B* **160** (1979) 151–207.
[439] R. K. Ellis, Z. Kunszt, K. Melnikov, and G. Zanderighi, "One-loop calculations in quantum field theory: From feynman diagrams to unitarity cuts," *Physics Reports* **518** no. 4–5, (Sept., 2012) 141–250. http://dx.doi.org/10.1016/j.physrep.2012.01.008.
[440] F. V. Tkachov, "A Theorem on Analytical Calculability of Four Loop Renormalization Group Functions," *Phys. Lett. B* **100** (1981) 65–68.
[441] K. G. Chetyrkin and F. V. Tkachov, "Integration by Parts: The Algorithm to Calculate beta Functions in 4 Loops," *Nucl. Phys. B* **192** (1981) 159–204.
[442] V. A. Smirnov, *Analytic tools for Feynman integrals*, vol. 250 of *Springer Tracts in Modern Physics*. Springer, Berlin, Heidelberg, 2012.
[443] R. K. Ellis and G. Zanderighi, "Scalar one-loop integrals for qcd," *Journal of High Energy Physics* **2008** no. 02, (Feb., 2008) 002–002. http://dx.doi.org/10.1088/1126-6708/2008/02/002.
[444] S. Weinzierl, *One-Loop Integrals*, pp. 135–154. Springer International Publishing, Cham, 2022. https://doi.org/10.1007/978-3-030-99558-4_5.
[445] V. A. Smirnov, *Evaluating Feynman Integrals*. Springer Berlin Heidelberg, 2005. http://dx.doi.org/10.1007/b95498.
[446] C. Anastasiou and K. Melnikov, "Higgs boson production at hadron colliders in NNLO QCD," *Nucl. Phys. B* **646** (2002) 220–256, arXiv:hep-ph/0207004.
[447] C. Anastasiou, L. J. Dixon, and K. Melnikov, "NLO Higgs boson rapidity distributions at hadron colliders," *Nucl. Phys. B Proc. Suppl.* **116** (2003) 193–197, arXiv:hep-ph/0211141.
[448] C. Anastasiou, L. J. Dixon, K. Melnikov, and F. Petriello, "Dilepton rapidity distribution in the Drell-Yan process at NNLO in QCD," *Phys. Rev. Lett.* **91** (2003) 182002, arXiv:hep-ph/0306192.
[449] C. Anastasiou, C. Duhr, F. Dulat, E. Furlan, F. Herzog, and B. Mistlberger, "Soft expansion of double-real-virtual corrections to Higgs production at N^3LO," *JHEP* **08** (2015) 051, arXiv:1505.04110 [hep-ph].
[450] R. Britto, "Loop Amplitudes in Gauge Theories: Modern Analytic Approaches," *J. Phys. A* **44** (2011) 454006, arXiv:1012.4493 [hep-th].
[451] R. N. Lee, "Presenting litered: a tool for the loop integrals reduction." 2012.
[452] R. N. Lee, "LiteRed 1.4: a powerful tool for reduction of multiloop integrals," *J. Phys. Conf. Ser.* **523** (2014) 012059, arXiv:1310.1145 [hep-ph].
[453] N. E. J. Bjerrum-Bohr, A. Cristofoli, P. H. Damgaard, and H. Gomez, "Scalar-Graviton Amplitudes," *JHEP* **11** (2019) 148, arXiv:1908.09755 [hep-th].
[454] D. Kosmopoulos, "Simplifying D-dimensional physical-state sums in gauge theory and gravity," *Phys. Rev. D* **105** no. 5, (2022) 056025, arXiv:2009.00141 [hep-th].
[455] D. Amati, M. Ciafaloni, and G. Veneziano, "Classical and Quantum Gravity Effects from Planckian Energy Superstring Collisions," *Int. J. Mod. Phys. A* **3** (1988) 1615–1661.
[456] D. Amati, M. Ciafaloni, and G. Veneziano, "Superstring Collisions at Planckian Energies," *Phys. Lett. B* **197** (1987) 81.
[457] D. Amati, M. Ciafaloni, and G. Veneziano, "Higher Order Gravitational Deflection and Soft Bremsstrahlung in Planckian Energy Superstring Collisions," *Nucl. Phys. B* **347** (1990) 550–580.
[458] D. Amati, M. Ciafaloni, and G. Veneziano, "Planckian Scattering Beyond the Semiclassical Approximation," *Phys. Lett. B* **289** (1992) 87–91.
[459] M. M. Anber and J. F. Donoghue, "On the running of the gravitational constant," *Phys. Rev. D* **85** (2012) 104016, arXiv:1111.2875 [hep-th].
[460] T. Kinoshita, "Mass singularities of Feynman amplitudes," *J. Math. Phys.* **3** (1962) 650–677.

[461] T. D. Lee and M. Nauenberg, "Degenerate Systems and Mass Singularities," *Phys. Rev.* **133** (1964) B1549–B1562.
[462] H. Hannesdottir and M. D. Schwartz, "S -Matrix for massless particles," *Phys. Rev. D* **101** no. 10, (2020) 105001, arXiv:1911.06821 [hep-th].
[463] H. Hannesdottir and M. D. Schwartz, "Finite S matrix," *Phys. Rev. D* **107** no. 2, (2023) L021701, arXiv:1906.03271 [hep-th].
[464] C. W. Bauer, S. Fleming, and M. E. Luke, "Summing Sudakov logarithms in $B \to X_s\gamma$in effective field theory.," *Phys. Rev. D* **63** (2000) 014006, arXiv:hep-ph/0005275.
[465] C. W. Bauer and A. V. Manohar, "Shape function effects in B —> X(s) gamma and B —> X(u) l anti-nu decays," *Phys. Rev. D* **70** (2004) 034024, arXiv:hep-ph/0312109.
[466] S. W. Bosch, B. O. Lange, M. Neubert, and G. Paz, "Factorization and shape function effects in inclusive B meson decays," *Nucl. Phys. B* **699** (2004) 335–386, arXiv:hep-ph/0402094.
[467] G. Sterman, "Mass divergences in annihilation processes. i. origin and nature of divergences in cut vacuum polarization diagrams," *Phys. Rev. D* **17** (May, 1978) 2773–2788. https://link.aps.org/doi/10.1103/PhysRevD.17.2773.
[468] G. Sterman, "Mass divergences in annihilation processes. ii. cancellation of divergences in cut vacuum polarization diagrams," *Phys. Rev. D* **17** (May, 1978) 2789–2799. https://link.aps.org/doi/10.1103/PhysRevD.17.2789.
[469] T. Becher and M. Neubert, "Infrared singularities of scattering amplitudes in perturbative QCD," *Phys. Rev. Lett.* **102** (2009) 162001, arXiv:0901.0722 [hep-ph]. [Erratum: Phys.Rev.Lett. 111, 199905 (2013)].
[470] Z. Bern, J. Parra-Martinez, and E. Sawyer, "Structure of two-loop SMEFT anomalous dimensions via on-shell methods," *JHEP* **10** (2020) 211, arXiv:2005.12917 [hep-ph].
[471] D. C. Dunbar and P. S. Norridge, "Infinities within graviton scattering amplitudes," *Class. Quant. Grav.* **14** (1997) 351–365, arXiv:hep-th/9512084.
[472] D. Chowdhury, P. Haldar, and A. Zahed, "Locality and analyticity of the crossing symmetric dispersion relation," *JHEP* **10** (2022) 180, arXiv:2205.13762 [hep-th].
[473] Y.-Z. Li, "Effective field theory bootstrap, large-N χPT and holographic QCD," *JHEP* **01** (2024) 072, arXiv:2310.09698 [hep-th].
[474] C. Song, "Crossing-Symmetric Dispersion Relations without Spurious Singularities," *Phys. Rev. Lett.* **131** no. 16, (2023) 161602, arXiv:2305.03669 [hep-th].
[475] J. Berman, "Analytic Bounds on the Spectrum of Crossing Symmetric S-Matrices," arXiv:2410.01914 [hep-th].
[476] A. Zahed, "A Review on Crossing Symmetric Dispersion Relations in QFTs and CFTs," *Springer Proc. Phys.* **277** (2022) 901–904.
[477] W. Rudin, *Fourier Analysis on Groups*. Wiley Classics Library. John Wiley & Sons, Nashville, TN, Jan., 1990.
[478] R. Contino, A. Falkowski, F. Goertz, C. Grojean, and F. Riva, "On the Validity of the Effective Field Theory Approach to SM Precision Tests," *JHEP* **07** (2016) 144, arXiv:1604.06444 [hep-ph].
[479] A. Garcon *et al.*, "The cosmic axion spin precession experiment (CASPEr): a dark-matter search with nuclear magnetic resonance," *Quantum Sci. Technol.* **3** no. 1, (2017) 014008, arXiv:1707.05312 [physics.ins-det].
[480] C. Gao, W. Halperin, Y. Kahn, M. Nguyen, J. Schütte-Engel, and J. W. Scott, "Axion Wind Detection with the Homogeneous Precession Domain of Superfluid Helium-3," *Phys. Rev. Lett.* **129** no. 21, (2022) 211801, arXiv:2208.14454 [hep-ph].
[481] J. W. Foster, C. Gao, W. Halperin, Y. Kahn, A. Mande, M. Nguyen, J. Schütte-Engel, and J. W. Scott, "Statistics and sensitivity of axion wind detection with the homogeneous precession domain of superfluid helium-3," *Phys. Rev. D* **110** no. 11, (2024) 115020, arXiv:2310.07791 [hep-ph].
[482] C. Brandenstein, S. Stelzl, E. Gutsmiedl, W. Schott, A. Weiler, and P. Fierlinger, "Towards an electrostatic storage ring for fundamental physics measurements," *EPJ Web Conf.* **282** (2023) 01017, arXiv:2211.08439 [hep-ex].
[483] I. M. Bloch, Y. Hochberg, E. Kuflik, and T. Volansky, "Axion-like Relics: New Constraints from Old

Comagnetometer Data," *JHEP* **01** (2020) 167, arXiv:1907.03767 [hep-ph].
[484] D. Aybas, H. Bekker, J. W. Blanchard, D. Budker, G. P. Centers, N. L. Figueroa, A. V. Gramolin, D. F. J. Kimball, A. Wickenbrock, and A. O. Sushkov, "Quantum sensitivity limits of nuclear magnetic resonance experiments searching for new fundamental physics," *Quantum Sci. Technol.* **6** no. 3, (2021) 034007, arXiv:2103.06284 [quant-ph].
[485] Y. Zhang, D. A. Tumturk, H. Bekker, D. Budker, D. F. J. Kimball, A. O. Sushkov, and A. Wickenbrock, "Frequency-scanning considerations in axionlike dark matter spin-precession experiments," *Annalen der Physik* **536** no. 1, (2023) 2300223.
[486] **DMRadio** Collaboration, L. Brouwer *et al.*, "Proposal for a definitive search for GUT-scale QCD axions," *Phys. Rev. D* **106** no. 11, (2022) 112003, arXiv:2203.11246 [hep-ex].
[487] A. Berlin *et al.*, "Searches for New Particles, Dark Matter, and Gravitational Waves with SRF Cavities," arXiv:2203.12714 [hep-ph].
[488] J. L. Ouellet *et al.*, "Design and implementation of the ABRACADABRA-10 cm axion dark matter search," *Phys. Rev. D* **99** no. 5, (2019) 052012, arXiv:1901.10652 [physics.ins-det].
[489] E. Boyers, G. Goldstein, and A. O. Sushkov, "Spin squeezing of macroscopic nuclear spin ensembles," *Phys. Rev. D* **111** no. 5, (2025) 052004, arXiv:2502.14103 [hep-ph].
[490] A. Banerjee, I. M. Bloch, Q. Bonnefoy, S. A. R. Ellis, G. Perez, I. Savoray, K. Springmann, and Y. V. Stadnik, "Momentum and Matter Matter for Axion Dark Matter Matters on Earth," arXiv:2502.04455 [hep-ph].
[491] J. Henriksson, B. McPeak, F. Russo, and A. Vichi, "Rigorous bounds on light-by-light scattering," *JHEP* **06** (2022) 158, arXiv:2107.13009 [hep-th].
[492] J. Distler, B. Grinstein, R. A. Porto, and I. Z. Rothstein, "Falsifying Models of New Physics via WW Scattering," *Phys. Rev. Lett.* **98** (2007) 041601, arXiv:hep-ph/0604255.
[493] M. F. Paulos, J. Penedones, J. Toledo, B. C. van Rees, and P. Vieira, "The S-matrix bootstrap. Part I: QFT in AdS," *JHEP* **11** (2017) 133, arXiv:1607.06109 [hep-th].
[494] M. F. Paulos, J. Penedones, J. Toledo, B. C. van Rees, and P. Vieira, "The S-matrix bootstrap II: two dimensional amplitudes," *JHEP* **11** (2017) 143, arXiv:1607.06110 [hep-th].
[495] J. Albert, J. Henriksson, L. Rastelli, and A. Vichi, "Bootstrapping mesons at large N: Regge trajectory from spin-two maximization," *JHEP* **09** (2024) 172, arXiv:2312.15013 [hep-th].
[496] Z.-Y. Dong, T. Ma, A. Pomarol, and F. Sciotti, "Bootstrapping the Chiral-Gravitational Anomaly," arXiv:2411.14422 [hep-th].